Simulation Studies and Characterisation of Monolithic Silicon Pixel-Detector Prototypes for Future Collider Detectors

&

Unsupervised Anomaly Detection in Belle II Pixel-Detector Data

Katharina Dort

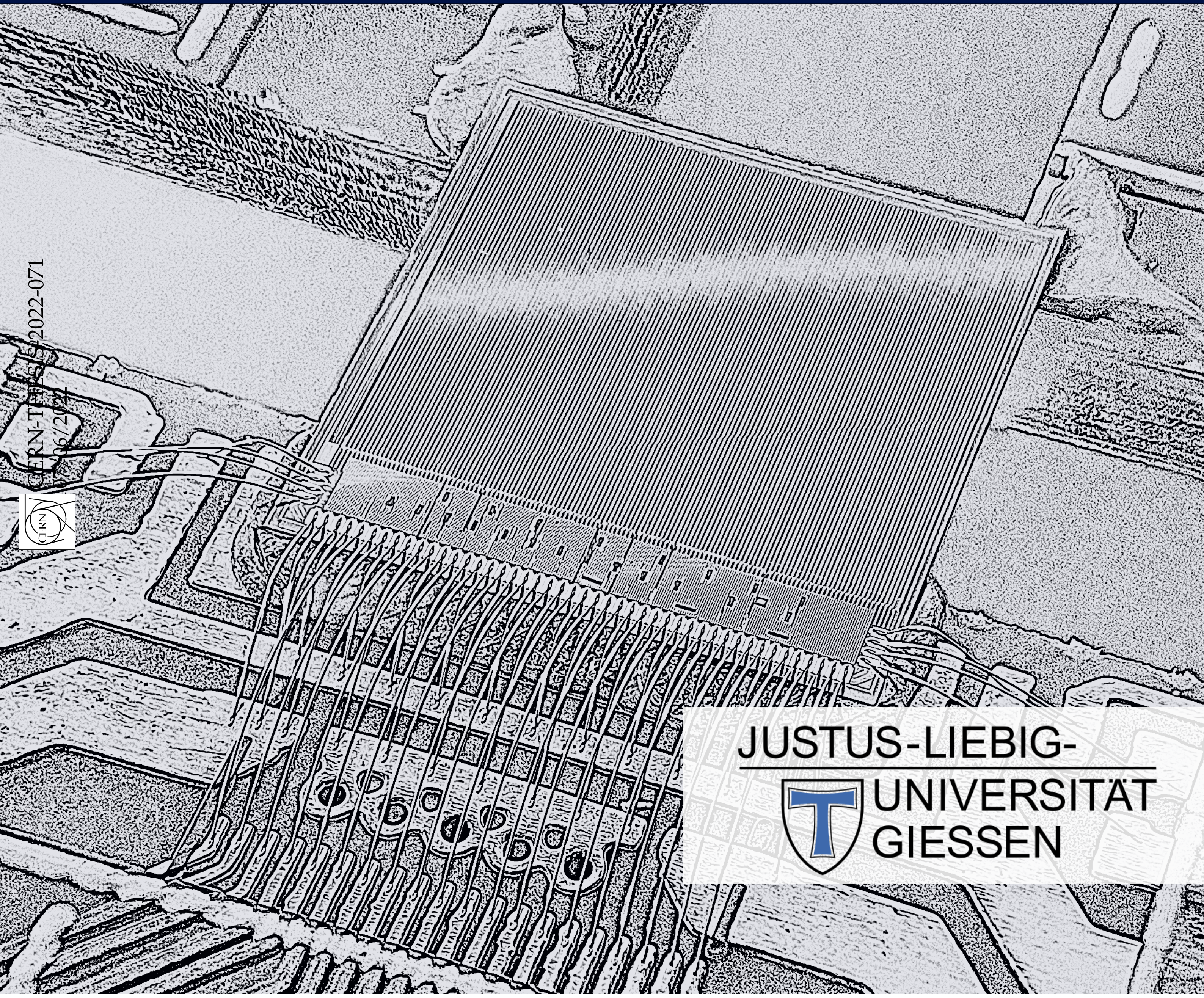

CERN-THESIS-2022-071
07/06/2022

JUSTUS-LIEBIG-
UNIVERSITÄT
GIESSEN

Simulation Studies and Characterisation of Monolithic Silicon Pixel-Detector Prototypes for Future Collider Detectors

&

Unsupervised Anomaly Detection in Belle II Pixel-Detector Data

Simulation Studies and Characterisation of Monolithic Silicon Pixel-Detector Prototypes for Future Collider Detectors & Unsupervised Anomaly Detection in Belle II Pixel-Detector Data

INAUGURALDISSERTATION

zur Erlangung des Doktorgrades am

FACHBEREICH MATHEMATIK UND INFORMATIK, PHYSIK, GEOGRAPHIE

der

JUSTUS-LIEBIG-UNIVERSITÄT GIESSEN

vorgelegt von

Katharina Dort

Gießen 2022

Aus dem II. Physikalischen Institut

Dekan: Prof. Dr. Stefan Björn Hennemann
Gutachter: apl. Prof. Dr. Jens Sören Lange
Gutachter: Prof. Dr. Michael Düren

To my loving family

Abstract

Present and future high-energy physics experiments pose challenging demands on the detector systems and analysis methods. This dissertation addresses both aspects by focusing on the optimisation and characterisation of a novel technology demonstrator for a monolithic silicon sensor design and the development of model-agnostic analysis techniques for the pixel detector at the Belle II experiment.

In the first part, the requirements of vertex and tracking detectors for future Higgs factories such as the Compact Linear e^+e^-– Collider (CLIC) or the Future Circular e^+e^-– Collider (FCCee) are addressed. The experimental conditions at these colliders require high-precision sensors with a low material content. The CLIC Tracker Detector (CLICTD) is a technology demonstrator for a monolithic pixel sensor fabricated in a modified 180 nm CMOS imaging process that targets the requirements of the CLIC tracker. The performance of the sensor is assessed for different operation conditions, pixel designs and wafer materials. A spatial resolution down to (3.9 ± 0.2) µm, time resolution down to (4.8 ± 0.1) ns as well as a hit detection efficiency >99.7 % over a wide range of detection thresholds is observed and the CLIC tracker requirements are found to be fulfilled.

Modern silicon sensors such as CLICTD incorporate complex sensor designs that are challenging to simulate and model. This dissertation presents a combination of electrostatic finite-element and transient Monte Carlo simulations to provide simultaneous access to precise sensor modelling and high-statistics simulation samples. The advanced simulation approach is validated against data and excellent agreement is found over a wide range of different operation conditions.

In the second part, patterns of minimally-processed pixel hits recorded by the Belle II pixel detector are investigated. In particular, a focus on model-agnostic approaches is placed that enable an unbiased exploration of data, while filtering out anomalous detector signatures that could hint at new physics scenarios. The identification of hypothetical magnetic monopoles against Belle II beam background is presented using Self-Organizing Kohonen Maps and Autoencoders. The two unsupervised algorithms are compared to a convolutional Multilayer Perceptron and a superior signal efficiency at high background-rejection levels is found for the unsupervised techniques.

Zusammenfassung

Heutige und zukünftige Experimente der Hochenergiephysik stellen hohe Anforderungen an die Detektorsysteme und Analysemethoden. Diese Dissertation befasst sich mit beiden Aspekten, indem sie sich auf die Charakterisierung eines neuartigen Technologiedemonstrators für ein monolithisches Silizium-Sensordesign und die Entwicklung von modellagnostischen Analysetechniken für den Pixeldetektor des Belle II Experiments konzentriert.

Im ersten Teil werden die Anforderungen an Vertex- und Tracker-Detektoren für zukünftige Higgs-Fabriken wie den Compact Linear e^+e^-– Collider (CLIC) oder den Future Circular e^+e^-– Collider (FCCee) behandelt. Die experimentellen Bedingungen an diesen Collidern erfordern hochpräzise Sensoren mit geringem Materialeinsatz. Der CLIC Tracker Detector (CLICTD) ist ein monolithischer Pixelsensor, der in einem modifizierten 180 nm CMOS Imaging Prozess hergestellt wird und die Anforderungen des CLIC Trackers anvisiert. Die Leistung des Sensors wird für verschiedene Betriebsbedingungen, Sensordesigns und Wafermaterialien bewertet, und es wird eine räumliche Auflösung von bis zu $3.9 \pm 0.2\,\mu\text{m}$, eine zeitliche Auflösung von bis zu $4.8 \pm 0.1\,\text{ns}$ sowie eine Detektionseffizienz besser als $99.7\,\%$ über einen breiten Schwellwertbereich gemessen, was die Anforderungen des CLIC-Trackers erfüllt.

Sensoren wie CLICTD verfügen über komplexe Sensordesigns, deren Simulation und Modellierung eine Herausforderung darstellt. In dieser Dissertation wird eine Kombination aus elektrostatischen Finite-Elemente- und transienten Monte-Carlo-Simulationen vorgestellt, die einen simultanen Zugang zu präziser Sensormodellierung und hoher Statistik ermöglichen. Der fortschrittliche Simulationsansatz wird anhand von Daten validiert, und es wird eine hervorragende Übereinstimmung über einen weiten Bereich unterschiedlicher Betriebsbedingungen festgestellt.

Im zweiten Teil werden Muster in Belle II Pixeldetektordaten untersucht. Insbesondere wird ein Schwerpunkt auf modellagnostische Ansätze gelegt, die eine unvoreingenommene Untersuchung der Daten ermöglichen und gleichzeitig anomale Detektorsignaturen herausfiltern, die auf neue physikalische Szenarien hindeuten könnten. Die Identifizierung hypothetischer magnetischer Monopole gegen Untergrund mit Hilfe von selbstorganisierenden Kohonenkarten und Autoencodern wird vorgestellt. Die beiden unüberwacht lernenden Algorithmen werden mit einem überwachten mehrlagigem Perzeptron verglichen, und es wird festgestellt, dass die unüberwachten Verfahren bei hoher Hintergrundunterdrückung eine bessere Signaleffizienz aufweisen.

Contents

Abstract v

Zusammenfassung vii

Contents ix

List of Figures xvii

List of Tables xxvii

Introduction 1

I Characterisation of Silicon Sensors 5

1 Introduction to Particle Physics 7

- 1.1 The Standard Model of Particle Physics . . . 7
  - 1.1.1 Particles and Interactions . . . 8
  - 1.1.2 Physics Beyond the Standard Model . . . 9
- 1.2 The Compact Linear Collider . . . 10
  - 1.2.1 Physics Case . . . 10
  - 1.2.2 CLIC Accelerator . . . 11
  - 1.2.3 Detector Concept . . . 12
  - 1.2.4 The CLIC Tracking System . . . 13

2 Fundamentals of Semiconductor Physics 15

- 2.1 Band Structure . . . 16
- 2.2 Intrinsic and Extrinsic Semiconductors . . . 17
- 2.3 Energy Deposition of Ionising Radiation . . . 18
  - 2.3.1 Energy Deposition of Charged Particles . . . 18
  - 2.3.2 Energy Deposition of Photons . . . 20
- 2.4 Charge Carrier Propagation . . . 21

2.4.1 Mobility 21
2.4.2 Drift 22
2.4.3 Diffusion 22
2.5 Charge Carrier Generation-Recombination Models 22
2.5.1 Shockley-Read-Hall Recombination 23
2.5.2 Auger Recombination 24
2.6 The pn-Junction 25
2.6.1 Application of External Voltage 26
2.6.2 Capacitance 26
2.6.3 Current-Voltage Characteristics 26

3 Silicon Pixel Detector Concepts 27
3.1 Signal Formation 27
3.2 Front-End Electronics 28
3.3 Electronics Noise Sources 30
3.4 Fabrication of Silicon Sensors 31
3.4.1 Fabrication of Silicon Wafers 32
3.4.2 Doping 32
3.5 Silicon Pixel Detector Types 32
3.5.1 Hybrid Pixel Detectors 33
3.5.2 Monolithic Pixel Detectors 34

4 The CLIC Tracker Detector Technology Demonstrator 37
4.1 The Sensor Design 38
4.2 The CLICTD Detection Channel 40
4.2.1 Analogue Front-End 41
4.2.2 Digital Logic 41
4.3 The Periphery and Interface 43
4.3.1 Injection of Test Pulses 43
4.4 Mode of Operation 44
4.4.1 Power Consumption 45
4.5 Overview of the CLICTD Sensor Types and Operation Conditions 46
4.6 Optimisation of Operation Parameters 47
4.6.1 Operation of High-Resistivity Czochralski Sensors 48

5 Laboratory Setups and Methodologies 51
5.1 The Caribou Data Acquisition System 51
5.2 The CLICTD Chipboard 53

5.3 X-ray Measurement Setup . . . 55
5.4 Sensitivity to Light and Temperature . . . 55
5.5 Methodology . . . 56
5.5.1 Current-Voltage Characterisation . . . 57
5.5.2 Threshold Calibration . . . 57
5.5.3 Equalisation . . . 58
5.5.4 Noise Characterisation . . . 59
5.5.5 Minimum Operation Threshold . . . 59
5.5.6 ToT Calibration . . . 59
5.5.7 Front-End Time Resolution . . . 60

6 Results of Laboratory Measurements 63
6.1 Current-Voltage Characteristics . . . 63
6.2 Threshold Calibration . . . 68
6.2.1 Determination of Signal Gain . . . 69
6.3 Equalisation . . . 72
6.4 Noise Characterisation . . . 74
6.5 Minimum Operation Threshold . . . 75
6.6 ToT Calibration . . . 78
6.6.1 Calibration of Test-Pulse Amplitude . . . 78
6.6.2 ToT-to-Voltage Conversion . . . 78
6.6.3 Voltage-to-Electrons Conversion . . . 82
6.6.4 Limitations of the ToT Calibration . . . 84
6.7 Front-End Time Resolution . . . 85
6.8 Conclusion . . . 87

7 The DESY II Test-Beam Facility and Reference Telescope 89
7.1 DESY II Test-Beam Facility . . . 89
7.2 The Reference Telescope . . . 90
7.3 Operation of the Device-Under-Test . . . 92
7.4 Rotation of the Device Under Test . . . 94

8 Test-Beam Reconstruction and Analysis 95
8.1 Reconstruction . . . 95
8.1.1 Offline Pixel Masking . . . 96
8.1.2 Event Building . . . 97
8.1.3 Clustering . . . 98
8.1.4 Correlations . . . 99

8.1.5 Particle-Track Reconstruction 99
8.1.6 Track-Cluster Association 100
8.2 Telescope and DUT Alignment 100
8.3 Cluster Position Reconstruction 102
8.4 Performance Evaluation 105
8.4.1 Cluster Size 105
8.4.2 Hit-Detection Efficiency 105
8.4.3 Spatial Resolution 105
8.4.4 Time Resolution 106
8.5 Uncertainties 106

9 Performance in Test-Beam Measurements 109
9.1 Charge Sharing 110
9.2 Signal 120
9.3 Hit-Detection Efficiency 121
9.4 Spatial Resolution 127
9.5 Time Resolution 134
9.6 Performance with Inclined Particle Tracks 141
9.7 Estimation of Active Depth 147
9.8 Alternative Cluster Position Reconstruction 150
9.8.1 Multilayer Perceptron 151
9.9 Conclusion 154

10 Simulation Approach 157
10.1 Finite-Element Simulations 157
10.1.1 Geometry 158
10.1.2 Electrostatic Simulation 161
10.1.3 Transient Simulation 162
10.1.4 Limitations 163
10.2 Monte Carlo Simulations 164
10.2.1 The Allpix Squared Simulation Framework 164

11 Validation and Application of Simulation 169
11.1 Validation of the Simulation 169
11.1.1 Systematic Uncertainties 170
11.1.2 Comparison to Transient 3D TCAD 170
11.1.3 Uncertainty on Doping Profiles 171
11.1.4 Comparison to Test-Beam Data 173

11.2 Application of the Simulation 179
  11.2.1 Sensor Capacitance 179
  11.2.2 Depletion Depth for Sensors with Epitaxial Layer 181
  11.2.3 Depletion Depth for Sensors on Czochralski Wafers 182
  11.2.4 Transient Current Pulses 186
  11.2.5 Charge Carrier Recombination 187
  11.2.6 Active Depth 188
  11.2.7 Systematic Uncertainties in X-ray Measurement 190
  11.2.8 Sensor Time-Resolution Studies 191
11.3 Conclusion 193

II Anomaly Detection in Belle II Pixel-Detector Data 195

12 The Belle II Experiment 197
12.1 Physics Motivation 197
12.2 The SuperKEKB Collider 198
  12.2.1 Luminosity 199
12.3 The Belle II Detector 199
  12.3.1 The Vertex Detector (VXD) 200
  12.3.2 The Central Drift Chamber (CDC) 201
  12.3.3 Particle Identification 201
  12.3.4 Electromagnetic Calorimeter (ECL) 202
  12.3.5 Superconducting Solenoid 202
  12.3.6 K_L and Muon Detector (KLM) 202
12.4 The Pixel Detector (PXD) 203
  12.4.1 The DEPFET Pixel Sensors 204
  12.4.2 The PXD Module 204
12.5 The Trigger System 205
12.6 The Data Acquisition System 205
  12.6.1 The PXD Data Acquisition 205
12.7 Background at the Belle II PXD 206
  12.7.1 Beam-Induced Background 206
  12.7.2 Luminosity-Dependent Background 207
  12.7.3 Conclusion 208
12.8 The Belle II Analysis Software Framework 208
  12.8.1 Full-Detector Simulation 209
  12.8.2 Background Simulation 209

13 Highly-Ionising Particles **211**
13.1 Magnetic Monopoles 211
13.1.1 Production Mechanism 212
13.1.2 Energy Loss in Matter 213
13.1.3 Trajectory in a Magnetic Field 213
13.1.4 Detection Sensitivity in the Belle II Detector 214

14 Machine Learning Techniques **217**
14.1 Supervised and Unsupervised Training 217
14.2 Artificial Neural Networks 218
14.3 Self-Organising Maps 219
14.3.1 The Learning Algorithm 220
14.4 Autoencoder 220
14.5 Performance Metrics 221
14.5.1 Receiver Operating Characteristic 222
14.5.2 Performance Evaluation 222

15 Reconstruction Strategy and Pre-Processing **225**
15.1 Event Simulation and Selection 225
15.2 Object Reconstruction 226

16 Comparison of Supervised and Unsupervised Anomaly Detection **229**
16.1 Supervised Multi-Layer Perceptron 229
16.2 Self-Organising Maps 231
16.3 Autoencoder 233
16.3.1 Signal in Training Data 236
16.3.2 Size of Pixel Matrix 236
16.3.3 Simulated Background 237
16.3.4 Different Background Sources 238
16.3.5 Monopole Mass 239
16.3.6 Monopoles and Anti-Monopoles 240
16.3.7 Extensions to the Autoencoder 241
16.3.8 Conclusion 242
16.4 Search for Anomalies in Data 243

17 Summary and Prospects **245**

A Mobility Parametrisation **251**

B Default CLICTD Configuration 253

C Simulation Parameters of TCAD 255

D Allpix Squared Configuration Files 257

E Corryvreckan Configuration Files 259

F Architecture of Machine Learning Algorithms for Anomaly Detection 265

G List of Publications 267

H Contributions From the Author 269

Bibliography 271

Acknowledgements 297

List of Figures

1.1 Schematic of the CLIC accelerator design at the final energy stage 11
1.2 Schematic of the CLIC detector design 12

2.1 Schematic representation of the energy band configuration in conductors, semiconductors and insulators 16
2.2 Schematic representation of the energy bands in n-doped and p-doped semiconductors 18
2.3 Schematic representation of the Shockley-Read-Hall and Auger recombination mechanisms 23

3.1 Schematic block diagram of a typical front-end processing chain 28
3.2 Schematic representation of the Time-over-Threshold (ToT) and Time-of-Arrival (ToA) computation 30
3.3 Schematic representation of time walk 31
3.4 Schematic representation of a bump-bonded hybrid assembly 33
3.5 Schematic representation of a large collection-electrode monolithic CMOS sensor 33
3.6 Schematic representation of a small collection-electrode monolithic CMOS sensor 33

4.1 Layout of the CLICTD chip 38
4.2 Different pixel flavours of the modified 180 nm CMOS imaging process . . 39
    4.2a No n-implant 39
    4.2b Continuous n-implant 39
    4.2c Segmented n-implant 39
    4.2d Extra p-well 39
4.3 Schematic of the CLICTD detection channel 41
4.4 Block diagram of the CLICTD detection channel 42

5.1 Picture of the Caribou setup 52
5.2 Custom Printed Circuit Board (PCB) for the CLICTD sensor 54

  - 5.2a PCB without cut-out below the sensor. 54
  - 5.2b PCB with cut-out below the sensor. 54
- 5.3 Schematic of the setup for X-ray fluorescence measurements 56

- 6.1 IV curves for different pixel flavours 64
  - 6.1a Substrate current. 64
  - 6.1b P-well current 64
- 6.2 IV curves for different p-well bias voltages 65
  - 6.2a Substrate current. 65
  - 6.2b P-well current 65
- 6.3 IV curves for different sensor thicknesses 66
  - 6.3a Substrate current. 66
  - 6.3b P-well current 66
- 6.4 IV curves for different wafer materials 66
  - 6.4a Substrate current. 66
  - 6.4b P-well current. 66
- 6.5 Threshold in units of voltage as a function of internal threshold DAC settings 67
- 6.6 X-ray occupancy curve for a titanium sample 67
- 6.7 X-ray fluorescence curve for a titanium sample 67
- 6.8 Energy calibration of the detection threshold 68
- 6.9 Gain as a function of the bias voltage 70
- 6.10 Gain as a function of substrate bias voltage 71
- 6.11 Gain for different n-implant doses 71
- 6.12 Sub-pixel baseline distributions 71
  - 6.12a All trim DAC settings. 71
  - 6.12b Central trim DAC settings and equalised matrix. 71
- 6.13 Sub-pixel baseline mapped onto the CLICTD pixel matrix after threshold equalisation 72
- 6.14 Threshold dispersion as a function of the bias voltage 73
- 6.15 Threshold dispersion for different n-implant doses 73
- 6.16 Single sub-pixel noise distribution 74
- 6.17 Single sub-pixel noise mapped onto the CLICTD pixel matrix. 75
- 6.18 Single sub-pixel noise as a function of the bias voltages. 76
- 6.19 Single sub-pixel noise for different n-implant doses 76
- 6.20 Noise hits for the entire pixel matrix versus detection threshold 76
- 6.21 Minimum operation threshold as a function of the bias voltage 77
- 6.22 Minimum operation threshold for different n-implant doses 77

6.23 Calibration of test-pulse DACs 78
  6.23a Calibration of `VANALOG1` 78
  6.23b Calibration of `VANALOG2` 78
6.24 ToT as a function of the injected test-pulse signal 79
  6.24a Sub-pixel with fast return to baseline 79
  6.24b Sub-pixel with slow return to baseline 79
6.25 Surrogate function fit parameter distributions 80
  6.25a Parameter a 80
  6.25b Parameter b 80
  6.25c Parameter c 80
  6.25d Parameter t 80
6.26 Surrogate function fit parameters across the CLICTD matrix 81
  6.26a Parameter a 81
  6.26b Parameter b 81
  6.26c Parameter c 81
  6.26d Parameter t 81
6.27 Fit χ^2/ndof distribution of the surrogate function fit 82
6.28 χ^2/ndof of the surrogate function fit mapped across the CLICTD matrix 82
6.29 Derivative of the occupancy curve for test-pulse injection with varying amplitudes 83
6.30 Energy calibration of the test-pulse signal 83
6.31 Distribution of the fit parameter p_0 for the conversion of test-pulse voltage levels to physical units 83
6.32 Fit parameter p_0 mapped across the CLICTD pixel matrix 84
6.33 Mean sub-pixel ToA mapped across the CLICTD pixel matrix 86
  6.33a Digital test-pulse injection 86
  6.33b Analogue test-pulse injection 86
6.34 Time residuals between the ToA values recorded for analogue and digital test-pulse injection 87
  6.34a Before time-walk correction. 87
  6.34b After time-walk correction. 87
6.35 Time resolution of the analogue front-end as a function of the recorded ToT value 88

7.1 Schematic of the test-beam generation at the DESY II Test Beam Facility 90
7.2 Telescope setup at the DESY II Test-Beam Facility 91
7.3 CLICTD triggered shutter-close readout scheme 92

7.4 Beam telescope setup with a rotated DUT. 93

8.1 Schematic of the Corryvreckan reconstruction and analysis chain 96
8.2 Schematic of the Corryvreckan event building scheme 97
8.3 Correlation distributions between the DUT and reference plane 99
    8.3a Spatial correlations 99
    8.3b Time correlations 99
8.4 Schematic of the Corryvreckan alignment chain. 101
8.5 Track χ^2 distribution 102
8.6 η-distribution for 2-pixel clusters in row direction 104
8.7 Distribution of kink angles at a MIMOSA-26 detector plane 108
8.8 Distribution of track angles 108

9.1 Total cluster size distribution : standard configuration 110
9.2 Cluster size distribution in row/column direction : standard configuration 111
    9.2a Column direction 111
    9.2b Row direction 111
9.3 In-pixel representation of the total cluster size for a sensor in standard configuration. 111
9.4 In-pixel cluster size in column/row direction : standard configuration . . 112
    9.4a Column direction 112
    9.4b Row direction 112
9.5 Cluster size versus threshold : standard configuration 113
9.6 Total Cluster size versus threshold : different p-well bias voltage 113
9.7 Cluster size versus threshold : different pixel flavours 115
9.8 Cluster size in column/row direction versus threshold : different pixel flavours 115
    9.8a Column direction 115
    9.8b Row direction 115
9.9 Cluster size versus threshold : different sensor thickness 117
    9.9a Continuous n-implant 117
    9.9b Segmented n-implant 117
9.10 Cluster size as a function of detection threshold for different wafer materials 118
9.11 Mean cluster size versus bias voltage : high-resistivity Czochralski samples 119
    9.11a Segmented n-implant 119
    9.11b Extra deep p-well 119
9.12 Cluster seed charge for two pixel flavours 120
9.13 In-pixel representation of the cluster seed charge for the standard configuration 121

9.14 Efficiency as a function of the cluster-track association cut 122
9.15 Detection efficiency versus threshold : standard configuration 122
  9.15a Full range 122
  9.15b Close-up of high-efficiency region 122
9.16 In-pixel efficiency : standard configuration 124
9.17 Detection efficiency versus threshold : different p-well bias voltage 124
9.18 Detection efficiency versus threshold : different pixel flavours 125
9.19 Detection efficiency versus threshold : different sensor thickness 126
  9.19a Continuous n-implant 126
  9.19b Segmented n-implant 126
9.20 Detection efficiency versus threshold : different wafer material 126
9.21 Detection efficiency versus bias voltage for samples on high-resistivity Czochralski wafer 127
  9.21a Segmented n-implant 127
  9.21b Extra deep p-well 127
9.22 Spatial resolution versus association cut 128
  9.22a Column direction 128
  9.22b Row direction 128
9.23 Spatial residuals for the standard configuration 129
  9.23a Column direction 129
  9.23b Row direction 129
9.24 In-pixel spatial resolution : standard configuration 130
  9.24a Before η-correction 130
  9.24b After η-correction 130
9.25 Spatial resolution versus threshold : standard configuration 131
  9.25a Column direction 131
  9.25b Row direction 131
9.26 Spatial resolution versus threshold : different p-well bias voltages 131
  9.26a Column direction 131
  9.26b Row direction 131
9.27 Spatial resolution versus threshold : different pixel flavours 132
  9.27a Column direction 132
  9.27b Row direction 132
9.28 Spatial resolution versus threshold : different sensor thickness 133
  9.28a Continuous n-implant 133
  9.28b Segmented n-implant 133
9.29 Spatial resolution versus threshold : different wafer material 135

9.30 Spatial resolution versus substrate bias voltage: high-resistivity Czochralski wafer . . . 135
  9.30a Segmented n-implant . . . 135
  9.30b Extra deep p-well . . . 135
9.31 Time residuals versus seed pixel ToT : standard configuration . . . 136
  9.31a Before time-walk correction . . . 136
  9.31b After time-walk correction . . . 136
9.32 Time residual distribution : standard configuration . . . 137
  9.32a Before time-walk correction . . . 137
  9.32b After time-walk correction . . . 137
9.33 In-pixel time residuals : standard configuration . . . 138
  9.33a Before time-walk correction . . . 138
  9.33b After time-walk correction . . . 138
9.34 Time resolution versus threshold: standard configuration . . . 138
9.35 Time resolution versus threshold: different pixel flavours . . . 139
9.36 Time resolution versus threshold: different sensor thickness . . . 140
  9.36a Continuous n-implant . . . 140
  9.36b Segmented n-implant . . . 140
9.37 Time resolution versus threshold: different wafer materials . . . 141
9.38 Time resolution versus bias voltage : high-resistivity Czochralski wafer . 142
  9.38a Segmented n-implant . . . 142
  9.38b Extra deep p-well . . . 142
9.39 Cluster size in column and row direction as a function of the rotation angle 142
9.40 Cluster size versus threshold : different inclination angles . . . 143
  9.40a Column direction . . . 143
  9.40b Row direction . . . 143
9.41 In-pixel representation of the cluster size in column direction showing two different rotation angles for the standard configuration . . . 144
  9.41a Rotation angle: 5° . . . 144
  9.41b Rotation angle: 60° . . . 144
9.42 Schematic representation of inclined particle tracks impinging on a pixel cell for two different angles . . . 145
  9.42a Rotation angle: 5° . . . 145
  9.42b Rotation angle: 60° . . . 145
9.43 Detection efficiency as a function of threshold using different rotation angles for the standard configuration . . . 145

9.44 Spatial resolution as a function of the rotation angle for different position reconstruction algorithms 146
9.45 Time resolution versus threshold : different inclination angles 147
9.46 Schematic representation of the cluster size dependence on the inclination angle of the particle track 147
9.47 Cluster size in column direction as a function of the tangent of the rotation angle for the standard configuration 149
9.48 Cluster size in column direction as a function of the tangent of the rotation angle for different sensor thicknesses 149
9.49 Active depth as a function of substrate voltage for a high-resistivity Czochralski sample with segmented n-implant 151
9.50 Spatial resolution versus rotation angle : different cluster position reconstruction techniques 153

10.1 Simulated three-dimensional pixel cell of the CLICTD sensor in TCAD . 158
10.2 Schematic representation of the simulated cell. 159
10.3 Mesh of the simulated structure 161
10.4 Electrostatic potential for pixel flavour with continuous n-implant 162
10.5 Current pulses extracted from transient 3D TCAD simulations for the pixel flavour with continuous n-implant and segmented n-implant 163
10.6 Schematic of the primary simulation chain for replicating the test-beam measurements 165
10.7 Schematic of the digitization step in the simulation chain for replicating the test-beam measurements 165
10.8 Cross section of weighting potential 166

11.1 Transient current pulses for 3D TCAD and Allpix^2 171
    11.1a No n-implant 171
    11.1b Continuous n-implant 171
    11.1c Segmented n-implant 171
11.2 Cluster size in column direction for different degrees of diffusion 172
    11.2a Varied diffusion at p-wells 172
    11.2b Varied diffusion at collection electrode 172
    11.2c Varied diffusion of the substrate dopants into the epitaxial layer . 172
11.3 Cluster size distributions of the total cluster size for data and simulation 174
11.4 Cluster size distributions of the size in column/row direction for data and simulation 174
    11.4a Cluster size in column direction 174

- 11.4b Cluster size in row direction 174
11.5 Cluster size as a function of the detection threshold for data and simulation 175
- 11.5a Total cluster size 175
- 11.5b Cluster size in row direction 175

11.6 Mean cluster column size as a function of the rotation angle for data and simulation 176
11.7 Detection efficiency as a function of the applied threshold for data and simulation 177
11.8 In-pixel distribution of the detection efficiency as a function of the particle incidence position 178
- 11.8a In-pixel efficiency – Data 178
- 11.8b In-pixel efficiency – Simulation 178

11.9 Distribution of the spatial residuals between reconstructed DUT particle position and reference track for data and simulation 179
11.10 Spatial resolution as a function of the detection threshold for data and simulation 179
11.11 Two-dimensional cross section of the electrostatic potential for three different doping levels of the deep n-type implant 180
11.12 Two-dimensional cross section of the electrostatic potential for different bias voltages 181
11.13 Simulated sensor capacitance as a function of the p-well bias voltage for the three different doping levels of the deep n-implant 182
11.14 Cluster size as a function of detection threshold for data and simulations assuming different doping levels of the Czochralski wafer material 183
11.15 Electrostatic potential for high-resistivity Czochralski samples 184
11.16 Simulated depletion depth as a function of substrate voltage 184
11.17 Transient current pulses for different charge injection positions 185
- 11.17a Continuous n-implant 185
- 11.17b Segmented n-implant 185

11.18 Integrated induced charge for different charge injection positions 185
- 11.18a Continuous n-implant 185
- 11.18b Segmented n-implant 185

11.19 Transient current pulse and integrated charge using full Monte Carlo simulation including statistical fluctuations 186
- 11.19a Transient sensor response 186
- 11.19b Integrated charge 186

11.20 Two-dimensional map of the recombination rate for a cross section of the yz plane through the sensor volume 188
11.21 Mean cluster column size as a function of the tangent of the rotation angle 189
  11.21a Different thresholds 189
  11.21b Different lateral diffusion at the p-well implants. 189
11.22 Simulation of the threshold-calibration procedure 190
  11.22a Pixel hits as a function of the detection threshold 190
  11.22b Derivative of the number of pixel hits as a function of the detection threshold 190
11.23 Time residuals as a function of the highest single pixel charge in a cluster 191
  11.23a Time residuals before correction 191
  11.23b Time residuals after correction 191
11.24 Width of the threshold-crossing time as a function of the detection threshold for different pixel pitches 192
11.25 Width of the threshold-crossing time as a function of the pixel pitch at a detection threshold of 150 e 192

12.1 Schematic of the SuperKEKB collider 198
12.2 Schematic of the Belle II detector 200
12.3 PXD module consisting of the active pixel matrix and the readout ASICs 203

13.1 Trajectories of magnetically-charged particles 214
  13.1a Different monopole masses for a fixed magnetic charge of 68.5 e . 214
  13.1b Different magnetic charges for a fixed mass of 4 GeV 214

14.1 Schematic of a Multilayer Perceptron (MLP) 218
14.2 Schematic representation of a Self-Organising Map (SOM) 219
14.3 Schematic of an Autoencoder 221
14.4 Schematic of a Receiver Operating Characteristic (ROC) curve 222

15.1 Pixel matrices for background and magnetic monopoles 227
  15.1a Matrices associated with simulated magnetic monopoles with a mass of 3 GeV 227
  15.1b Matrices associated with background particles 227
15.2 PXD cluster size for beam background and simulated magnetic monopoles 227
  15.2a Cluster size in u-direction 227
  15.2b Cluster size in v-direction 227

16.1 MLP loss as a function of training epoch for training and testing set . . . 230

16.2 MLP classification distribution for signal and background 230
16.3 ROC for the Multilayer Perceptron (MLP), Self-Organizing Map (SOM) and Autoencoder (AE) 231
  16.3a Full axes range 231
  16.3b Close-up of the upper part of the ROC. 231
16.4 SOM classification distribution for signal and background. 233
16.5 Input and reconstructed pixel matrices associated with background particles 234
  16.5a Input matrices 234
  16.5b Reconstructed matrices 234
16.6 AE loss as a function of training epochs for training and testing set . . . 235
16.7 AE classification distribution for signal and background. 235
16.8 Input and reconstructed pixel matrices associated with simulated magnetic monopoles 235
  16.8a Input matrices 235
  16.8b Reconstructed matrices 235
16.9 ROC for different signal levels in the training sample 237
16.10 ROC for different sizes of the pixel matrix 237
16.11 ROC for two Autoencoders trained on clusters from real background data and from simulated background 238
16.12 ROC for Autoencoders trained on simulated clusters from different background processes 238
16.13 Cluster charge distribution from two-photon and Touschek background particles 239
16.14 ROC for Autoencoders trained on clusters from magnetic monopoles with different masses 240
16.15 ROC for Autoencoders trained on simulated clusters from monopoles and anti-monopoles 240
16.16 Cluster size in v-direction for different monopole masses 241
16.17 Cluster size in v-direction for monopoles and anti-monopoles 241
16.18 Classification distribution for data pertaining to randomly triggered events 243
16.19 Pixel matrices with classification loss exceeding 1800 244
16.20 Cluster seed charge distribution for the clusters with classification loss exceeding 1800 244

List of Tables

1.1 Elementary fermions of the Standard Model 8
1.2 Requirements for the CLIC tracker 13

4.1 Main design parameters of the CLICTD sensors 37
4.2 Selectable measurement modes in the CLICTD sensor 44
4.3 Power consumption of the CLICTD sensor 45
4.4 Overview of the tested CLICTD sensors 49

5.1 Estimation of material content X/X_0 of the CLICTD sensor and the carrier PCB 55
5.2 Energy and mean number of liberated charge carriers for the target materials used in the X-ray calibration measurements 57

9.1 Cluster size at the minimum operation threshold for two different p-well bias voltages 114
9.2 Mean cluster size at the minimum operation threshold for different pixel flavours 114
9.3 Total cluster size at the minimum operation threshold for CLICTD sensors with different thicknesses 116
9.4 Mean cluster size: different wafer material 118
9.5 Spatial resolution in row and column direction for the different bias voltages 130
9.6 Spatial resolution in row and column direction for the different pixel flavours 132
9.7 Spatial resolution in row direction at the minimum operation threshold for CLICTD sensors with different thicknesses 134
9.8 Spatial resolution at the minimum operation threshold for CLICTD sensors with different wafer materials 134
9.9 Time resolution for the different pixel flavours 139
9.10 Time resolution at the minimum operation threshold for CLICTD sensors with different thicknesses 140

9.11 Time resolution at the minimum operation threshold for CLICTD sensors with different wafer materials 141
9.12 Active depth for all investigated sensors with an epitaxial layer and low-resistivity substrate 149
9.13 Architecture of the Multilayer Perceptron (MLP) used for the cluster position reconstruction 152
9.14 Principle performance parameters for the CLICTD sensor using particle beams perpendicular to the sensor surface 155

11.1 Simulation of cluster size for different diffusions of the collection electrode, p-well implants and the substrate 172
11.2 Mean cluster size and spatial resolution in row direction for data and simulation 175
11.3 Estimation of active depth for different detection thresholds 188
11.4 Estimation of active depth for different lateral diffusions at the p-well implants 190
11.5 X-ray energies using an S-curve and a Gaussian fit 190

16.1 Hyperparameters for the Multilayer Perceptron 230
16.2 Performance metrics of the investigated machine learning techniques for the default evaluation set 231
16.3 Hyperparameters used for the Self-Organizing Map 232
16.4 Hyperparameters used for the Autoencoder 233
16.5 Performance metrics for the AE trained on different simulated background sources 238
16.6 Performance metrics for the AE evaluated with pixel matrices from magnetic monopoles with different masses 240
16.7 Performance metrics for the Autoencoder evaluated separately with monopoles and anti-monopoles 241

B.1 Default configuration of the slow control registers of the CLICTD sensor 253

F.1 Network architecture of the MLP 265
F.2 Network architecture of the AE 265

Introduction

Equipped with our five senses, along with telescopes and microscopes and mass spectrometers and seismographs and magnetometers and particle accelerators and detectors across the electromagnetic spectrum, we explore the universe around us and call the adventure science.

— Neil DeGrasse Tyson

Curiosity and the innate human desire for problem solving are the originators for scientific endeavours for millennia of human history and are the driving force behind innumerable technologies, rigorous theories and ever-improving innovations. Modern science is marked by the advent of the scientific method, whose central pillar is the acquisition of knowledge by empirical methods, whereby hypotheses are formulated, consequences are derived by logical reasoning and experiments are carried out to challenge and refine the initial assumptions. The measurement-based assessment of testable hypotheses can range from table-top experiments to the largest machine ever built by humans: the Large Hadron Collider (LHC) [1].

The search for new knowledge has led to the investigation of the fundamental constituents of matter and their interactions. The theoretical and experimental efforts culminated in the formulation of the highly-successful Standard Model of Particle Physics, that summarises our current understanding of elementary particles and processes. A major scientific milestone was marked by the discovery of the Higgs Boson by LHC experiments in 2012 [2,3], which was considered the last missing puzzle piece in the Standard Model. However, the quest for undiscovered particle physics is far from complete. In the face of inexplicable phenomena and incomplete formulations, extensions to the Standard Model are urgently called for. The search for Beyond the Standard Model physics as well as stringent tests of Standard Model predictions are thus cornerstones in the physics programmes of present and future High-Energy Physics experiments.

The instrumental facet of this endeavour requires the development of detectors with ever-increasing accuracy, which can withstand harsh experimental environments, while maintaining reliable operation. In addition, the flood of complex data from these detectors requires in-depth analyses with cutting-edge algorithms operating and pushing at the frontier of today's computing capabilities. This thesis is focused on the development of new instruments and methods in both fields: the characterisation and simulation of a novel silicon pixel sensor as well as the investigation of innovative analysis techniques for today's and tomorrow's High-Energy Physics experiments.

For this purpose, the thesis is divided into two parts: The first part is dedicated to the characterisation of a technology demonstrator for a monolithic silicon sensor design using laboratory studies, experiments with charged particle beams and simulations. In the second part, a proof-of-concept for unsupervised anomaly detection in pixel detector data is demonstrated, which represents a principle change of paradigm compared to traditional data analysis techniques in High-Energy Physics.

Silicon vertex and tracker detectors have contributed to groundbreaking discoveries by providing high-resolution spatial and temporal information of charged particle trajectories. In the face of ever-increasing demands for high-performance detectors, innovative design concepts for silicon sensors making up vertex and tracker detectors are needed. In this dissertation, a pixelated monolithic silicon sensor is characterised and its performance is assessed against the requirements for future tracker detectors at high-energy lepton colliders such as the Compact Linear Collider (CLIC). CLIC is a concept for a linear electron-positron collider with centre-of-mass energies up to 3 TeV, whose physics objectives include precision measurements of the Standard Model top quark and Higgs boson as well as direct and indirect searches for Beyond the Standard Model physics. To this end, the CLIC detector requires a low-mass tracker detector with a large surface area of $137\,\mathrm{m}^2$, which combines a spatial resolution of $\lesssim 7\,\mu\mathrm{m}$ with a time resolution of $\lesssim 5\,\mathrm{ns}$ and excellent hit-detection efficiency. The CLICTD sensor is a technology demonstrator for advanced front-end and sensor design concepts that aims to fulfil these requirements, while being equally relevant for other applications as well such as future upgrades of the LHC detectors [4].

In this thesis, the novel design choices are studied in laboratory measurements and in charged particle beams. The sensor is assessed and various design flavours and operation settings are compared. The measurements are also used for the verification of an advanced simulation approach involving three-dimensional finite-element and transient Monte Carlo simulations. These simulations enable a combination of a precise sensor modelling from the finite-element method with high-statistics simulation samples provided by the Monte Carlo approach. Once validated, they help to comprehend and interpret measurement results by giving insight into underlying processes that are not directly accessible in the measurement data. They also aid in the optimisation of sensor designs and are therefore indispensable tools in various stages in the silicon-detector development cycle.

The second part of this thesis is dedicated to the detection of anomalous particle signatures in Belle II pixel detector data. The Belle II experiment is located at the asymmetrical electron-positron collider SuperKEKB. Its innermost sub-detector - the pixel detector (PXD) - is subject to high data rates that require a sophisticated data handling. This dissertation explores a possible extension to the PXD readout scheme to increase sensitivity to anomalous data that could indicate undiscovered physics scenarios. The study is based on machine learning techniques that have proven to be a valuable tool in reconstruction and analysis tasks for High-Energy Physics [5]. In particular, the classification of signal and background using machine learning algorithms has sparked significant interest. The majority of these algorithms are trained in a supervised manner, and therefore rely on a prior definition of signal provided by a theoretical framework and simulations. However, detector signatures corresponding to elusive Beyond the Standard Model Physics (BSM) processes might be missed owing to a narrow signal definition or a mis-modelling of either signal or background.

Unsupervised and semi-supervised methods aim at the identification of signal features while minimizing predictions about signal or background. A data-driven approach is adopted allowing for a model-agnostic analysis that has the advantage of being independent from theoretical assumptions and therefore not confined to specific signal hypotheses and background modelling. In this thesis, unsupervised machine learning methods are presented with the objective to identify anomalous detector patterns that are potential indicators for unaccounted physics scenarios.

To demonstrate the approach, hypothetical long-lived magnetic monopoles are simulated and discriminated against measured pixel-detector background data. Two classes of unsupervised algorithms are investigated: Self-Organising Maps and Autoencoders. They are compared to a convolutional Multilayer Perceptron, that is trained in a supervised manner and their suitability for anomaly detection is assessed.

Outline

The content of this thesis is structured as follows: The first part presents the motivation and theoretical background starting from the Standard Model of Particle Physics in Chapter 1 to the principles of semiconductors as detector material in Chapter 2 and concepts related to silicon pixel detectors in Chapter 3. In Chapter 4, the principal object of investigation - the CLICTD technology demonstrator - is introduced. Chapters 5 and 6 cover the laboratory measurements by first introducing the setup and methodical background and subsequently the measurement results. Measurements with charged particle beams (*test beams*) were conducted at the DESY II Test-Beam Facility. Chapter 7 introduces the test-beam infrastructure and the experimental setup. The reconstruction and analysis strategies of the test-beam data are presented in Chapter 8 and the results in Chapter 9. The simulation setup is introduced in Chapter 10 and the validation and application of the simulation approach is presented in Chapter 11.

In the second part, the Belle II experiment is briefly outlined in Chapter 12. Subsequently, highly-ionising particles and in particular hypothetical magnetic monopoles are introduced in Chapter 13, as they represent the main research objects to assess the anomaly detection techniques. Chapter 14 presents the machine learning algorithms used in this thesis. After the analysis and reconstruction strategy is outlined in Chapter 15, the algorithms are applied first to simulation and then to data in Chapter 16. Lastly, a summary and an outlook to future developments is given.

Part I

Characterisation of Silicon Sensors

Chapter 1

Introduction to Particle Physics

In this chapter, the theoretical background of our present state of knowledge and future endeavours in High-Energy Physics (HEP) are introduced with a focus on collider experiments for particle physics. First, the Standard Model of Particle Physics is briefly outlined, as it summarises our current understanding of fundamental particle physics. Next, limitations of the Standard Model are discussed and the necessity for an extended model is motivated.

Novel theoretical approaches require careful experimental testing. In HEP, measurements at particle colliders have proven to be successful instruments to probe fundamental particles and interactions and search for physics beyond the Standard Model. In particular, concepts for future lepton colliders target high-precision measurements to challenge the predictions of the Standard Model. The Compact Linear Collider (CLIC) is a concept for a future linear electron-positron collider, which is reviewed in more detail, since the requirements for its tracking detector motivate the development of the new silicon sensor prototype presented in this thesis.

1.1 The Standard Model of Particle Physics

The Standard Model (SM) of particle physics is the theoretical basis for our present understanding of fundamental particles and the interactions between them [6]. The model has proven to deliver accurate predictions of experimental measurements in a wide energy range from a few eV to several TeV [7].

The SM is based on elementary particles, that can be divided into two groups: *fermions* and (gauge) *bosons*. While the former are the building blocks of matter, the latter function as mediators of interactions. Three of the four fundamental interactions are described by the SM: the electromagnetic, weak and strong interaction. Mathematically, the SM is described by a relativistic Quantum Field Theory (QFT), with the equations of motions derived from a Lagrangian density [8].

In the following, a brief overview of the particles and interactions in the SM are given. Subsequently, the limitations of the SM are described and possible extensions are discussed.

1.1.1 Particles and Interactions

Table 1.1. Elementary fermions of the Standard Model and the fundamental interactions they participate in.

	Generation			Interaction		
	1st	2nd	3rd	Strong	Weak	Electromagnetic
Quarks	u	c	t	✓	✓	✓
	d	s	b	✓	✓	✓
Leptons	e	μ	τ		✓	✓
	ν_e	ν_μ	ν_τ		✓	

The strong interaction is described by Quantum Chromodynamics (QCD) and features the symmetry group $\mathrm{SU}_C(3)$, where the subscript C denotes the colour charge. Eight QCD gauge bosons (*gluons*) exist that couple to the colour charge. The weak interaction is mediated by three massive gauge bosons Z^0, $W^\pm$ [9, 10] and the electromagnetic interaction by the photon coupling to electric charge [11, 12]. A unification of the weak and electromagnetic interaction gives rise to the concepts of weak isospin I and weak hypercharge Y [13–15]. The theory adheres to the $\mathrm{SU}_L(2)$ and $U_Y(1)$ symmetry groups, where L denotes the weak isospin of left-handed particles. The Higgs mechanism [16, 17] evokes electroweak symmetry breaking, through which the Z^0, $W^\pm$ acquire their mass [18, 19]. The mechanism introduces the Higgs field, whose non-zero vacuum expectation value results in the scalar Higgs boson that was experimentally verified at LHC experiments [20]. Altogether, the symmetry group of the SM Lagrangian can be summarised as $\mathrm{SU}(3)_\mathrm{C} \otimes \mathrm{SU}(2)_L \otimes \mathrm{U}(1)_Y$ [21].

An overview of the fundamental fermions in the SM is given in Table 1.1. Quarks and leptons are grouped in three different generations, with increasing mass from the first to the third generation. Within each generation, two quark types exist with different quantum numbers. Similarly, each lepton generation has a charged particle and an associated neutrino that is only liable to the weak interaction. While quarks are subject to all three interactions, leptons have no colour charge and are therefore unable to participate in the strong interaction. Each fermion has a partner with opposite charges, referred to as *antiparticle* [22, 23].

1.1.2 Physics Beyond the Standard Model

Despite its outstanding phenomenological success, there is theoretical and experimental evidence indicating that the SM is not a complete theory. Some of the most compelling reasons to search for extensions of the SM are outlined in the following:

- Firstly, only three of the four fundamental interactions are described in the SM, since it falls short of including gravitation in a fully coherent manner [24].
- Among the most critical questions presently unanswered by the SM is the matter-antimatter asymmetry in the universe [25], which is a major physics motivation for various experiments such as Belle II [26] or LHCb [27].
- The SM cannot explain certain cosmological phenomena such as the rotational behaviour of certain galaxies [28] and gravitational lensing [29], that suggest the existence of a new type of matter (*dark matter*) [30] [1].
- Similarly, cosmological observations such as distant type Ia supernovae [33] and studies of the cosmic microwave background (CMB) [34] imply an accelerated expansion of the universe, that could indicate the existence of *dark energy*.
- From a theoretical perspective, the SM has some undesirable properties such as free parameters [35] and the lack of an explanation as to why there are exactly three generations of fermions [36].

There are a number of theoretical approaches attempting to answer these unresolved questions such as Supersymmetry [37], Grand Unification theories [38] or Extra Dimensions [39]. Details about some prevalent theories are presented elsewhere [40, 41].

The majority of these theoretical frameworks predict the existence of undiscovered particles or mechanisms. Presently, no experimental confirmation for any of the proposed theories can be given. However, with the advent of new experimental endeavours operating at the energy and intensity frontier, a previously inaccessible parameter region will be explored. At the time of writing, preparations for a high-luminosity upgrade of the LHC (HL-LHC) [4] are in full swing, which is foreseen to run up to 2040 [42]. There are several propositions for the successor of the LHC such as the Future Circular e^+e^-

---

[1] Alternative theoretical approaches exist that e.g. introduce a modification to the theoretical description of gravity such as Modified Newtonian Dynamics (MOND) [31, 32]

Collider (FCC-ee) [43] or the Compact Linear Collider (CLIC) [44]. Both propositions are lepton colliders and can be considered as *Higgs factories* due to their strong focus on precision Higgs physics. In this thesis, the more stringent technological requirements of the CLIC experiment are considered to develop and characterise a new detector prototype. The technological advances of the detector components is a crucial ingredient in the search for BSM physics, since they pave the way for high-precision measurements while withstanding harsh experimental conditions.

1.2 The Compact Linear Collider

The Compact Linear Collider (CLIC) [44] is a design concept for a future linear electron-positron collider for the post HL-LHC period. The CLIC accelerator is intended to be built in three centre-of-mass (CM) energy stages, starting with $E_{\mathrm{CM}} = 380\,\mathrm{GeV}$. In the second stage, the CM energy is increased to $E_{\mathrm{CM}} = 1.5\,\mathrm{TeV}$ and in the final stage the CM energy reaches $E_{\mathrm{CM}} = 3.0\,\mathrm{TeV}$. So far, CLIC is the only design concept for a multi-TeV electron-positron collider. The multi-stage construction and the resulting wide energy range enables an extensive physics program, which is introduced in the following.

1.2.1 The Physics Case

Lepton colliders provide well-defined initial conditions and reduced background levels from quantum chromodynamics processes compared to hadron colliders. Therefore, they are well-suited for precision measurements and direct or indirect searches for undiscovered particles.

The CLIC physics programme consists of detailed studies of Standard Model particles such as the Higgs boson [45] and the top quark [46,47] as well as searches for BSM physics. The search techniques comprise direct detection as well as indirect searches, which are based on precision measurements of parameters such as coupling constants or particle masses [48]. As the Higgs boson couples strongly to B mesons, resolving secondary B meson vertices using precise tracking measurements with the vertex and tracker detectors is of utmost importance, as detailed below.

The centre-of-mass energy of 380 GeV, available in the initial energy stage, is particularly suited for detailed SM top quark and SM Higgs boson studies. The model-independent determination of the Higgs boson decay width and the measurement of the top quark mass using an energy scan around the top quark pair production threshold are foreseen. The first stage would run for up to eight years and collect a total integrated luminosity of $\mathcal{L}_{\mathrm{int}} = 1.0\,\mathrm{ab}^{-1}$. For the second energy stage of 1.5 TeV, the coupling of

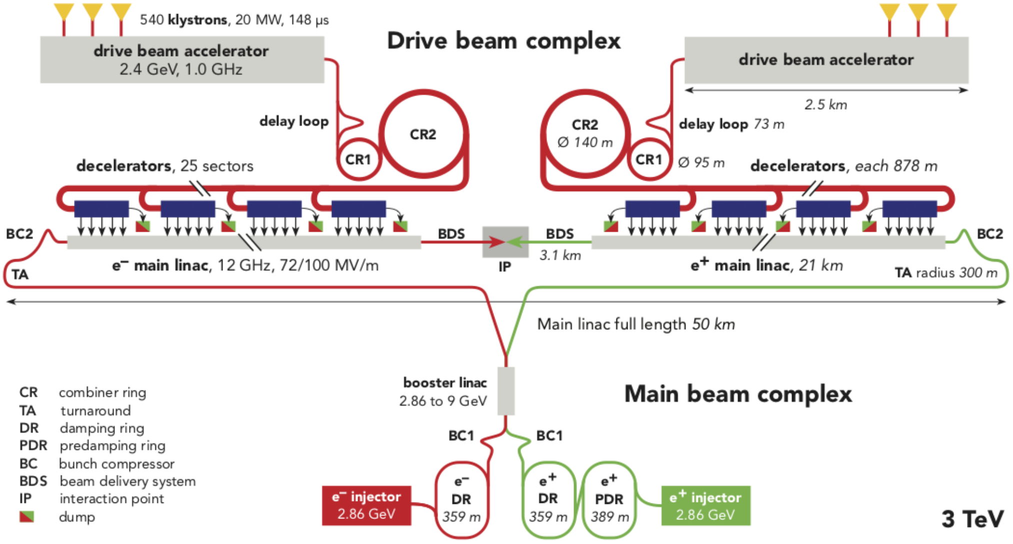
540 klystrons, 20 MW, 148 μs
drive beam accelerator
2.4 GeV, 1.0 GHz
Drive beam complex
drive beam accelerator
2.5 km
delay loop
CR2
CR1
CR2
Ø 140 m
CR1
delay loop 73 m
Ø 95 m
decelerators, 25 sectors
decelerators, each 878 m
BC2
TA
e⁻ main linac, 12 GHz, 72/100 MV/m
BDS
IP
BDS
3.1 km
e⁺ main linac, 21 km
BC2
TA radius 300 m
Main linac full length 50 km
booster linac
2.86 to 9 GeV
Main beam complex
BC1
BC1
CR combiner ring
TA turnaround
DR damping ring
PDR predamping ring
BC bunch compressor
BDS beam delivery system
IP interaction point
dump
e⁻ injector
2.86 GeV
e⁻
DR
359 m
e⁺
DR
359 m
e⁺
PDR
389 m
e⁺ injector
2.86 GeV
3 TeV

Figure 1.1. Schematic of the CLIC accelerator design at the final energy stage. From [50].

the top quark to the Higgs boson and the Higgs branching ratios can be determined with high precision allowing for a detailed comparison against SM predictions. Most notably, the top-Yukawa coupling and the Higgs self-coupling would be investigated and a total luminosity of $\mathcal{L}_{\text{int}} = 2.5\,\text{ab}^{-1}$ in about eight years would be collected. In the final energy stage of 3.0 TeV, rare Higgs decays and the Higgs self-coupling can be probed further. In addition, a strong focus is placed on searches for BSM physics [49]. The integrated luminosity of the last stage is foreseen to amount to $\mathcal{L}_{\text{int}} = 5.0\,\text{ab}^{-1}$.

1.2.2 CLIC Accelerator

Accelerator Design Compared to circular lepton colliders, the linear design of the CLIC accelerator has the advantage of reducing energy losses related to synchrotron radiation [51]. However, a linear accelerator has to reach the final collision energy in a single pass through the acceleration structures. For a maximum collider length of approximately 50 km, acceleration gradients of $100\,\text{MVm}^{-1}$ must be obtained to reach 3 TeV. To this end, an innovative two-beam acceleration scheme has been developed that is able to achieve high gradients using room temperature acceleration structures [50]. The schematic layout of the acceleration complex is depicted in Fig 1.1. First, a low-energy, high-current drive-beam is generated using klystron accelerating cavities. Subsequently, the energy of the drive beams is transferred to low-current high-energy main beams that are brought to collision at the interaction point.

Nanometre bunch sizes of $40\,\text{nm} \times 1\,\text{nm}$ in the transverse plane are required to reach the CLIC design luminosity of $5.9 \times 10^{34}\,\text{cm}^{-1}\,\text{s}^{-1}$ at 3 TeV. The longitudinal bunch size

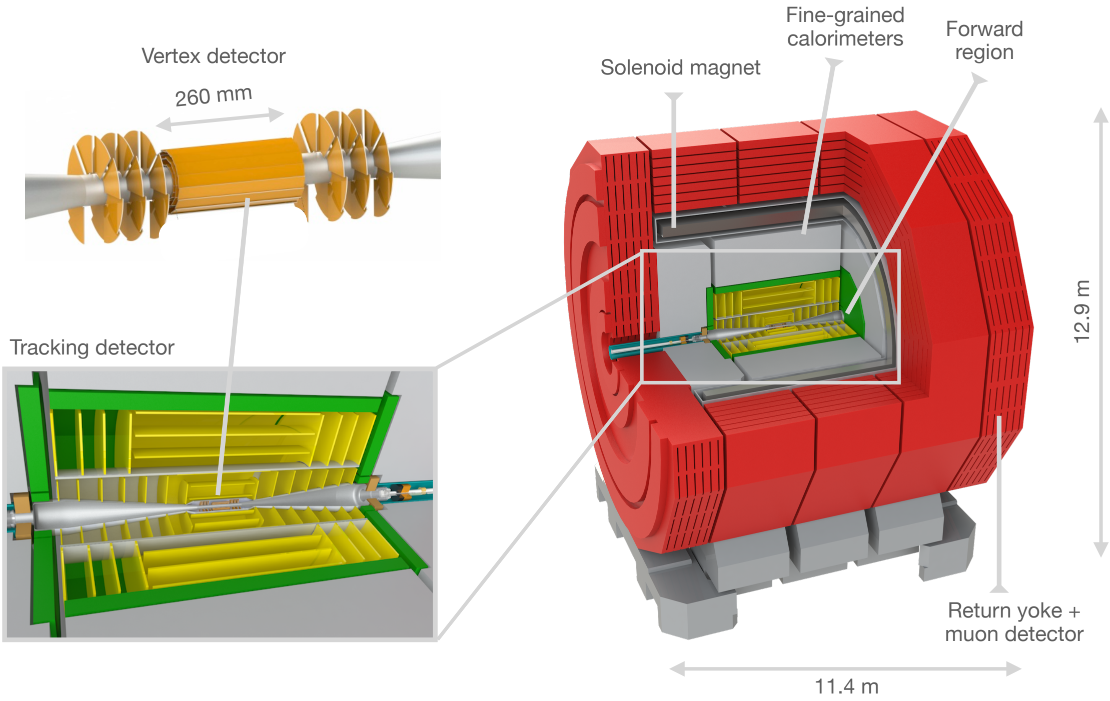

Figure 1.2. Schematic of the CLIC detector design. Close-ups of the tracking and vertex detectors are depicted on the left of the figure. Modified from [54].

is foreseen to be 44 µm. 312 of these small bunches are combined into so-called *bunch trains*, that last for a duration of 156 ns. The repetition rate of the bunch trains is 50 Hz, which yields a duty cycle of less than 0.001 % [44].

Beam Background The main source of beam background is related to the electromagnetic interaction of beam particles with the opposing beam (*Beamstrahlung photons*) [52]. Most notably, incoherently produced e^+e^- pairs and $\gamma\gamma \rightarrow$ hadrons events arise from the Beamstrahlung photons [53]. The suppression of background events is crucial to achieve the intended physics objectives. The CLIC detector system is therefore optimised to cope with the beam background, as outlined in the next section.

1.2.3 Detector Concept

The CLIC detector needs to be optimised for its intended physics programme and the experimental conditions of a high-energy linear lepton collider. The *CLICdet* detector design is based on detailed full-detector simulation studies and experiences from extensive technology R&D [55, 56]. It is optimised for operation at the highest energy stage since this stage has the most challenging experimental conditions. A schematic of the detector design is displayed in Fig. 1.2.

CLICdet targets precision measurements based on Particle Flow Analysis (PFA) [57].

Table 1.2. Requirements for the CLIC tracker. Data from [55].

Parameter	**Value**
Spatial resolution (transversal)	$7\,\mu\text{m}$
Granularity (longitudinal)	$1 - 10\,\text{mm}$
Hit-time resolution	$5\,\text{ns}$
Hit detection efficiency	$> 99.7\,\%$
Material content (per layer)	$1 - 2\,\%\,X_0$
Power dissipation	$150\,\text{mWcm}^{-2}$
Non-Ionizing Energy Loss (inner layer)	$< 10^{10}\text{n}_{\text{eq}}\text{cm}^{-2}\text{y}^{-1}$
Total Ionizing Dose (inner layer)	$1\,\text{Gyy}^{-1}$

PFA enables the combination of information from a high-resolution tracking system with fine-grained calorimeter energy measurements. The combined analysis allows for the identification of individual particles within jets and from beamstrahlung. The all-silicon vertex and tracking system makes up the inner region of CLICdet. It consists of a central barrel and several disks in the endcap sections, as depicted in the close-ups in Fig. 1.2. The tracking system is discussed in more detail in the next section. A highly-granular silicon-tungsten sampling electromagnetic calorimeter (ECAL) is used for the energy measurement of charged particles. It consists of 40 alternating layers of absorber material and silicon detectors as active layer. It is surrounded by the hadronic calorimeter (HCAL) measuring the energy of hadronic particles. It follows the same design principle as the ECAL, with 60 alternating planes of steel absorber material and scintillator plates equipped with Silicon Photomultipliers as an active layer. The inner sub-detectors are surrounded by a central superconducting solenoid magnet with a magnetic field of 4 T. The magnet return yoke is interleaved with detectors for muon identification.

Two calorimeters are foreseen for the forward region of the detector: The luminosity calorimeter (*LumiCal*) and the beam calorimeter (*BeamCal*) that provide luminosity measurements and forward electron-tagging of Bhabha scattered electrons.

1.2.4 The CLIC Tracking System

The CLIC tracking system consists of the vertex and tracker detectors. The principle task of the former is an accurate reconstruction of displaced vertices of heavy quark flavours or of τ leptons. To this end an impact parameter resolution of $\sigma(d_0) = 5 \oplus 15/(p[\text{GeV}]\sin^{3/2}\theta)\,\mu\text{m}$ is needed. As this thesis addresses the R&D for the tracker, the following section focuses solely on its layout and detector requirements. Detector studies for the CLIC vertex detector can be found elsewhere [58]

The CLIC tracker comprises six layers in the barrel as well as eleven discs on each detector side, as illustrated in Fig. 1.2. The total sensor area spans $137\,\mathrm{m}^2$. The tracking detector is required to have a transverse momentum resolution for high-p_T tracks ($\geq 100\,\mathrm{GeV}$) of $\sigma_{p_T}/p_T^2 \leq 2 \times 10^{-5}\,\mathrm{GeV}^{-1}$, which is needed for precision measurements of e.g. the Higgsstrahlung process [59]. To achieve this resolution in a 4 T magnetic field, a single point resolution of less than 7 µm is required in the direction perpendicular to the magnetic field. In the direction parallel to the magnetic field, the maximum allowed pixel size is limited by the expected occupancy to 1 – 10 mm. Smaller cell sizes may be enforced by the chosen technology. The hit-time tagging of the tracking detector needs to be better than approximately 5 ns to suppress the impact of beam-induced background. The hit-detection efficiency is required to exceed 99.7 % [59].

The material content is required to be below 1 –2% of radiation length X_0 per layer. A water-based cooling system enables an average power dissipation of $150\,\mathrm{mWcm}^{-2}$ for room temperature operation. Requirements on the radiation hardness of the detector are less stringent compared to hadron colliders. The radiation level from non-ionising energy loss at the inner-most tracker layers is expected to be of the order of $10^{10}\mathrm{n}_{\mathrm{eq}}\mathrm{cm}^{-2}\mathrm{y}^{-1}$ and the total ionising dose is approximately 100 Gy per year. The requirements are summarised in Table 1.2.

Power Pulsing The low duty cycle of the CLIC accelerator allows for a power-pulsing scheme [60]. Hereby, the front-end electronics are switched to a low-power mode between bunch crossings in order to reduce the average power consumption and heat dissipation. In this way, meeting the stringent requirements on cooling and the material content is facilitated for the CLIC vertex and tracker detectors [61]. Power pulsing also has implications for the readout scheme of the silicon detectors, as they can be switched to an inactive state between collisions (cf. Section 4.2).

Chapter 2

Fundamentals of Semiconductor Physics

Semiconductor detectors have become indispensable instruments in HEP experiments and have successfully contributed to historical discoveries and high-precision measurements in the past years [62]. The rapid advancement of the semiconductor industry allows for technology-driven innovations that provide ever-improving materials. In particular, silicon-based detectors are prevalent in innumerable experimental setups and are the main focus of this thesis. To lay the theoretical basis for the results shown in subsequent chapters, the fundamental principles of semiconductor physics in view of detector applications are described in the following. Instead of detailing full theoretical frameworks, the focus is placed on selected phenomenological models that are especially relevant for this thesis. Most importantly, these models are an essential input to the simulations introduced in Chapter 10.

First, the band structure of semiconductors as well as the difference between intrinsic and extrinsic semiconductors is outlined. Subsequently, the interaction between ionising radiation and semiconductor material is described, with a particular focus on energy deposition models for charged particles and photons. In addition, the propagation of liberated charge carriers within the semiconductor is covered and different transport mechanisms are described. Charge carrier recombination models are discussed as well due to their high relevance for the simulations. Lastly, the functionality of a pn-junction is outlined. Detailed reviews of semiconductor physics for HEP applications can be found for example in [63–65]

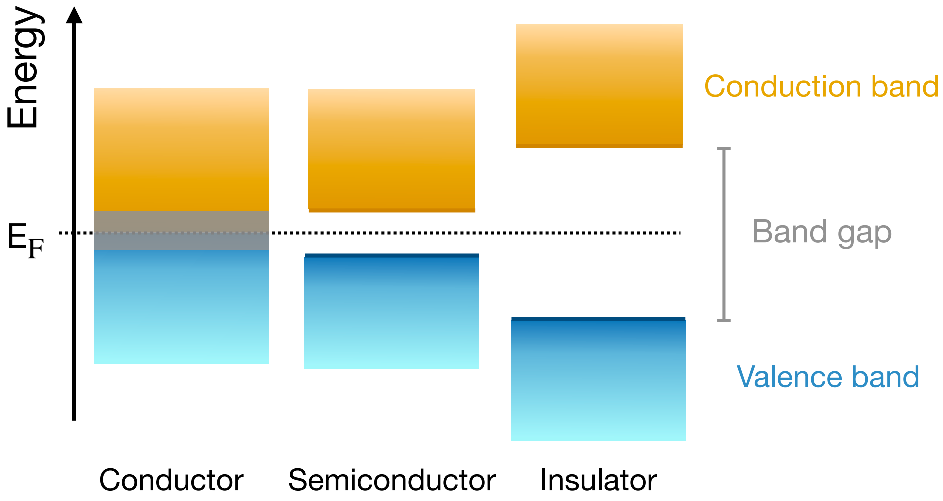

Figure 2.1. Schematic representation of the energy band configuration in conductors, semiconductors and insulators. The Fermi energy E_F is shown as well.

2.1 Band Structure

In crystalline materials, electrical properties are determined by the arrangement and density of atomic energy levels. The energy levels in a crystal lattice are subject to an energy split caused by the interaction of neighbouring atoms [64]. However, their high energetic density with energy distances of the order of meV, allows them to be treated as continuous *energy bands*. The probability of electrons occupying specific energy levels (*occupancy probability*) follows the Fermi-Dirac statistics [66]. The *Fermi energy* E_F is a hypothetical energy level that is characterised by an occupancy probability of $1/2$ at thermal equilibrium [67]. At 0 K, the energy levels up to the Fermi level are filled, with the highest fully occupied band denoted as *valence band*. Above the valence band, the *conduction band* is characterised by unoccupied energy states, that contribute to the conductivity of the material. The energy distance (*band gap*) between the two bands is essential for the electric properties of solid state materials. According to the width of the band gap, solid-state materials are classified as *insulators*, *semiconductors* or *conductors*.

In insulators, the strong binding force between neighbouring atoms gives rise to a large band gap ($\approx 10\,\mathrm{eV}$) between the valence and the conduction band, as schematically illustrated in Fig. 2.1. While the valence band is fully occupied, the conduction band is devoid of electrons. The electrons are tightly bound in the valence band and therefore do not contribute to the electrical conductivity.

In semiconductors, the energy band gap is of the order of a few eV [64]. Hence, thermal or electrical excitation can induce the transition of an electron from the valence into the conduction band. Owing to the unoccupied energy states in the conduction band, electrons are able to propagate freely resulting in a higher conductivity compared to insulators. The freed energy state in the valence band is referred to as a *hole*. Like electrons in the conduction band, holes in the valence band can transition between energy states, thus contributing to the overall electrical conductivity.

For conductors, the conduction band is either partially occupied or valence and conduction band overlap. As a result, conductors exhibit a characteristically high conductivity.

The energy distance between valence and conduction band is determined by the lattice constant of the material. Temperature and external pressure can thus affect the size of the band gap [68]. For silicon at room temperature (300 K) and standard atmospheric pressure (1013 hPa) the band gap is approximately 1.12 eV [7].

2.2 Intrinsic and Extrinsic Semiconductors

In *intrinsic* semiconductors, the concentrations of electrons in the conduction band n and holes in the valence band p is balanced for a given temperature. The intrinsic carrier concentration n_i is then given by:

$$n \cdot p = n_i^2. \tag{2.1}$$

The intrinsic carrier concentration is a function of the temperature and the properties of the semiconductor such as the width of the band gap [64]. At room temperature, silicon has an intrinsic charge carrier concentration of $n_i \approx 10^{10}\,\mathrm{cm}^{-3}$ [69].

The electrical properties of semiconductors can be tuned by introducing impurities into the crystal lattice that add additional energy levels between valence and conduction band. The controlled insertion of impurities is referred to as *doping*. The doping of silicon by a group V element such as phosphorous or arsenic increases the number of electrons in the conduction band, which then exceed the number of holes in the valence band (*n-type* doping). As a result, the Fermi energy level is shifted closer to the conduction band, as schematically depicted in Fig. 2.2.

Conversely, using a group III element as dopant such as boron, the number of holes in the valence band becomes larger than the number of electrons in the conduction band (*p-type* doping) and the Fermi energy is shifted closer to the valence band. A doped semiconductor is referred to as *extrinsic*.

A measure of the doping concentration is the electrical resistivity ρ, that is given by [70]:

$$\rho = (q \cdot N \cdot \mu)^{-1}, \tag{2.2}$$

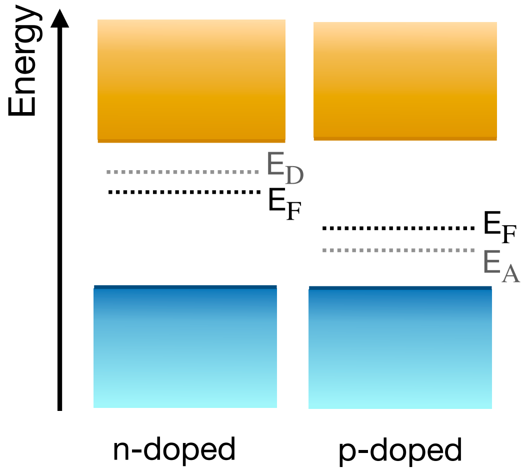

Figure 2.2. Schematic representation of the energy bands in n-doped and p-doped semiconductors. The donator E_D and acceptor E_A energy levels are displayed as well.

where q is the charge, N the doping concentration and μ the mobility of the majority charge carriers. Further details about the charge carrier mobility are presented in Section 2.4.

A locally restricted placement of dopants in a bulk material is referred to as *implant*. Implants are often characterised by a high doping concentration, which is indicated by the symbols n^+ or p^+

2.3 Energy Deposition of Ionising Radiation

The detection of particles is based on their interaction with detector material, leading to the deposition of a fraction or all of their energy. Different mechanisms are responsible for the energy transfer of ionising radiation. The ones relevant for this thesis are reviewed in the following. The section is split into two parts: First, the energy deposition of charged particles is described and second the interaction of photons with matter is presented.

2.3.1 Energy Deposition of Charged Particles

Charged particles traversing matter undergo Coulomb interactions with the medium. When the interaction is purely elastic, the particle is only deflected from its original path. In inelastic interactions, part of the particle's energy is transferred to the medium or emitted via e.g. bremsstrahlung. Depending on the medium and the properties of the incoming particle, the energy transfer can lead to ionisation or excitation of electrons. In semiconductor materials, the excitation of electrons into the conduction band (*electron-*

hole-pair creation) is particularly relevant. The mean energy loss of the particles can be described by the so-called *stopping power*, that is outlined in the following.

Mean Energy Loss The stopping power can be expressed by the Bethe formula, that relates the mean energy loss for an infinitesimal path $\langle \mathrm{d}E/\mathrm{d}x \rangle$ to the properties of the incoming particle and the medium [7, 71]:

$$\langle \mathrm{d}E/\mathrm{d}x \rangle \propto \frac{Z}{A\beta}\left[\ln\left(\frac{2m_e c^2\beta^2\gamma^2 T_{\mathrm{max}}}{I^2}\right) - \beta^2\right], \tag{2.3}$$

where Z, A and I are the atomic number, mass and the mean excitation energy of the medium, respectively. The charge of the incoming particle is denoted by z and β as well as γ are related to the particle velocity via $\beta = v/c$ and $\gamma = 1/\sqrt{1-\beta^2}$. The electron mass is given by m_e and c denotes the speed of light. The maximum energy transfer in a single collision is represented by T_{max}. Over the years, various correction terms to the Bethe formula have been introduced such as Bloch corrections [72], Fermi density corrections [73] or corrections for the Barkas-Andersen-effect [74]. The formula is not applicable to electrons.

Eq. 2.3 is commonly parametrised in units of $\beta\gamma$, which allows for the identification of characteristic energy loss regions: At low $\beta\gamma << 3$, particles are highly ionising and deposit a large amount of energy in the material. At $\beta\gamma \sim 3$, a global minimum is reached and the energy loss is comparably low. Particles in this regime are referred to as *Minimum Ionising Particles (MIPs)* [1]. At larger $\beta\gamma$, radiative processes lead to a shallow increase in energy loss.

Energy Loss Fluctuations Stochastic fluctuations around the mean energy loss are caused by variations in the transferred energy in each interaction and differences in the number of interactions per unit length. For instance, a head-on collision of the incident particle with an orbital electron in the material leads to a large energy transfer causing the electron to be knocked out of the bound state. These electrons, referred to as δ-electrons, can create additional electron-hole pairs resulting in a large fraction of energy deposition in the medium [75].

For sufficiently thick materials, the energy loss fluctuations can be approximated by a Landau-Vavilov distribution [76, 77]. The distribution is characterised by a Gaussian core and a pronounced tail towards large values caused by δ-electrons. Therefore, the *Most Probable Value (MPV)* of the distribution is lower compared to its mean.

---

[1] Typically, the term MIP is also used for particles with a $\beta\gamma$ value slightly higher than three due to the shallow slope of the function towards increasing $\beta\gamma$ values.

For thin materials, statistical fluctuations play a prominent role due to the low number of interactions between incoming particle and the medium [78]. Instead of the Landau-Vavilov model, the Bichsel model [75] provides a better description, which is especially relevant for sensors with a thin active layer. Alternatively, the Photo Absorption Ionization (PAI) model [79] predicts the energy loss in thin materials with high accuracy as well and is compatible with results from the Bichsel model [80, 81]. The PAI model is implemented in the simulations performed in later chapters.

Multiple Scattering A particle beam is subject to Coulomb scattering with the nuclei in solid state materials and even in ambient air [82]. The scattering processes are responsible for a deflection of the particle trajectory, which has important implications for the track reconstruction of charged particles. Multiple scattering describes the occurrence of several subsequent scattering events with small scattering angles. The RMS of the total angular dispersion θ_{RMS} is described by [83, 84]:

$$\theta_{\mathrm{RMS}} = \frac{13.6\,\mathrm{MeV}}{\beta c p} z \sqrt{x/X_0}\,(1 + 0.038 \ln(x/X_0))\,, \tag{2.4}$$

where (x/X_0) is the material content in radiation lengths, p is the particle momentum, z is the charge and βc the velocity. The radiation length is a characteristic property of the material and expresses the mean distance over which the energy of a high-energy electron decreases to a fraction of $1/e$ of its original energy.

For singly-charged, highly-relativistic particles and material contents in the range $10^{-3} < x/X_0 < 100$, an accuracy of 11 % is expected from Eq 2.4 [7].

2.3.2 Energy Deposition of Photons

Unlike charged particles, the interaction of photons with matter is localised and follows three main mechanisms: the photoelectric effect, Compton scattering and pair production.

- **The photoelectric effect** dominates at low photon energies ($\lesssim 0.01\,\mathrm{MeV}$ in silicon). The incident photon transfers all of its energy to a silicon atom by exciting a bound electron out of its orbit. The liberated photo-electron carries the energy difference between the incoming photon energy and the binding energy and can further ionise or excite the material.

- **The Compton effect** becomes relevant in the energy range between 0.01 MeV and 1 MeV in silicon. The incoming photon is subject to incoherent scattering with bound or free electrons. The photon transfers a fraction of its initial energy to an electron and is thereby deflected by the scattering angle θ. If the binding energy of electrons is negligible compared to the photon energy, they can be treated as quasi-free and the differential cross section for Compton scatting can be expressed by the Klein-Nishina formula [85].

- **Electron-positron pair production** dominates at high photon energies exceeding approximately 1 MeV, whereby the incoming photon converts into an electron-positron pair by interacting with the electric field of a nucleus. The energy of the photon needs to be larger than the rest mass of the final-state particles ($E_\gamma \gtrsim 1.022\,\mathrm{MeV}$) to initiate the process. This mechanism is of no importance for the calibration measurements performed in this thesis, since the relevant photon energies are well below the production threshold.

2.4 Charge Carrier Propagation

The energy deposited by ionising radiation is converted into electron-hole pairs in semiconductor materials such as silicon. These charge carriers are subject to *drift* in the presence of electric fields and random *diffusion* that resembles a Brownian motion. Before these two transport mechanisms are described in more detail, the concept of charge carrier mobility is introduced.

2.4.1 Mobility

Charge carriers propagating through a semiconductor are constantly subject to scattering processes with lattice vibrations (phonons), impurities, surfaces or other imperfections [86]. In the transport equations, the charge carrier mobility is used to account for these microscopic effects. It is thus linked to the charge carrier velocity as presented in Sections 2.4.2 and 2.4.3.

The mobility depends on various macroscopic parameters such as the temperature, doping concentration or the electric field. Phenomenological mobility models are typically valid for a restricted parameter space, which makes the selection of the appropriate model for a given problem an essential task.

In this thesis, the mobility is parametrised by a combination of the Masetti [87] and the Canali model [88]. The parametrisation takes the mobility dependence on the electric field E, the temperature T and the doping concentration N into account. In addition, the velocity saturation for high electric field values is modelled to avoid an overestimation of the mobility. The Masetti-Canali mobility is given by:

$$\mu_{\text{MasettiCanali}} = \frac{\mu_m(N)}{\left(1 + (\mu_m(N) \cdot E/v_m)^{\beta'}\right)^{1/\beta'}}, \tag{2.5}$$

where v_m and β' are phenomenological parameters from the Canali model, which depend on temperature and the charge carrier type and $\mu_m(N)$ is the doping-dependent Masetti mobility. Details about the parametrisation of these quantities can be found in the Appendix A.

2.4.2 Drift

Drift occurs in the presence of electric fields. Charge carriers propagate with an average drift velocity v_{drift} that results from acceleration caused by the electric field E and microscopic scattering events. The velocity is therefore expressed by

$$v_{\mathrm{drift},e/h} = \mu_{e/h} E, \tag{2.6}$$

where $\mu_{e/h}$ denotes the electron/hole mobility that accounts for the scattering processes. A macroscopic current density J_{drift} can be defined:

$$J_{\mathrm{drift},e/h} = n_{e/h} \mu_{e/h} q E, \tag{2.7}$$

with the electron/hole concentration $n_{e/h}$ and the charge q [64].

2.4.3 Diffusion

Diffusion is based on *random walk* of charge carriers in the material. In case of a non-uniform distribution of charge carriers, a diffusion along the charge carrier gradient takes place.

Diffusion can be parametrised by introducing a diffusion constant $\mathrm{D}_{e/h}$ for electrons/holes, that is related to the charge carrier mobility according to the Einstein-Smoluchowski relation [89, 90]:

$$D_{e/h} = \frac{k_B \cdot T \cdot \mu_{e/h}}{q}; \tag{2.8}$$

where k_B is the Boltzmann constant, T the temperature and q the charge of the particle.

The diffusion current density J_{diff} is then given by the concentration gradient Δn and the diffusion constant

$$J_{\mathrm{diff},e/h} = -q D_{e/h} \Delta n. \tag{2.9}$$

2.5 Charge Carrier Generation-Recombination Models

Semiconductors are constantly subject to generation-recombination mechanisms that take place to keep a state of equilibrium. However, the generation of electron-hole pairs

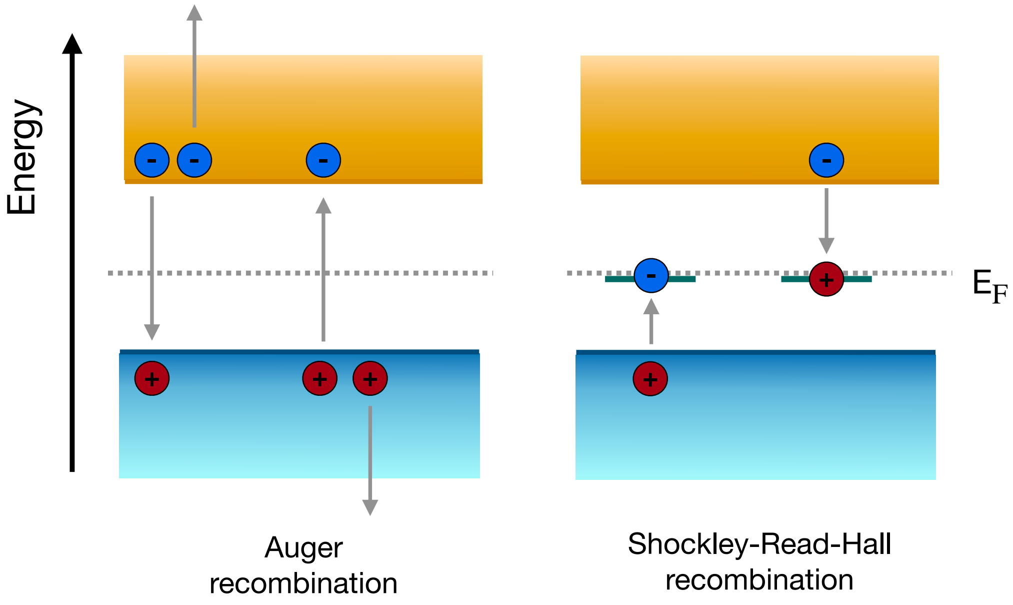

Figure 2.3. Schematic representation of the Shockley-Read-Hall and Auger recombination mechanisms. For the Auger recombination, the e-e-h (left) and the e-h-h (right) processes are shown. In the Shockley-Read-Hall recombination, a hole/electron in the valence/conduction band recombines with an electron/hole trapped in an energy level in the band gap.

by ionising radiation causes a disturbance in the system. To return to equilibrium, a net recombination occurs, which depends critically on semiconductor properties such as temperature or doping concentration [86].

Similar to the mobility models, generation-recombination mechanisms are typically described by empirical models that apply to a specific parameter space. For this thesis, two main recombination mechanisms are relevant: the Shockley-Read-Hall (SRH) and the Auger recombination.

2.5.1 Shockley-Read-Hall Recombination

The Shockley-Read-Hall recombination mechanism [91, 92] is mediated by additional energy levels in the band gap, as schematically shown in Fig. 2.3. Electrons/holes trapped in these energy levels can recombine with holes/electrons in the valence/conduction band.

As the energy levels are created by dopants, defects and impurities, the doping level of the semiconductor plays an essential role in the SRH recombination. If the recombination centres are close to the middle of the band gap, the minority charge carrier lifetime τ_{SRH} is given by [93, 94]:

$$\tau_{\mathrm{srh}}(N_d) = \frac{\tau_0}{1 + N_d/N_{d0}} \tag{2.10}$$

where N_d is the doping concentration. τ_0 and N_{d0} are the reference lifetime and reference doping concentration, respectively, which are taken from [93] as

$$\begin{aligned} \tau_{0,e} &= 1 \times 10^{-5}\,\mathrm{s} & \tau_{0,h} &= 4.0 \times 10^{-4}\,\mathrm{s} \\ N_{d0,e} &= 1 \times 10^{16}\,\mathrm{cm}^{-3} & N_{d0,h} &= 7.1 \times 10^{15}\,\mathrm{cm}^{-3} \end{aligned}$$

for electrons and holes, respectively.

2.5.2 Auger Recombination

The Auger recombination mechanism becomes increasingly important at high doping levels exceeding $5 \times 10^{18}\,\mathrm{cm}^{-3}$ [95]. The model assumes that the excess energy created by electron-hole recombinations is transferred to another electron (*e-e-h process*) or another hole (*e-h-h process*), as depicted schematically in Fig. 2.3. The total recombination rate is then given by [96]:

$$R_a = C_n n^2 p + C_p n p^2$$

where C_n and C_p are the Auger coefficients. The first term corresponds to the e-e-h process and the second term to the e-h-h process. In highly-doped silicon, the Auger lifetime for minority charge carriers can be written as

$$\tau_\mathrm{a} = \frac{1}{C_a \cdot N_d^2} \tag{2.11}$$

where $C_a = C_n + C_p$ is the ambipolar Auger coefficient. The coefficients can be determined experimentally and for the simulations presented in this thesis, the values have been taken from [97] as

$$\begin{aligned} C_n &= 2.8 \times 10^{-31}\,\mathrm{cm}^{-6}/\mathrm{s} \\ C_p &= 0.99 \times 10^{-31}\,\mathrm{cm}^{-6}/\mathrm{s}, \end{aligned}$$

resulting in $C_a = 3.79 \times 10^{-31}\,\mathrm{cm}^{-6}/\mathrm{s}$.

Combination The two charge carrier recombination models are combined by inversely summing the individual lifetimes calculated by the models via

$$\tau^{-1}(N_d) = \tau_{srh}^{-1}(N_d) + \tau_a^{-1}(N_d). \tag{2.12}$$

Other recombination mechanism such as recombinations at surfaces are less relevant for the sensor types presented in this thesis.

2.6 The pn-Junction

While the number of free charge carriers in intrinsic silicon is of the order of $10^{10}\,\mathrm{cm}^{-3}$ at a temperature of 300 K [69], the number of electron-hole pairs created by a charged particle is about 10^4 for the entire sensor [98]. It is therefore beneficial to reduce the number of free charge carriers, which act as a noise source, in order to use silicon as a detection medium. To this end, a region depleted of free charge carriers is created by combining a p- and n-type doped semiconductor. The interface between the two materials is referred to as *pn-junction*.

In the p-doped material, holes are the majority charge carriers and in the n-doped material electrons are more abundant. At the interface of the two, the difference in charge carrier concentration leads to a diffusion current I_{diff}. Electrons in the n-doped region propagate into the p-doped material and vice versa. Owing to recombination processes between electrons and holes, the interface region becomes depleted of free charge carriers and is therefore referred to as *depletion zone*. As the bound atoms in the depletion zone are ionised, the n-doped part of the zone is characterised by a positive space charge and the p-doped material by a negative one. Consequently, there is an electrical field between the differently doped materials which gives rise to a current (*drift current*) I_{drift}. In absence of an external field, the drift and diffusion current are in a thermal equilibrium. The electrostatic potential in the equilibrium is referred to as *built-in potential* Φ. It can be obtained by solving the Poisson equation [64]:

$$\frac{\mathrm{d}^2\Phi(x)}{\mathrm{d}^2x} = -\frac{\rho(x)}{\epsilon_0\epsilon_r}, \tag{2.13}$$

where $\rho(x)$ is the charge density at position x; ϵ_0 and ϵ_r denote the permittivity in vacuum and silicon, respectively. For a one-dimensional planar interface, the equation is solved by

$$\Phi(x) = \begin{cases} -\frac{N_A}{2\epsilon_0\epsilon_r}(x+d_p)^2 & \text{for} \quad \text{p-type region} \\ \frac{N_D}{2\epsilon_0\epsilon_r}(x+d_n)^2 & \text{for} \quad \text{n-type region,} \end{cases} \tag{2.14}$$

where N_A/N_D are the doping concentrations and d_p/d_n the thickness of the depleted region for acceptors/donors, respectively. The built-in voltage U_{bi} can be calculated by evaluating Eq. 2.14 at the boundary of the n- and p-doped region:

$$U_{bi} = \frac{1}{2\epsilon_0\epsilon_r} \cdot |N_{\mathrm{eff}}| \cdot d^2, \tag{2.15}$$

with the effective doping concentration is given by $N_{\mathrm{eff}} = N_D - N_A$ and d is the total thickness of the depleted region.

2.6.1 Application of External Voltage

The depleted region can be extended or compressed by the application of an external voltage U_{bias}:

$$d(U_{\text{bias}}) = \begin{cases} \sqrt{\frac{2\epsilon_0\epsilon_r}{|N_{\text{eff}}|}(U_{bi} + U_{\text{bias}})} & \text{for} \quad (U_{bi} + U_{\text{bias}}) > 0 \\ 0 & \text{for} \quad (U_{bi} + U_{\text{bias}}) \leq 0. \end{cases} \tag{2.16}$$

If the sum of the built-in voltage and the bias voltage is negative, the depletion thickness reduces to 0 and a current can flow through the pn-junction (*forward bias*). For the opposite polarity of the bias voltage, the depletion region is enlarged proportional to the square root of the applied bias voltage U_{bias} (*reverse bias*). Moreover, the thickness follows an inverse square law in relation to the effective doping concentration. A lower doping concentration (higher resistivity) is therefore beneficial to obtain a large depleted region. Semiconductor detectors are usually operated in reversed bias mode.

2.6.2 Capacitance

The capacitance of a pn-junction has a crucial impact on the sensor performance as presented in Chapter 6. In a simplified model, a planar pn-junction can be treated as a plate capacitor, which yields the following relation for reversed bias operations:

$$C = A\frac{\epsilon_0\epsilon_R}{d(U_{\text{bias}})} = A\sqrt{\frac{\epsilon_0\epsilon_r|N_{\text{eff}}|}{2(U_{bi} + U_{\text{bias}})}}, \tag{2.17}$$

where A is the surface area of the pn-junction. A reduction of the capacitance is obtainable with higher bias voltages, lower doping concentrations or a smaller surface area.

2.6.3 Current-Voltage Characteristics

Leakage current is characterised by a steady flow of current in the absence of external radiation. There are several effects contributing to leakage current such as the motion of charge carriers into the depleted volume and the thermal generation of charge carriers [99]. The latter represents the main contribution to the leakage current in silicon detectors and is proportional to

$$I_{\text{thermal}} \propto T^2 e^{-E_g(T)/2k_BT} \tag{2.18}$$

with the temperature-dependent energy gap $E_g(T)$ and the Boltzmann constant k_B. An increase in temperature is therefore expected to lead to high leakage currents.

The leakage current is also increased by radiation-induced damage [100]. Since the tolerance of sensors to radiation damage is not presented in this thesis, it is not addressed in more detail.

Chapter 3

Silicon Pixel Detector Concepts

Silicon detectors are used in a wide-range of HEP experiments. They are typically segmented to improve position sensitivity, decrease their input capacitance and limit hit occupancy of individual readout channels. Two main segmentation schemes have emerged: *strip detectors* and *pixel detectors*. While the former partitions the sensitive area only in one dimension, a pixel structure provides a two-dimensional division. Pixels are typically designed in a rectangular shape [1] and can be characterised by the distance between repeating unit cells (*pixel pitch*), which is of the order of tens of micrometers in modern HEP experiments.

In this chapter, the concepts of silicon pixel detectors are outlined with a focus on design characteristics relevant for this thesis. To begin with, the signal formation in silicon detectors is described and subsequently an overview of typical front-end components is given. Electrical noise sources stemming from the front-end components are discussed as well. Lastly, different detector types are introduced.

3.1 Signal Formation

The electron-hole pairs generated by an incident particle need to be collected in order to contribute to the signal. For this purpose, an external electric field is applied to the sensor, which induces a drift of charge carriers towards the readout electrodes. In their vicinity, the motion of charge carriers induces a current on the electrodes, which can be modelled by the Shockley-Ramo theorem [103, 104]. The instantaneous current I^{ind} induced by the infinitesimal motion of a charge q with velocity $\vec{v}$ can be calculated from the *weighting field* $\vec{E}_w$:

$$I^{\mathrm{ind}} = q\vec{E_w}\vec{v}. \tag{3.1}$$

---

[1] Notable exceptions with e.g. a hexagonal pixel shape exist such as the FASTPIX sensor [101, 102]

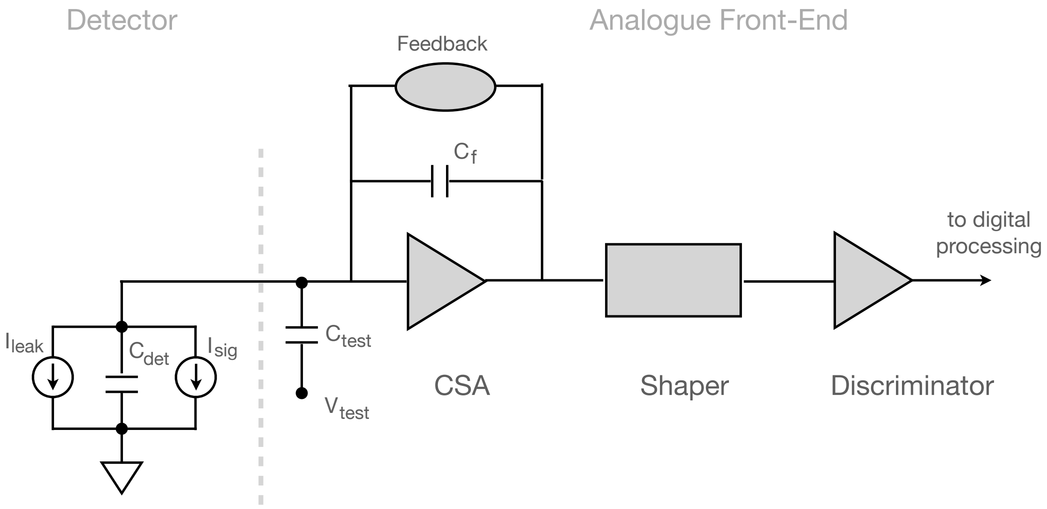

Figure 3.1. Schematic block diagram of a typical front-end processing chain in pixel detectors for HEP applications. Based on [99]

The theorem requires knowledge of the weighting field or the weighting potential ϕ_w, that is obtainable using analytical calculations or by means of finite-element simulations by setting the electrode of the pixel under consideration to unit potential, and all other electrodes to ground [105].

The Shockley-Ramo theorem then relates the induced charge Q_{ind} to differences in the weighting potential ϕ_w between the previous location $\vec{x_0}$ at time t_0 and the current position $\vec{x}_1$ at time t_1:

$$Q_{\text{ind}} = \int_{t_0}^{t_1} I^{\text{ind}} \mathrm{d}t = q \left[\phi_w(\vec{x}_1) - \phi_w(\vec{x}_0) \right]. \tag{3.2}$$

3.2 Front-End Electronics

The on-chip readout electronics are responsible for signal processing of the induced current. For HEP applications, they are specifically designed to cater to the needs of the experiment [106], leading to complex demands such as a fast processing speed or high radiation tolerance.

The fundamental building blocks of the front-end electronics are *Metal Oxide Semiconductor Field-Effect Transistors (MOSFETs)*. In particular, *Complementary Metal Oxide Semiconductor (CMOS)* transistors are used in modern pixel detector electronics and more details about their functionality can be found in e.g. [107]. A schematic block diagram of a generic readout chain for one readout channel is portrayed in Fig. 3.1. The individual parts are briefly outlined in the following and a detailed explanation can be found for example in [99].

- **Sensor:** In the block diagram, one sensor channel is represented by an effective detector capacitance C_{det}. The current induced on the collection electrode is modelled by a current source I_{sig} and in parallel to that the leakage current is given by I_{leak}.
- **Charge-Sensitive Amplifier (CSA):** First, an amplification stage integrates the current pulse and converts it into a voltage step with an amplitude proportional to the integrated signal. The gain of the CSA is determined by the feedback capacitance C_{f} around it. In order to probe the response of the analogue front-end, a test pulse can be injected. To this end, a test-pulse capacitor C_{test} is discharged to generate a signal at the CSA input.
- **Feedback Circuit:** The feedback circuit around the CSA allows for the removal of signal charge at the CSA input and the return to initial values at the CSA output.
- **Shaper:** Sensors typically employ a shaper after the amplification stage to suppress high-and low-frequency noise. The shaper also shortens the pulse duration to prevent signal pile-up.
- **Discriminator:** A discriminator compares the output of the shaper to a configurable threshold. Signals below the threshold are excluded from further processing in order to cut away noise contributions with a low amplitude. If a signal exceeds the threshold, it is passed on to the digital logic. The logic can be placed in the periphery or directly in the pixel.

Three types of readout schemes are commonly used in silicon detectors for HEP applications: the *frame-based*, the *data-driven* and the *trigger-based* readout. In the frame-based readout, data is collected in discrete time windows called frames. A shutter signal controls the data acquisition. Once the shutter is opened, the frame starts and the device is active for a configurable amount of time. Afterwards, the shutter is closed and the signal processing begins. A data-driven device aims for constant data acquisition leading to a continuous readout and data stream. A trigger-based readout relies on an external trigger signal. Data is stored for a specified latency interval and only shifted out if a trigger signal arrives during this time.

The digital logic can be responsible for the extraction of time and energy information from the processed signal. In a shutter-based device, the *Time Of Arrival (ToA)* can be determined with respect to the shutter close signal. The calculation is illustrated schematically in Fig. 3.2. Once the amplifier output crosses the detection threshold while the shutter is open, the number of clock cycles until the falling edge of the shutter is

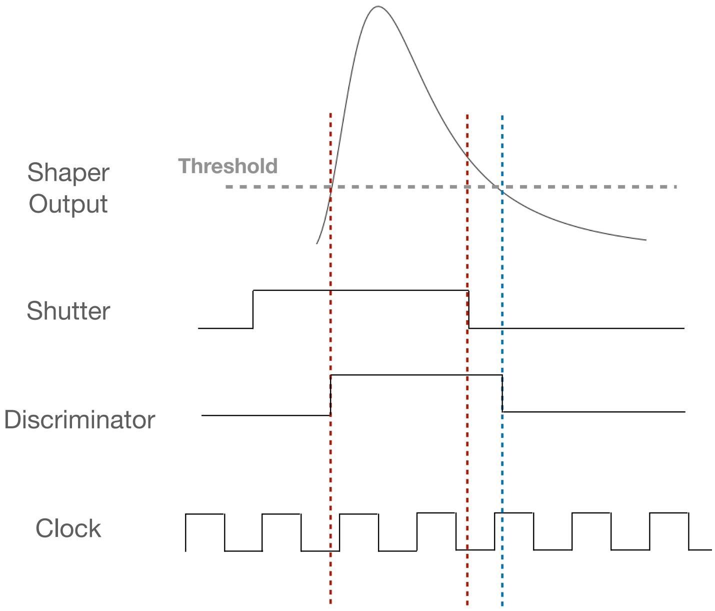

Figure 3.2. Schematic representation of the Time-over-Threshold (ToT) calculation in blue and Time-of-Arrival (ToA) computation in red.

counted. The ToA measurement is affected by a systematic signal-dependent shift denoted as *time walk* and depicted in Fig. 3.3. The slope of the signal depends on its height leading to a later threshold crossing for small signals, which is responsible for a degradation of the time resolution. If a simultaneous energy measurement is available, the time-walk effect can be mitigated by correcting the ToA based on energy values [2].

For the energy measurement, the number of clock cycles above threshold is considered (*Time over Threshold (ToT)*), exploiting that the signal length is linked to the amount of energy deposited in the active part of the sensor. The measurement principle is depicted in Fig. 3.2 as well. The threshold crossing of the amplifier output sets the discriminator, which remains high until the signal falls below threshold again. The number of clock cycles between the two threshold crossings defines the ToT, even if the falling edge of the discriminator is outside of the active shutter window.

3.3 Electronics Noise Sources

The occurrence of noise is an inherent property in all measurement procedures presented in this thesis. While noise can originate from all steps in the measurement chain, electrical noise is expected to be the dominant source for the sensors in this thesis. Specific examples of the most prominent noise sources are listed in the following. A detailed treatment can be found elsewhere [108].

---

[2] This time-walk correction may not be feasible in online applications despite the energy information.

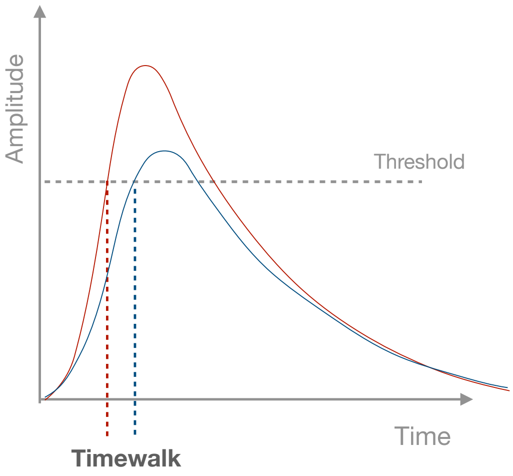

Figure 3.3. Schematic representation of time walk. The signal height affects the slope and therefore the threshold-crossing time at the discriminator leading to different ToA values.

- **Thermal Noise** is related to the Brownian motion of charge carriers and is therefore correlated with temperature. Thermal noise is considered to be *white noise* i.e. it covers a wide frequency range

- **Shot Noise** originates from the discrete nature of charge carriers and occurs at potential barriers. In silicon sensors, the statistical generation of individual electron-hole pairs is subject to shot noise and results in variations of the current level. Therefore, shot noise can manifest itself in leakage current. Owing to its stochastic nature, shot noise can be modelled by a Poisson process.

- $1/f$ **Noise** subsumes all noise sources that have a frequency-dependent noise spectrum that falls with $1/f$, where f denotes the frequency. For electrical circuits, $1/f$ noise is commonly related to capture processes with random relaxation times.

3.4 Fabrication of Silicon Sensors

The fabrication of silicon detectors is an intricate multistage process that combines a plethora of different technologies. In the following, two steps in the fabrication process are outlined that have a high relevance for the results obtained in this thesis: the fabrication of the silicon wafers and the introduction of dopants.

3.4.1 Fabrication of Silicon Wafers

The silicon wafer used as bulk material for the sensor is obtained from large cylindrical single silicon crystals (*boules*). Two main fabrication techniques are commonly used to manufacture a boule: the *float-zone* and the *Czochralski* fabrication.

The float-zone method [109] employs vertical zone melting to produce high-purity silicon. A polysilicon rod is passed through an RF heating coil, creating a molten zone, from which impurities segregate, since they are typically more soluble then the crystal. The melt then solidifies to a single crystal, which can have resistivities up to $50\,\mathrm{k}\Omega\,\mathrm{cm}$ [63] The ambient air is evacuated or filled with an inert gas to prevent the introduction of new impurities. In industry, the float-zone method is used for devices such as high-voltage MOSFETs.

In the Czochralski method [110], high-purity polysilicon fragments are melted in a crucible. A seed crystal is dipped into the melt and then pulled upwards in a rotational movement to produce a single-crystal silicon ingot. The technique requires exact control of the speed in the upwards movement and the rotation to obtain the desired result. Impurity control is more complicated compared to the float-zone technique, resulting in typical resistivities lower than $50\,\Omega\,\mathrm{cm}$. The Czochralski method is commonly used for integrated circuits.

3.4.2 Doping

To obtain n- or p-type silicon, dopants must be introduced in the material. There are two principle methods: *doping by diffusion* and *ion implantation.*

In the former, the silicon is heated to $800 - 1000^\circ\,\mathrm{C}$ in a gaseous atmosphere enriched with the desired dopant. The doping concentration is controlled by the heating temperature and the exposure time.

Ion implantation [111] on the other hand enables a precise control of doping concentrations and depth. The dopants are ionised and accelerated to energies from keV up to MeV. A dopant beam is directed onto the silicon bulk, whereby dopants are implanted in interstitial sites. They are bound into the lattice using thermal annealing, whereby the dopants diffuse further into the material than placed by the initial implantation step.

3.5 Silicon Pixel Detector Types

Due to the wide-spread applications in HEP and the resulting diverse requirements, different detector types have emerged, each with its particular advantages and disadvantages. The detector types can be divided into *hybrid* and *monolithic* silicon detectors, depending

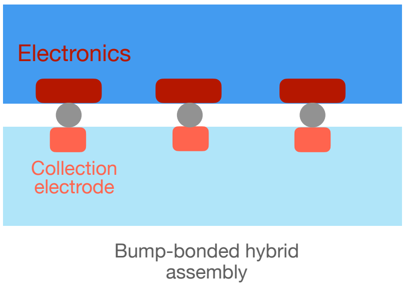
Electronics
Collection electrode
Bump-bonded hybrid assembly

Figure 3.4. Schematic representation of a bump-bonded hybrid assembly. The readout electronics are indicated in dark red and the collection electrode in light red.

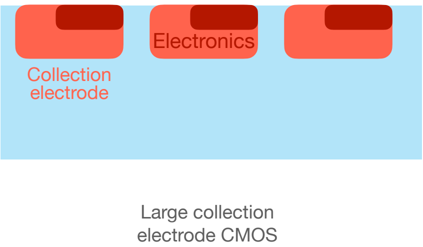
Electronics
Collection electrode
Large collection electrode CMOS

Figure 3.5. Schematic representation of a large collection-electrode monolithic CMOS sensor.

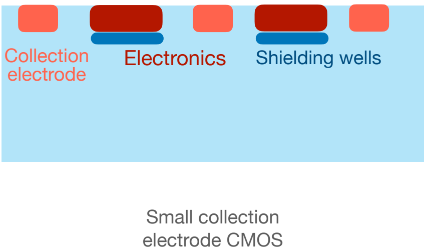
Collection electrode
Electronics
Shielding wells
Small collection electrode CMOS

Figure 3.6. Schematic representation of a small collection-electrode monolithic CMOS sensor.

on the integration of the readout electronics on a different chip or in the active sensor volume. In the following, the main differences between hybrid and monolithic pixel detectors are outlined and a few example technologies are presented. This section does not claim to be exhaustive, but only focuses on a limited selection of technologies relevant for this thesis.

3.5.1 Hybrid Pixel Detectors

Hybrid pixel detectors consist of two separate components: a sensor and a readout ASIC. While the sensor acts as the sensitive part of the detector, the readout chip houses the readout electronics such as amplifiers, state machines or discriminators. For the interconnection of the two components, different techniques are available. Typically solder bump bonds are used, though alternative interconnection techniques are explored as well such as capacitive coupling using a layer of glue [112] or anisotropic conductive films [113, 114]. A schematic of a bump-bonded hybrid assembly is depicted in Fig. 3.4. The lower part represents the active sensor with its collection electrodes and the upper chip houses the electronics.

A major advantage is the possibility to optimise the sensor and readout ASIC independently. In this way, advanced industry processes and innovative sensor concepts can be explored. The interconnection between the two components represents the main challenge for the hybrid technology, since it can result in a higher material content, additional costs in the fabrication process and a limitation on the pixel size. Alternative interconnection techniques could partially mitigate these challenges.

The development of hybrid pixel detectors was strongly driven by the RD19 collaboration [115] and one of the first applications was the pixel detector in the DELPHI experiment [116]. They are presently used in the inner detector setups of the major LHC experiments [62] and are also considered in detector upgrades for experiments at the high-luminosity LHC and additionally for the vertex detector in CLIC [58].

3.5.2 Monolithic Pixel Detectors

In monolithic pixel detectors, the readout electronics are integrated in the detection volume. Therefore, no interconnection between different components is required, which reduces the material content of the sensor. Typically, monolithic sensors are fabricated in commercially available CMOS processes with some modifications to adapt them to HEP applications. Mass production can therefore profit from the established fabrication capabilities of the CMOS industry, which can result in a significant reduction in cost per sensor.

A major challenge in this design is the interaction between the active sensor and the readout electronics. Part of these electronics are placed in the periphery of the sensor, that is separated from the active pixel matrix and another part is integrated directly in the pixel (*on-pixel*). Two main pixel designs were developed with different approaches to cope with the integration of the readout circuitry into the pixel, that are presented below.

Monolithic CMOS sensors gained notable popularity in the early 1990s in various scientific disciplines [117]. For high-energy physics applications, significant progress was made by the IPHC/IRFU collaboration [118], resulting in a sensor for beam telescope applications and the STAR vertex detector [119], which is presently operating at RHIC.

Large Collection-Electrode Design In the large collection-electrode design, the readout circuitry is placed into the collection electrode [120], as schematically depicted in Fig. 3.5. Inside the electrode, the electronics are well-shielded from the rest of the sensor, which enables the application of a high bias voltage $\mathcal{O}(100\,\mathrm{V})$ that leads to a sizeable depletion region and uniform field configurations. The size of the collection electrode is driven by the necessity to house the required on-pixel electronics. As a consequence, its large surface results in a high sensor capacitance, that can limit the achievable signal-to-noise ratio, as explained in Section 2.6, The large collection-electrode design is used e.g. in the *Mu3e* experiment [121] and also studied for the CLIC tracker [122].

Small Collection-Electrode Design In the small collection-electrode design, the readout electronics are placed on deep well structures that are separated from the collection electrode, as illustrated in Fig 3.6. As a result, the size of the electrode can be minimised, which is beneficial for a low sensor capacitance. In the following, the example of an n-type collection electrode embedded in a p-type substrate and p-type shielding wells is described.

In this design, the bias voltage can be applied to the deep p-type wells (*p-wells*). Non-depleted regions in the sensor lead to the connection of the bias voltage to the substrate and the depletion can then evolve from the pn-junction of the collection electrode with the sensor substrate. However, the pn-junction between on-pixel NMOS transistors used for readout and the shielding p-wells is also affected by the bias voltage, which has important implications for the front-end performance of the sensor. Therefore, the applicable bias voltage is limited, to avoid breakdown of the NMOS transistors [123].

As a consequence of the limited depletion voltage and the small pn-junction from which the depletion evolves, only a fraction of the sensor is depleted. The pixel implants are typically embedded in a high-resistivity material to achieve a larger depletion region. However, since parts of the sensor can remain undepleted, modifications of the sensor design have been developed to mitigate this challenge, as discussed in Section 4.1

The small collection-electrode design is used for instance in the ALICE Inner Tracking System upgrade [124] and is considered for the future CBM Micro-Vertex Detector [125]. It is also used in the CLICTD sensor, which is the main focus of this thesis. In the following chapter, CLICTD is described in detail.

Chapter 4

The CLIC Tracker Detector Technology Demonstrator

The CLIC Tracker Detector (CLICTD) is a technology demonstrator for a monolithic silicon sensor fabricated in a modified 180 nm CMOS imaging process, which combines complex sensor layouts with an innovative front-end design [127]. While CLICTD targets the requirements for the CLIC tracker that were discussed in Section 1.2.4, its design characteristics are also of broad interest beyond CLIC, e.g. for HL-LHC tracking detector upgrades.

The CLICTD sensor features a matrix of 16 × 128 detection channels with a size of 300 µm × 30 µm. In the 300 µm column dimension, the channels are segmented into eight sub-pixels with a size of 37.5 µm × 30 µm as detailed below. The main design parameters of the chip are summarised in Table 4.1 and its layout is depicted in Fig. 4.1. The pixel matrix is shown in the upper 3.84 mm of the sensor. The lower part contains the analogue and digital periphery. The local coordinate system is defined by columns from left to right and rows from bottom to top.

In the following, the sensor process used for CLICTD is described. Subsequently, the

Table 4.1. Main design parameters of the CLICTD sensors. Values taken from [55].

Parameter	**Value**
ASIC size	5 mm × 5 mm
Sensitive area	3.84 mm × 4.8 mm
Matrix size	128 × 16 detection channels
Detection channel pitch	30 µm × 300 µm
Sub-pixel pitch	30 µm × 37.5 µm
Readout scheme	Shutter-based

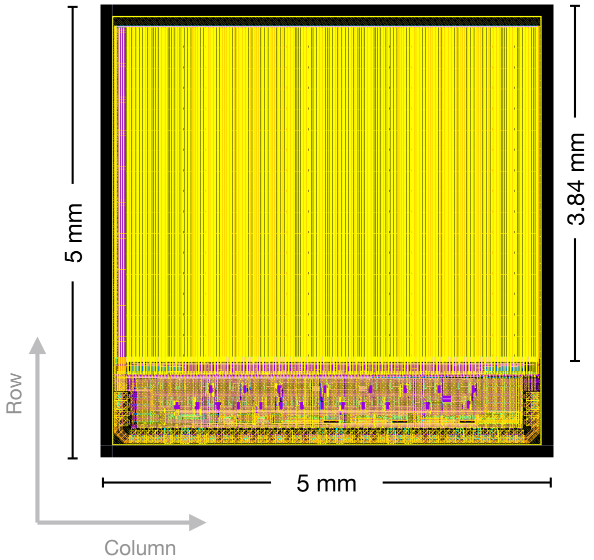

Figure 4.1. Layout of the CLICTD chip. The upper 3.84 mm are part of the pixel matrix and the lower part shows the analogue and digital periphery. Modified from [126]

design of the analogue front-end and the digital logic is outlined and the relevant aspects for this thesis are pointed out. After the operation mode of the sensor is reviewed, an overview of all sensor types and operation conditions investigated in this thesis is presented. Lastly, the optimisation of operation and front-end parameters is briefly explained.

4.1 The Sensor Design

In this thesis, a monolithic 180 nm CMOS imaging process is considered that is modified for HEP applications [128]. Different pixel flavours have been fabricated in this process, as sketched in Fig. 4.2. Whereas the sensor geometry differs between the pixel flavours, the readout circuitry are identical. All pixel flavours pertain to the small collection-electrode design having an n-type collection electrode that is placed on a high resistivity p-type epitaxial layer with a thickness of 30 µm. A 0.8 V reset voltage is applied to the electrode, leading to the collection of electrons that induce a measurable signal. The epitaxial layer is grown on top of a low-resistivity p-type substrate, amounting in a total sensor thickness of 300 µm. CLICTD sensors with smaller thicknesses were produced by removing substrate material, as described in Section 4.5.

The on-channel electronics, which are described in Section 4.2, are placed on deep p-wells separated from the n-type collection electrode. The deep p-wells shield the CMOS transistors from the electric field inside the sensor and prevent the injection of noise

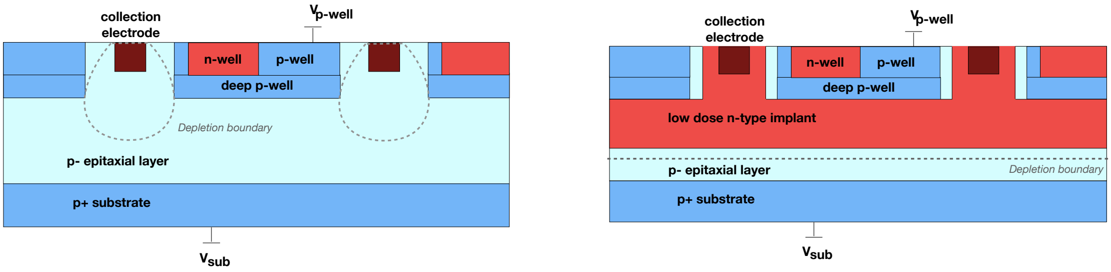
collection electrode
$V_{p\text{-well}}$
n-well
p-well
deep p-well
Depletion boundary
p- epitaxial layer
p+ substrate
V_{sub}
collection electrode
$V_{p\text{-well}}$
n-well
p-well
deep p-well
low dose n-type implant
p- epitaxial layer
Depletion boundary
p+ substrate
V_{sub}

(a) No n-implant **(b)** Continuous n-implant

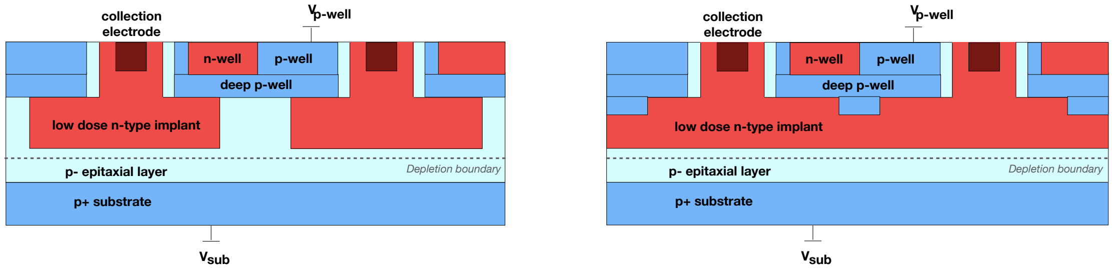
collection electrode
$V_{p\text{-well}}$
n-well
p-well
deep p-well
low dose n-type implant
p- epitaxial layer
Depletion boundary
p+ substrate
V_{sub}
collection electrode
$V_{p\text{-well}}$
n-well
p-well
deep p-well
low dose n-type implant
p- epitaxial layer
Depletion boundary
p+ substrate
V_{sub}

(c) Segmented n-implant **(d)** Extra p-well

Figure 4.2. Different pixel flavours of the modified 180 nm CMOS imaging process. CLICTD is fabricated in the following flavours: continuous n-implant, segmented n-implant and extra p-well. The dashed line indicates the edge of the depleted volume. Not to scale.

into the sensor due to fast-switching circuitry components. Moreover, the shielding is required to avoid charge loss owing to charge collection by electrodes other than the collection electrode.

The Pixel Flavours The investigated small-collection electrode sensor process is fabricated in different pixel flavours. The first pixel flavour in Fig. 4.2a was already successfully tested within the framework of the ALPIDE sensor development for the ALICE Inner Tracking System upgrade [129, 130]. The second flavour in Fig. 4.2b is optimised to achieve full lateral depletion in the epitaxial layer. To this end, a continuous low-dose deep n-implant is introduced underneath the p-wells [131]. In the third pixel flavour in Fig. 4.2c, the deep n-implant is segmented to obtain a lateral doping gradient below the p-wells. The gradient generates a lateral electric field, which leads to an accelerated propagation of charge carriers towards the collection electrode [132]. The fourth pixel flavour in Fig. 4.2d invokes a similar effect: an extra deep p-implant is added underneath the p-wells as an additional vertical junction resulting in an increase of the lateral electric field and consequently a faster charge collection.

In the flavour without n-implant, a reverse bias voltage is applied to terminals in the p-wells. The voltage is connected with the low-resistivity substrate of the sensor owing to non-depleted regions between the pixel cells. With increasing voltage, the depletion starts to grow from the small collection electrode into the p-type epitaxial layer. The maximum applicable bias voltage is limited to -6 V to avoid breakdown of the on-channel NMOS transistors in the p-wells [123]. The small size of the collection electrode and the low bias voltage limits the achievable depleted volume.

With the integration of the n-type implant in the second pixel flavour, an additional pn-junction is introduced between the n-type implant and the p-type epitaxial layer (*deep planar junction*). A second bias voltage is applied to the substrate of the sensor leading to growth of the depletion from the deep planar junction into the high-resistivity p-type epitaxial layer. The difference between p-well and substrate voltage is limited by the punch-through current between the two nodes, as detailed in Section 6.1. A second pn-junction is formed by the deep n-implant with the p-wells. The depletion grows from this junction into the deep n-implant, towards the n-type collection electrode. The applied bias voltage at the p-wells, the doping concentration of the deep n-implant, as well as the size of the p-wells determine the extent of the depletion region in the epitaxial layer.

The depletion region for the flavour with segmented deep n-implant and extra deep p-well evolve in a similar fashion. However, a potential punch-through between the p-wells and the substrate nodes is aggravated by the gap in the low-resistivity implant or by the protruding p-well structure, respectively.

CLICTD is fabricated in the flavour with continuous n-implant, segmented n-implant and extra deep p-well and therefore no measurements for the design without n-implant are presented in this thesis. Comprehensive experimental studies for this pixel flavour can be found for instance in [123, 133]. A few examples involving the flavour with no n-implant are only presented in the simulation studies in Chapter 11.

The available CLICTD samples are summarised in Section 4.5.

4.2 The CLICTD Detection Channel

The CLICTD sensor consists of 16 × 128 elongated detection channels with a size of 300 µm × 30 µm. In the 300 µm column direction, the channels are segmented into eight sub-pixels, each featuring its own collection electrode and analogue front-end. The discriminator outputs of the eight front-ends are combined in one digital logic of the detection channel. The architecture is depicted schematically in Fig. 4.3. The segmentation scheme ensures a fine pixel pitch while reducing the digital footprint of the device. In the following, the analogue front-end and the digital logic are outlined. A detailed description with focus on the implementation of the electronics is given elsewhere [126]

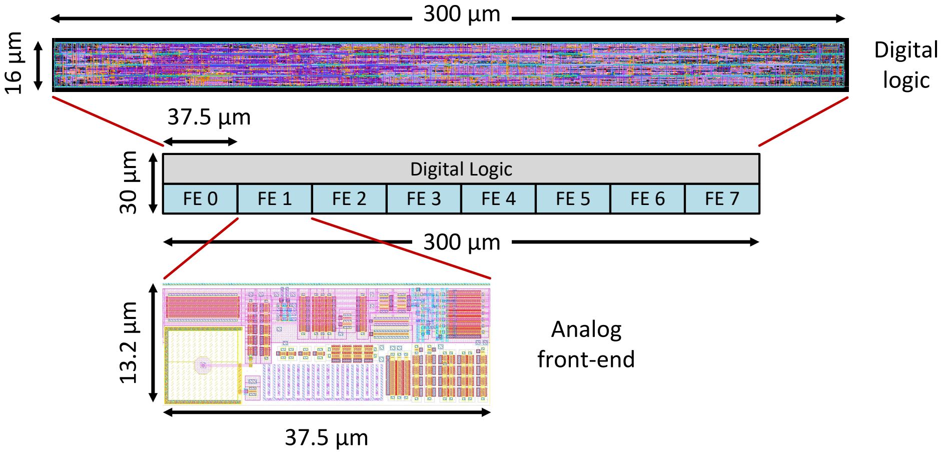

Figure 4.3. Schematic of the CLICTD detection channel. The channel features a common digital logic for eight analogue front-ends pertaining to eight sub-pixels. From [127].

4.2.1 Analogue Front-End

Eight analogue front-ends are integrated in one detection channel. A block diagram of the channel is presented in Fig. 4.4. At the left side of the diagram, a compact representation of only two analogue front-ends is shown instead of eight, due to the repetitive nature of the front-end architecture. Each front-end pertains to one sub-pixel and comprises a collection diode connected to a reset transistor to ensure a continuous reset of the diode. The diode is attached to a level shifter, which in turn is linked to a voltage amplifier that amplifies the signal. An analogue test pulse can be injected at the input of the amplifier using the capacitance C_{Test} (cf. Section 4.3.1).

The amplified voltage pulse is compared to a global threshold V_{TH} at the discriminator of each sub-pixel. Variations of the effective threshold at the discriminator can be corrected with a local threshold tuning DAC that is implemented as a 3-bit binary weighted current source. The discriminator outputs of the eight sub-pixels are connected to the on-channel digital logic.

4.2.2 Digital Logic

The on-channel digital logic can be divided into two parts: The first consists of eight flip-flops that store the binary hit pattern of the eight sub-pixels, as shown in the block diagram in Fig. 4.4. Each of the eight front-end inputs can be masked individually to prevent further processing. Moreover, a digital test pulse can be injected to probe the digital logic independent from the analogue front-end of the device.

The second part implements a logic *OR* to combine the discriminator outputs of the

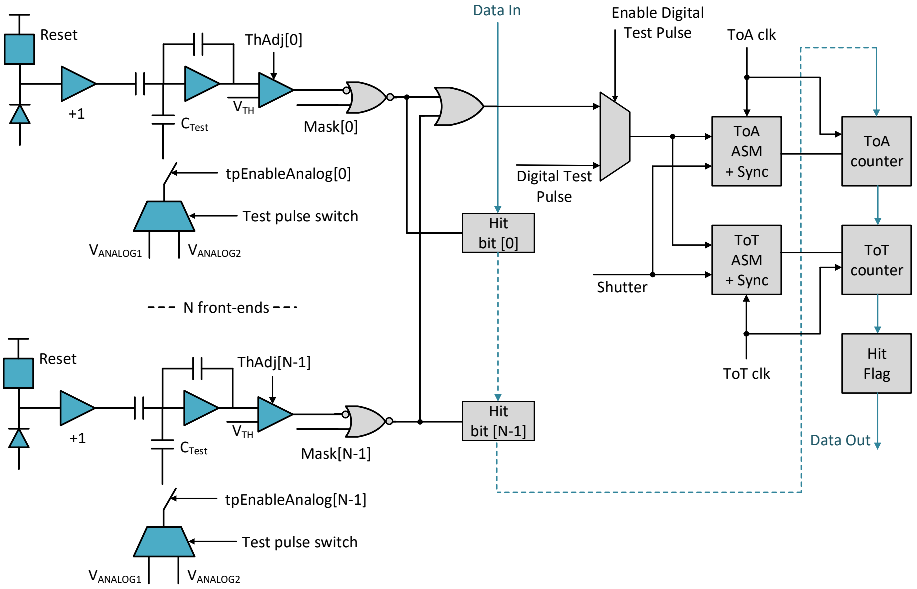
Reset
+1
ThAdj[0]
V_{TH}
C_{Test}
Mask[0]
tpEnableAnalog[0]
Test pulse switch
$V_{ANALOG1}$
$V_{ANALOG2}$
N front-ends
Reset
+1
ThAdj[N-1]
V_{TH}
C_{Test}
Mask[N-1]
tpEnableAnalog[N-1]
Test pulse switch
$V_{ANALOG1}$
$V_{ANALOG2}$
Data In
Hit bit [0]
Hit bit [N-1]
Enable Digital Test Pulse
Digital Test Pulse
Shutter
ToA clk
ToA ASM + Sync
ToT ASM + Sync
ToT clk
ToA counter
ToT counter
Hit Flag
Data Out

Figure 4.4. Block diagram of the CLICTD detection channel. On the left-hand side, two analogue front-end blocks are depicted, the other six are omitted, since they are conceptually identical. The right-hand side shows the digital logic with its Asynchronous State Machines (ASM) connected to the ToA and ToT counters. From [127].

eight sub-pixels. As CLICTD can be configured to perform simultaneous time and energy measurements, the ToA and ToT of the combined signal is computed as well. The ToA measurement is based on a 100 MHz clock, yielding ToA bins of 10 ns. A global shutter signal sets the time reference for the ToA, which is defined as the number of clock cycles from crossing the detection threshold until the shutter is closed. The granularity of the ToA bins sets a lower limit of $10\,\mathrm{ns}/\sqrt{12} = 2.9\,\mathrm{ns}$ to the measured time resolution. Noise and jitter in the amplifier originating e.g. from the input clock and the digital logic can degrade the resolution even further.

For the ToT measurements, a programmable clock divider is used to divide the 100 MHz clock by a factor 2-16, depending on the length of the signal. For the measurements presented in this document, the clock divider is fixed to the highest value, yielding a 6.25 MHz clock.

When the sub-pixel discriminator outputs are combined, the ToA is set by the sub-pixel with the earliest time stamp. The ToT corresponds to the number of clock cycles during which at least one sub-pixel is above threshold. This readout scheme limits the achievable measurement precision if more than one sub-pixel detects a signal above threshold, due to the ambiguity of the ToA and ToT assignment in this case. The implications will be discussed in Chapter 6.

4.3 The Periphery and Interface

The CLICTD periphery at the bottom of the sensor contains analogue and digital components (cf. Fig. 4.1). The analogue part contains Digital-to-Analogue Converters to bias the analogue front-end. In addition, it houses differential receivers and drivers for clock in/-outputs and for data readout. The digital periphery features a slow-control interface for programming of the chip as well as the readout logic for data acquisition. The slow control is based on an $\mathrm{I^2C}$ interface [134] and handles the configuration of DACs, programming the pixel matrix, sending test pulses and initiating the readout [126]. Test-pulse injection and issuing readout commands is also possible through I/O pins, which profits from an increased speed and controlled timing.

4.3.1 Injection of Test Pulses

The injection of test pulses in the analogue front-end and the digital logic probes the on-channel electronics, while excluding contributions from the sensor. In this way, the

Table 4.2. Selectable measurement modes in the CLICTD sensor.

Mode	**Description**
ToA + ToT	8-bits time stamping + 5-bits energy
Long ToA	13-bits time stamping
Photon counting	13-bits number of hits above threshold

front-end and logic can be characterised independently [1]. Test pulsing can be enabled for individual sub-pixels or for the entire matrix.

Once enabled, the analogue test pulse signal is generated in the analogue periphery using the voltage difference between two DACs (`VANALOG1` and `VANALOG2`). The signal is propagated from the periphery along the column until it reaches the sub-pixels with enabled test pulsing. The signal charges the test pulse capacitor C_{Test}, which is connected to the input of the on-pixel amplifier, thus mimicking charge induction on the collection diode. Similarly, the digital test pulse is introduced at the output of the logic *OR* in the digital logic of individual detection channels while masking the front-end output.

4.4 Mode of Operation

CLICTD employs a shutter-based (or frame-based) data acquisition mode, whereby a shutter signal opens the acquisition window for a configurable duration. Once the shutter is closed, the acquisition window ends and the readout is initiated. A serial readout based on a 40 MHz clock is used and data is shifted out of the matrix column by column. During the readout, the shutter remains closed and no pixel hits can be recorded, resulting in a dead time of the sensor.

The frame-based readout is suitable for the low duty cycle of $< 0.001\,\%$ in the CLIC operation scheme (cf. Section 1.2.2). During the bunch train crossing, the shutter is opened and the chip records data. In the 20 ms before the next bunch train arrives, the readout takes place and afterwards the chip is switched to a low-power mode to reduce power dissipation.

During readout, a zero-compression algorithm can be enabled. As the maximum expected pixel-hit occupancy in the CLIC tracker is approximately 1 %, the data volume is drastically reduced by only reading out the detection channel that detects a hit. For the other channels, only one bit indicating the lack of a hit is stored. The compression algorithm reduces the readout time and the amount of data per shutter frame by a factor

---

[1] It should be noted that the front-end is still indirectly affected by the sensor due to the required operation conditions such as the application of a bias voltage to the p-wells.

Table 4.3. Power consumption of the CLICTD sensor. The power consumption during readout are extracted from simulations and the average power consumption assumes a duty cycle with 30 µs acquisition time, 340 µs readout time and 20 ms standby time. Data from [127]

Component	**Acquisition**	**Readout**	**Standby**	**Average**
Analogue - matrix [mW/cm^2]	524	2	2	2.8
Analogue - periphery [mW]	9	9	9	9
Digital - matrix [mW/cm^2]	279	112	0.6	2.9
Digital - periphery [mW]	40	40	40	40
Total - matrix [mW/cm^2]	803	114	2.6	5.7
Total - periphery [mW]	49	49	49	49

of 15 for hit occupancies expected in the CLIC tracker [126].

The different measurement modes available in CLICTD are listed in Table 4.2. The combined ToA and ToT mode enables simultaneous acquisition of time and energy information and is the main operation mode for test-beam measurements. Long ToA is needed for timing studies in test-beam measurements with low hit rates. The photon counting mode delivers binary hit information and is beneficial in several laboratory measurements, where occupancy curves are relevant.

4.4.1 Power Consumption

The CLICTD sensor profits from a power-pulsing scheme introduced in Section 1.2.4 in order to reduce the average power consumption. Between acquisitions, the chip can be switched to a low-power standby mode. In the analogue part, the main on-channel current consuming nodes (level-shifter, voltage amplifier, discriminator and threshold-tuning DAC) are switched to a low-power mode, enabling an average reduction by a factor of about 50 [126]. In the digital domain, clock gating is employed by enabling the clock only for those columns that are read out. In this way, the number of switching gates is minimised. In contrast to the on-channel electronics, no power pulsing is applied to the periphery, since the power consumption is expected to scale only minimally with the matrix size. In potential larger versions of the CLICTD sensors, their contribution is therefore expected to remain similar.

The power consumption during acquisition, readout and standby are listed in Table 4.3. The values for acquisition and standby are extracted from static measurements and the values for the readout phase are taken from simulations. The average values assume a duty cycle consisting of 30 µs acquisition time, 340 µs readout time and 20 ms standby time. The acquisition time is significantly longer than the bunch-crossing duration of 156 ns to ensure that the chip stabilises before data is recorded. The readout time corresponds to the time required to read out a $1\,\mathrm{cm}^2$ matrix with a 40 MHz clock and compression algorithm enabled, assuming a hit occupancy of 1 %. The values are well within the requirements for the CLIC tracker, which foresees an average power consumption of less than $150\,\mathrm{mWcm}^{-2}$ (cf. Section 1.2.4). As the active periods are comparably small, the power consumption is dominated by the standby power, which underlines the importance of a low-power mode.

4.5 Overview of the CLICTD Sensor Types and Operation Conditions

The CLICTD sensor was produced in various design flavours. To facilitate comparison between the different designs and operation parameters, a *standard configuration* is defined, against which design and operation variations are assessed. The standard configuration denotes samples fabricated on wafers with epitaxial layer with a continuous low-dose n-implant and a sensor thickness of 300 µm. The samples are operated at a p-well and substrate bias voltage of -6 V and their respective minimum operation threshold.

The following variations from the standard configuration are considered:

- **Different Detection Thresholds:** The test-beam measurements were performed at various threshold points, allowing for an investigation of all performance parameters as a function of varying detection sensitivity. Typically, different sensor designs or operation conditions are compared by means of these threshold scans.

- **Different Inclination Angles:** Similar to the detection threshold, the angle between beam axis and sensor surface is varied systematically to investigate the effect of oblique particle incidence.

- **Different Bias Voltages:** Since a fixed limit of -6 V for the p-well voltage is set, only a decrease in absolute bias voltage is explored. In all test-beam measurements involving samples with epitaxial layer, the p-well and substrate bias voltages are lowered simultaneously to avoid high leakage currents or potential damage to the device. For the samples fabricated on high-resistivity Czochralski material, the absolute substrate voltage can be increased substantially with respect to the p-well bias voltage and is therefore varied independently.

- **Different Pixel Flavours:** The three pixel flavours realised in CLICTD are the ones with continuous deep n-implant, segmented deep n-implant and extra deep p-well. The optional segmentation and extra deep p-well are only applied in the column direction. In the row direction, a high degree of charge sharing is desired in order to improve the spatial resolution, as presented in Section 9.4.

- **Different Doping Concentrations of the Deep n-implant:** Three different doping concentrations of the low-dose deep n-implant are available that are denoted as *low*, *intermediate* and *high*. The doping concentration influences how the depletion evolves in the upper part of the sensor, which has important implications for the sensor capacitance. In addition, the doping concentration of the deep n-type implant is crucial for a high radiation tolerance. The radiation tolerance is not considered in this thesis and results can be found elsewhere [135].

- **Different Sensor Thicknesses:** CLICTD sensors with different thicknesses were produced by removing substrate material from 300 µm thick sensors via backside grinding. In this way, devices with thicknesses of 100 µm, 50 µm and 40 µm were produced. The quoted thickness includes a metal stack on top of the sensor, which has an extent of approximately 10 µm [136].

- **Different Wafer Materials:** The vertical size of the depleted volume is limited by the thickness of the high-resistivity epitaxial layer. To increase the depletion depth, an alternative wafer material is investigated. Instead of an epitaxial layer on top of a low-resistivity substrate, the pixel implants are directly implemented on a high-resistivity (few kΩ cm) p-type Czochralski substrate without an additional epitaxial layer [137]. The advantages of the high-resistivity wafer material are two-fold: First, the isolation between p-well and substrate bias nodes is improved, allowing for a larger difference of the two voltages. Second, the depletion can evolve further in depth owing to the larger size of the high-resistivity volume.

An overview of all CLICTD sensors investigated in this thesis is presented in Table 4.4.

4.6 Optimisation of Operation Parameters

The on-channel NMOS transistors are affected by the negative bias voltage applied to the p-well biasing nodes [127].

As a result, the transistors are not operated in optimal conditions and are expected to slow down. This effect is not well-modelled in simulations, since the original transistor fabrication process does not foresee the application of such a high negative bias voltage to the transistor bulk. Consequently, the operating point of nodes in the circuit required re-tuning for bias voltages lower than -3 V. The modified DAC configurations are listed in the Appendix B.

With the optimised DAC settings, the sensor operation down to -6 V is ensured, which is essential to obtain the optimal performance of the device. However, the effect is not fully mitigated and manifests itself e.g. in non-linearities of the ToT measurement and the threshold-tuning DAC, which is further investigated in the laboratory measurements in Chapter 6.

4.6.1 Operation of High-Resistivity Czochralski Sensors

For the high-resistivity Czochralski samples, the default configuration of the sensor listed in Appendix B needs to be modified. The sensors fabricated on high-resistivity Czochralski wafers have a larger depleted volume, especially if high substrate bias voltages are applied (cf. Section 9.7). In these conditions, the sensors are also subject to a larger leakage current that saturates the first stage of the readout electronics and makes the sensor inoperable.

To counteract the saturation, the front-end settings are adapted such that a faster return to baseline at the input node is achieved. With these settings, the sensor can be operated up to -20 V substrate bias voltage before any saturation effects set in. However, the adaptations reduce the signal gain, which leads to coarser steps in the threshold settings and a larger minimum operation threshold, since the front-end is operated in conditions it was not optimised for. The higher thresholds have important implications for the sensor performance, as presented in Chapter 9.

It should be emphasised that the higher threshold is not related to the sensor or the high-resistivity wafer material itself, but to the front-end architecture that was solely optimised for sensors with a thin epitaxial layer. The front-end could be adapted in a new submission of the CLICTD sensor, which would allow for the application of higher substrate bias voltages without an increase in threshold.

Table 4.4. Overview of the tested CLICTD sensors. Cont. - Continuous n-implant, Segm. - Segmented n-implant, Extra P. - Extra deep p-well, Epi. - Epitaxial layer, Cz. - High-resistivity Czochralski substrate, Lab. - Laboratory measurements, TB - Test-beam measurements.

ID	**Flavour**	**n-impl. Dose**	**Thickness** [µm]	**Material**	**Measurements**
A1	Cont.	Low	300	Epi.	Lab. + TB
A2	Cont.	Low	300	Epi.	Lab. + TB
A3	Cont.	Low	300	Epi.	Lab.
A4	Cont.	Low	300	Epi.	Lab. + TB
A5	Cont.	Low	100	Epi.	Lab.
A6	Cont.	Low	50	Epi.	Lab. + TB
A7	Cont.	Low	100	Epi.	Lab. + TB
A8	Cont.	Low	40	Epi.	Lab.
A9	Cont.	Low	40	Epi.	Lab.
A10	Cont.	Low	40	Epi.	Lab. + TB
B1	Segm.	Low	300	Epi.	Lab. + TB
B2	Segm.	Low	300	Epi.	Lab. + TB
B3	Segm.	Low	300	Epi.	Lab.
B4	Segm.	Low	300	Epi.	Lab. + TB
B5	Segm.	Low	100	Epi.	Lab. + TB
B6	Segm.	Low	50	Epi.	Lab.
B7	Segm.	Low	50	Epi.	Lab. + TB
B8	Segm.	Low	40	Epi.	Lab.
B9	Segm.	Low	40	Epi.	Lab.
B10	Segm.	Low	40	Epi.	Lab. + TB
W8	Extra P.	Intermediate	100	Epi.	Lab. + TB
W15	Segm.	Intermediate	100	Cz.	Lab. + TB
W18	Extra P.	High	100	Cz.	Lab. + TB

Chapter 5

Laboratory Setups and Methodologies

The first tests of novel pixel detector prototypes are laboratory studies, whereby basic functionalities are examined. Only if satisfactory results are established, further studies involving charged particle beams are justified. Besides these fundamental quality checks, the well-controlled laboratory environment allows for the characterisation of the sensor response, in particular with focus on the front-end components, which can be probed independently from the sensor. The characterisation involves tuning of operation settings and their calibrations, which is an indispensable input to advanced measurements with particle beams. In this regard, laboratory measurements support and complement all other aspects of the development cycle of novel silicon sensors.

The following chapter presents the setups and the methodical background of the laboratory measurements shown in this thesis. It comprises an overview of the readout system, different measurement setups and the analysis strategies of each measurement. The measurement results are presented in Chapter 6.

5.1 The Caribou Data Acquisition System

The Caribou versatile data acquisition system is used for powering, slow-control and readout of the CLICTD sensor [138–140]. The flexible modular design of the Caribou framework allows for the adjustment of the DAQ system to various detector prototypes, thus reducing cost and time required for the integration and testing of new devices. A picture of the setup is shown in Fig. 5.1.

The hardware consists of a Xilinx Zynq System-on-Chip (SoC) on a ZC706 evaluation board (*Zynq board*) [141]. The SoC contains a Kintex-7 Field Programmable Gate Array (FPGA) and a dual-core ARM Cortex-A9 CPU, which has an Ethernet connec-

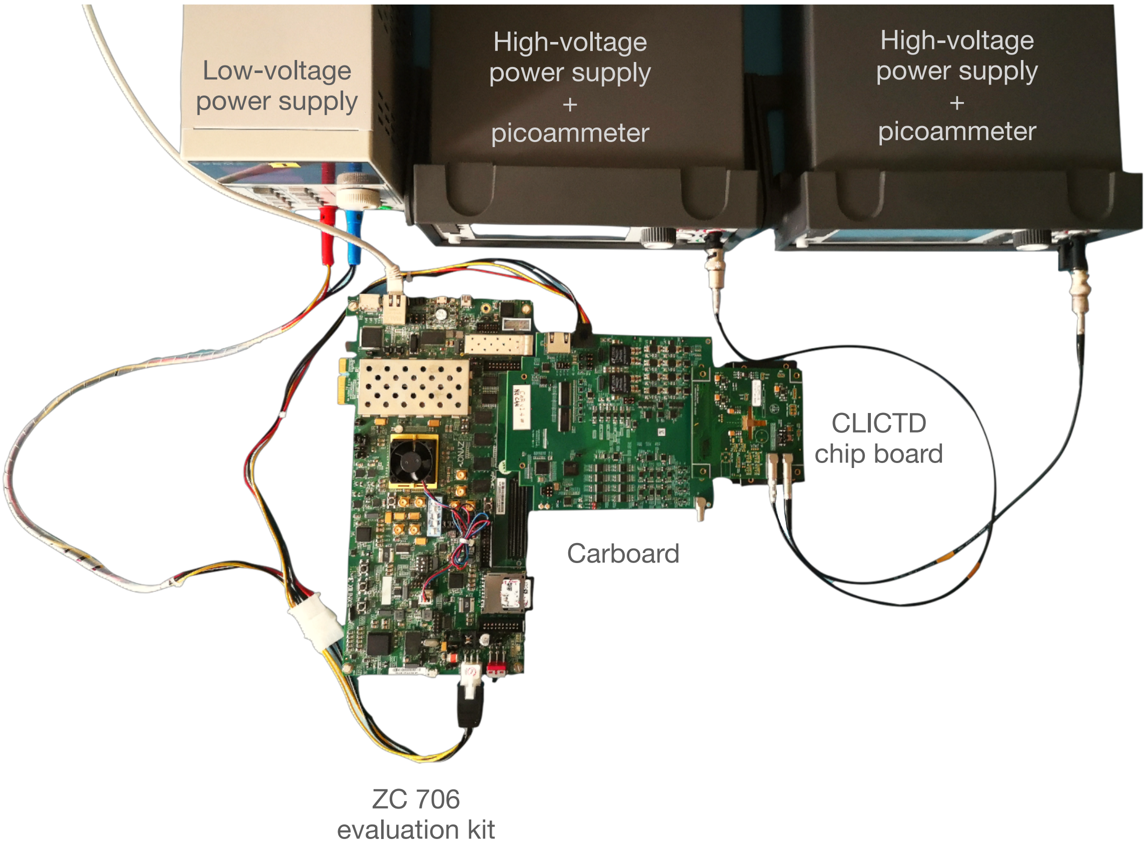
Low-voltage power supply
High-voltage power supply + picoammeter
High-voltage power supply + picoammeter
CLICTD chip board
Carboard
ZC 706 evaluation kit

Figure 5.1. Picture of the Caribou setup. The ZC706 evaluation kit (*Zynq board*) is connected to the Carboard. The CLICTD chipboard is connected to the Carboard as well and receives the two reverse bias voltages from high-voltage Keithley power supplies. A low-voltage power supply delivers power to the setup.

tion to the network for remote operation. The FPGA fabric handles data acquisition and configuration of the prototype by providing a hardware interface to the device. The FPGA registers are coupled to the ARM processor using an AXI bus, thus rendering reading/writing of registers possible within software. The Zynq board is connected to the Carboard using an FPGA Mezzanine Card (FMC) connection. The Carboard houses the hardware environment for several target sensors such as analogue-to-digital converters and adjustable voltage/current references [55]. Additionally, the Carboard can receive input from external clocks and trigger signals provided by a *Trigger Logic Unit (TLU)*.

The Carboard is connected to a *Printed Circuit Board (PCB)*, which houses the prototype sensor (*CLICTD chipboard*). Connection is established using a 320 pin SEARAY connector [142] and communication with the CLICTD sensor is handled by an I^{2}C interface bus on the Carboard. The sensor itself is glued [143] and wire-bonded to the chipboard, which is described in the subsequent section.

An external power supply provides 12 V DC to power the entire Caribou setup. In addition, two Keithley 2450 SourceMeter power supplies [144] are used to provide the bias voltages to the CLICTD sensor and to monitor the leakage currents. They are connected directly to the chipboard as detailed below.

The data acquisition software Peary enables software-based communication with the Caribou system [145]. A Hardware Abstraction Layer acts as an interface between hardware and software and allows the user to control and communicate with different periphery components. A Command Line Interface can be used for stand-alone applications such as laboratory measurement and an Application Programming Interface enables integration into other DAQ systems, which is beneficial for test-beam operation, where the device needs to be synchronised with other detectors.

For the CLICTD prototypes, the sensor is configured using matrix and pattern configuration files that are read in with the Peary software interface and executed in a state machine on the FPGA. The matrix file contains the configuration of each sub-pixel including the local threshold DAC settings or flags to indicate if the sub-pixel is masked or if test pulsing is enabled. The pattern file specifies the operation time pattern such as the assertion of the shutter signal or the injection time of test pulses.

5.2 The CLICTD Chipboard

The CLICTD sensor is glued and wire-bonded to a dedicated PCB, which is depicted in Fig. 5.2. The chipboard design ensures compatibility with the Caribou readout system, to which it can be connected using a SEARY connector as explained above. The chipboard houses only passive components and the power is provided by the Carboard. The only

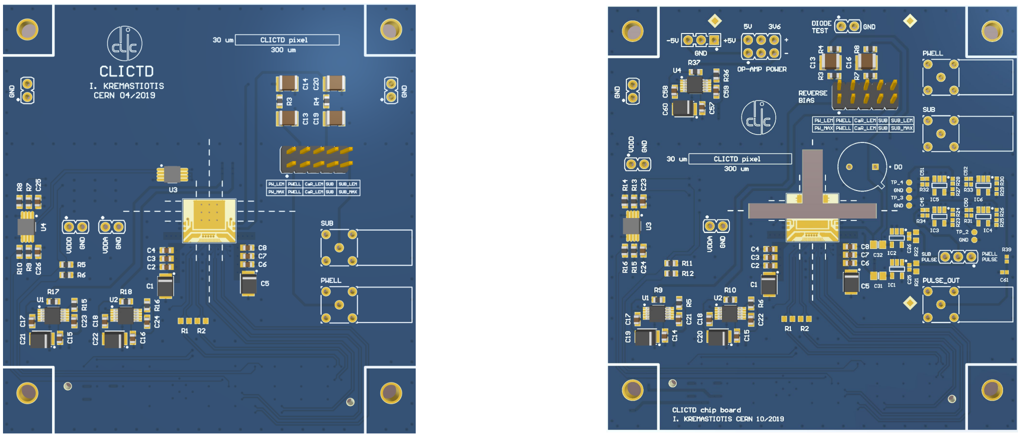

(a) PCB without cut-out below the sensor. **(b)** PCB with cut-out below the sensor.

Figure 5.2. Custom Printed Circuit Board (PCB) for the CLICTD sensor. The sensor is glued and wire-bonded to the PCB. (a) PCB without cut-out behind the sensor and (b) PCB with cut-out to reduce material content in the beam. From [126]

exceptions are the external bias voltages, which can be applied directly to the PCB using two Lemo connectors, where one connector handles the voltage to the p-wells and the other one the voltage to the substrate. A detailed description of the board is provided in [126].

Material Content The amount of material traversed by a charged particle beam determines the contributions of multiple scattering to the particle trajectory. It is thus crucial to reduce the material content, which the beam has to traverse. It is equally important to map the material content out to account for multiple scattering in the reconstruction of particle tracks and for realistic simulations.

For the estimation of the material content of CLICTD prototypes including the PCB layers behind the sensor, the material contribution of each component is expressed as percentage of radiation length, as presented in Table 5.1. The first rows display the material of the CLICTD sensor itself, assuming a metal stack with a thickness of 10 µm [136]. Since the device was thinned to thicknesses ranging between 40 µm and 300 µm, the total material content varies over a range of 0.043 % to 0.321 %.

The custom chip board was fabricated in two versions: the first has PCB material behind the sensor and the second features a cut-out to minimise material content for a particle beam passing through the setup. For the latter, the total material content in the beam only comprises the sensor and no additional calculation of the PCB is needed. For the former, the material of the PCB is shown in the lower rows of Table 5.1 and the total material content of the PCB evaluates to 2.16 %. The PCB has nine vias, each with a diameter of 0.3 mm. Their contribution is neglected, due to their comparably low fill

Table 5.1. Estimation of material content X/X_0 of the CLICTD sensor and the carrier PCB. X_0 is the radiation length of the material and X the thickness of the component. The values for the radiation length X_0 are taken from [146, 147].

Layer	**Material**	X_0 [mm]	X [µm]	X/X_0 [%]
Sensor			**40 - 300**	**0.043 - 0.321**
Sensor	Silicon	93.6	30 - 290	0.032 - 0.31
Metal stack	Aluminium	88.9	10	0.011
PCB			**1744**	**2.16**
Metal layers	Copper	14.3	144	1.00
Substrate	Glass fibre (60% of FR-4)	97.66	960	0.98
Resin	Epoxy resin (40% of FR-4)	349.89	640	0.18

factor of a few percent.

5.3 X-ray Fluorescence Measurement Setup

X-ray fluorescence measurements are performed for the energy calibration of CLICTD samples, as detailed below. The experimental setup is shown schematically in Fig. 5.3. Primary X-ray photons are created in an X-ray machine model PW3373/10 Ceramic Tube Cu LFF [148] by accelerating electrons onto a copper target. The primary photons are directed onto a secondary target, from which secondary fluorescence X-rays are emitted that are incident on the Device Under Test (DUT). The energy spectrum of the secondary photons is determined by the material of the secondary target. For this study, different secondary targets consisting of titanium, calcium, iron and copper are used.

5.4 Sensitivity to Light and Temperature

While the frontside of the CLICTD sensors is covered with metal layers (cf. Section 5.2), the backside is unprocessed and susceptible to incoming photons from ambient light sources. For CLICTD sensors with epitaxial layer and a thickness exceeding 50 µm, the light from the backside is largely absorbed in the first tens of micrometers [149], which is inactive sensor material (cf. Section 9.7). Therefore, no significant number of photons can enter the active sensor region and the sensor remains unaffected by ambient light.

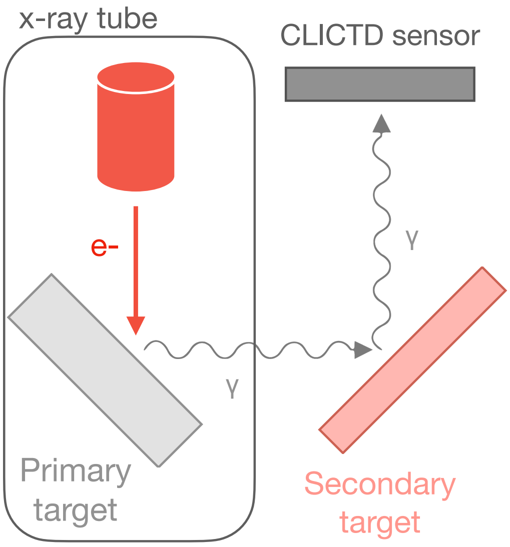

Figure 5.3. Schematic of the setup for X-ray fluorescence measurements. The symbol e- denotes electrons and γ represents X-ray photons.

However, for 40 µm thick sensors, the inactive material is mostly removed (cf. Section 9.7) and a substantial amount of light enters the active sensor volume resulting in a saturation of the readout from the increased leakage current. To mitigate this effect and protect the sensor from ambient light, a thin black sheet is used to cover the cut-out of the PCB. For sensors that were operated with the sheet in place, the material budget calculations in Section 5.2 are corrected to account for the extra material.

The thin sensors are also prone to over-heating due to insufficient heat transfer to the PCB or ambient air. As a result, the leakage current can increase to the point, where the sensor is inoperable. To prevent over-heating, the samples are constantly air-cooled by employing a low-power fan. The air-cooling allows for sufficient heat transfer and no additional cooling system is needed.

5.5 Methodology

In the following, the methodologies and analysis strategies for the laboratory measurements are presented. In all measurements, the Caribou readout system is employed to operate the sensor and to handle data acquisition. The measurements are performed at room temperature and with ambient lighting, unless explicitly stated otherwise. The samples are cooled using a fan that provides a laminar air flow over the sensor surface. While the p-well and substrate bias voltages is varied in the different measurements, the voltage at the collection diode is always fixed to 0.8 V.

Table 5.2. Energy and mean number of liberated charge carriers for the target materials used in the X-ray calibration measurements [153]. The expected amount of created charge is calculated assuming a mean electron-hole pair creation energy of $3.66 \pm 0.03\,\mathrm{eV}$ in silicon [151,152].

Target	K_α **energy [keV]**	**Created charge** $[e]$
Calcium	3.69	1008 ± 8
Titanium	4.51	1232 ± 10
Iron	6.4	1749 ± 14
Copper	8.05	2199 ± 18

5.5.1 Current-Voltage Characterisation

The current-voltage characteristics allow for an electrical characterisation of the sensors and are used to determine the voltage range, in which they can be operated. Current-voltage (IV) curves are recorded by setting the p-well bias voltage to a fixed value and scanning the substrate voltage. The scan range starts from the fixed negative p-well voltage level and is gradually increased to higher absolute bias voltages using a step size of 1 V. It is interrupted once the leakage current exceeds 700 µA to prevent damage of the device. The scan is repeated ten times and the mean of the recorded p-well and substrate currents is calculated per scan step.

5.5.2 Threshold Calibration

The detection threshold is calibrated using the X-ray fluorescence setup presented above. The K_α lines of the fluorescence spectra have characteristic well-defined energies with line widths of a few eV [150]. The known energies of these K_α peaks are therefore ideal as an energy reference in order to convert the threshold DAC steps into physical units.

Up to four different target materials are used in the measurement, resulting in four relevant K_α lines that are listed in Table 5.2. The expected amount of charge that is created in the silicon is also shown, assuming a mean creation energy of $3.66 \pm 0.03\,\mathrm{eV}$ per electron-hole pair [151,152].

For a given target, the threshold DAC step is determined that corresponds to the K_α energy of the material. To this end, the DUT is exposed to the fluorescence X-rays and the pixel hits are recorded in a 1 ms shutter window. The sensor is operated in photon-counting mode and the counts for the entire matrix are aggregated to a single value per shutter. During the exposure, the threshold DAC setting is scanned by increasing the DAC step by one unit after each acquisition. The scan is repeated 200 times and the mean count value per threshold DAC step is calculated.

Subsequently, the number of counts as a function of threshold (*occupancy curve*) is fitted with an S-shaped function

$$\mathrm{Cnts}(x) = A \cdot \left(1 - \mathrm{erf}\left(-\frac{x-\mu_S}{\sqrt{2}\sigma}\right)\right) + B, \tag{5.1}$$

where $\mathrm{Cnts}(x)$ is the number of counts for a given threshold x. B is a constant offset, A a normalisation constant, μ_S is the turn-on threshold associated with the mean K_α energy of the X-rays and σ is related to the threshold dispersion and noise. The error function $\mathrm{erf}(x)$ is defined as:

$$\mathrm{erf}(x) = \frac{2}{\sqrt{\pi}} \int_0^x e^{-t^2} \mathrm{d}t. \tag{5.2}$$

The analysis is repeated for all targets and the different turn-on thresholds μ_s are plotted against the known energy of the fluorescence K_α lines. A linear function is fitted, that provides the calibration parameters for the conversion between threshold DAC steps and physical energy units.

The method is cross-checked by employing a modified analysis technique, whereby the derivative of the occupancy curve is used. The derivative represents the fluorescence X-ray spectrum, which allows for a visual identification of the K_α peak. A Gaussian function is fitted to the peak, where the mean of the Gaussian μ_g corresponds to the turn-on energy of the mean K_α energy and the width σ is associated with the threshold dispersion and the noise level. Although the turn-on threshold and the mean of the Gaussian are mathematically equivalent, their fitted value can differ due to the different fitting procedures. Similar to the method above, the mean of the Gaussian is plotted against the energy of the K_α peaks for different targets and a linear fit is used to find a relation between the threshold DAC step and the energy in physical units.

5.5.3 Equalisation

The effective threshold applied to each sub-pixel is uniformised by using a local 3-bit tuning DAC. The correct tuning DAC code for each sub-pixel is selected by considering the sub-pixel baseline distributions. To do so, a fixed tuning DAC step is set for the entire matrix and the threshold DAC setting is scanned over the full DAC range, while the corresponding noise hits are being recorded. Ten acquisitions per threshold are measured and the mean number of noise hits is considered in the analysis. During the scans, only 1/16-th of the sub-pixels are responsive, the rest of the matrix is masked to avoid saturation of the readout and to inhibit a large voltage drop along the power lines due to the increased power consumption when the entire matrix responds. In this way, multiple hits in the same detection channel are prevented as well, thus ensuring an unambiguous assignment of the measured value to the correct sub-pixel. The scan is therefore repeated 16 times with different parts of the matrix unmasked.

Subsequently, the noise hits as a function of threshold are considered for each tuning DAC step. The peaks of the distributions are extracted as single sub-pixel baselines. The sub-pixel baseline distributions for two central tuning DAC steps are plotted and the average of the two mean values is used to define a target baseline. Next, the optimal tuning DAC step for each sub-pixel is determined by selecting the DAC step such that the distance of the sub-pixel baseline to the target baseline is minimised.

The remaining threshold dispersion is calculated as the RMS of the sub-pixel baseline distribution after the equalisation procedure.

5.5.4 Noise Characterisation

The single sub-pixel noise is determined from the threshold scans taken for the equalisation procedure. For each sub-pixel, the number of noise hits as a function of threshold is considered and the RMS of the noise hit distribution is extracted. The distribution of single sub-pixel noise RMS is plotted and the most probable value is determined.

5.5.5 Minimum Operation Threshold

The minimum operation threshold is defined as the lowest global threshold at which a noise-free operation ($< 1 \times 10^{-3}$ hits/sec for the pixel matrix) of the sensor is possible. Exceptionally noisy pixels are excluded from this definition by masking them online. The number of masked sub-pixels is less than one per mille of the entire matrix. It should be noted that data taking is in principle feasible below the minimum operation threshold without significant performance loss, since minor noise contributions can be removed in the data reconstruction.

5.5.6 ToT Calibration

For the conversion of ToT values to physical units, a ToT calibration is required. The calibration is performed in a two-step procedure: First, a calibration of ToT values to equivalent voltage levels is performed using test pulses injected into the analogue front-end. Second, a calibration between voltage levels and energy in electrons is computed using the results of the threshold calibration. Combining the two calibrations yields a direct conversion from ToT values to physical units.

ToT-to-Voltage Conversion Test-pulses with varying amplitudes are injected into the analogue front-end. The test-pulse injection is triggered 1 µs before the end of a

500 µs long CLICTD frame and is repeated 50× per sub-pixel. Only 1 out of 16 sub-pixels is pulsed at a time to avoid cross talk.

For each sub-pixel, the test-pulse voltage as a function of the mean recorded ToT is evaluated and a surrogate function is fitted:

$$\mathrm{ToT} = ax + b - \frac{c}{x - t}, \tag{5.3}$$

where a, b, c and t are the fit parameters and x the amplitude of the injected test pulse. The inverse of the function is used to compute an equivalent voltage level for a given ToT. A fit with the surrogate function is chosen since it captures the shape of the ToT turn-on curve. The physical interpretation of the fit parameters is discussed in Section 6.6.

Voltage-to-Energy Conversion For the conversion from voltage levels to energy, the results from the threshold calibration are exploited by setting a fixed threshold and varying the test-pulse amplitude using the same settings as before. The derivative of the number of recorded hits with respect to the test-pulse amplitude is computed and the central part of the distribution is fitted with a Gaussian function for every sub-pixel individually. The known relationship between the threshold DAC values and physical charge is used to relate the mean of the Gaussian function to a physical charge value. The procedure is repeated for various threshold points and a linear function is fitted between the physical charge values and the test-pulse amplitudes extracted from the Gaussian fits μ_x:

$$\mathrm{Charge} = p_0 \cdot \mu_x + p_1, \tag{5.4}$$

where p_0 is used as conversion factor and p_1 is an offset that should be close to zero.

5.5.7 Front-End Time Resolution

The front-end time resolution is determined using the response-time difference of test pulses injected into the analogue front-end and digital logic of each sub-pixel. The test-pulse injection is triggered approximately 1 µs before the end of a CLICTD frame and occurs asynchronously to the ToA clock to ensure a random phase between the clock and the injection time. The test-pulse amplitude is scanned and the mean ToA of 200 acquisitions per amplitude is calculated.

For each sub-pixel, a correction for time-walk effects is performed and the corrected value is used in the analysis. The correction is based on ToT values and cross-checked using the test-pulse amplitude, which allows for a finer granularity.

The residuals of the corrected ToA values for the analogue and the digital test-pulse injection are evaluated to estimate the front-end time resolution. A lower limit of the resolution is determined by considering only pulse heights that induce a ToT of 11, which is equivalent to the most probable energy deposition of a minimum ionising particle, as presented in Section 9.2.

Chapter 6

Results of Laboratory Measurements

The following chapter summarises the laboratory measurements for the CLICTD sensor. The laboratory-based characterisation allows for a first assessment of the detector performance and enables the identification of performance differences between sensor designs and operation conditions. In addition, the calibration of the detector response and the impact of front-end electronics on the performance of the device is studied, which is an essential input to the test-beam measurements in Chapter 9.

This chapter is based on the setups and methodologies presented in Chapter 5. First, the electrical properties of the sensors are studied by investigating the current-voltage characteristics. Subsequently, a calibration of the threshold DAC is performed and the signal gain is determined. The pixel matrix is then equalised by determining the appropriate threshold-tuning DAC for each sub-pixel and the sensor noise is characterised. Moreover, the minimum operational threshold is determined. Finally, a calibration of the ToT values is presented and the front-end time resolution is investigated. For all studies except for the ToT/ToA calibration, the sensor is operated in photon-counting mode. The chapter only shows results from selected CLICTD samples. Measurements from the other samples listed in Section 4.5 agree with the example results and are therefore not shown.

6.1 Current-Voltage Characteristics

The operation range and optimal configuration of the bias voltages are determined from IV characteristics. In the following IV scans, the current is measured for the full chip.

First, different pixel flavours are studied for a fixed p-well bias voltage in order to identify differences between the sensor designs. Next, only the pixel flavour with segmented n-implant is considered and the p-well bias voltage is varied. Afterwards, samples with different thicknesses are investigated and lastly a sensor fabricated from high-resistivity

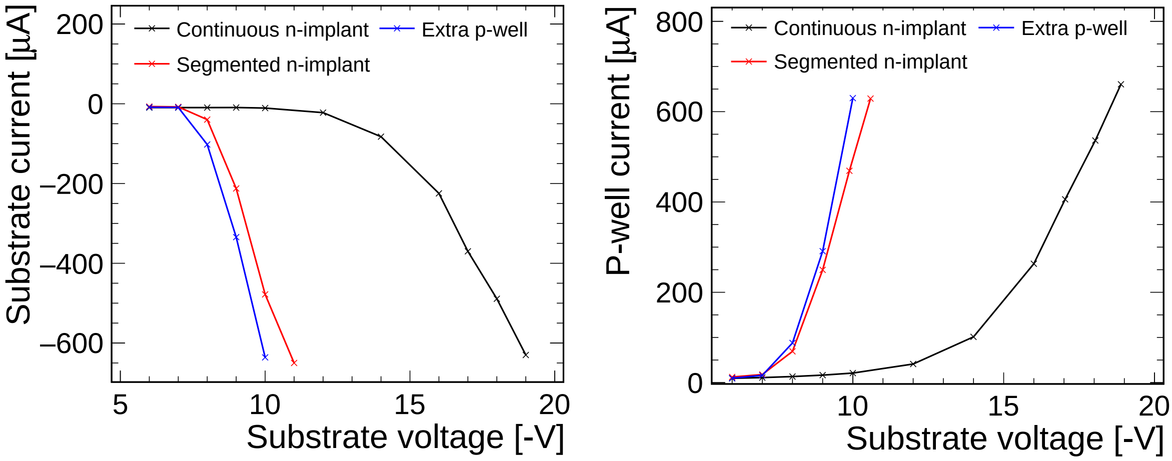

(a) Substrate current.

(b) P-well current

Figure 6.1. IV curves for different pixel flavours at a p-well bias voltage of -6 V. The sensors have a thickness of 100 µm.

Czochralski material is compared to a sample with epitaxial layer.

Pixel Flavours The substrate and p-well currents as a function of the substrate voltage are presented in Fig. 6.1 for the three available pixel flavours. For all samples, a fixed bias voltage of -6 V is applied to the p-wells.

The onset of a punch-through between the nodes in the p-wells and substrate is visible by the simultaneous increase in both substrate and p-well current with higher absolute substrate voltage. The pixel flavour with continuous n-implant can sustain higher substrate voltages owing to the blanket n-implant that acts as an isolation between the p-well and substrate nodes. The isolating structure is disrupted for the flavour with segmented n-implant resulting in higher currents for a given substrate voltage. The same holds true for the flavour with extra deep p-well, where the protruding p-well structure gives rise to an earlier onset of the punch-through current.

Despite the possibility to apply higher substrate voltages for the flavour with continuous n-implant, no significant improvement in performance is expected for higher voltages, since the depletion depth is limited to the thin epitaxial layer. Details are discussed in Section 11.2.2, where device simulations of the sensors are presented.

The following paragraphs only present IV curves for the pixel flavour with segmented n-implant, since the trends are qualitatively the same for all pixel flavours.

P-well Bias Voltage IV scans are recorded for different voltages at the p-wells, as presented in Fig. 6.2 for the pixel flavour with segmented n-implant. The current rises rapidly for an increasing difference between p-well and substrate voltage. The measurements in-

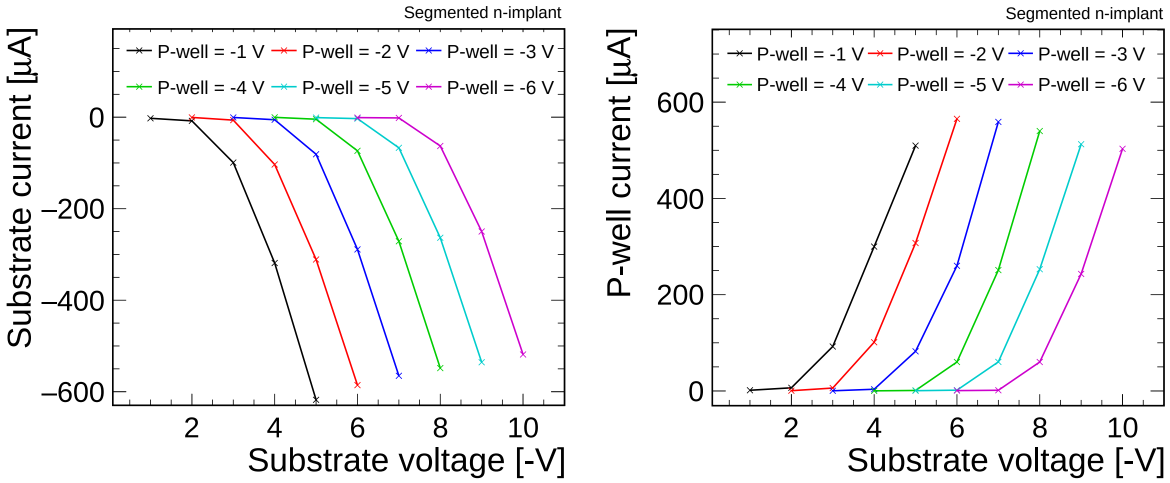

(a) Substrate current.

(b) P-well current

Figure 6.2. IV curves for different p-well bias voltages using the pixel flavour with segmented n-implant. The sensor has a thickness of 300 µm.

dicate that a similar bias voltage should be applied to the two nodes, as measurements with different voltages result in a high current in the sensor.

Thinned Samples IV curves for different sensor thicknesses are displayed in Fig. 6.3 for the pixel flavour with segmented n-implant and a bias voltage of -6 V applied to the p-wells. While results are similar for sensor thicknesses between 50 µm and 300 µm, the current is slightly elevated for the 40 µm sample. Similar results are observed for other pixel flavours as well, which implies a degraded isolation between the two biasing nodes and potentially an increase in defect current related to sensor damage introduced by the backside grinding [154, 155].

Starting Materials The high-resistivity Czochralski material benefits from an improved electrical isolation between the p-well and substrate nodes. As a consequence, the onset of the punch-through current is strongly suppressed, as displayed in Fig. 6.4 for samples with segmented n-implant and a bias voltage of -6 V at the p-wells.

Compared to the samples with epitaxial layer, the depletion can evolve further into the sensor, since a larger fraction of the sensor contains high-resistivity silicon (cf. Section 11.2.3). The enlarged depletion zone has important implications for the sensor performance, as presented in Chapter 9.

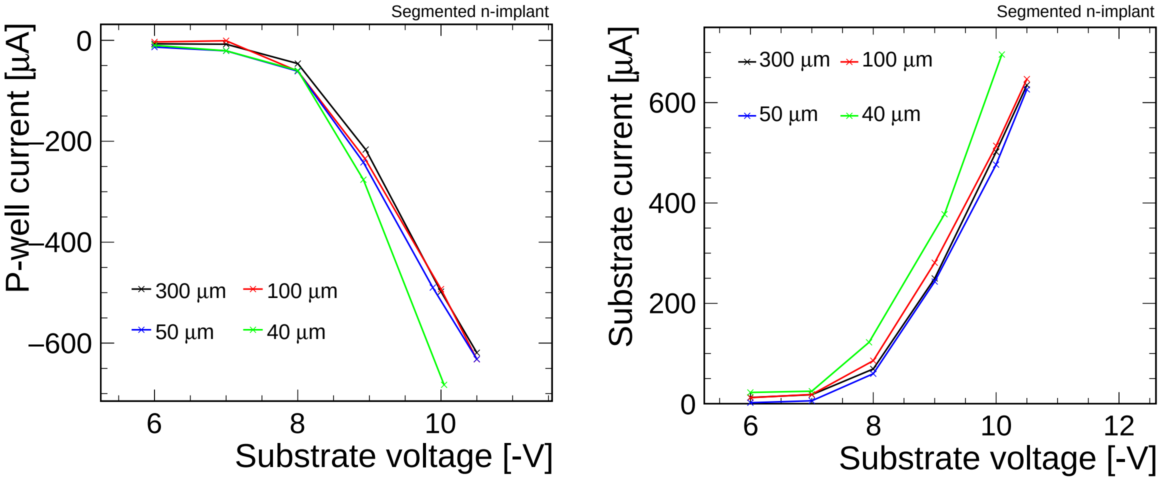

(a) Substrate current.

(b) P-well current

Figure 6.3. IV curves for different sensor thicknesses for the pixel flavour with segmented n-implant. A bias voltage of -6 V is applied to the p-wells.

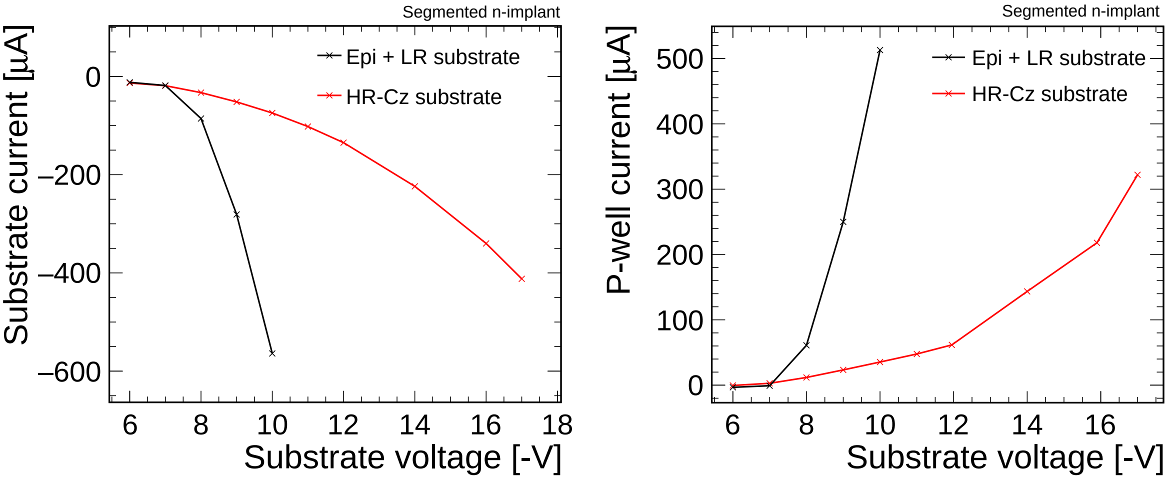

(a) Substrate current.

(b) P-well current.

Figure 6.4. IV curves for different wafer materials. The samples have a segmented n-implant, a thickness of 100 µm and are biased at -6 V.

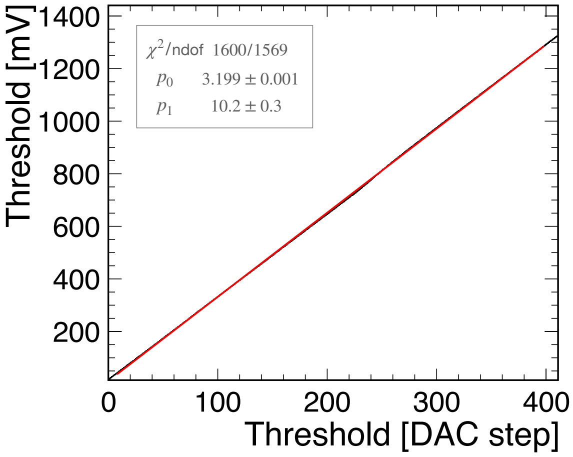

Figure 6.5. Threshold in units of voltage as a function of internal threshold DAC settings. The red line marks a linear fit to the data points.

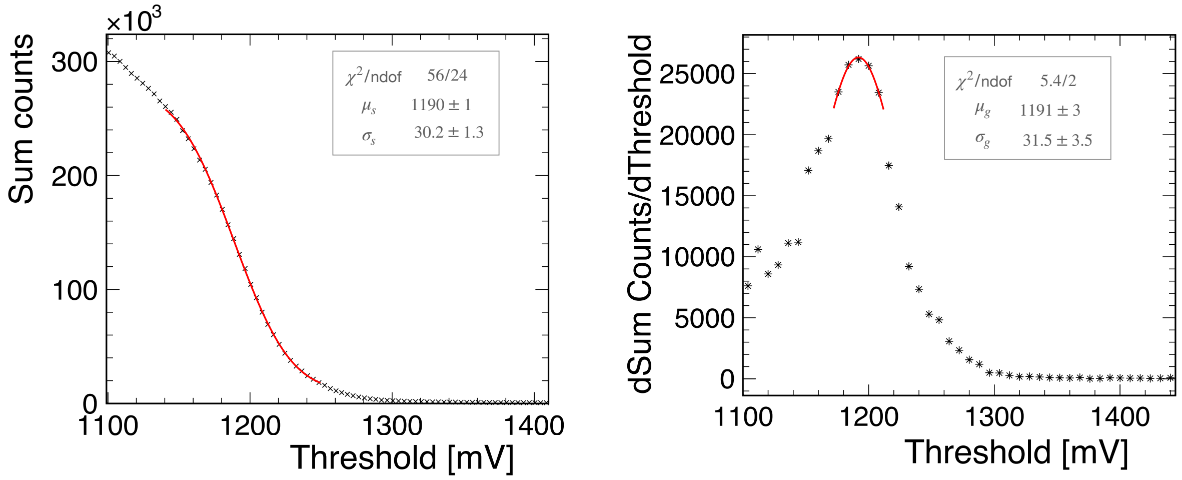

Figure 6.6. Sum of counts for the full matrix as a function of threshold for a titanium target. The S-curve fit is shown in red.

Figure 6.7. Measurement of the fluorescence spectrum of titanium. A Gaussian fit to the K_α peak is shown in red.

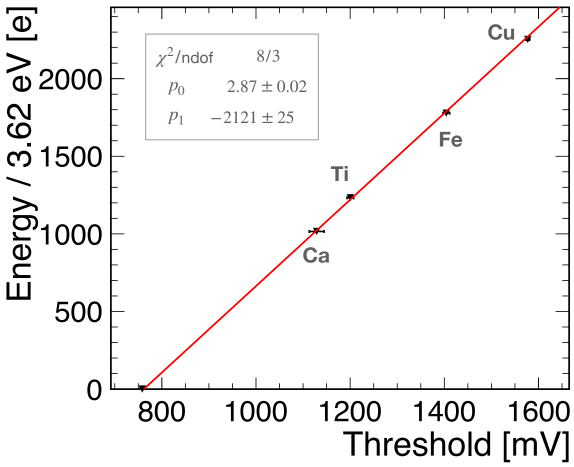

Figure 6.8. Energy calibration of the detection threshold using fit results to the K_α peak of the X-ray fluorescence spectra of different target materials.

6.2 Threshold Calibration

In the following, the X-ray calibration procedure is exemplified with a sensor in the standard configuration. The threshold is set with an external voltage to achieve a better threshold resolution. The conversion between the internal threshold DAC settings and voltage levels is determined by recording the voltage for each DAC step and fitting the distribution with a linear function, as depicted in Fig. 6.5. The slope evaluates to $3.199 \pm 0.001\,\mathrm{mV/DAC}$ step and is used as conversion factor between the two quantities.

The sum of pixel counts for the full matrix as a function of the external detection threshold is displayed in Fig. 6.6 for a titanium target. The S-shaped function in Eq. 5.2 is fitted to the distribution and a turn-on threshold of $\mu_s = (1190 \pm 1)\,\mathrm{mV}$ is extracted.

To cross check the results, the derivative of the occupancy curve is considered in Fig. 6.7. A peak corresponding to the K_α line is distinguishable. The width of the peak is dominated by the detector resolution since the natural line width is of the order of few eV [150]. The non-Gaussian region left of the peak has a strong contribution from hits, where the created charge carriers are not collected by a single pixel but shared to its neighbours. In addition, contributions from the K_β peak to the right of the peak are expected, which also promotes a non-Gaussian shape of the tail. For this reason, only the central part of the peak is fitted and a mean of $\mu_g = (1191 \pm 3)\,\mathrm{mV}$ is extracted in accordance with the results from the S-curve fit.

The procedure is repeated with different target materials. In Fig. 6.8, the turn-on thresholds for the different targets is plotted against their respective K_α energies. As expected, a linear trend is observable between the turn-on thresholds and physical energies. The measured points are therefore fitted with a linear function and the slope of the fit is used as conversion factor between the threshold DAC and physical energies. The slope in Fig. 6.8 evaluates to 2.9 e/mV, which corresponds to 8.9 e/DAC steps. The conversion factor of other samples with the same design and operation characteristics is within ±0.2 e/DAC steps of this value.

Systematic uncertainties Different sources of systematic uncertainties are studied to quantify their impact on the final conversion factors. First, the analysis is repeated with different types of target materials and varied fit ranges to exclude systematic effects related to the analysis itself. A maximum deviation of ±0.2 e/DAC steps is found.

Second, simulation studies based on finite-element and Monte Carlo simulations indicate a charge collection loss of approximately 20 e, as detailed in Section 11.2.7. The charge carrier loss is related to sub-threshold effects and to recombinations in the transition region to the highly-doped substrate, where the charge carrier lifetime is only a few nanoseconds (cf. Section 11.2.5). Taking this estimate on charge collection loss into account yields a one-sided uncertainty of −0.07 e/DAC steps. The statistical uncertainty amounts to ±0.02 e/DAC steps. The total uncertainty is propagated to all laboratory and test-beam measurements.

6.2.1 Determination of Signal Gain

The signal gain is affected by a convolution of the input capacitance of the sensor and electronics effects from the front-end. In the measurements shown in the following section, the signal gain is determined for a minimum-capacitance configuration, where the pixel layout and the sensor operation are chosen such that the input capacitance is minimised. Subsequently, operation configurations with increased capacitance are presented to study the impact of the capacitance on the signal gain. The reason for the different input capacitance is investigated in simulation presented in Section 11.2.1.

Minimum-Capacitance Configuration The capacitance is minimal for sensors in the standard configuration, i.e. a sensor with deep low-dose continuous n-implant with a bias voltage of -6 V/-6 V at the p-wells/substrate is investigated. The signal gain corresponds to the inverse of the slope of the linear fit in Fig. 6.8 and is consequently the inverse of the conversion factor. For the minimum-capacitance configuration, it evaluates to $359^{+39}_{-54}\,(\text{syst.}) \pm 3\,(\text{stat.})$ mV/ke, taking the systematic and statistical uncertainties into account, that were presented above.

Configurations with Increased Capacitance The capacitance is increased with decreasing absolute bias voltage applied to the p-well terminals. Therefore, the signal

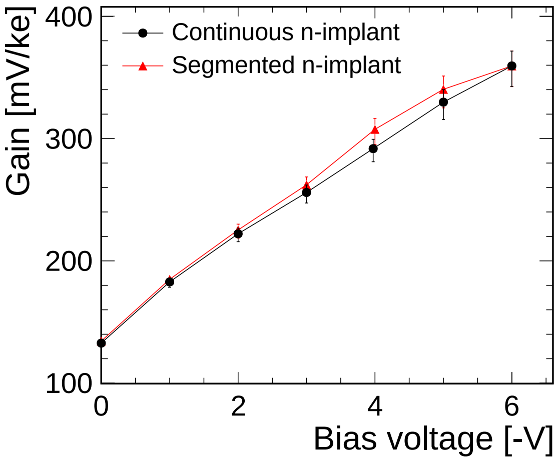

Figure 6.9. Gain as a function of the bias voltage applied to the p-wells and substrate for two different pixel flavours.

gain decreases, as depicted in Fig. 6.9, where the measured gain as a function of the p-well and substrate bias voltage is presented for two different pixel flavours. The two voltages are varied simultaneously to avoid an increase in leakage current. As expected, the different pixel designs have no impact on the gain, but the decrease in bias voltage reduces it by a factor of 2.5 from -6 V to 0 V. Qualitatively, the findings are confirmed by the simulations in Section 11.2.1.

On the other hand, variations of the substrate bias voltage alone have a minor effect on the capacitance and consequently only a small impact on the signal gain, as illustrated in Fig. 6.10. In the measurements, the p-well voltage is fixed to -3 V and the substrate voltage is scanned from -3 V to -7 V. The increase in gain for a step of -1 V is approximately 0.6 %, which confirms that the effect of the substrate bias is negligible compared to the p-well bias voltage.

The sensor capacitance is also affected by different doping concentrations in the deep n-well implants. Consequently, the signal gain changes, as displayed in Fig. 6.11, where the gain for three different doping levels is shown. A bias voltage of -6 V/-6 V was applied to all three sensors.

While the high n-well dose lowers the gain by approximately 30 %, a comparably small decrease is observable for the intermediate dose, implying that the two samples have a similar sensor capacitance.

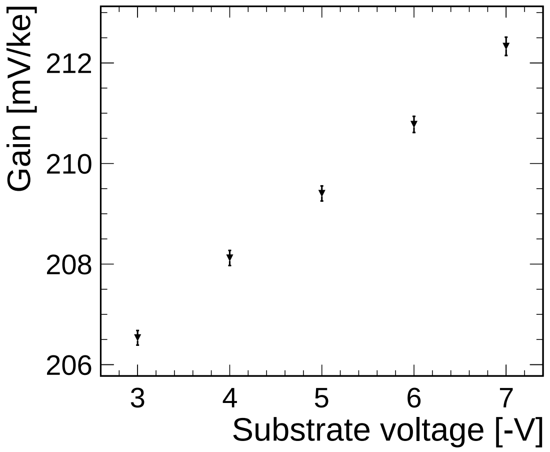

Figure 6.10. Gain as a function of substrate bias voltage for a fixed p-well bias voltage of -3 V.

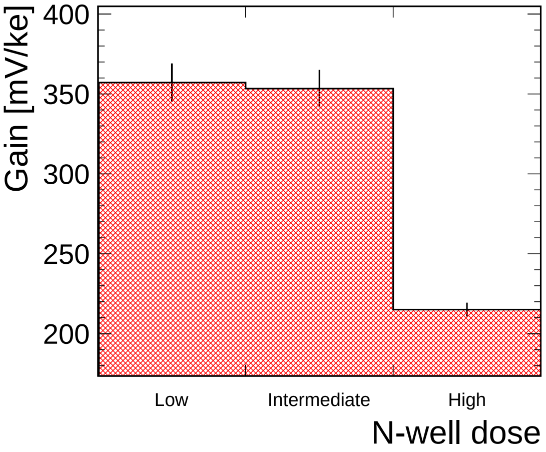

Figure 6.11. Gain for different n-implant doses. The bias voltage is fixed to -6 V/-6 V at the p-wells/substrate.

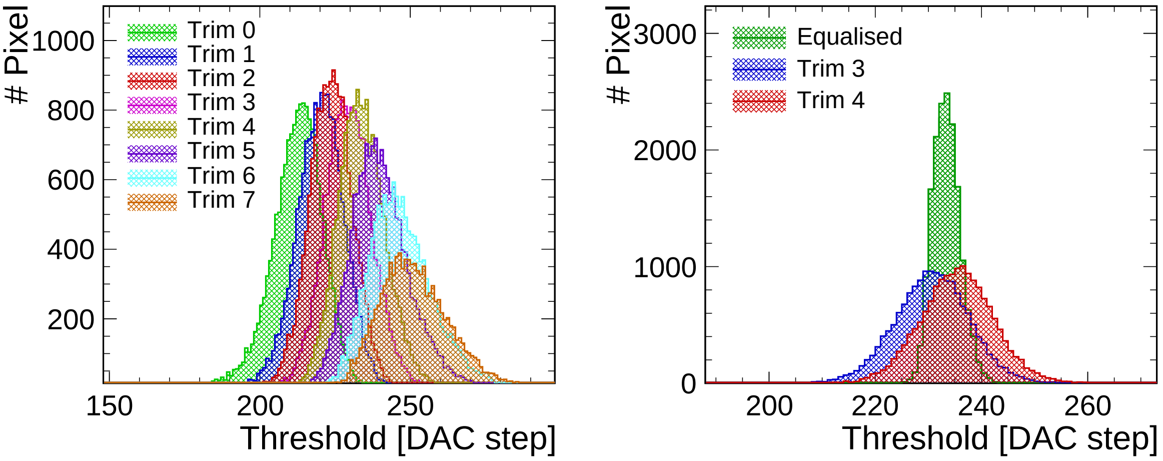

(a) All trim DAC settings.

(b) Central trim DAC settings and equalised matrix.

Figure 6.12. Sub-pixel baseline distributions for (a) all trim DAC settings (b) the equalised matrix and the central trim DAC settings 3,4.

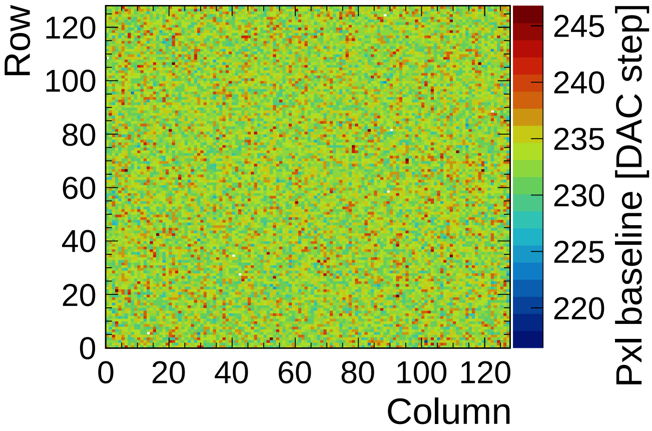

Figure 6.13. Sub-pixel baseline mapped onto the CLICTD pixel matrix after threshold equalisation.

6.3 Equalisation

Pixel-by-pixel variations in the manufacturing process are responsible for differences in the local threshold level of each individual pixel [99]. For a given global threshold, the variations in local threshold lead to a non-homogeneous pixel response across the matrix, which is uniformised using the 3-bit threshold tuning DAC in every sub-pixel.

An example for the pixel baseline distributions for all tuning DAC settings is presented in Fig. 6.12a. The mean of the distributions increases with increasing tuning DAC setting, which confirms its functionality. The threshold dispersion is defined as the RMS of the individual distributions and widens as well from approximately 100 e for the central trim DAC settings to about 400 e for trim 7. The increase in width is an unintentional artefact of non-linearities in the threshold-tuning DAC settings, as explained in Section 4.6. For this reason, the threshold equalisation cannot benefit from established equalisation procedures, which leverage the linearity of the tuning DAC like in e.g. [58, 156]. Instead, the equalisation is adapted by probing all tuning DAC settings for all sub-pixels, as described in Section 5.5.3.

Systematic uncertainties The systematic uncertainty is estimated by propagating the uncertainty on the threshold conversion factor to the threshold dispersion, which yields $^{+0.5}_{-0.8}$ e. Additional sources of systematic uncertainties are studied by repeating the equalisation with different environmental conditions and readout schemes. In total, a maximum deviation of ±3 e is found. The statistical uncertainty is in the sub-electron range and therefore negligible.

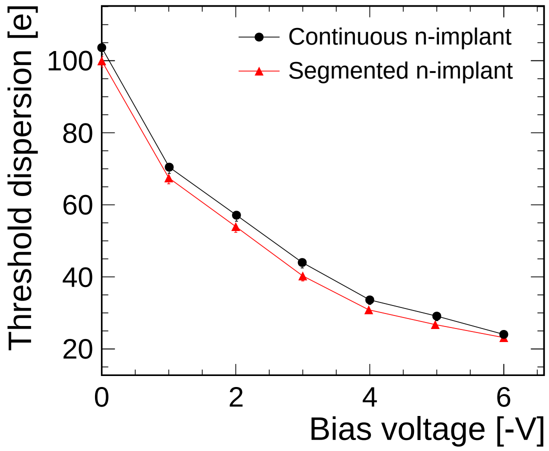

Figure 6.14. Threshold dispersion as a function of the bias voltages applied to the p-wells and substrate for two different pixel flavours.

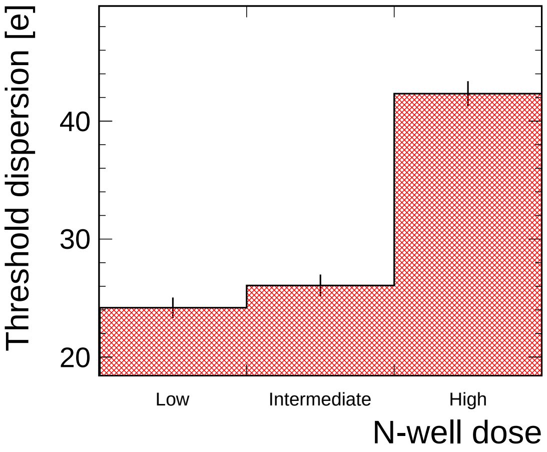

Figure 6.15. Threshold dispersion for different n-implant doses. The bias voltage is fixed to -6 V/-6 V at the p-wells/substrate.

Minimum-Capacitance Configuration The sub-pixel baseline distribution before and after equalisation is displayed in Fig. 6.12b for a sample in the minimum-capacitance configuration. The threshold dispersion for the equalised curve evaluates to 29 ± 3 e. For other samples in the minimum-capacitance configuration, the dispersion is found to be between 27 e and 35 e after the equalisation procedure. These values are about three times lower compared to the threshold dispersion without equalisation, which underlines its importance to obtain the optimal sensor performance.

The equalised sub-pixel baseline mapped onto the CLICTD pixel matrix in Fig. 6.13 does not exhibit any visible patterns, which indicates that there are no unaccounted systematic effects across the matrix related to e.g. the routing of lines.

Configurations with Increased Capacitance The threshold dispersion increases with decreasing p-well bias voltage, as illustrated in Fig. 6.14. The error bars correspond to the systematic uncertainties described above. At 0 V bias voltage, the dispersion is increased threefold with respect to the value at -6 V. The effect is only partially covered by the lower signal gain, which yielded a reduction by a factor of 2.5. Instead, the remaining difference in threshold dispersion is associated with the tuning of the front-end parameters (cf. Section 4.6). As the parameters were optimised for high absolute bias voltages applied to the p-wells, the performance at lower bias voltages deteriorates with the chosen front-end tuning.

The threshold dispersion also increases for higher doping levels of the deep n-implant, as depicted in Fig. 6.15. Within the uncertainties, the increase is covered by the simultaneous decrease in signal gain.

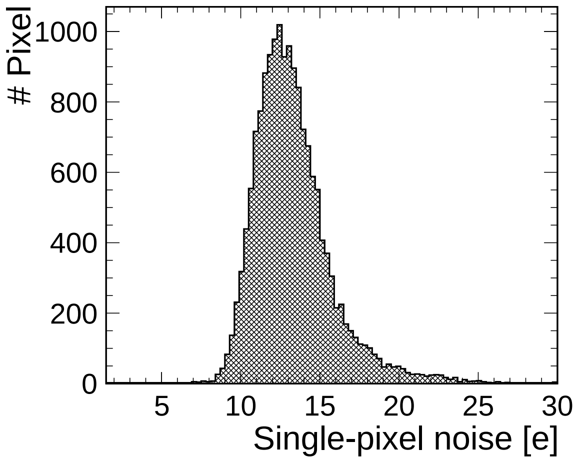

Figure 6.16. Single sub-pixel noise distribution for the minimum-capacitance configuration.

6.4 Noise Characterisation

The small collection-electrode design results in low noise levels owing to a small input capacitance. It is thus essential to keep the capacitance minimal and avoid sensor designs or operation conditions that increase it. To gauge the effects of an increased capacitance on the noise level, sensors operated in the optimal minimum-capacitance configuration are compared to sensors in high-capacitance configurations.

Minimum-Capacitance Configuration The single sub-pixel noise is extracted from threshold scans, as detailed in Section 5.5.4. An example distribution is presented in Fig. 6.16 for the minimum-capacitance conditions. The most probable value evaluates to $11 \pm 1\,\mathrm{e}$, where the uncertainty is calculated with the same procedure as for the threshold dispersion. For other sensors in the minimum-capacitance configuration, the single sub-pixel noise ranges between $10\,\mathrm{e}$ and $14\,\mathrm{e}$.

A two-dimensional map of the single sub-pixel noise across the CLICTD pixel matrix is displayed in Fig. 6.17. A regular pattern along the column direction is distinguishable, which corresponds to the channel layout of the device i.e. the single sub-pixel noise depends on the sub-pixel position within a channel. Since the digital logic of the front-end spans the entire channel, differences in parasitic capacitances along the layout or different sources of noise coupling give rise to the pattern.

The pattern in row direction is related to the integration of additional buffers in the digital logic that repeat every 8 rows. The buffers are responsible for the distribution of the clock and shutter signals from the periphery to the top of the matrix. The modified layout in these rows is responsible for a difference in the single sub-pixel noise that leads to the observed pattern.

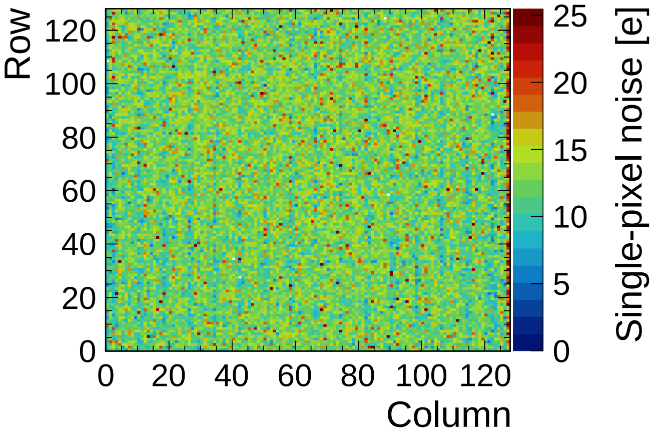

Figure 6.17. Single sub-pixel noise mapped onto the CLICTD pixel matrix.

The visible tail in Fig. 6.16 is caused by the columns and rows with an exceptionally high single sub-pixel noise .

Configurations with Increased Capacitance In Fig. 6.18, the single sub-pixel noise is displayed as a function of the p-well bias voltage. The noise increases with decreasing absolute bias voltage by a factor of 3 - 3.5 from -6 V to 0 V. The increase in noise is rooted in the lower signal gain and is also affected by the front-end tuning, similar to the threshold dispersion presented above. A similar effect is observable for the different doses of the deep n-implant presented in Fig. 6.19. The higher noise has important implications for the minimum operation threshold, which will be discussed in the following section.

6.5 Minimum Operation Threshold

Operating the CLICTD sensors at low detection thresholds is beneficial for all performance parameters (cf. Chapter 9). The minimum achievable threshold is dictated by the single sub-pixel noise and threshold dispersion and thus depends critically on the sensor capacitance [1].

Minimum-Capacitance Configuration To determine the minimum operation threshold, the number of noise hits as a function of the detection threshold is considered in Fig. 6.20. The non-Gaussian noise hits at the right-hand side of the distribution are

---

[1] In long-term operations, the detection threshold needs constant adaptation due to e.g. radiation damage or changing environmental conditions.

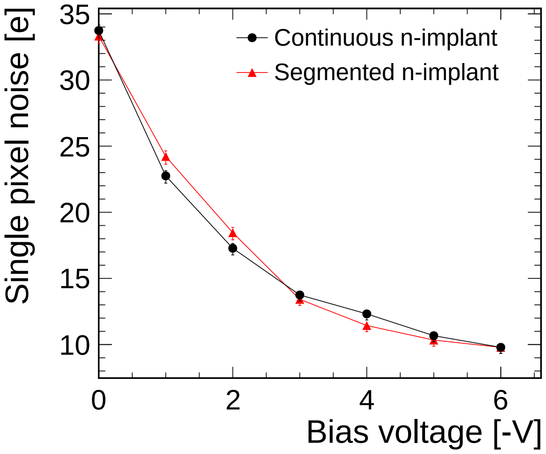

Figure 6.18. Single sub-pixel noise as a function of the bias voltages applied to the p-wells and substrate for two pixel flavours.

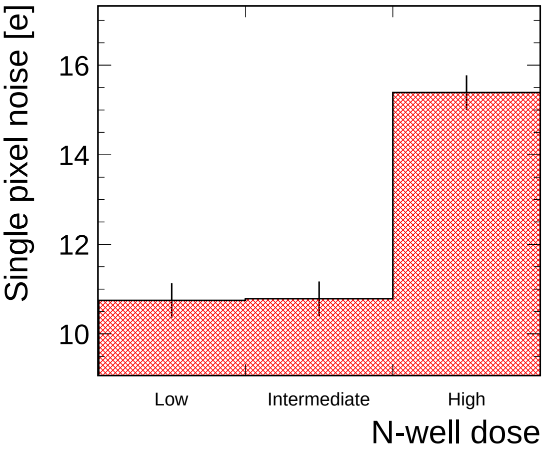

Figure 6.19. Single sub-pixel noise for different n-implant doses. The bias voltage is fixed to -6 V/-6 V at the p-wells/substrate.

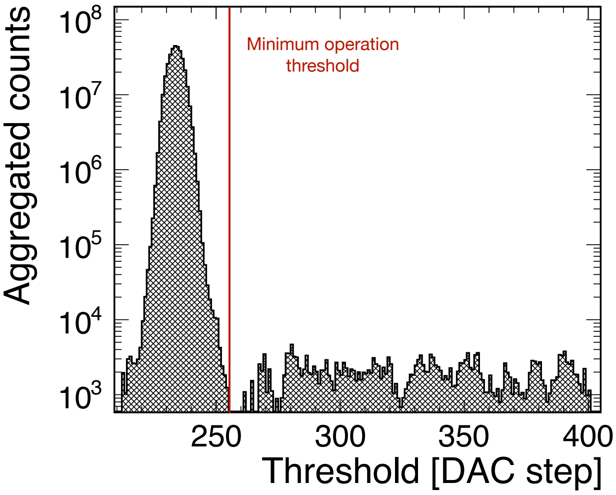

Figure 6.20. Noise hits as a function of detection threshold in a 1 ms shutter window. The red line represents the minimum operation threshold.

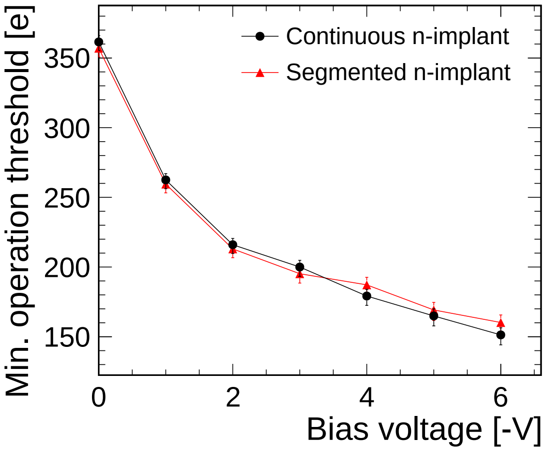

Figure 6.21. Minimum operation threshold as a function of the bias voltages applied to the p-wells and substrate for two pixel flavours

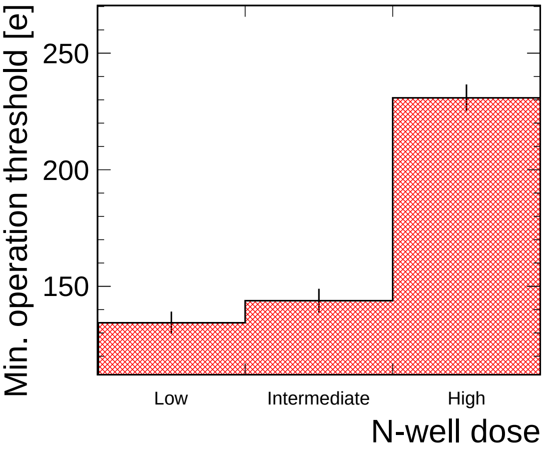

Figure 6.22. Minimum operation threshold for different n-implant doses. The bias voltage is fixed to -6 V/-6 V at the p-wells/substrate.

caused by a few noisy pixels, which are masked online and thus excluded from the data taking in order to achieve a lower operation threshold. The number of masked pixels per CLICTD sample varies between 0.03 % and 0.13 % of the pixel matrix depending on the sample.

The minimum operation threshold for the sensor in Fig. 6.20 evaluates to 135^{+4}_{-5} e according to the definition in Section 5.5.5. The uncertainty is purely systematic and was propagated from the uncertainty on the threshold conversion factor. The minimum operation threshold for other samples ranges between 120 e and 160 e for the minimum-capacitance configuration.

Configurations with Increased Capacitance An increased sensor capacitance leads to a higher minimum operation threshold, as illustrated in Fig. 6.21. While the operation threshold increases by approximately 30 % between -3 V and -6 V, it is about 2.5 times larger at 0 V compared to -6 V, which results in a severe degradation of the sensor performance.

The minimum operation threshold also increases with a higher n-well dose, as presented in Fig. 6.22. Similar to the results above, the difference between low and intermediate dose is negligible within the error bars. The high dose on the other hand leads to a 80 % increase in operation threshold.

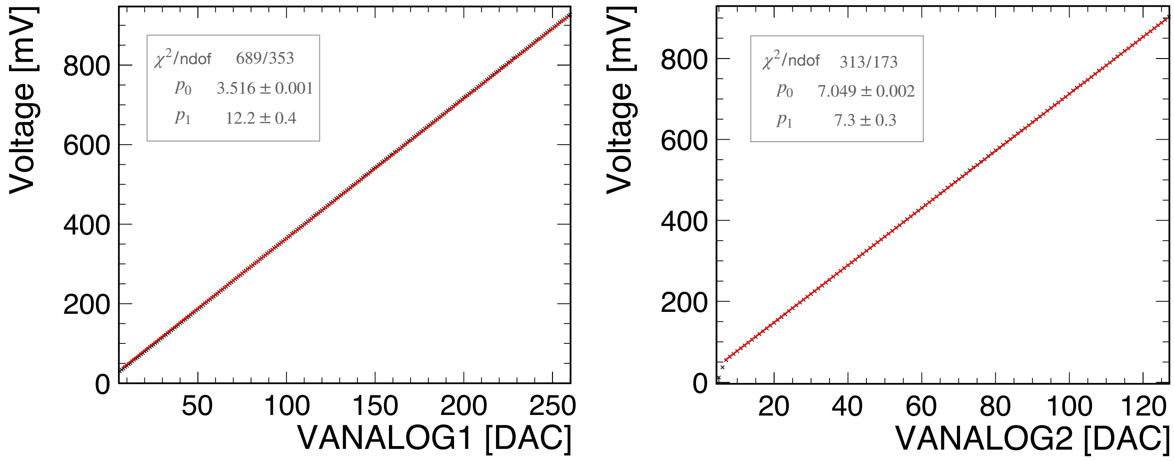

(a) Calibration of `VANALOG1`. `VANALOG2` is fixed to 5.

(b) Calibration of `VANALOG2`. `VANALOG1` is fixed to 5.

Figure 6.23. Calibration of (a) `VANALOG1` and (b) `VANALOG2`, which control the test-pulse amplitude.

6.6 ToT Calibration

A calibration of ToT values to physical units is performed using the methods described in Section 5.5.6.

6.6.1 Calibration of Test-Pulse Amplitude

The amplitude of the injected test pulses is configurable using the two test-pulse DACs `VANALOG1` and `VANALOG2`, as described in Section 4.3.1. To calibrate the test-pulse amplitude and confirm its linearity, the pulse height as a function of `VANALOG1` and `VANALOG2` DAC values is measured, as illustrated in Fig. 6.23. Only one DAC is scanned at a time while the other one is fixed. Both `VANALOG1` and `VANALOG2` are found to be sufficiently linear over a wide range. A linear fit to the curves gives a conversion factor of $3.516 \pm 0.001\,\mathrm{mV/DAC}$ for `VANALOG1` and $7.049 \pm 0.002\,\mathrm{mV/DAC}$ for `VANALOG2`.

6.6.2 ToT-to-Voltage Conversion

Test pulses with varying amplitude are injected into the analogue front-end and the corresponding ToT values are recorded, as exemplified by the two distributions in Fig. 6.24 that were obtained for single sub-pixels. The two distributions exhibit a distinct difference in the smoothness of the curves: while the sub-pixel in Fig. 6.24a displays discrete steps that are related to the individual ToT values, the response in Fig. 6.24b is smoothed out. In addition, the maximum achievable ToT value is 13 for the sub-pixel on the right and

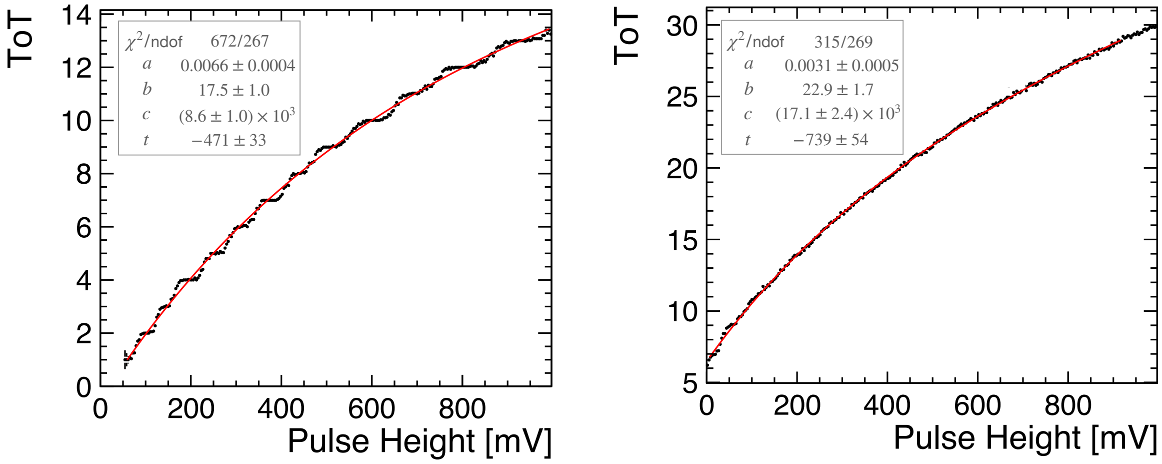

(a) ToT response curve for a sub-pixel with fast signal return to baseline.

(b) ToT response curve for a sub-pixel with slow signal return to baseline.

Figure 6.24. ToT as a function of the injected test-pulse signal for a sub-pixel with (a) slow and (b) fast signal return to baseline. The surrogate function Eq. 5.3 is fitted to the curves.

reaches 25 for the sub-pixel on the left, which indicates that the variance of ToT values for the same voltage levels can be substantial.

The difference between individual sub-pixel ToT curves is related to variations in the analogue pulses at the discriminator. A faster signal return to the baseline level for some sub-pixels causes a shorter time interval above threshold leading to a lower ToT value for a given signal. The lower maximum ToT value for the sub-pixel in Fig. 6.24a is a direct consequence of this phenomenon. In addition, the amplitude jitter is inversely proportional to the slope of the pulse. Therefore, a slow return to baseline results in a high amplitude jitter, that smears out the ToT steps in Fig. 6.24b. These sub-pixel by sub-pixel variations are caused by differences in the effective current pulling the signal back to baseline level.

The surrogate function Eq. 5.3 is fitted to the ToT curves of every sub-pixel and the fit parameters are extracted. Distributions of the fit parameters for one exemplary CLICTD pixel matrix are shown in Fig. 6.25. All parameters display two distinctive peaks that arise from column-by-column and row-by-row variations that are also observable in Fig. 6.26, where the four parameters are plotted across the CLICTD matrix. The regular pattern that repeats every 8 sub-pixels is similar to the results for the single sub-pixel noise in Section 6.4. The origin of the pattern is related to the layout of the digital logic as detailed above.

The goodness of the surrogate function fit is checked by computing the fit χ^2 divided by the degrees of freedom (ndof). The distribution for all sub-pixels in a matrix is shown

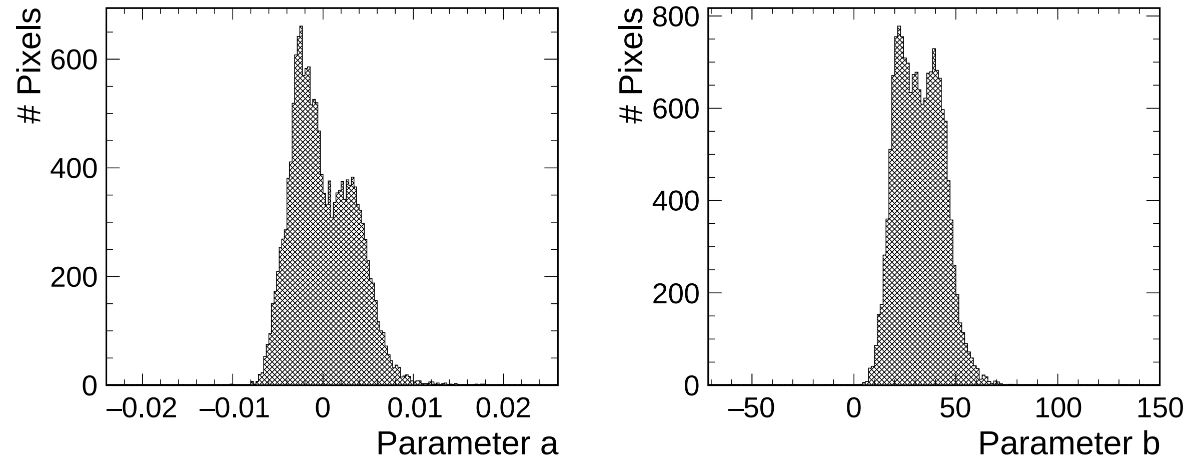

(a) Parameter a

(b) Parameter b

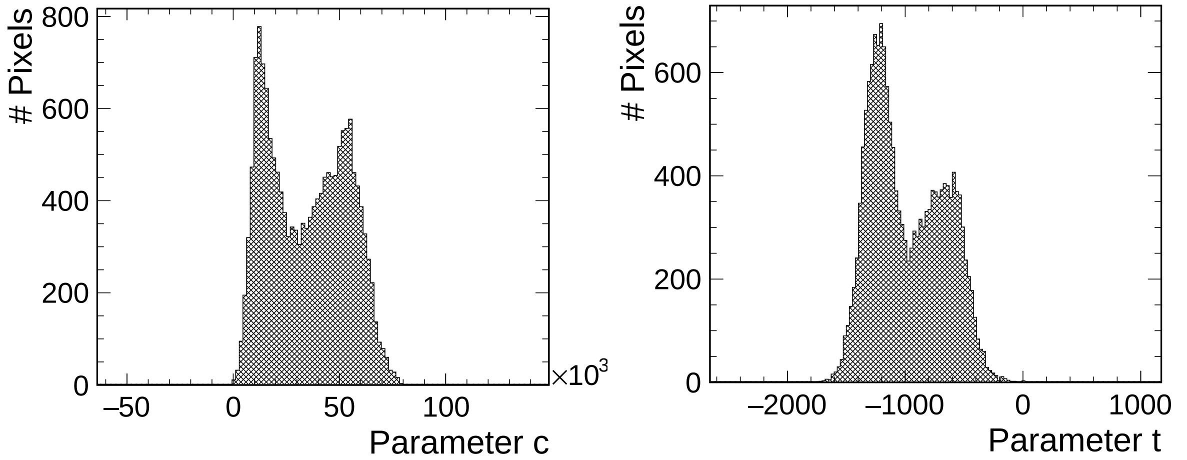

(c) Parameter c

(d) Parameter t

Figure 6.25. One-dimensional distributions of the surrogate function fit parameters.

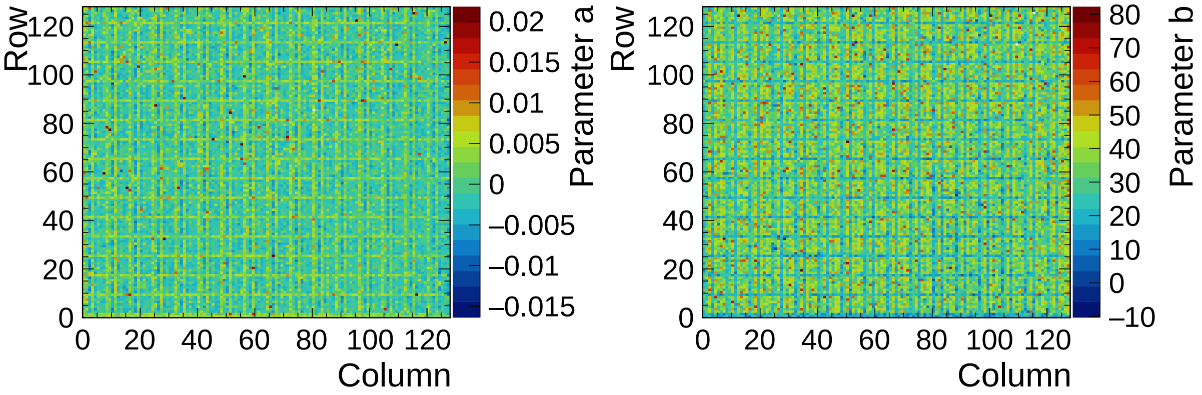

(a) Parameter *a*

(b) Parameter *b*

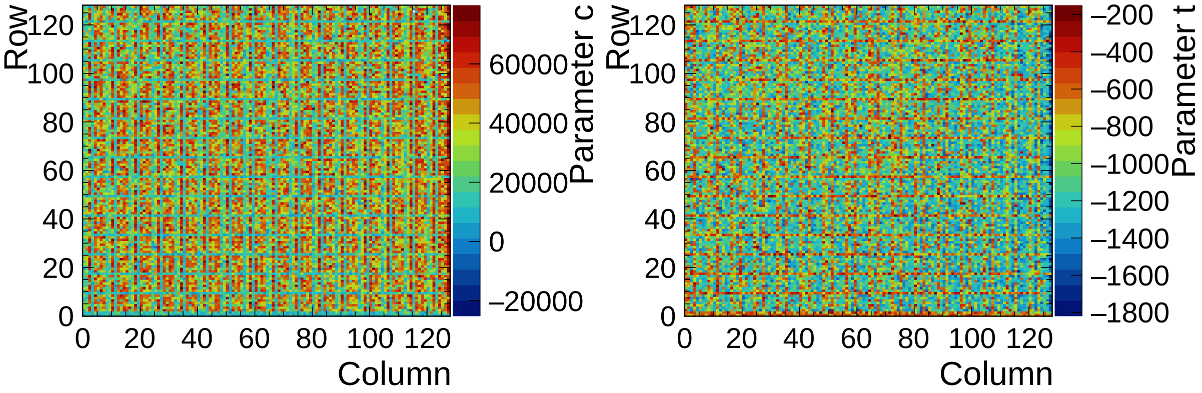

(c) Parameter *c*

(d) Parameter *t*

Figure 6.26. Two-dimensional distributions of the surrogate function fit parameters mapped across the CLICTD matrix.

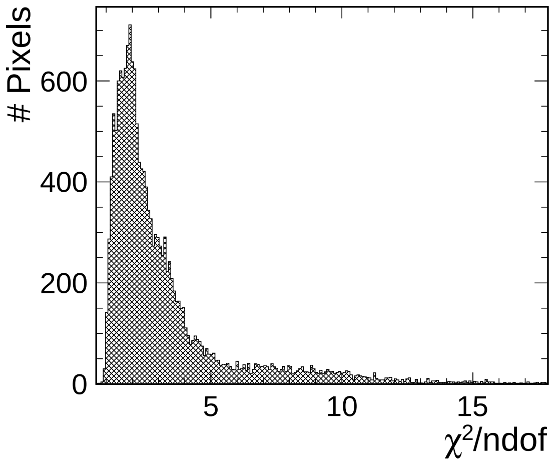

Figure 6.27. Fit χ^2/ndof distribution for the sub-pixels in the CLICTD matrix.

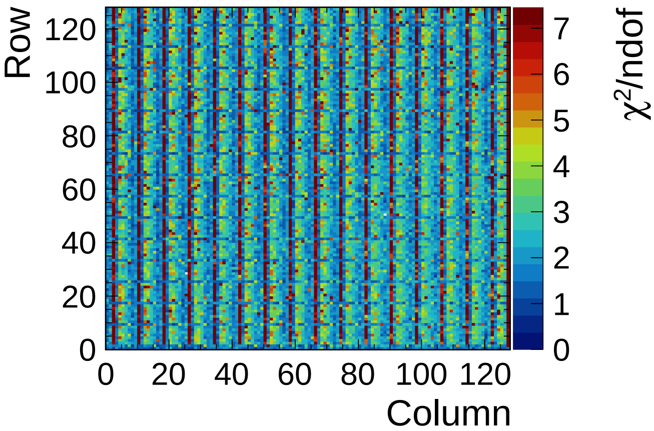

Figure 6.28. Two-dimensional fit χ^2/ndof mapped across the pixel matrix.

in Fig. 6.27. While the peak at a value of $\chi^2/\mathrm{ndof} = 1$ indicates satisfactory fit results, a pronounced tail that extends up to $\chi^2/\mathrm{ndof} = 15$ is observable. The two dimensional representation of the distribution in Fig. 6.28 reveals a regular pattern as well. Sub-pixels in the tail of the distribution are associated with specific sub-columns in the pixel matrix.

6.6.3 Voltage-to-Electrons Conversion

The derivative of the recorded pixel hits as a function of the test-pulse amplitude is shown in Fig. 6.29 for a detection threshold of approximately 1770 e, which corresponds to the mean charge creation by K_α X-rays associated with the iron target. The peak of the distribution is fitted with a Gaussian function and the fitted mean is extracted. It is plotted against the corresponding K_α energy as displayed in Fig. 6.30 for two different

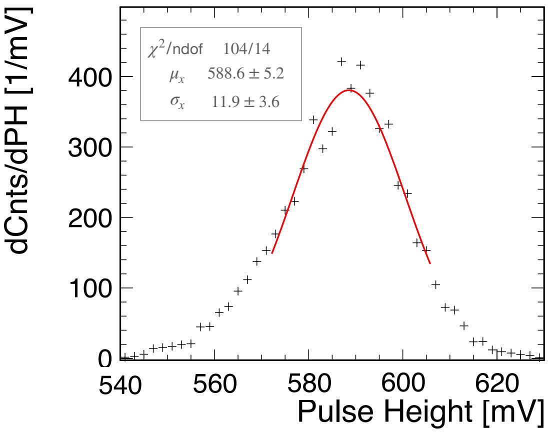

Figure 6.29. Derivative of the recorded counts as a function of the test-pulse amplitude at a threshold of approximately 1770 e corresponding to the X-ray K_α energy of the iron target. A Gaussian is fitted to the peak of the distribution.

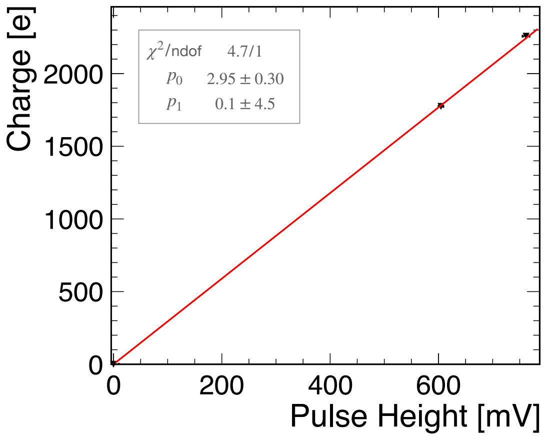

Figure 6.30. Calibration of the test-pulse injection for a single sub-pixel. The pulse height is extracted from the Gaussian fit to the derivative of the recorded counts for a given target. The error bars correspond to the uncertainty on the mean of the Gaussian fit.

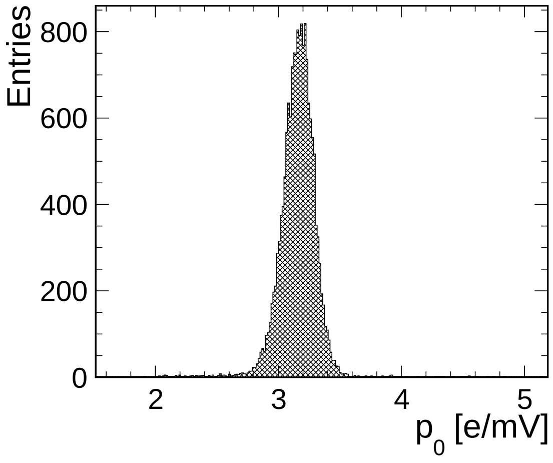

Figure 6.31. Distribution of the fit parameter p_0 for the conversion of test-pulse voltage levels to physical units.

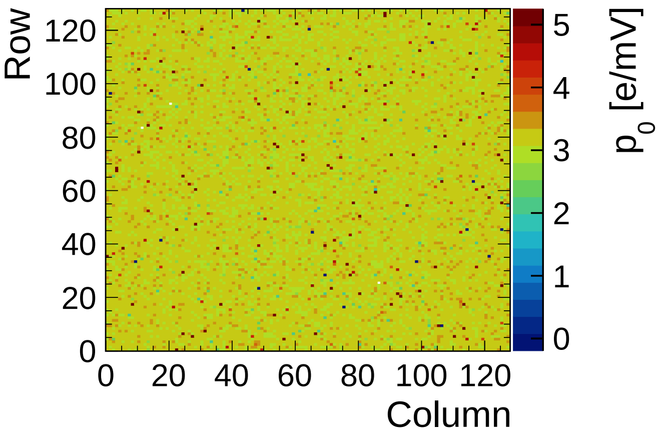

Figure 6.32. Fit parameter p_0 mapped across the CLICTD pixel matrix.

thresholds.

A linear calibration for each sub-pixel is performed by fitting Eq. 5.4 and extracting the slope of the linear function. A two-dimensional map of the extracted slope values p_0 across the CLICTD pixel matrix is displayed in Fig. 6.32. No visible pattern over the matrix is discernible and the few outliers are randomly distributed across the matrix.

The conversion of test-pulse voltage to physical units combined with the ToT calibration to test-pulse voltage allows for a sub-pixel specific conversion of ToT values to physical units. The application of the calibration will be shown on test-beam data in Section 9.2. However, the calibration suffers from a number of shortcomings limiting its applicability, that will be discussed in the following.

6.6.4 Limitations of the ToT Calibration

The ToT calibration was found to have limited precision for the following reasons:

- The capacitance of the test-pulse injector is insufficient to trigger the highest possible ToT in all sub-pixels, as illustrated for the sub-pixel in Fig. 6.24a. Some of the sub-pixels are therefore not calibrated correctly in the high-ToT range. This constraint affects single sub-pixel signals with $\gtrsim 2.1\,\mathrm{ke}$ and is therefore relevant for the high-energy tail of the MIP signal.

- The on-channel NMOS transistors are affected by the negative bias voltage applied to the p-wells. As a consequence, the operation margin of the circuits is reduced leading to a strong non-uniformity and non-linearity in the ToT response [127].

- The combination of the sub-pixel discriminator outputs in a detector channel yields a single value. If several sub-pixels in a channel are hit in the same readout frame, the combined ToT value cannot be attributed to a specific sub-pixel. In the laboratory measurements, only one sub-pixel per channel is pulsed at a time to avoid this ambiguity. In test-beam measurements at the operation threshold, the simultaneous detection of more than one sub-pixel hits per channel occurs for 6% of all clusters for pixel flavours optimised for fast charge collection such as the one with segmented n-implant and 20% of all clusters for the pixel flavour with continuous n-implant, for which charge sharing is more prominent. In these cases, the ToT value is attributed to all sub-pixel hits in the channel and the conversion is performed for each sub-pixel individually i.e. the sub-pixel specific conversion factors are used to convert ToT to electrons.

These constraints complicate the application of the ToT conversion for the test-beam reconstruction, since it introduces major systematic uncertainties, that are not easily quantifiable. For this reason, the conversion is not applied, except for the cluster charge measurements in Section 9.2.

6.7 Front-End Time Resolution

The time resolution of the analogue front-end is determined by evaluating the time residuals between test-pulse injection into the digital and analogue front-end. First, the ToA after digital test-pulse injection is studied, followed by an investigation of the front-end time resolution using analogue test pulses.

Digital Test Pulsing In Fig. 6.33a, the mean of the sub-pixel ToA distributions after digital test-pulse injection is mapped across the CLICTD pixel matrix. The vertical gradient is related to the signal propagation speed of the ToA clock and the shutter signal through the matrix. The signals are distributed from the periphery at the bottom of the matrix to the top and the propagation speed is limited by signal buffers in every 8th row that were implemented to reduce the capacitive load and prevent spikes in the digital power consumption. As a consequence, the actual test-pulse injection time with respect to the ToA clock is different in the vertical direction of the matrix resulting in the pattern visible in Fig. 6.33a. Likewise, the slight column dependence of the mean ToA arises from the horizontal distribution of the ToA clock and shutter signal through the matrix.

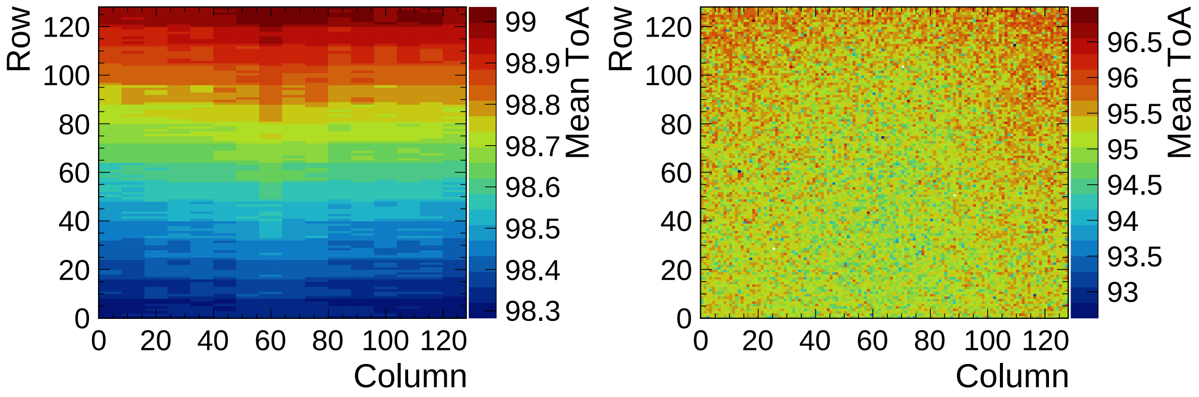

(a) Digital test-pulse injection.

(b) Analogue test-pulse injection.

Figure 6.33. Mean sub-pixel ToA mapped across the CLICTD pixel matrix after (a) digital and (b) analogue test-pulse injection. The nominal delay between injection and closing of the shutter is 1 µs.

Analogue Test-Pulsing The same procedure is repeated with test pulses injected into the analogue front-end. The mean of the sub-pixel-specific ToA distributions is presented in Fig. 6.33b. The mean ToA values are at least 3 units lower compared to the injection into the digital logic due to the processing time of the analogue readout chain. Moreover, the variance of the recorded ToA values is significantly higher as a result of jitter and noise contributions in the analogue electronics. Similar patterns as for the digital test-pulse injection are distinguishable that also arise from the finite signal propagation speed through the matrix and the different way the analogue/digital power supplies are distributed over the matrix.

Time Resolution of the Analogue Front-End For each sub-pixel, the time residuals between the ToA values recorded for the analogue and digital test pulse are evaluated. An example distribution showing the time residuals as a function of the recorded ToT is displayed in Fig. 6.34a. Low signal heights cross the threshold later, which leads to the slow tail for low ToT values (cf. Section 3.2). This time-walk effect is corrected by subtracting the mean time residual for each ToT bin separately, which yields the distribution shown in Fig. 6.34b. A considerable variance in the time residuals at low ToT values is still observable, which is related to time jitter at the threshold-crossing point.

The RMS of the time residuals for each ToT is depicted in Fig. 6.35. For low ToT values, the RMS of the time residuals can be as high as 20 ns. For higher ToT values, a

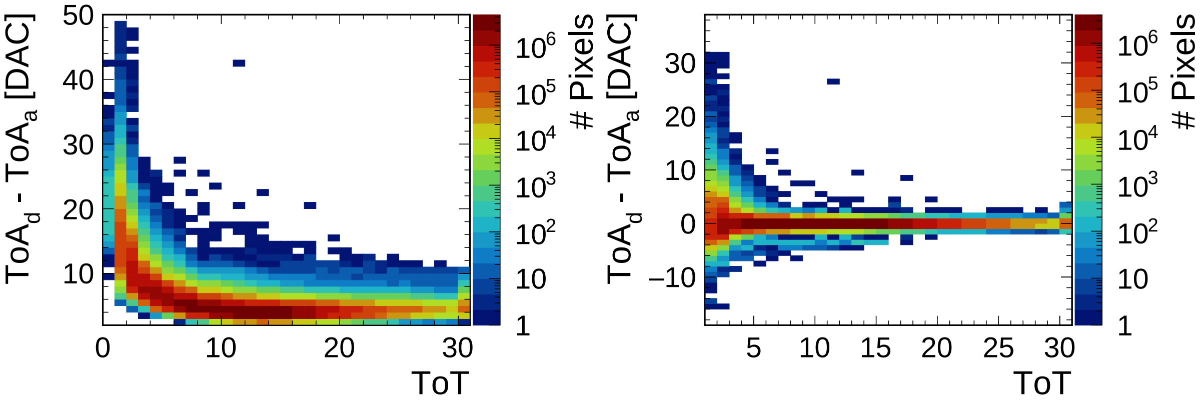

(a) Before time-walk correction. **(b)** After time-walk correction.

Figure 6.34. Time residuals between the ToA values recorded for analogue and digital test-pulse injection (a) before and (b) after time-walk correction.

plateau at approximately 5 ns is distinguishable. The most probable energy deposition of a minimum ionising particle is equivalent to ToT 11, which is well within the plateau region of the distribution. To estimate a lower limit on the front-end time resolution, the RMS at ToT 11 is extracted.

For this measurement, systematic uncertainty introduced by the uncertainty on the threshold conversion factor is negligible. The analysis is repeated by lowering and raising the considered signal range by one ToT bin and a deviation of ±0.1 ns is found. The statistical uncertainty is ±0.1 ns. Therefore, the measurement yields an RMS of the ToA residual distribution of:

$$5.1 \pm 0.1\ \text{(stat.)} \pm 0.1\ \text{(syst.)}\ \text{ns}.$$

The front-end time resolution after time-walk correction is therefore larger than expected from a 10 ns ToA binning (cf. Section 4.2). The time resolution of the entire device is a convolution of the front-end resolution and the sensor resolution. From simulation studies presented in Section 11.2.8, the sensor time resolution is expected to be a few nanoseconds, which implies that the front-end dominates the time resolution and therefore places a fixed limit to the achievable performance of the detector (cf. Section 9.5).

6.8 Conclusion

The CLICTD front-end design, in which the discriminator outputs of eight sub-pixels are combined in a shared digital logic, was confirmed to operate successfully in laboratory

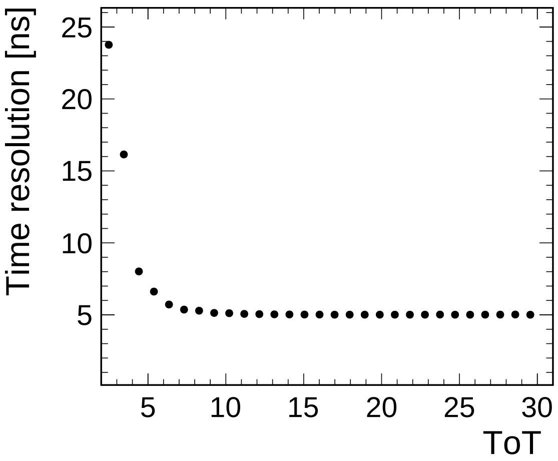

Figure 6.35. Time resolution of the analogue front-end as a function of the recorded ToT value.

measurements. Solely the ToT calibration and the front-end time resolution were shown to be limited due to non-linearities in the front-end that are caused by the bias voltage applied to the p-wells.

After threshold equalisation of the pixel matrix, the noise-free minimum operation threshold evaluates to $< 150\,\mathrm{e}$ for sensors in the minimum-capacitance configuration. If the absolute bias voltage at the p-wells is lowered or sensors with increased doping levels of the deep n-type implant are used, the input capacitance increases and the minimum operation threshold rises as well. Similarly, the single-pixel noise was determined to be $< 15\,\mathrm{e}$ and the threshold dispersion $< 35\,\mathrm{e}$ for the minimum-capacitance configuration, but increases significantly if the capacitance is increased. In the test-beam measurements presented in the next sections, the focus is thus placed on sensor types and operation conditions, which minimise the capacitance in order to guarantee the optimal sensor performance.

Chapter 7

The DESY II Test-Beam Facility and Reference Telescope

Measurements involving a beam of charged particles (*test beam*) allow for a realistic characterisation of silicon sensors, beyond the studies that are feasible in the laboratory. They enable an in-depth assessment of the sensor response to ionising particles in a scenario that is similar to the foreseen operation conditions in vertex or tracking detectors.

As the availability of high-energy particle beams is linked to an exceptional technological and infrastructural effort, there are dedicated test-beam facilities that offer particle beams with often unique beam properties regarding energy, particle species or intensity. The test-beam measurements performed for this thesis were carried out at the DESY II Test-Beam Facility that is introduced in the following section. Moreover, the test-beam setup is described and the operation of the CLICTD sensors during the measurements is detailed.

7.1 The DESY II Test-Beam Facility

The DESY II Test-Beam Facility [157] is located at the Deutsches Elektronen-Synchrotron (DESY) in Hamburg, Germany. The generation of test beams starts in the DESY II synchrotron with a circumference of 292.8 m, that receives 450 MeV electrons or positrons from the linear accelerator LINAC II (LINear ACcelerator). A bunch of electrons is stored for two magnet cycles in the DESY II synchrotron and is twice accelerated to a default energy of 6.3 GeV, which is extendable up to 7 GeV. Besides being the injector for the PETRA III synchrotron light source, the primary beam from the DESY II synchrotron is also used to produce the test beams by employing double conversion instead of direct extraction.

First, a fiber target in the beam orbit induces bremsstrahlung photons, as schemati-

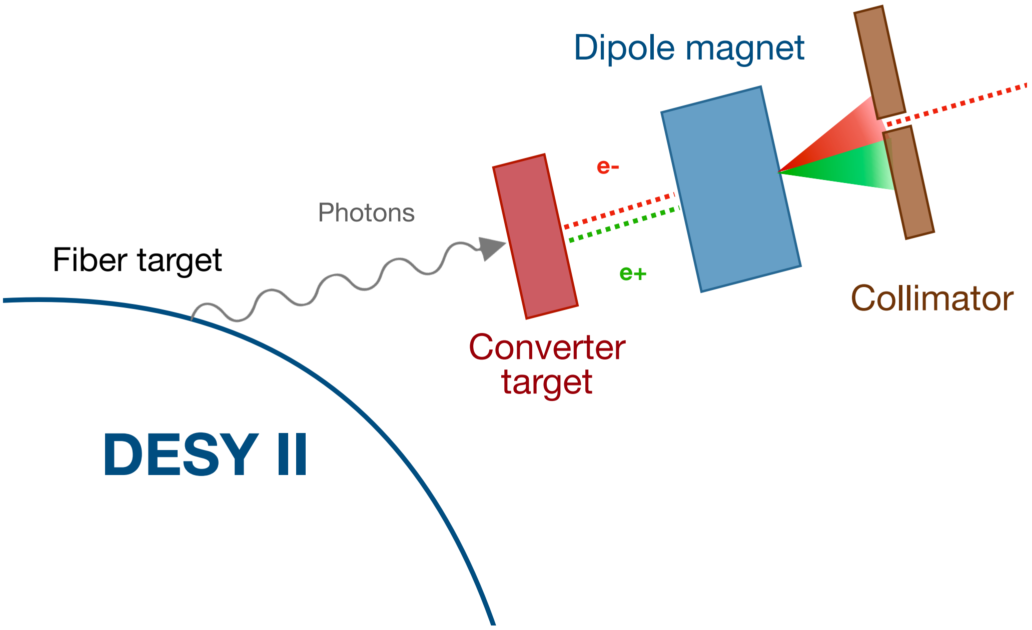

Figure 7.1. Schematic of the test-beam generation at the DESY II Test Beam Facility. Based on [157]

cally illustrated in Fig. 7.1. Next, the generated photons interact with a secondary target producing electron-positron pairs. The particle species and the momentum can be selected by changing the polarity and strength of a magnetic dipole field placed in front of a collimator. There are three beam lines, each with a dedicated primary target, that allow for an independent selection of beam parameters. For this thesis, an electron beam with a momentum of 5.4 GeV was chosen. The selected beam is then steered towards the beam line, where the CLICTD sensors were installed in a reference beam telescope. All of the three beam lines were used in the measurements presented in this thesis.

7.2 The Reference Telescope

An external reference is required to evaluate the sensor response in an unbiased manner. In measurements with charged particles, a beam telescope consisting of well-characterised sensors can provide such an external reference by reconstructing the incoming particle tracks. In this way, the performance of the DUT is determined against the well-defined trajectory of beam particles, which enables detailed studies beyond the intrinsic resolution of the DUT.

The beam telescope used in this thesis is depicted in Fig. 7.2. While the upper part shows a photograph of the telescope setup, the lower part is a schematic illustration of the individual components. The beam telescope is based on six MIMOSA-26 telescope

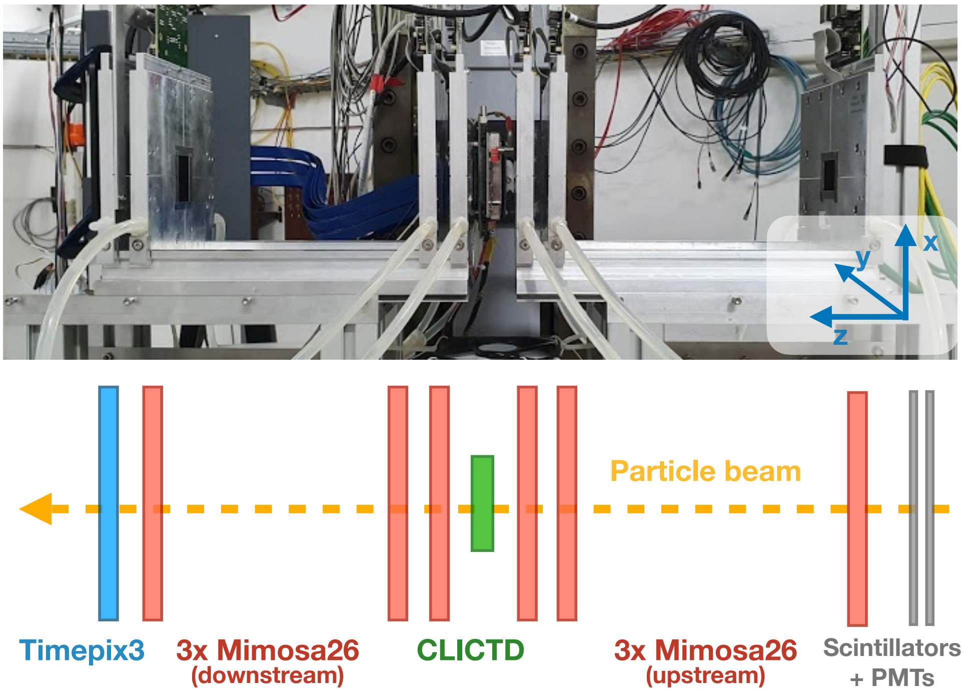

Figure 7.2. Telescope setup at the DESY II Test-Beam Facility. The DUT is placed between three MIMOSA-26 planes in the upstream and downstream arm, respectively. An additional Timepix3 plane is placed behind the last MIMOSA-26 plane in the downstream arm.

planes and a single Timepix3 plane at the end [158]. The global coordinate system is depicted on the bottom right of the photograph. The beam enters the telescope along the z-axis. The first three planes are referred to as *upstream planes* and the other ones as *downstream planes*.

In the following, the individual components of the telescope are described. The data acquisition for all devices is handled by the EUDAQ2 framework [159].

- The **AIDA Trigger Logic Unit** (TLU) [160] generates a global clock signal and time reset that is communicated to all other components in the telescope. Two trigger devices placed in front of the first telescope plane are connected to the TLU. Their trigger acceptance is comparable to the acceptance of the telescope planes. The trigger devices consist of a scintillator attached to a photomultiplier tube and register the passage of beam particles. The TLU issues a trigger, if it receives a signal from both trigger devices in coincidence. The trigger is distributed to the other sensors in order to initiate a synchronous readout.

- Six **MIMOSA-26 telescope planes** are grouped in the upstream and downstream arm around the DUT. Each telescope plane is equipped with one well-characterised MIMOSA-26 sensor [161,162]. The monolithic sensors have an active area of 1152×576 pixels, each measuring $18.4\,\mu\text{m} \times 18.4\,\mu\text{m}$, and a thickness of $50\,\mu\text{m}$. The planes

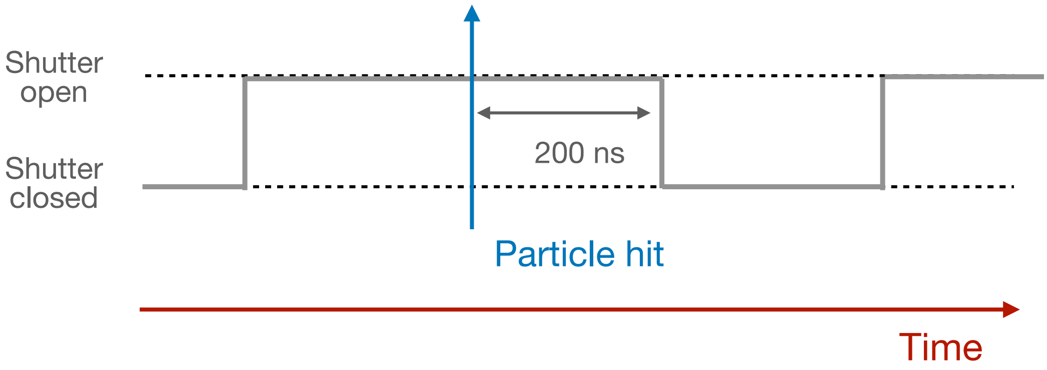

Figure 7.3. Schematic representation of the triggered shutter-close readout scheme. The shutter is closed 200 ns after CLICTD receives a trigger signal.

are read out continuously in a rolling shutter readout scheme with a periodicity of 115.2 µs. The data is stored if the telescope planes receive a trigger from the TLU, otherwise it is discarded. A trigger ID is assigned to the read-out pixel hits to facilitate offline synchronisation (cf. Section 8.1).

- A **Timepix3 plane** is placed behind the last downstream MIMOSA-26 plane. The plane features a Timepix3 hybrid pixel detector assembly [163] that is composed of a 100 µm thick n-in-p type sensor with a pixel pitch of 55 µm × 55 µm bump-bonded to a readout ASIC. It is read out by the SPIDR DAQ system [164] in a continuous data-driven acquisition mode. The Timepix3 plane is used to obtain a precise track time reference with a resolution of 1.1 ns after offline correction [165].

The particle beam traverses the sensors in *perpendicular incidence* (perpendicular to the sensor surface). The positioning of the telescope planes is crucial to minimise multiple scattering contributions and thereby optimise the track reconstruction and the pointing resolution of the track at the position of the DUT. In the default configuration, the MIMOSA-26 planes adjacent to the DUT are placed as close as mechanically possible to the DUT. The outer-most planes on the other hand are positioned at the edges of the telescope rail to increase the interpolation length for the reconstructed track.

7.3 Operation of the Device Under Test

During test-beam measurements, the DUT is integrated into the data-acquisition system controlled by the EUDAQ2 framework. While the readout is still handled by the Caribou system, the sensor is not operated independently like in the laboratory but has to adhere to the constraints imposed by the other telescope devices.

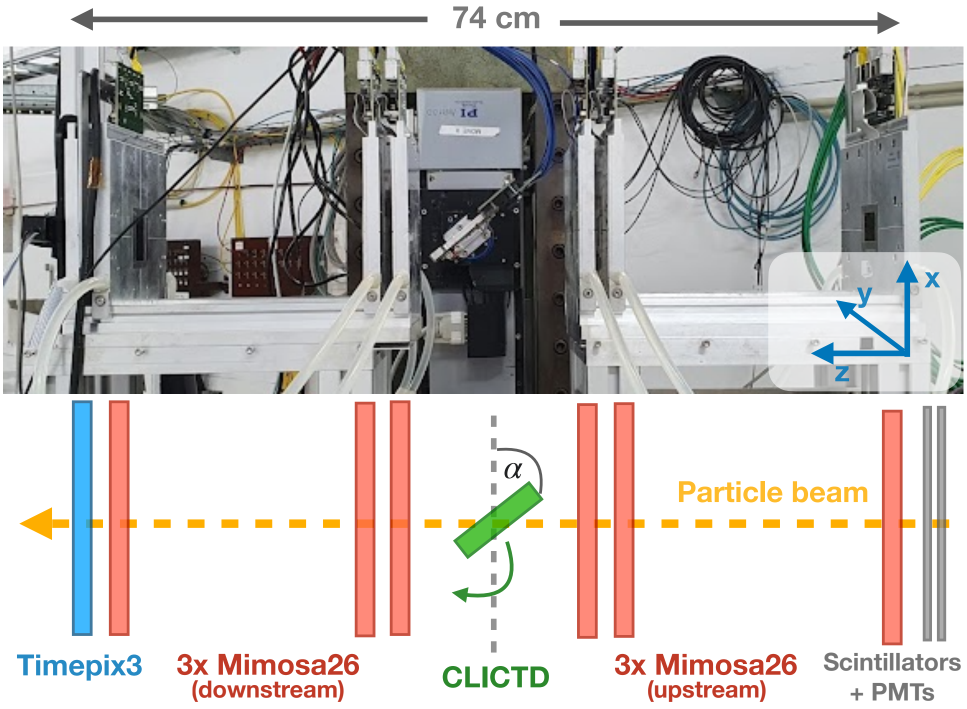

Figure 7.4. Beam telescope with a rotated DUT. The rotation angle is measured between the global x-axis and the DUT. The telescope planes closest to the DUT are adjusted to provide enough clearance for the rotation.

Data Acquisition Mode In order to increase data taking efficiency, CLICTD is operated in a *triggered shutter-close* data-acquisition mode, which is illustrated schematically in Fig. 7.3. When a trigger signal is issued by the TLU, the CLICTD shutter is closed after a fixed delay of 200 ns and the readout is initiated. During readout, the sensor experiences a dead time, where it is insensitive to incoming particles. The length of the dead time is proportional to the hit occupancy and is of the order of $\lesssim 100\,\mu s$ for $1\,\%$ occupancy. Once the readout is completed, the shutter is opened again until the next trigger signal arrives.

During test-beam data taking, the zero compression algorithm is enabled, which ensures that only data from channels that registered a hit is shifted out (cf. Section 4.2). In a low-occupancy environment with approximately $1\,\%$ of the matrix registering a hit, the readout frequency is of the order of 1 kHz.

The sensor is operated in 5-bit ToT plus 8-bit ToA mode to enable simultaneous energy and time measurements. The same DAC settings as for the laboratory measurements are used (cf. Appendix B).

7.4 Rotation of the Device Under Test

To assess the performance of prototype sensors to inclined particle tracks, the DUT is rotated with respect to the beam axis. To this end, the DUT is mounted on a *Physikalische Instrumente M-060* precision rotation stage with an estimated precision of less than 40 µrad [166].

A photograph of the rotation setup is depicted on the top part of Fig. 7.4. A schematic of the arrangement of telescope planes is depicted at the bottom. The rotation angle is defined as the angle between the surface of the DUT and the global x-axis. The distance between the telescope planes and DUT is increased compared to the previous setup to provide sufficient clearance for rotation. The planes are adjusted such that rotations up to 80° are possible without contact between the DUT and telescope planes. The wide plane configuration is maintained for smaller rotation angles as well to retain a similar track pointing resolution at the DUT, which suppresses the introduction of systematic uncertainties related to tracking. The rotation studies are performed around both DUT axes.

Chapter 8

Test-Beam Reconstruction and Analysis

The reconstruction and analysis of test-beam data is an intricate multi-step procedure. The following chapter will present each of these steps by starting with the data reconstruction, which includes tasks such as event building, clustering, or the track reconstruction. Moreover, the telescope and DUT alignment procedures are detailed and the analysis techniques are explained including the systematic uncertainties that arise from these methods. In particular, the cluster position reconstruction is described using different reconstruction techniques that were tested and are compared in Section 9.8.

In the test-beam reconstruction and analysis, the CLICTD sub-pixels are treated as regular pixel cells, and therefore the term *sub-pixel* is replaced by *pixel* to emphasise this choice.

8.1 Reconstruction

The reconstruction and analysis of test-beam data is based on dedicated software tools such as the Corryvreckan framework [167–169]. Corryvreckan has a modular setup to enable a flexible approach to the reconstruction and analysis. An example of a reconstruction and analysis chain used in this thesis is presented in Fig. 8.1. Each of the boxes represents a module and data objects are passed from left to right through the module chain. In the following, each reconstruction step is described and the corresponding modules are introduced. The detailed configuration of the module parameters is listed in the Appendix E.

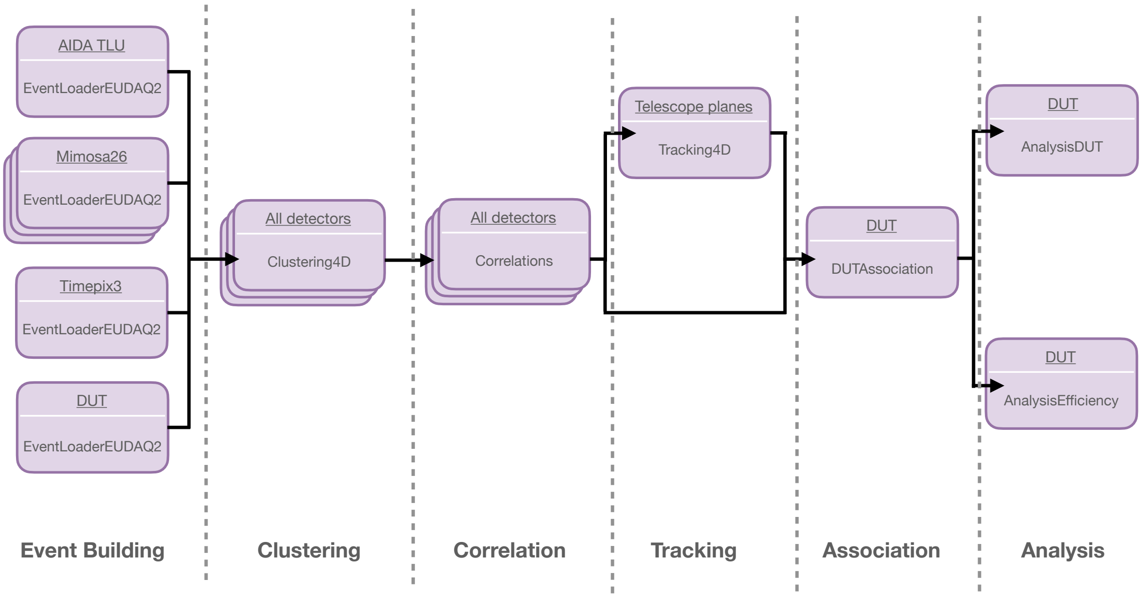
AIDA TLU
EventLoaderEUDAQ2
Mimosa26
EventLoaderEUDAQ2
Timepix3
EventLoaderEUDAQ2
DUT
EventLoaderEUDAQ2
All detectors
Clustering4D
All detectors
Correlations
Telescope planes
Tracking4D
DUT
DUTAssociation
DUT
AnalysisDUT
DUT
AnalysisEfficiency
Event Building
Clustering
Correlation
Tracking
Association
Analysis

Figure 8.1. Schematic of the Corryvreckan reconstruction and analysis chain. The boxes represent individual Corryvreckan modules and data is passed from left to right through the module chain.

8.1.1 Offline Pixel Masking

To guarantee a high hit-detection efficiency of the sensor planes, their detection threshold is set to the lowest possible value with a tolerable noise rate. At the selected threshold, the noise is dominated by the contribution from a limited number of pixel cells (*noisy pixels*) [161]. A veto can be applied to these pixels to exclude them from the reconstruction and analysis (*offline masking*). The exclusion of the noisy pixels lowers computation times and reduces the noise floor in the final plots.

The `MaskCreator` module creates a detector-specific noise mask based on the distribution and frequency of pixel hits. As this module is only applied once before the rest of the reconstruction and analysis, it is not shown explicitly in Fig. 8.1.

For each sensor, the single-pixel hit rate is calculated. The rate is compared to the local noise rate of neighbouring pixel cells. If a significant deviation from the local hit rate is found, the pixel is masked automatically. The radius of the considered neighbours and the degree of deviation is tuned for each test-beam period due to small differences in the data taking conditions (e.g. different MIMOSA-26 telescope, temperature in the hall, achievable beam rate etc.). For each MIMOSA-26 telescope plane, approximately 0.2 % of the matrix is masked. A noise mask for the Timepix3 sensor is not needed, as the noisy pixels are already masked during data taking.

The noise mask for the DUT is established manually by considering the hit rates in

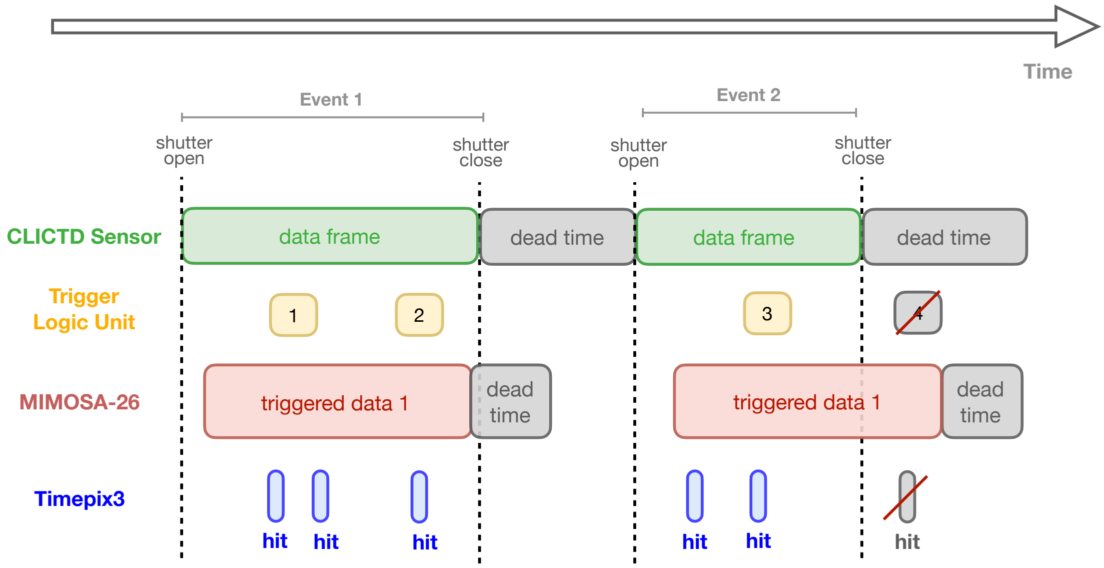
Time
Event 1
Event 2
shutter open
shutter close
shutter open
shutter close
CLICTD Sensor
data frame
dead time
data frame
dead time
Trigger Logic Unit
1
2
3
4
MIMOSA-26
triggered data 1
dead time
triggered data 1
dead time
Timepix3
hit
hit
hit
hit
hit
hit

Figure 8.2. Schematic of the Corryvreckan event building scheme. The CLICTD frames define the events and data from the other sensors are assigned based on their hit-time stamp or trigger number. Not to scale.

a single run and identifying pixels with hit rates at least one order of magnitude above the mean hit rate of the matrix. Typically, less than 10 pixels are masked with this procedure, which corresponds to less than 0.1 % of the matrix.

8.1.2 Event Building

The raw data is decoded and sorted into *events* to have manageable data chunks for the subsequent reconstruction steps. An event contains data from all devices in a finite time interval that is much shorter than the total run length. Event building is the process of dividing data into these time windows by comparing either time or trigger information. The subsequent reconstruction steps are then processed event-by-event i.e. only a single event at a time is considered.

Different `EventLoader` modules are available in Corryvreckan to handle the decoding and the event building. The generic `EventLoaderEUDAQ2` module is capable of decoding data written in the EUDAQ2 binary file format and is therefore used to handle the data files from all devices: the MIMOSA-26 sensors, the TLU, the Timepix3 plane and the CLICTD sensor.

A natural segmentation of the data stream is already provided by the CLICTD frames. The frames are therefore exploited for event building by defining the start of an event as the opening of the CLICTD shutter and the event end by the closing of the shutter. In-between the frames, the readout of the CLICTD sensor leads to a dead time, which depends on the amount of recorded data in the previous frame. The dead time is not considered in the event building i.e. CLICTD is required to be operational for the entire event. This event building scheme is schematically depicted in Fig. 8.2.

Data from the other devices need to be assigned to the correct event. The Timepix3 assembly provides a continuous stream of data with time stamps associated to each pixel hit. Comparing these time stamps to the event times enables the assignment to the correct event. The individual MIMOSA-26 sensors do not store precise hit time stamps. Instead, the trigger number can be exploited by using the TLU information, that provides both a time stamp as well as a trigger number allowing a link to be established between the two quantities. The approach is illustrated in Fig. 8.2: A time window is spanned around each TLU trigger to account for the MIMOSA-26 integration time. The time window covers 115 µs (one rolling shutter readout cycle) before and 230 µs (two rolling shutter readout cycles) after the trigger time [170].

If a trigger is within a CLICTD frame, the trigger number is assigned to the respective event and the corresponding MIMOSA-26 pixel hits are considered. The trigger number is discarded, if the trigger occurs outside the event, as depicted for trigger number 4 in the schematic.

This event building scheme guarantees that data is only considered, if it was recorded during the active window of CLICTD. In this way, an accurate determination of the CLICTD efficiency is ensured (cf. Section 8.4), since the CLICTD dead time should not lower the calculated efficiency.

8.1.3 Clustering

Several pixels may register a hit from a single ionising particle, due to the motion of charge carriers to neighbouring pixels or from inclined particle tracks that traverse several adjacent cells. Neighbouring pixel hits are therefore grouped into *clusters* and treated as a single object. The Corryvreckan module `Clustering4D` clusters pixel hits based on their spatial and temporal proximity. For the MIMOSA-26 sensors, pixel hits that are direct neighbours to a cluster are added to it [1]. A gap between pixel hits is not permitted. The same requirement is imposed for the clustering of CLICTD pixel hits, except for the CLICTD data-taking periods, where the sensor is inclined with respect to the beam axis. In this case, a gap of one pixel hit is allowed (*split clusters*). The time information of CLICTD is not considered in the clustering.

For the Timepix3 plane, the same requirements on the spatial distance are imposed and additionally a time cut is employed: The pixel hits are required to be within a 200 ns

---

[1] The clustering starts from a single pixel hit, which acts as a seed for the cluster.

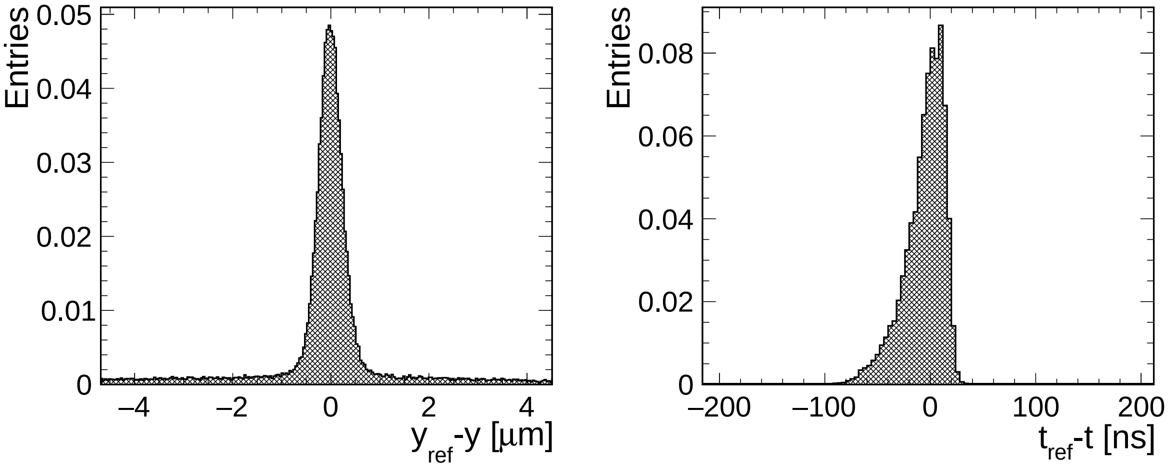

(a) Spatial correlations **(b)** Time correlations

Figure 8.3. (a) Spatial correlations in y-direction and (b) time correlations between the DUT and a reference plane.

time interval with respect to the earliest pixel hit in the cluster.

The cluster position is reconstructed with the methods described in Section 8.3.

8.1.4 Correlations

Correlations between the telescope planes and the DUT are a useful indicator for data quality. The relatively quick calculations provide a fast in-situ feedback of the data quality before results from in-depth analyses are available. In addition, correlations are considered to identify an appropriate starting point for the alignment procedure (cf. Section 8.2).

The Corryvreckan module `Correlations` calculates the spatial and time residuals between all detector planes and a reference plane. In Fig. 8.3, examples of the spatial and temporal correlation peaks are depicted. The spatial correlation in y direction is computed between the DUT and the last MIMOSA-26 upstream plane. As expected, the core of the peak resembles a Gaussian and the entries outside of the peak are related to noise and combinatorics. The temporal correlation is considered between the DUT and the Timepix3 plane. The peak exhibits a prominent tail to the left, which is associated with time walk (cf. Section 3.2). The phenomenon is studied in more detail in Chapter 9.

8.1.5 Particle-Track Reconstruction

Reconstructed tracks are used as a reference for the assessment of the DUT performance. The tracking procedure is therefore an essential step that requires careful optimisation, since a high track quality ensures an accurate sensor evaluation in the later stages.

The formation of particle tracks is a two-step procedure: First in the *track finding*, track candidates are identified by connecting pairs of clusters on the first and last telescope plane with a straight line and consecutively adding clusters from the inner planes if they are within selectable spatial and temporal cuts. In this stage, the reference track is continuously updated.

Second, a *track fitting* is employed using an appropriate track model. A straight-line track fit is a common choice, which requires a negligible effect of multiple scattering (cf. Section 2.3.1). This condition is only met if high-energy beams and a sufficiently small material content of the telescope planes are available. At the DESY II Test-Beam Facility, multiple scattering has to be accounted for owing to the low beam momentum. Therefore, a *General Broken Lines* track fit [171, 172] is chosen, that allows for kink angles in the fitted track at the position of each scatterer and in air.

The reconstructed tracks are required to have an associated cluster on each of the seven telescope planes. In addition, the spatial search radius is set to 240 µm on the MIMOSA-26 planes and 600 µm on the Timepix3 plane. An implicit time cut is applied by only considering data associated to a given CLICTD frame. The DUT is excluded to guarantee an unbiased tracking procedure. Instead, it is considered as passive scatterer, which allows for a kink in the track model at the position of the DUT.

8.1.6 Track-Cluster Association

Once the reference tracks are generated, they are associated to clusters on the DUT. The correct association is critical for the calculation of performance parameters such as residuals or the hit-detection efficiency (cf. Section 8.4).

The association is performed by interpolating each reference track to the position of the DUT. The distance between the track intercept with the DUT and each reconstructed DUT cluster is determined. A cluster is associated with a specific track if the cluster edge is within a configurable distance from the intercept. If more than one cluster is within the search radius, the closest cluster to the intercept is selected. The optimisation of the spatial association cut is presented in Section 9.4.

8.2 Telescope and DUT Alignment

A precise knowledge of the positions of the detector planes is required to guarantee a high track quality and correct association with DUT clusters. A manual measurement is not sufficient since the required resolution is of the order of $< 5\,\mu\text{m}$ in x and y-direction.

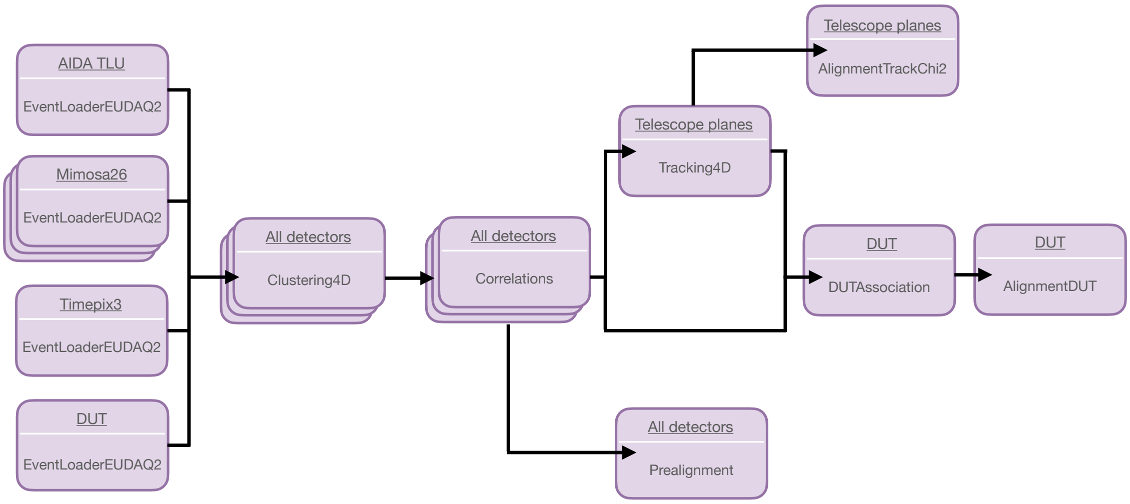
Telescope planes
AlignmentTrackChi2
AIDA TLU
EventLoaderEUDAQ2
Telescope planes
Tracking4D
Mimosa26
EventLoaderEUDAQ2
All detectors
Clustering4D
All detectors
Correlations
DUT
DUTAssociation
DUT
AlignmentDUT
Timepix3
EventLoaderEUDAQ2
DUT
EventLoaderEUDAQ2
All detectors
Prealignment

Figure 8.4. Schematic of the Corryvreckan alignment chain. Three different alignment steps are performed.

Instead, the precise plane positions in x/y are determined in Corryvreckan using a multi-stage alignment procedure. Alignment in z-direction (parallel to the beam direction) is not performed for geometrical reasons and is instead measured with an accuracy of approximately 1 mm. Systematic uncertainties arising from a potential misalignment in z-direction are addressed in Section 8.5.

Three consecutive steps are performed: the prealignment, the telescope alignment and finally the DUT alignment. A Corryvreckan reconstruction and analysis chain with these three alignment modules is presented in Fig. 8.4.

Prealignment First, a prealginment is needed as a starting point to achieve convergence in the subsequent steps. The `Prealignment` module performs a translational alignment by centering the spatial correlation peaks in x- and y-direction. The correlations are calculated with respect to the last MIMOSA-26 upstream plane. While this method ignores rotational misalignment and is too inaccurate for the precision needed in the DUT analysis, it provides a starting point for the more precise track-based alignment.

Telescope Alignment The telescope alignment is based on the iterative minimisation of the χ^2 value of the fitted track. For this purpose, the Corryvreckan module `AlignmentTrackChi2` is employed. In each step, a translational and rotational movement of the telescope planes is performed and the tracks are re-fitted until the χ^2 is minimal and convergence is achieved. The minimisation procedure is handled by the Mi-

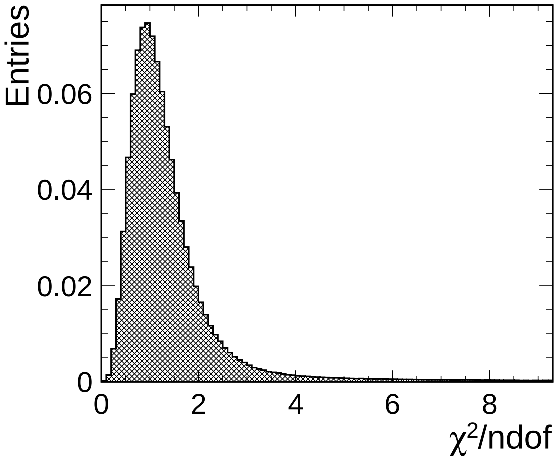

Figure 8.5. Distribution of χ^2 divided by the number of degrees of freedom (ndof) after track-based alignment. The General Broken Line track model is fitted to the track candidates.

nuit2 package, that is specifically conceived to identify the minimum of a multi-parameter function [173]. In total, three rotational degrees of freedom (around the x-, y- and z-axes) and two translational degrees of freedom (in x- and y-direction) per detector plane are considered.

A distribution of the fit χ^2 divided by the number of degrees of freedom (ndof) is displayed in Fig. 8.5. The distribution has a maximum at one after the track-based alignment has converged, which indicates good fit results. A pronounced tail towards larger values is discernible, which is related to strong contributions from multiple scattering. In the subsequent analysis, a cut at $\chi^2/\mathrm{ndof} = 3$ is applied to exclude the tail.

DUT Alignment The position of the DUT is not calculated in the telescope alignment procedure, since it is excluded from the tracking. Instead, the `AlignmentDUT` module is employed to deliver rotational and translational alignment by minimising the unbiased spatial residuals between the DUT and the reference tracks. Similar to the telescope alignment, the z-direction is not considered but taken from mechanical measurements. To avoid misalignment related to poor track fits, solely tracks with a χ^2/ndof smaller than three are considered.

8.3 Cluster Position Reconstruction

Silicon sensors are segmented into strips or pixels to obtain position information about particles traversing the sensor. If individual segments (strips or pixels) only register whether the induced signal exceeds a given threshold (*binary hit information*), the achievable spatial resolution σ_x is driven by the segmentation pitch p

$$\sigma_x^2 = 1/p \int_{-p/2}^{p/2} x^2 dx = p^2/12, \tag{8.1}$$

assuming that the contribution of charge carrier diffusion is negligible. Eq. 8.1 represents the variance of a uniform distribution across one pixel cell.

The availability of charge information in each segment enables a charge-weighted interpolation that can improve the position reconstruction. Various algorithms have been developed to optimise the reconstruction. Ultimately, the operation conditions and sensor properties determine the success of a particular algorithm. In the following, the position reconstruction techniques employed in this thesis are described. In addition, an alternative approach based on machine learning is developed and evaluated in Section 9.8.

Centre-of-Gravity Algorithm A charge-weighted centre-of-gravity algorithm (CoG) determines the cluster centre x_c as the charge-weighted single pixel positions x_i divided by the total cluster charge:

$$x_c = \frac{\sum_i q_i x_i}{\sum_i q_i}, \tag{8.2}$$

where q_i is the single-pixel charge of the i-th pixel in the cluster. If no charge information is available all q_i are set to one and the algorithm yields the geometrical cluster centre.

In this thesis, the centre-of-gravity algorithm is employed for the MIMOSA-26 sensors and the Timepix3 device. For CLICTD, the cluster position is first estimated with the centre-of-gravity algorithm and subsequently corrected to account for non-linear charge sharing as detailed in the following.

η-Correction The centre-of-gravity algorithm assumes a linear relationship between the amount of deposited energy and reconstructed charge in a given pixel cell. An overestimation/underestimation in a pixel cell would bias the cluster position towards/away from this pixel. The non-uniform field configuration in the CLICTD sensor is responsible for a non-linear diffusion of charge carriers between pixel cells contrary to the assumptions of the centre-of-gravity algorithm. Therefore, a correction for the non-linear charge sharing is necessary, which is provided by the so-called η-algorithm [174, 175].

The η-algorithm used in this thesis is a data-driven method, that is based on the η-function which provides a link between the cluster position reconstructed with the CoG algorithm and the more accurate position given by the telescope reference track. First, the construction of the η-distribution for pixels with a size of two in a given spatial dimension is considered. In this case, the reconstructed cluster position relative to the edge between the two pixels (*in-pixel position*) is plotted against the in-pixel intercept

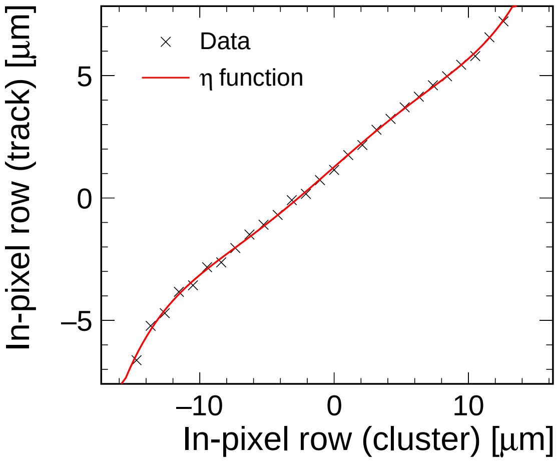

Figure 8.6. η-distribution for 2-pixel clusters in row direction. The collection electrodes of the adjacent pixels are located at ±15 µm. A 5-th order polynomial η-function is fitted to the distribution.

position of the reference track with the DUT. An example of the η-distribution in row direction is displayed in Fig. 8.6. A 5th order polynomial fitted to the distribution is used to correct the reconstructed cluster position.

For the CLICTD sensor, cluster sizes larger than two in a given spatial dimension are rare if the beam enters perpendicularly to the sensor surface (cf. Section 9.1). If the sensor is rotated relative to the beam, larger clusters can occur and the η-correction needs to be adapted by using only the two pixels with the highest single-pixel charge.

Head-Tail Algorithm The Head-Tail algorithm assumes that the outer pixels in a cluster (the *head* and *tail*) contain most information to reconstruct the cluster position [176, 177]. The cluster position x_{HT} is therefore given by:

$$x_{\mathrm{HT}} = \frac{x_{\mathrm{head}} - x_{\mathrm{tail}}}{2} + \frac{q_{\mathrm{head}} - q_{\mathrm{tail}}}{2\bar{q}} \cdot \mathrm{pitch}, \tag{8.3}$$

where $x_{\mathrm{head/tail}}$ and $q_{\mathrm{head/tail}}$ are the position and charge of the head/tail pixel, respectively, and $\bar{q}$ is the average single pixel charge in the cluster.

In the case of two-pixel clusters, the head-tail algorithm is identical to the centre-of-gravity reconstruction. Therefore, the head-tail algorithm is only used for CLICTD studies involving inclined particle tracks, where the cluster size in one dimension exceeds two.

8.4 Performance Evaluation

Once tracks are reconstructed, they are used as external reference to assess the performance of the DUT. In this way, the spatial and time resolution are evaluated and the hit-detection efficiency is determined. In addition, the cluster size is studied, as it is particularly suited to investigate the charge-sharing behaviour.

8.4.1 Cluster Size

Charge sharing describes the energy deposition in several pixel cells or the motion of created charge carriers to adjacent pixels. The degree of charge sharing is encoded in the number of pixels in a reconstructed cluster (*cluster size*), which therefore serves as an observable to investigate charge-sharing properties. Owing to the asymmetrical pixel pitch and sensor layout of CLICTD, charge sharing in row and column direction is expected to be different. For this reason, the projection of the cluster onto the row and column direction is studied as well. It should be noted that the cluster size depends critically on the detection threshold, since charge carriers reaching pixel cells that do not exceed the threshold are effectively lost (*sub-threshold effect*).

8.4.2 Hit-Detection Efficiency

The hit-detection efficiency is defined as the number of tracks associated to a CLICTD cluster over the total number of tracks. The tracks used for the hit-detection efficiency calculation are required to pass through the acceptance region of the DUT, which comprises the physical pixel matrix of the sensor excluding one column/row at the matrix edge. It has been verified that the exclusion of additional columns/rows close to the matrix edge does not alter the results. If the track intercept position on the DUT lies within a masked pixel or its direct neighbours, the track is rejected.

8.4.3 Spatial Resolution

The spatial resolution is calculated from the spatial residuals x_{residual} between the reconstructed cluster position x_{DUT} and the intercept of the reference track on the DUT x_{ref}:

$$x_{\mathrm{residual}} = x_{\mathrm{ref}} - x_{\mathrm{DUT}}. \tag{8.4}$$

The residuals are referred to as *unbiased*, since the DUT is excluded from the tracking to avoid biasing the measurement. The reduced RMS of the central $3\,\sigma$ of the unbiased residual distribution $\sigma_{\mathrm{RMS},3\sigma}$ is determined and the track pointing resolution at the position of the DUT σ_{track} is quadratically subtracted from the value:

$$\sigma_{\text{resolution}} = \sqrt{\sigma^2_{\text{RMS},3\sigma} - \sigma^2_{\text{track}}}, \tag{8.5}$$

which yields the spatial resolution $\sigma_{\text{resolution}}$. Eq. 8.5 is only exact if the distributions are identical to Gaussian functions.

An estimate for the telescope pointing resolution is calculated using the *GBL Track Resolution Calculator* [178]. The calculator uses the GBL formalism to take multiple scattering in the telescope planes and the surrounding air into account. For the narrow telescope configuration, the track pointing resolution at the position of the DUT is between 2.4 µm and 2.8 µm depending on the exact plane positions. For the rotation studies, a wide telescope configuration is required resulting in a track pointing resolution between 4.8 µm and 6.5 µm.

8.4.4 Time Resolution

Similar to the spatial resolution, the time residual t_{residual} is obtained from the time difference between the DUT measurement t_{DUT} and the track time t_{ref}

$$t_{\text{residual}} = t_{\text{ref}} - t_{\text{DUT}}. \tag{8.6}$$

The RMS of the central $3\,\sigma$ of the time residual distribution $\tau_{\text{RMS},3\sigma}$ is calculated and the track time resolution τ_{track} is quadratically subtracted:

$$\tau_{\text{resolution}} = \sqrt{\tau^2_{\text{RMS},3\sigma} - \tau^2_{\text{track}}}. \tag{8.7}$$

The track time resolution corresponds to the time resolution of the Timepix3 plane. After offline corrections that are detailed elsewhere [165, 179], the time resolution of the Timepix3 plane evaluates to 1.1 ns [122].

8.5 Uncertainties

Statistical uncertainties arise from the limited amount of data recorded for a particular measurement. In the test-beam measurements presented in this thesis, statistical uncertainties at the minimum operation threshold are of the order of $< 0.1\,\%$ of the measured value and therefore negligible. At higher thresholds, the statistical uncertainty can increase to a few percent and is indicated by uncertainty bands or error bars.

The principle source of systematic errors is linked to the calibration of the detection threshold (cf. Section 6.2). To account for the threshold uncertainty, it is propagated to the test-beam observables by interpolating between measurements performed at two different threshold.

The other sources of systematic uncertainty are specific to the measured value. They are listed in the following:

- **Efficiency:** The statistical uncertainties arise from the uncertainties on the efficiency values calculated using a Clopper-Pearson confidence interval of one sigma [180]. No additional sources of systematic uncertainties are considered.
- **Spatial resolution:** Systematic uncertainties arise from the calculation of the track pointing resolution (cf. Section 8.4.3). The single plane resolution entering the calculation is varied within its uncertainties given in [158]. In addition, the plane positions in z-direction are shifted independently by $\pm 1\,\mathrm{mm}$. The quadratic sum of the individual deviations is computed and yields a total uncertainty of $\pm 0.1\,\mu\mathrm{m}$.
- **Time resolution:** The main uncertainty emerges from variations in the front-end time resolution related to the sub-pixel position in the detection channel . Therefore, each analysis is repeated for every sub-pixel position individually and the spread of the resulting time resolutions is extracted. A maximum deviation of $\pm 0.1\,\mathrm{ns}$ is found.
- **Rotation studies:** While the relative precision of the rotation stage is well below $0.01°$, a global offset of the rotation angles is a potential source of systematic uncertainties (cf. Section 7.4). The offset is determined from the expected DUT orientation computed by the alignment procedure. In all analyses, the offset is used to correct the expected rotation angle. It was confirmed that the alignment has converged by manually modifying the plane orientation by $\pm 0.5°$ and repeating the alignment. A deviation of less than $0.01°$ is found with respect to the initial alignment.

  In addition, the influence of multiple Coulomb scattering on the rotation angle is investigated. To this end, the expected scattering angle θ_{RMS} is calculated with Eq. 2.4, using a momentum of $pc = 5.4\,\mathrm{GeV}$ and a material content (x/X_0) that is equivalent to $55\,\mu\mathrm{m}$ of silicon and two $25\,\mu\mathrm{m}$ Kapton foils on either side of the sensor [158] and a value of $\theta_{\mathrm{RMS}} = (2.9 \pm 0.3) \times 10^{-3}\,\mathrm{deg}$ is found. An uncertainty of 11 % is expected, according to [7].

  The scattering angle at each plane is also reconstructed during tracking. An example distribution of scattering angles at the second MIMOSA-26 plane is displayed in Fig. 8.7. The RMS of the distribution evaluates to $(2.5 \pm 0.1) \times 10^{-3}\,\mathrm{deg}$, which is in reasonable agreement with the theoretical expectation presented above.

  The angular distribution of beam particles entering the telescope is considered as well by using a straight-line track fit instead of the GBL fit and extracting the track

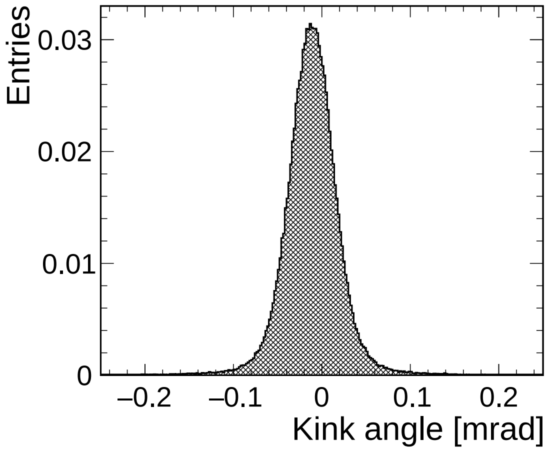

Figure 8.7. Distribution of kink angles at a MIMOSA-26 detector plane.

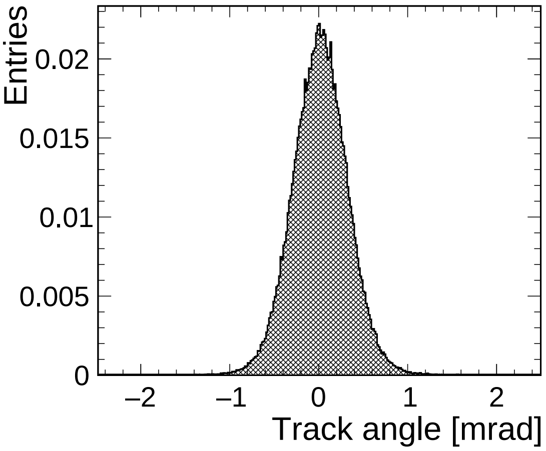

Figure 8.8. Distribution of track angles using a straight-line fit.

angles with respect to the nominal beam axis. The distribution of track angles is depicted in Fig. 8.8. As the spread of scattering and track angles are less than a few mrad, they are considered to be negligible compared to the rotation angle.

All test-beam measurements are cross-checked with several CLICTD samples in order to exclude additional systematic uncertainties and the results are found to agree within the stated uncertainties.

Chapter 9

Performance in Test-Beam Measurements

This chapter summarises the measurement results from five one-week and one two-week test-beam campaigns between 2019 and 2021 at the DESY II Test-Beam Facility. In total, about 80×10^6 events of the recorded data were used to obtain the results presented in the following chapter. The test-beam facility and the reference telescope are described in Chapter 7 and the reconstruction and analysis techniques are explained in Chapter 8. In addition, this chapter uses the calibration and front-end tuning results obtained in Chapter 6.

The chapter is divided according to the observables discussed in Section 8.4, namely charge sharing, hit-detection efficiency as well as time and spatial resolution. First, measurements with perpendicular incidence of the beam are discussed and subsequently the impact of oblique incidence angles is studied. These inclined particle trajectories are also exploited to estimate the active sensor depth. Lastly, the evaluation of different cluster position reconstruction techniques to improve the spatial resolution is presented including a novel approach using neural networks.

The chapter aims to pin down the performance and characteristics for the different operation conditions, sensor designs and wafer materials. To this end, most sections follow a similar structure, where the results for the standard configuration are presented first, followed by measurements with varied p-well bias voltages and the different pixel flavours. Next, the impact of the sensor thickness on the measurements is shown and lastly the results for different wafer materials is described, including measurements with different substrate bias voltages.

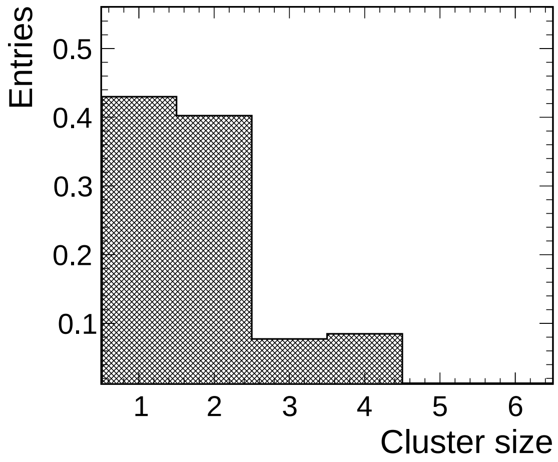

Figure 9.1. Total cluster size distribution for the standard configuration.

9.1 Charge Sharing

Charge sharing between adjacent pixels has important implications for all performance figures and thus needs to be adapted to the specific requirements of the silicon device. The geometrical features of the pixel cell, the field configurations and the depleted regions within the sensor determine the charge-sharing behaviour. Their impact is therefore studied using measurements from CLICTD samples with different designs or in different operation scenarios. First, the standard configuration is shown and subsequently deviations from the standard configuration are studied.

Standard Configuration The total cluster size distribution for the standard configuration is presented in Fig. 9.1. For each measurement shown in this section, error bars or uncertainty bands are included in the figure, but may not be visible owing to their small size. The majority of clusters consist of more than one pixel, confirming that the motion of charge carriers to neighbouring pixels has a considerable impact on the sensor response. Projections of the cluster in column and row direction are depicted in Fig. 9.2. The fraction of two-pixel clusters is higher in row direction due to the smaller pixel pitch in this dimension, which enhances the degree of charge sharing.

The cluster size is expected to depend on the impact position of a beam particle within the pixel cell. The effect is visualised in the in-pixel representation of the total cluster size, as shown in Fig. 9.3. In this representation, the cluster size is plotted as a function of the reconstructed track-incident position within a pixel cell by folding data from a full CLICTD pixel matrix into a single cell. The origin of single-pixel clusters is confined to the innermost part of the pixel since charge carriers are created in the lateral vicinity of the collection electrode. The largest clusters originate from the pixel corners

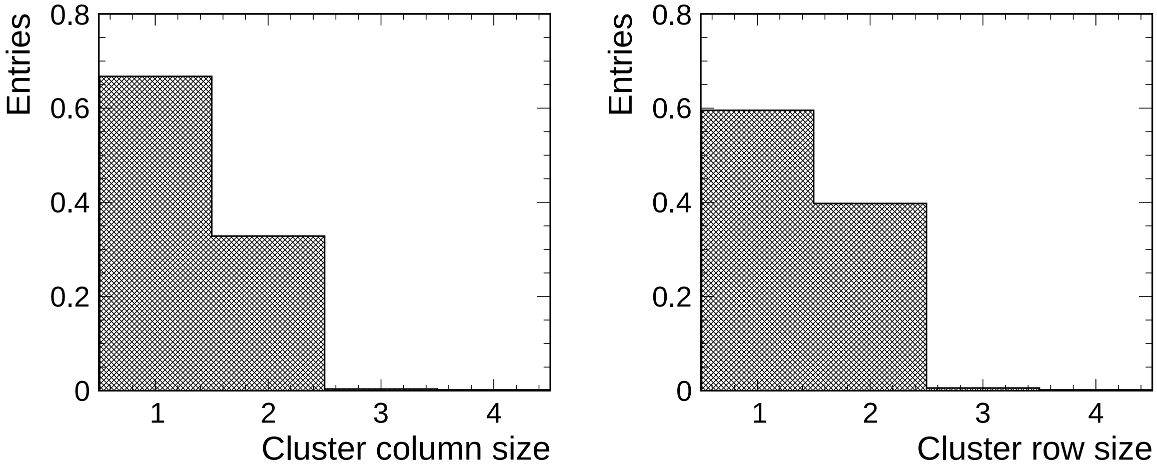

(a) Cluster size in column direction

(b) Cluster size in row direction

Figure 9.2. Cluster size distribution in (a) column and (b) row direction for the standard configuration.

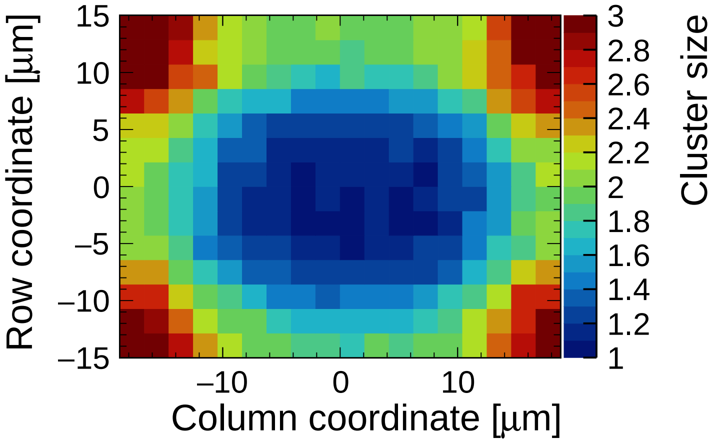

Figure 9.3. In-pixel representation of the total cluster size for a sensor in standard configuration.

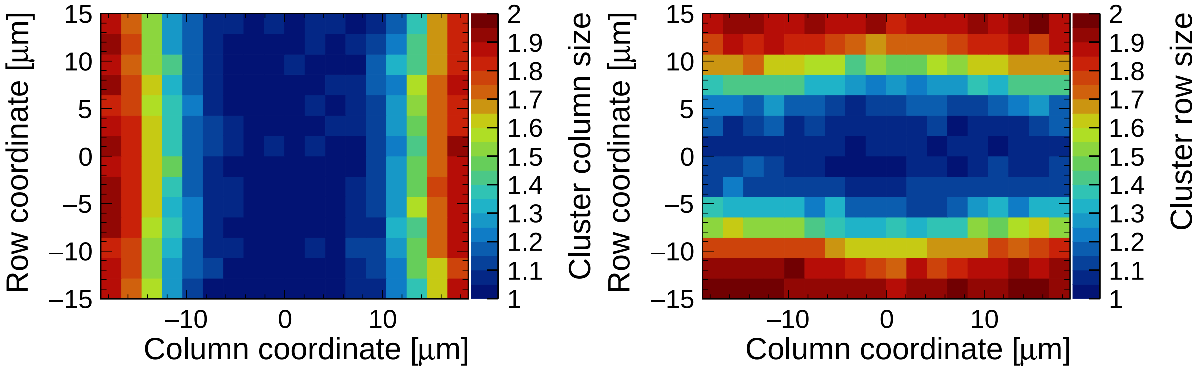

(a) Cluster size in column direction

(b) Cluster size in row direction

Figure 9.4. In-pixel cluster size in (a) column and (b) row direction for the standard configuration.

owing to geometrical effects and the low electric field in this region resulting in a high contribution from charge carrier diffusion.

A similar effect is observable in the in-pixel representation of the cluster size in row and column direction, which are depicted in Fig. 9.4. Whereas clusters with a single pixel in column direction originate from particles impinging in a 20 µm wide band around the middle of the pixel cell, two-pixel clusters only occur for particles incident on the pixel borders. A similar effect is visible in row direction, although the region associated with two-pixel clusters extends further into the pixel cell due to the smaller pixel pitch.

The cluster size is highly sensitive to the detection threshold, since individual pixel signals can remain below the applied threshold, thus reducing the size of the cluster. To study the impact of the threshold in detail, the mean cluster size is depicted in Fig. 9.5 as a function of the detection threshold. The shaded area around the curve represents the uncertainty discussed in Section 8.5. With increasing detection threshold, more and more pixels fall below it, thus decreasing the cluster size. At approximately 1500 e, the curve has converged to a cluster size close to one, since only the pixel with the highest charge (*seed pixel*) remains above threshold.

Bias Voltage The p-well bias voltage affects the depletion regions in the upper part of the sensor. It is shown in Section 6.2 that a lower absolute p-well bias voltage results in a lower gain and consequently a higher operational detection threshold. Although, the cluster size for a given threshold is not affected by the p-well bias voltage, as illustrated in Fig. 9.6, the difference in minimum operation threshold affects the maximum achievable

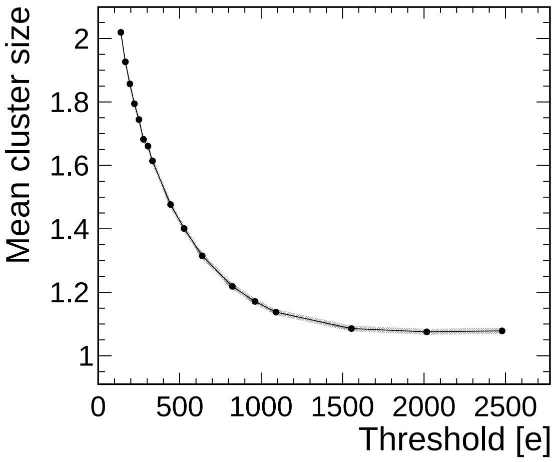

Figure 9.5. Total cluster size as a function of the detection threshold for the standard configuration. The shaded area around the curve represents the uncertainty discussed in Section 8.5.

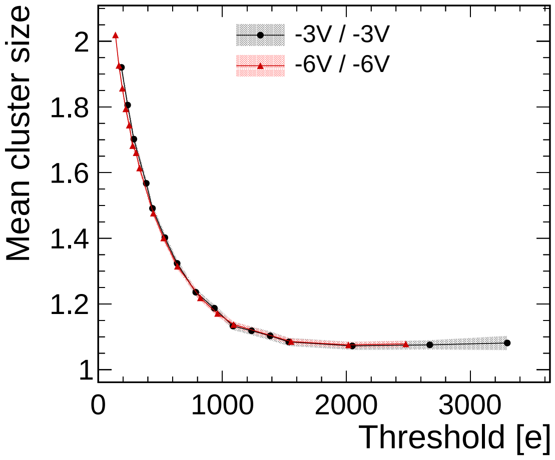

Figure 9.6. Total cluster size as a function of detection threshold for two different p-well/substrate bias voltages using a sample with continuous n-implant and a thickness of 300 µm.

Table 9.1. Cluster size at the minimum operation threshold for two different p-well bias voltages. The investigated sensor has a continuous n-implant and a thickness of 300 µm.

Bias [-V]	Thd [e]	Cluster size	Cluster size (col.)	Cluster size (row)
3	200^{+4}_{-5}	1.92 ± 0.01	1.37 ± 0.01	1.45 ± 0.01
6	139^{+4}_{-5}	1.99 ± 0.01	1.40 ± 0.01	1.48 ± 0.01

Table 9.2. Mean cluster size at the minimum operation threshold for different pixel flavours. All sensors were operated at a bias voltage of -6 V/-6 V at the p-well/substrate nodes.

Flavour	Thd [e]	Cluster size	Cluster size (col.)	Cluster size (row)
Continuous n-implant	139^{+4}_{-5}	1.99 ± 0.01	1.40 ± 0.01	1.48 ± 0.01
Segmented n-implant	136^{+4}_{-5}	1.82 ± 0.01	1.30 ± 0.01	1.46 ± 0.01
Extra deep p-well	148^{+4}_{-5}	1.84 ± 0.01	1.31 ± 0.01	1.47 ± 0.01

cluster size. The difference is quantified in Table 9.1, where the mean cluster size for the two operation points is listed at their respective minimum threshold. The cluster size for the higher absolute bias voltage is considerably larger owing to the lower minimum operation threshold. The same holds true for the projection of the cluster size in both directions. The larger cluster size has important implications for the position resolution, as presented in Section 9.4.

Pixel Flavours The pixel flavours with segmented n-implant and extra deep p-well were designed to accelerate charge collection and consequently reduce charge sharing. This is reflected in the total cluster size as a function of the detection threshold in Fig. 9.7, where sensors operated at -6 V bias voltage with a total thickness of 100 µm were used. As expected, a decrease in the cluster size in column direction for the flavour with segmented n-implant and extra deep p-well is observable owing to the suppressed charge sharing.

The mean cluster size in column and row direction are presented in Fig. 9.8. A difference in cluster size is only seen in column direction, where the implant modifications were applied. The cluster size in row direction remains unaffected since the pixel layout is the same for all pixel flavours. The mean cluster size at the minimum operation threshold in Table 9.2 underlines the results: while the cluster size in column direction is approximately 7 % smaller for the optimised flavours, the size in row direction is the same within the uncertainties.

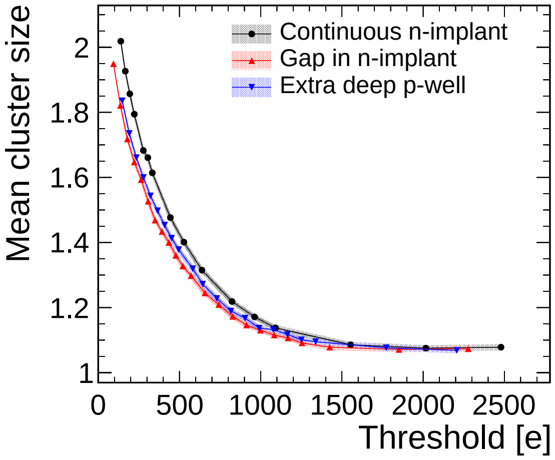

Figure 9.7. Total cluster size as a function of the detection threshold for the different pixel flavours. The sensors have a thickness of 100 µm and were operated at a bias voltage of -6 V/-6V.

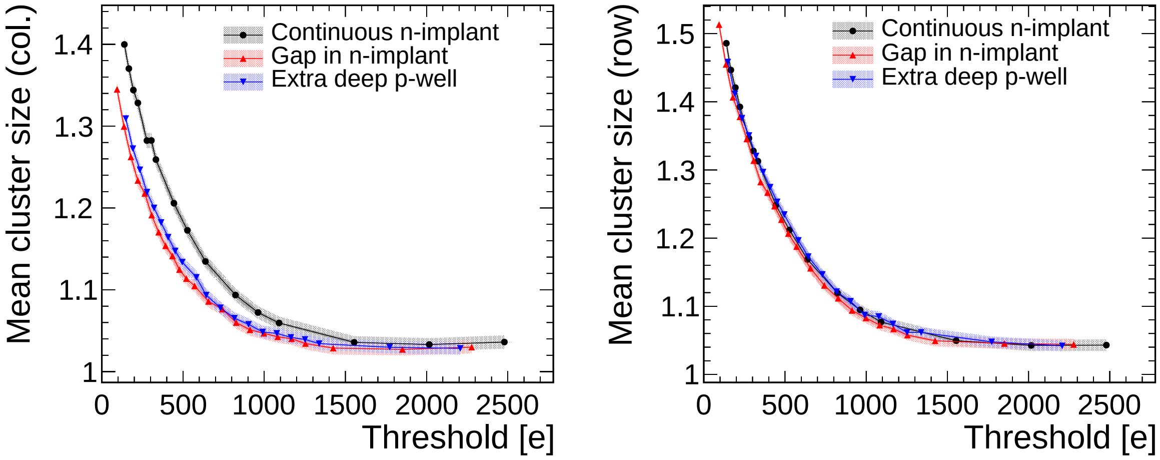

(a) Mean cluster size in column direction. **(b)** Mean cluster size in row direction.

Figure 9.8. Total cluster size as a function of the detection threshold in (a) column and (b) row direction for the different pixel flavours. The sensors have a thickness of 100 µm and were operated at a bias voltage of -6 V/-6 V.

Table 9.3. Total cluster size at the minimum operation threshold for CLICTD sensors with different thicknesses. A bias voltage of -6 V/-6 V was applied to all sensors.

Thickness [µm]	**Flavour**	**Threshold** [e]	**Cluster size**
300	Continuous n-implant	139^{+4}_{-5}	1.99 ± 0.01
100	Continuous n-implant	136^{+4}_{-5}	1.94 ± 0.01
50	Continuous n-implant	140^{+4}_{-5}	1.91 ± 0.01
40	Continuous n-implant	181^{+4}_{-5}	1.86 ± 0.01
300	Segmented n-implant	136^{+4}_{-5}	1.82 ± 0.01
100	Segmented n-implant	140^{+4}_{-5}	1.81 ± 0.01
50	Segmented n-implant	131^{+4}_{-5}	1.83 ± 0.01
40	Segmented n-implant	130^{+4}_{-5}	1.73 ± 0.01

Thinned Sensors The low material content of thin sensors is beneficial to reduce multiple scattering and thus enables precision measurements. However, if sensor thinning involves the removal of active sensor volume, the performance of the device might get compromised owing to the lower number of liberated electron-hole pairs that can contribute to the signal. In case of the CLICTD sensor fabricated with an epitaxial layer on a low-resistivity substrate, the active sensor volume is expected to span only the upper part of the sensor. Thus charge carriers generated in the lower low-resistivity substrate are unable to propagate to the vicinity of the collection electrode, where they would induce a current. The lower part of the sensor is therefore considered to be *inactive* material and removing it should leave the total signal unaltered.

This assumption is challenged experimentally by investigating CLICTD sensors with different sensor thicknesses. The total cluster size as a function of the detection threshold for four different thicknesses is displayed in Fig. 9.9 using CLICTD samples with continuous and segmented n-implant. For a given threshold, the cluster size stays unaltered for sensors with a thickness of 300 µm, 100 µm and 50 µm. The same holds true for the mean cluster size at the minimum operation threshold listed in Table 9.3. This observation confirms that the removed sensor volume was inactive material that did not contribute to the signal and only the upper part of the structure is essential to maintain the same sensor properties.

On the other hand, the 40 µm thick sample exhibits a noticeable reduction in cluster size, both in the threshold scan and at the minimum operation threshold. The sample consists of approximately 10 µm of metal layers and 30 µm sensor material, implying that the low-resistivity substrate is largely remove, since the nominal thickness of the epitaxial

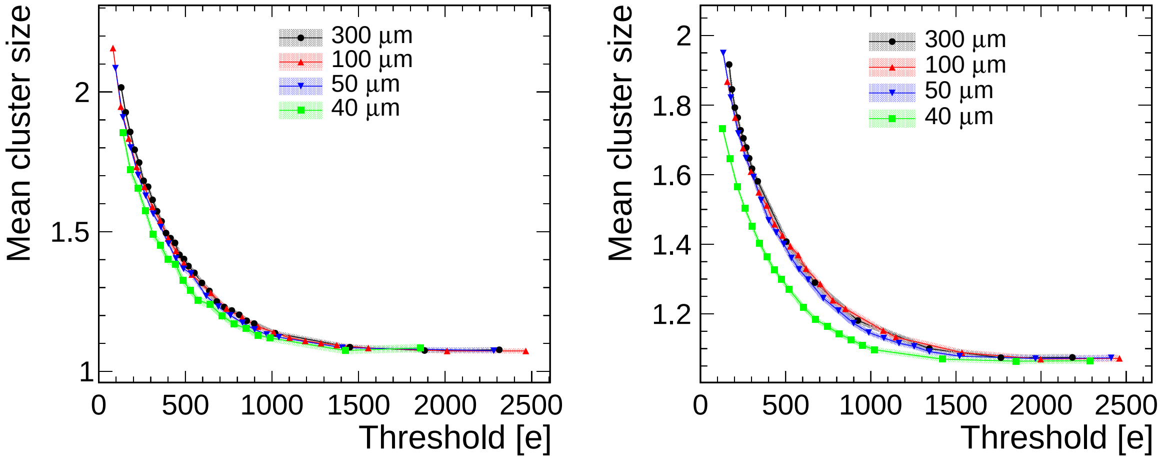

(a) Continuous n-implant **(b)** Segmented n-implant

Figure 9.9. Total cluster size as a function of detection threshold for different sensor thicknesses using CLICTD sensors with (a) continuous and (b) segmented n-implant. The sensors were operated at a bias voltage of -6 V/-6 V.

layer is 30 µm as well [1]. In addition, sensor damage is expected from the grinding process that could further decrease the active sensor volume [181]. Consequently, the smaller cluster size is assumed to arise from the removal of active sensor material that leads to a lower signal. This conjecture is tested in the coming sections using other observables as well.

The reduction in cluster size is more pronounced for the flavour with segmented n-implant compared to the one with continuous implant, which is consist with the reduced charge sharing for the former. A higher amount of charge sharing leads to the distribution of the total signal to several adjacent pixel cells, thus reducing the amount of signal per pixel. In particular, charge carriers generated at the lower border of the active sensor region are subject to intense charge sharing, since their longer propagation path allows for a stronger contribution of diffusion processes. If the induced signal on a given pixel is not enough to surpass the threshold, the charge carriers that propagated to this cell are effectively lost (sub-threshold effect). Therefore, this phenomenon is particularly important for the flavour with continuous n-implant and affects mostly charge carriers from the lower part of the active sensor volume. A removal of this volume is thus less severe, since a fraction of charge carriers are anyway lost due to sub-threshold effects. The stronger concentration of charge carriers in the seed pixel for the segmented n-implant avoids the charge-sharing-induced signal loss and is consequently more sensitive to the

---

[1] There is however no sharp border between the epitaxial layer and the substrate but a smooth transition as explained in Section 10.1.1.

Table 9.4. Mean cluster size at the minimum operation threshold for CLICTD sensors with different wafer materials. Both sensors have a segmented implant, a thickness of 100 µm and are biased at -6 V/-6 V.

Material	Threshold [e]	Cluster size
Epi	157^{+4}_{-5}	1.86 ± 0.01
Cz	151^{+4}_{-5}	2.36 ± 0.01

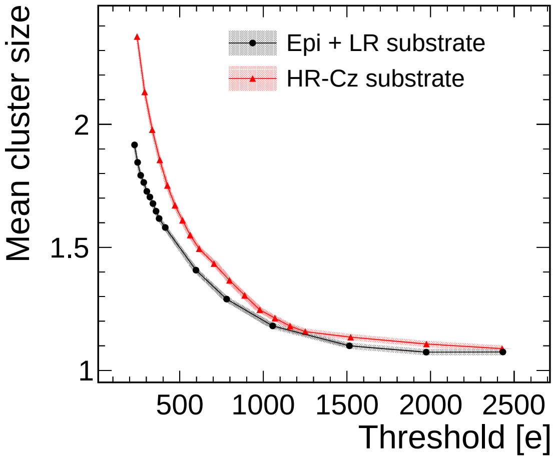

Figure 9.10. Cluster size as a function of detection threshold for samples fabricated with an epitaxial layer on a low-resistivity substrate (Epi + LR substrate) and a high-resistivity Czochralski substrate (HR-Cz substrate). Both sensors have a segmented n-implant, a thickness of 100 µm and are biased at -6 V/-6 V.

thinning procedure.

Wafer Material In the previous paragraph, it was shown that large parts of the 300 µm thick sensor can be removed without a loss of signal, since the active sensor depth only covers the upper < 50 µm of the device. While this result allows sensors to be thinned to a few tens of micrometers, it also implies that the maximum achievable signal is limited to a few thousand electrons per MIP (cf. Section 2.3.1). Since a higher signal is expected to improve the sensor performance, a larger high-resistivity layer is desirable to increase the thickness of the active sensor volume. Unlike samples with epitaxial layer, the availability of high-resistivity Czochralski wafers provides such a large high-resistivity region, since its thickness is not limited to tens of micrometers but can easily scale to hundreds of micrometers.

The effect of the alternative sensor material is first studied in the threshold scan of the mean cluster size, as displayed in Fig. 9.10. Both sensors have a thickness of

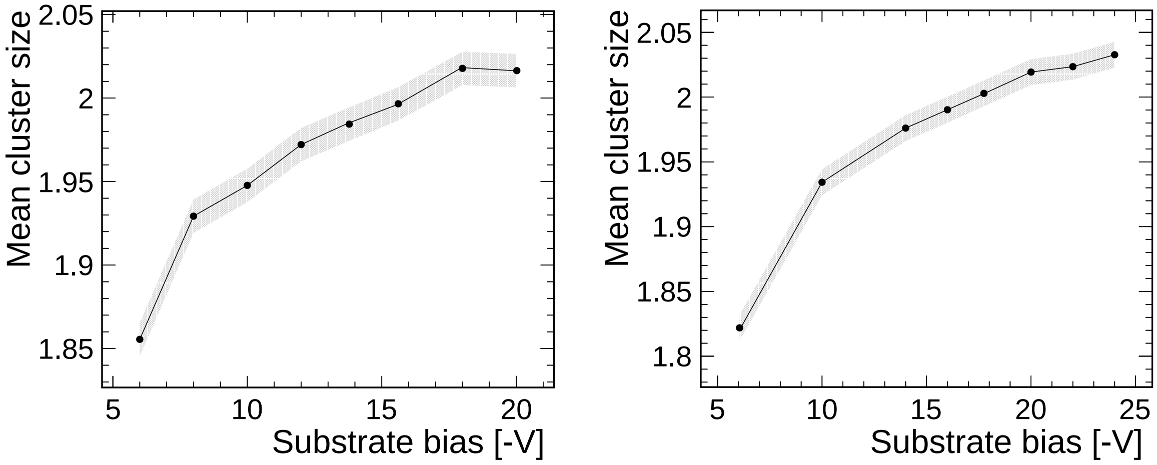

(a) Segmented n-implant at a detection threshold of 348 e.

(b) Extra deep p-well at a detection threshold of 488 e.

Figure 9.11. Cluster size as a function of substrate voltage for samples with high-resistivity Czochralski wafer. The samples have a (a) segmented n-implant and (b) extra deep p-well. The p-well bias voltage is fixed to -6 V/-6 V.

100 µm, a segmented n-implant and are operated at a bias voltage of -6 V/-6 V for direct comparison, although the high-resistivity Czochralski samples could be biased at lower substrate bias voltages. The cluster size for the Czochralski sample is clearly larger, which is also reflected in the mean cluster size at the minimum operation threshold in Table 9.4. There, the increase in mean cluster size even exceeds 25 %.

Since the implant structures are the same for both samples, a higher amount of charge sharing on its own is not expected to lead to this increase in cluster size. Instead, the larger size is expected to arise from a higher number of electron-hole pairs that generate a higher signal, as conjectured above. The coming sections will investigate this assumption in more detail.

The depletion region within the high-resistivity Czochralski sample is not expected to cover the entire sensor at a bias voltage of -6 V/-6 V, which still limits the active sensor depth. An increase in substrate bias voltage, increases the depletion depth and therefore also affects the active depth, as illustrated in Fig. 9.11, where the mean cluster size as a function of the substrate bias voltage is displayed for two different flavours. Both sensors are 100 µm thick and the p-well voltage remains at -6 V. A detection threshold of 348 e is applied to the sample with segmented n-implant and 488 e to the one with extra deep p-well, which is significantly higher than the minimum operation threshold at -6 V/-6 V. The high threshold results from the different front-end operation settings that are necessary to achieve high efficiency with these samples, as explained in Section 4.6.1.

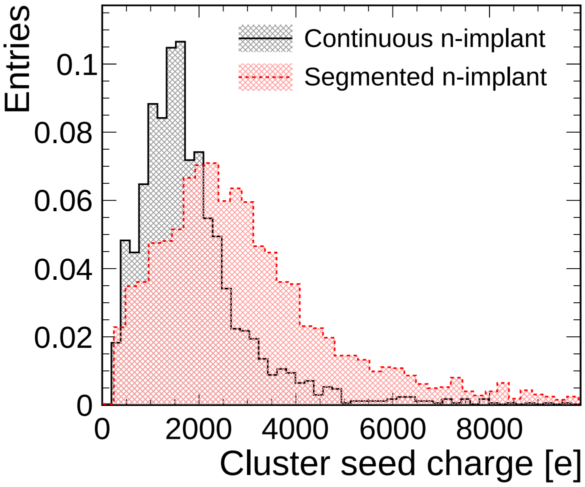

Figure 9.12. Cluster seed signal distribution for the pixel flavour with continuous and segmented n-implant. The sensors have a thickness of 300 µm and a bias voltage of -6 V/-6 V is applied.

9.2 Signal

The seed signal as the highest single-pixel signal in a cluster is shown in Fig. 9.12 for pixel flavours with continuous and segmented n-implant. The seed signal is converted to physical units using the ToT calibration from Section 6.6. The distributions are not expected to follow Landau-Gauss functions owing to charge sharing and the limitations of the charge measurement and calibration. However, it is still instructive to observe the lower seed signal for the pixel flavour with continuous n-implant, which is a consequence of the higher degree of charge sharing.

The cluster charge is not evaluated quantitatively in this document owing to the limited precision in the conversion of ToT values to physical units. In addition, all further reconstruction steps that require charge information are performed using the ToT values in order to prevent the introduction of systematic effects from the conversion. The consequences of using ToT values will be reflected in the following sections.

The in-pixel representation of the cluster seed charge is presented in Fig. 9.13 for the standard configuration. As expected, the seed pixel charge exhibits a maximum in the pixel centre and decreases towards the pixel corners due to increased charge sharing. The in-pixel distribution of the seed pixel has important implications for the detection efficiency, as presented in the next section.

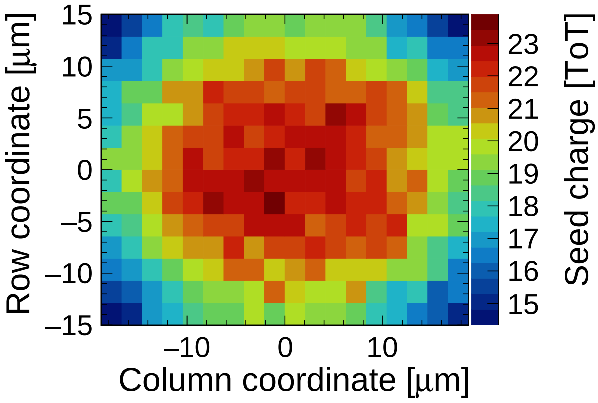

Figure 9.13. In-pixel representation of the cluster seed charge for the standard configuration. The seed charge is not calibrated and therefore given in ToT values.

9.3 Hit-Detection Efficiency

An inefficient sensor is detrimental for detectors operating in high-energy physics experiments, since data taking can become incomplete or even meaningless. A high hit-detection efficiency is therefore fundamental for satisfactory measurement results and is consequently a principle performance indicator for silicon sensors. In this section, the hit-detection efficiency is investigated as a function of numerous parameters and sensor types. First, the standard configuration is presented and afterwards the same modifications as introduced above are studied.

Standard Configurations The hit-detection efficiency depends on the association cut between reconstructed telescope track and clusters on the DUT. If the cut is too small, the signal is cut out and the sensor is falsely labelled as inefficient. If it too wide, noise might be wrongly identified as particle hits leading to an artificial increase in efficiency. For the CLICTD sensor, the later restriction is of no practical concern, since the sensor and operation characteristics enable minimal noise levels that prevent a false increase in efficiency. For the former constraint, the cluster-track association cut is tuned to data, as presented in Fig. 9.14. The plot depicts the hit-detection efficiency as a function of the association cut in column direction. The decrease in efficiency sets in below 30 µm, which is less than the pixel pitch of 37.5 µm in this direction. The association cut is therefore fixed to 1.5 times the pixel pitch, which gains enough margin to avoid cutting into the signal.

With the fixed association cut, the hit-detection efficiency is calculated for different detection thresholds, as presented in Fig. 9.15 for the standard configuration. A close-up

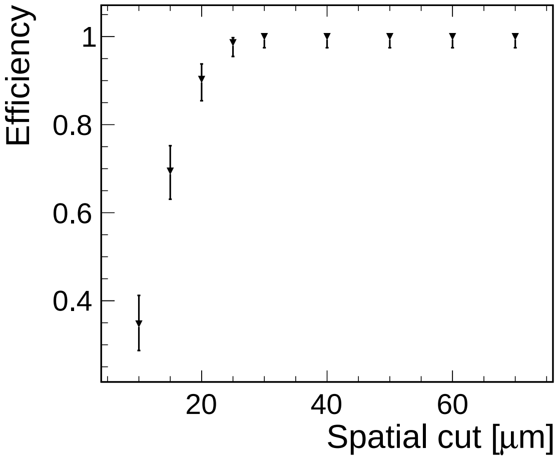

Figure 9.14. Efficiency as a function of the cluster-track association cut in column direction. The pixel pitch in this direction is 37.5 μm and the nominal association cut is selected to be 1.5 times the pixel pitch.

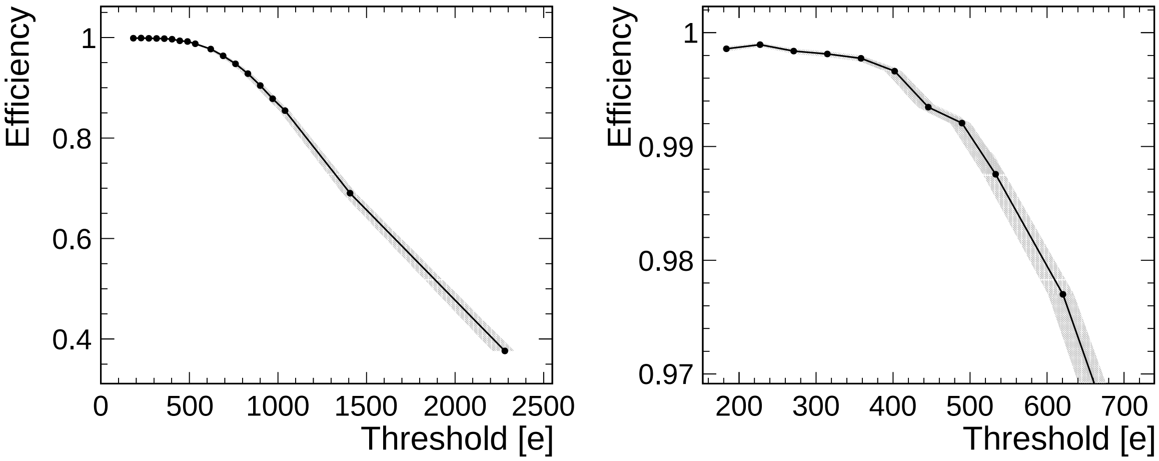

(a) Wide threshold range.

(b) Close-up of the high-efficiency region.

Figure 9.15. Efficiency as a function of the detection threshold in the standard configuration.

of the high-efficiency region is shown in Fig. 9.15b. The sensor achieves efficiencies well above 99 %, which is in agreement with other sensor prototypes using similar pixel layouts such as the ALPIDE sensor [182]. Remaining inefficiencies at low thresholds are most likely related to the low-energy tail of the energy deposition distribution.

In accordance with the CLIC tracker requirements, the sensor is declared *fully efficient* if the efficiency exceeds $> 99.7\,\%$ (cf. Section 1.2.4). While full efficiency is achieved at low detection thresholds, the efficiency deteriorates for values greater than 500 e, since all pixel signals in a cluster fall below the detection threshold. The threshold range in which the sensor is fully efficient is denoted as *efficient operation window*. It is calculated by subtracting the minimum operation threshold from the threshold, at which the efficiency is inferior to the 99.7 % limit. In Fig. 9.15, the efficient operation window evaluates to

$$207 \pm 12\ (\text{stat.})^{+5}_{-7}\ (\text{syst.})\,\text{e}.$$

Therefore, the detection threshold can be varied in a range of several hundred electrons before a reduction of efficiency is to be expected. For long-term data-taking scenarios, where alteration in the detection thresholds might become necessary due to radiation damage or increased noise levels, this result gives room to adapt to changing operation conditions.

For high thresholds, inefficient regions start to form at the pixel edges, as illustrated in Fig. 9.16, where the in-pixel hit-detection efficiency is shown at a threshold of 1950 e for the standard configuration. The diffusion of charge carriers to neighbouring pixels is enhanced at the edges, leading to a smaller signal per pixel. In particular, the measured signal in the seed pixel is closely related to the detection efficiency: If the seed charge of a given cluster falls below the applied threshold, the cluster is lost leading to inefficiencies.

Bias Voltage The detection efficiency for bias voltages of -3 V/-3 V and -6 V/-6 V is depicted in Fig. 9.17. For a given threshold, the efficiency is insensitive to the difference in bias voltage. Since a similar charge sharing behaviour for the two bias voltages was found in the previous section, it can be concluded that the overall signal above threshold is independent of the bias voltage in the range -3 V to -6 V. This observation is supported by simulations presented in Section 11.2.2 and is different to standard planar silicon sensors, where a higher absolute bias voltage increases the depleted volume and consequently the signal. However, with the limited depletion depth in the samples with epitaxial layer, the increase in bias voltage has no effect on the active depth or the signal.

Pixel Flavours The detection efficiency for the different pixel flavours is presented in Fig. 9.18. The flavours with segmented n-implant and extra deep p-well exhibit a higher

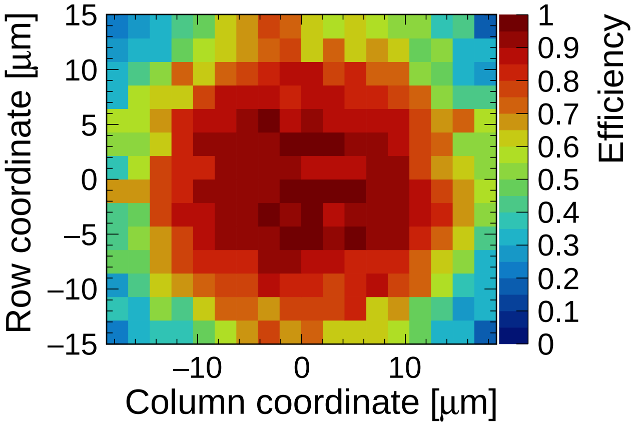

Figure 9.16. In-pixel representation of the hit-detection efficiency for the standard configuration at a threshold of 1950 e.

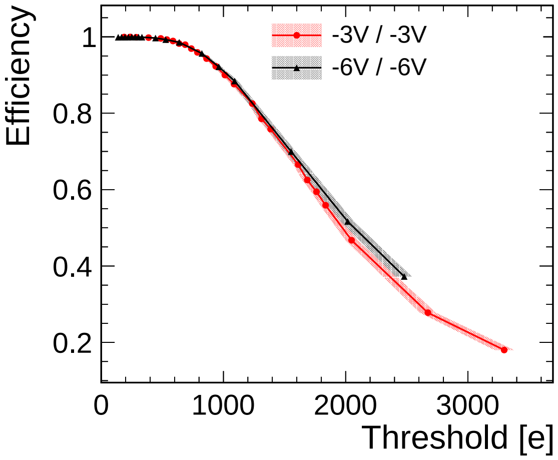

Figure 9.17. Detection efficiency as a function of threshold for two different bias voltages. The investigated sensor has a thickness of 300 µm, a continuous n-implant and are biased at -6 V/-6 V.

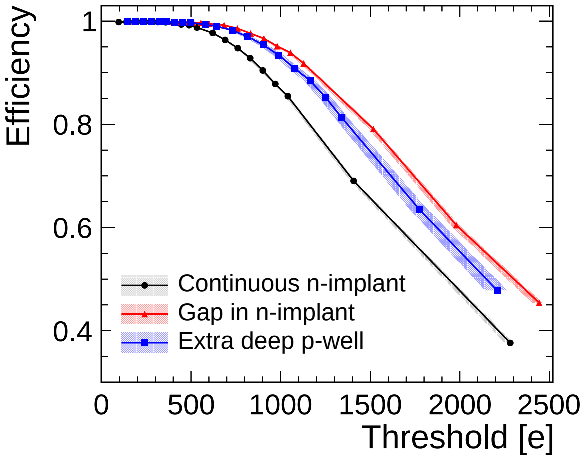

Figure 9.18. Detection efficiency as a function of threshold for the three pixel flavours. The samples have a thickness of 100 µm and are operated at -6 V/-6 V bias voltage.

efficiency at high threshold values due to to the reduced charge sharing that leads to a stronger concentration of charge carriers in the seed pixel. The suppression of charge sharing is slightly enhanced for the flavour with segmented n-implant in accordance with the reduced cluster size shown in the previous section.

This result has important implications for future sensor prototypes with thin active sensor volumes such as current developments for monolithic sensors using a 65 nm CMOS process [183]. The pixel flavours with reduced charge sharing might become obligatory to guarantee fully efficient operations.

Thinned Sensors The efficiency as a function of the detection threshold is studied for different sensor thicknesses in Fig. 9.19 for the flavour with continuous n-implant and segmented n-implant. A similar performance is observed for sensor thicknesses ranging between 50 µm and 300 µm.

For the 40 µm thick sample, the efficiency plateau becomes narrower at high threshold values. In agreement with the smaller cluster size observed in the previous section, the degraded efficiency indicates an overall reduction in signal compared to the thicker samples. These results underpin the assumption of a smaller active depth due to the removal of active sensor volume. The pixel flavour with segmented n-implant exhibits a stronger deterioration in efficiency. Similar to the cluster size, the reduced charge sharing prevents sub-threshold charge carrier loss in the lower parts of the active region leading to a stronger degradation in efficiency when this part is removed.

Wafer Material The larger active sensor volume expected from the high-resistivity wafers has important implications for the efficiency at high thresholds, as depicted in

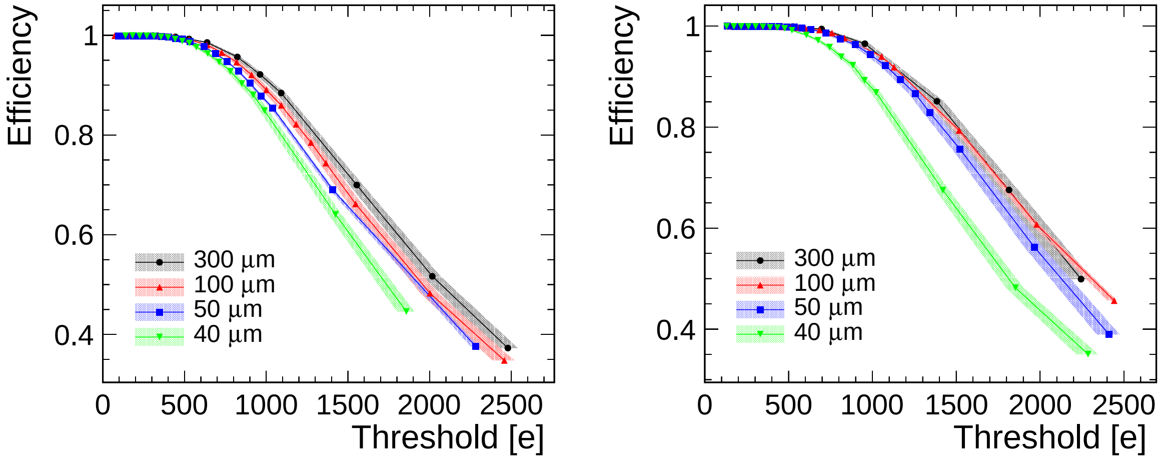

(a) Continuous n-implant

(b) Segmented n-implant

Figure 9.19. Efficiency as a function of detection threshold for different sensor thicknesses. A bias voltage of -6 V/-6 V is applied to all sensors.

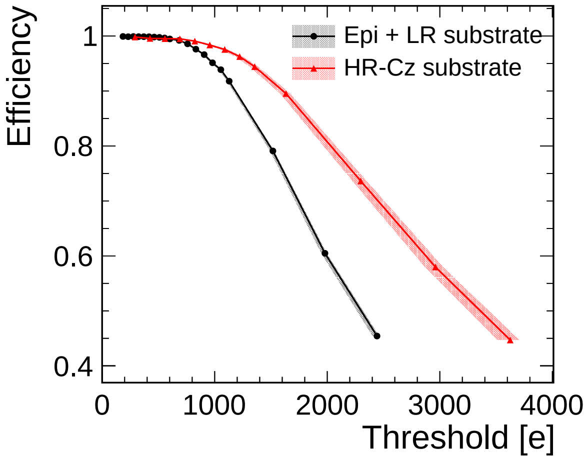

Figure 9.20. Detection efficiency as a function of threshold for the different wafer materials. The sensors have a thickness of 100 µm, a segmented n-implant and are biased at -6 V/-6 V.

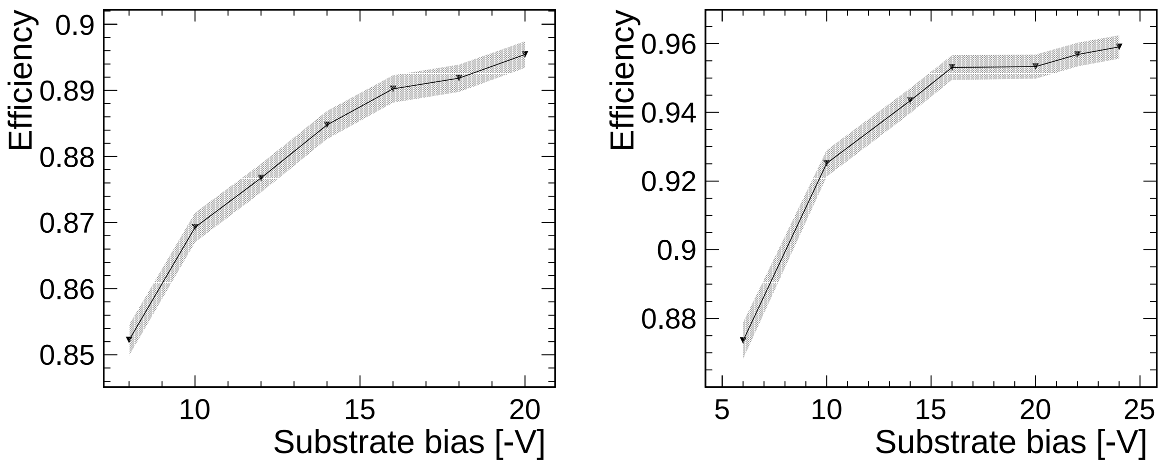

(a) Segmented n-implant at a detection threshold of 1692 e

(b) Extra deep p-well at a detection threshold of 1647 e.

Figure 9.21. Efficiency as a function of substrate voltage for a sample on high-resistivity Czochralski wafer material. The sensors have a thickness of 100 µm and a bias voltage of -6 V at the p-well terminals.

Fig. 9.20. In the plot, the efficiency is displayed for different wafer materials as a function of the detection threshold for samples with a thickness of 100 µm and segmented n-implant. The efficient operation window is significantly extended for the high-resistivity wafers owing to a larger seed signal. The higher seed signal with the simultaneous increase in cluster size discussed in the previous section, supports the notion of a larger active sensor depth.

The impact of the substrate voltage on the efficiency is shown in Fig. 9.21a for a high-resistivity sample with segmented n-implant at a threshold of 1692 e and in Fig. 9.21b for a sample with extra deep p-well at a threshold of 1647 e. Since these threshold values are about one order of magnitude higher than the minimum operation threshold, a significant reduction in efficiency is measured in both cases. The efficiency loss is less severe for high substrate voltages, since a higher seed signal is expected from the increased depletion depth. For the sample with extra deep p-well, the efficiency increases by about 10 % between -6 V and -25 V substrate bias voltage.

9.4 Spatial Resolution

The intrinsic spatial hit resolution of vertex and tracking detectors is essential to resolve secondary vertices and to achieve a high momentum resolution. Besides the physical pixel size, charge sharing is a strong driving force to obtain an excellent spatial resolution. To

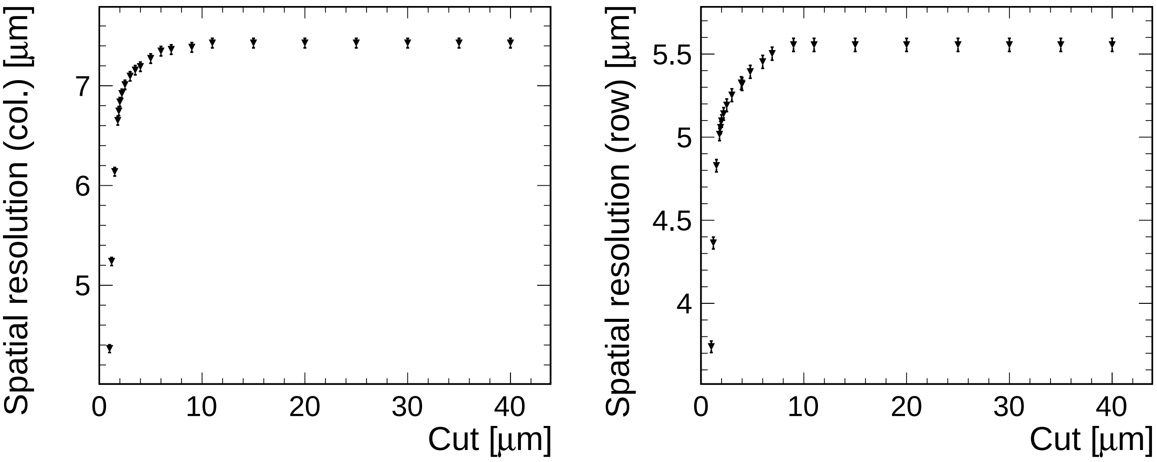

(a) Spatial resolution in column direction **(b)** Spatial resolution in row direction

Figure 9.22. Spatial resolution as a function fo the association cut in (a) column and (b) row direction. The telescope resolution is not subtracted.

study the impact of charge sharing on the spatial resolution, different CLICTD samples with their heterogeneous charge sharing properties are investigated. In the following, the spatial resolution is introduced first for the standard configuration followed by the same modifications described above.

Standard Configuration Similar to the hit-detection efficiency, a wrong choice of the track-cluster association cut can distort the reconstruction of the spatial resolution. Therefore, the resolution as a function of the association cut is studied, as presented in Fig. 9.22. The spatial resolution is artificially improved for cut values below 10 µm, since clusters in the tails of the residual distributions are rejected. In the plateau region, the spatial resolution is stable confirming that the association cut lies outside the tails of the residual distribution. Moreover, the plateau region has a flat shape, which demonstrates that no false associations with CLICTD noise hits are occurring owing to the low noise rate of the sensor. The association cut is left at 1.5 times the pixel pitch in accordance with the results from the efficiency measurement.

The unbiased spatial residuals between the reconstructed cluster position and the track intercept on the DUT are presented in Fig. 9.23 for the standard configuration. In row direction, the η-correction was applied to account for non-linear charge sharing. The RMS of the central $3\,\sigma$ (99.7%) of the distribution amounts to 8.1 µm in column and 5.4 µm in row direction. After the track pointing resolution of 2.8 µm is subtracted in quadrature, the spatial resolution evaluates to 7.6 ± 0.2 µm and 4.6 ± 0.2 µm in column and row direction, respectively (cf. Section 8.4.3). The uncertainties are purely systematic,

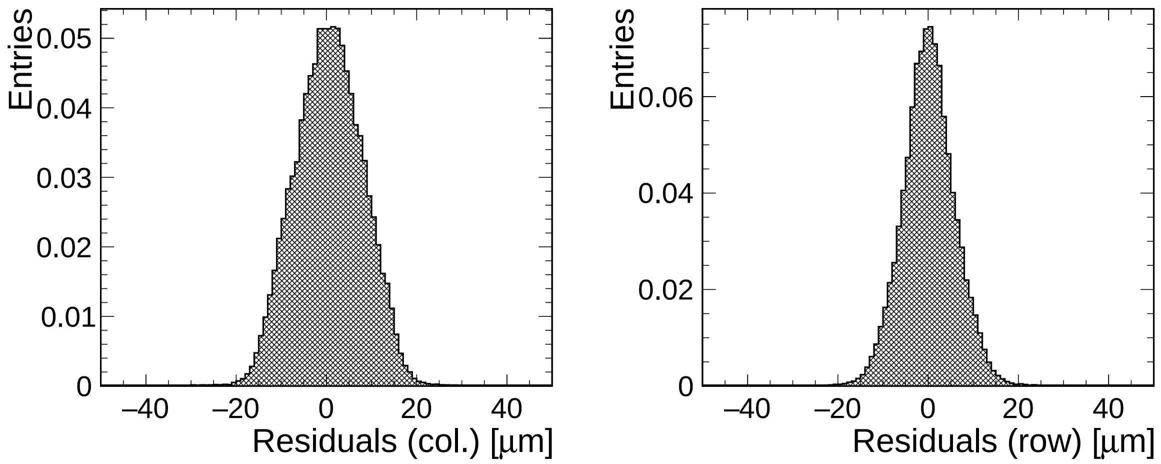

(a) Column direction

(b) Row direction

Figure 9.23. Spatial residuals in (a) column and (b) row direction between the telescope incident position and the reconstructed cluster position for the standard configuration.

as explained in Section 8.5. The binary resolution is given by pitch/$\sqrt{12}$ and evaluates to 10.8 µm in column direction and 8.7 µm in row direction. The measured resolution is therefore far superior to the binary resolution, which underlines the importance of charge interpolation for this measurement.

The achievable resolution depends on the impact position of a particle in the pixel cell. The in-pixel representation of the spatial resolution in row direction is depicted in Fig. 9.24 with and without η-correction. The best spatial resolution is observed for incident positions close to the middle of the pixel cell along the row dimension. Without η-correction, the spatial resolution deteriorates towards to pixel edges, where two-pixel clusters are most common, as shown in Fig. 9.4b. Despite the additional charge information from the adjacent pixel, the spatial resolution deteriorates, since the non-linearity in the charge sharing is not considered.

After applying the η-correction, the spatial resolution improves at the pixel edges, as displayed in Fig. 9.24a. The in-pixel region ±6 µm from the pixel centre exhibits the worst performance owing to a considerable fraction of single-pixel clusters, that cannot profit from additional charge information of neighbouring pixels. The lack of information leads to the position reconstruction of these single-pixel clusters at the pixel centre, which introduces the dominant imprecision of the measurement, since the particle incident position is a few micrometers off from the centre. Therefore, a lower detection threshold or increased charge sharing in these pixel regions could further improve the spatial resolution. For the CLICTD sensor, whose spatial resolution is already well within the CLIC tracker requirements, such improvements are not needed.

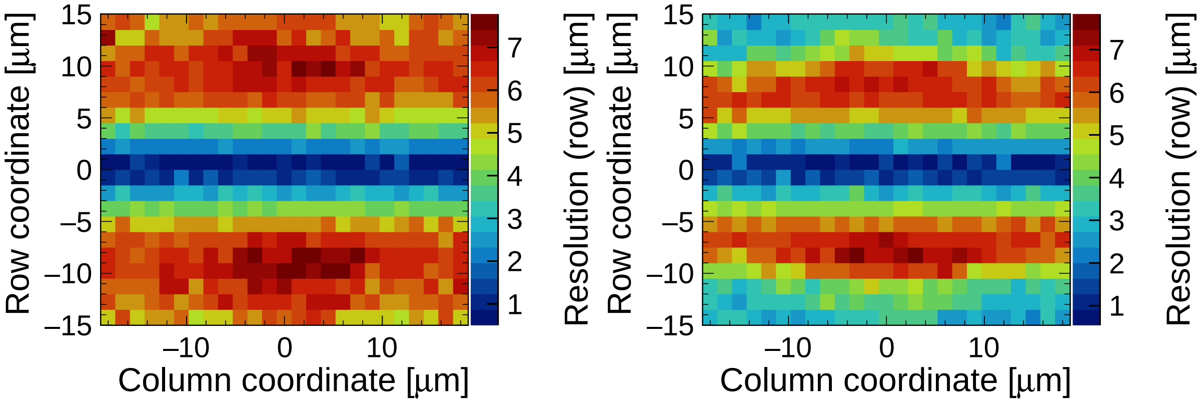

(a) Spatial resolution in row direction without η-correction

(b) Spatial resolution in row direction with η-correction

Figure 9.24. In-pixel representation of the spatial resolution in row direction (a) before (b) after η-correction for the standard configuration.

Table 9.5. Spatial resolution in row and column direction for the different bias voltages. The investigated sample has a thickness of 300 µm and a continuous n-implant.

Bias voltage	Thd [e]	Spatial res. (col.)	Spatial res. (row)
3	200^{+4}_{-5}	7.3 ± 0.2	5.2 ± 0.2
6	139^{+4}_{-5}	6.7 ± 0.2	4.6 ± 0.2

With increasing threshold, the cluster size decreases and the charge information from neighbouring pixels is lost. The impact on the spatial resolution is illustrated in Fig. 9.25, where the resolution as a function of the detection threshold is displayed. The spatial resolution deteriorates at higher thresholds, but never exceeds the binary resolution of 10.8 µm in column and 8.7 µm in row direction. For threshold values above 1000 e, an improvement of the spatial resolution is caused by the formation of inefficient regions at the pixel edges, as displayed in Fig. 9.16. These inefficiencies lead to an effectively smaller pixel pitch that results in an artificial improvement in spatial resolution.

Bias Voltages The spatial resolution for different p-well bias voltages is depicted in Fig. 9.26 for a 300 µm sample with continuous n-implant. As expected, the resolution for a given threshold remains unaffected owing to the similar cluster size observed in Section 9.1. The spatial resolution at the minimum operation threshold is listed in Table 9.5. The lower detection threshold that is achievable with the higher absolute bias

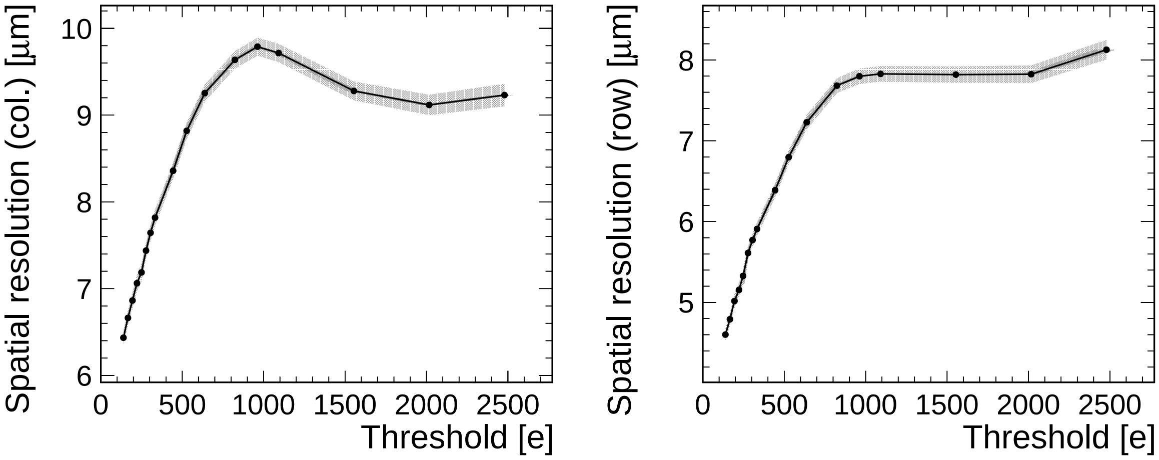

(a) Spatial resolution in column direction.

(b) Spatial resolution in row direction.

Figure 9.25. Spatial resolution in (a) column and (b) row direction as a function of detection threshold for the standard configuration.

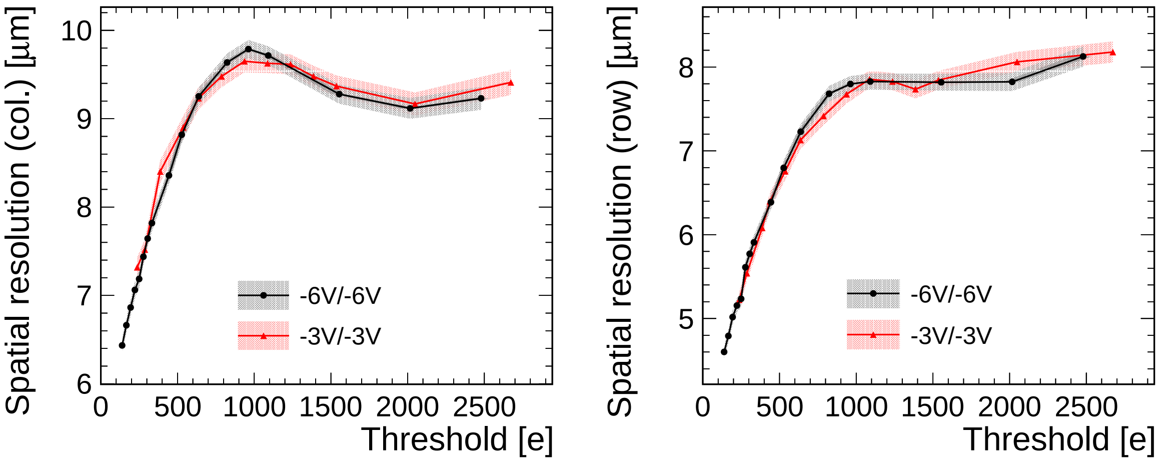

(a) Spatial resolution in column direction

(b) Spatial resolution in row direction.

Figure 9.26. Spatial resolution in (a) column and (b) row direction as a function of detection threshold for different p-well bias voltages. A sample with a thickness of 300 µm and continuous n-implant is used and a bias voltage of -6 V/-6 V is applied.

Table 9.6. Spatial resolution in row and column direction for the different pixel flavours. The samples have a thickness of 100 µm and are operated at -6 V/-6 V bias voltage.

Flavour	Thd [e]	Spatial res. (col.)	Spatial res. (row)
Continuous n-implant	139^{+4}_{-5}	6.5 ± 0.2	4.6 ± 0.2
Segmented n-implant	136^{+4}_{-5}	7.6 ± 0.2	4.6 ± 0.2
Extra deep p-well	148^{+4}_{-5}	7.2 ± 0.2	4.7 ± 0.2

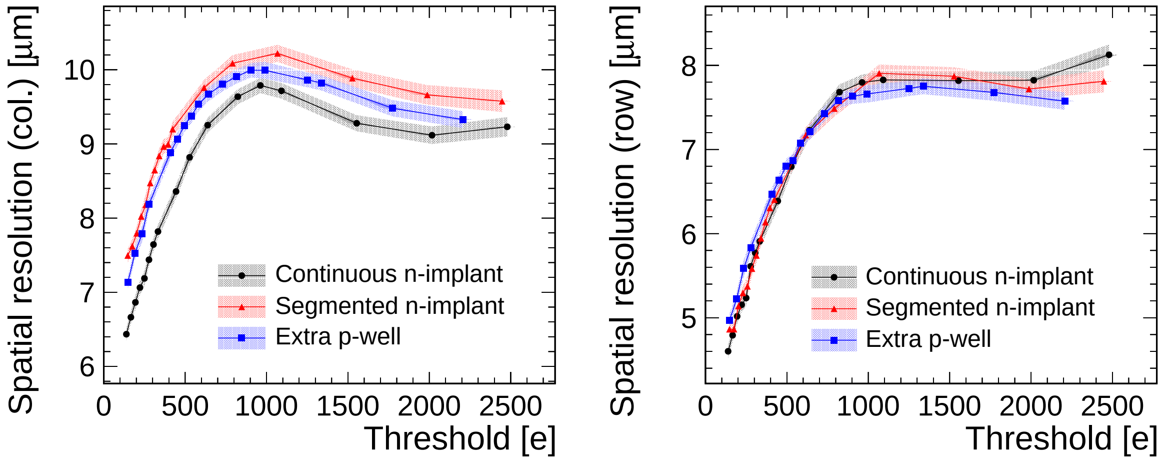

(a) Spatial resolution in column direction. **(b)** Spatial resolution in row direction.

Figure 9.27. Spatial resolution in (a) column and (b) row direction as a function of detection threshold for the different pixel flavours. The samples have a thickness of 100 µm and are biased at -6 V/-6 V .

voltage allows for a 10 % improvement of the spatial resolution in both directions.

Pixel Flavours The modifications in the pixel design affect the charge sharing and are therefore expected to alter the spatial resolution as well. The threshold scans of the spatial resolution in column direction in Fig. 9.27 confirm this assumption. The resolution in column direction for the sensor with continuous n-implant is superior to the other flavours due to the higher cluster size at a given threshold (cf. Section 9.1). The spatial resolution at the minimum operation threshold is approximately 15 % better for this pixel flavour, as listed in Table 9.6. Since there are no stringent requirements on the spatial resolution in the column direction, this result is of no practical concern for the target application in the CLIC tracker but is mostly instructive in order to comprehend the impact of the implant modifications on the spatial resolution.

The resolution in row direction is unaffected, since no modifications in the sensor design were applied in this direction. The CLIC requirement demanding a spatial resolution

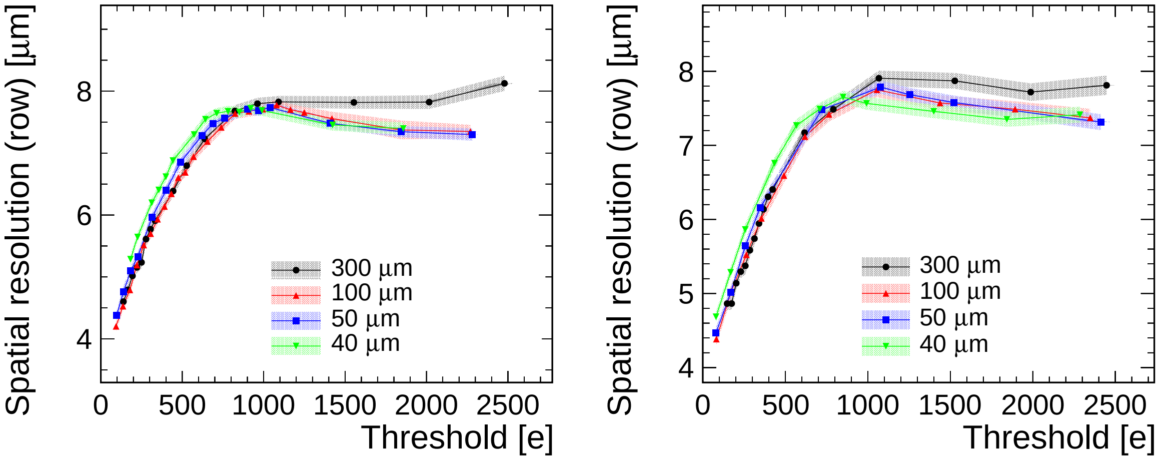

(a) Continuous n-implant

(b) Segmented n-implant

Figure 9.28. Spatial resolution in row direction as a function of detection threshold for different sensor thicknesses. The samples have a (a) continuous and (b) segmented n-implant and are biased at -6 V/-6 V.

below 7 µm in row direction is therefore reached by all pixel flavours.

Thinned Sensors Hereafter, only the spatial resolution in row direction is presented, since stringent demands imposed by the CLIC tracker requirements only apply in this direction. Qualitatively, the trends discussed in the following are also observed in the column direction.

The spatial resolution for different sensor thicknesses is presented in Fig. 9.28 for the pixel flavour with continuous and segmented n-implant. Within the uncertainties, the spatial resolution for sensors $\geq$ 50 µm are in good agreement owing to the similar cluster size at a given threshold. The deviations for the 300 µm thick samples at high thresholds are related to challenges in the reconstruction caused by limited statistics. The spatial resolution at the minimum operation threshold is presented in Table 9.7 and confirms that the resolution is unaffected by the sensor thickness, except for the 40 µm thick sample, which performs slightly worse. The smaller cluster size leads to a deterioration in spatial resolution, in particular for thresholds below 1000 e. The difference vanishes at high thresholds, where single-pixel cluster dominate for all sensor thicknesses.

Wafer Material The higher signal from high-resistivity Czochralski sensors leads to a larger cluster size and consequently an improved spatial resolution, as displayed in Fig. 9.29. The difference is particularly noticeable at small threshold values in accordance with the larger difference in cluster size that was shown in Fig. 9.10. At the minimum operation threshold listed in Table 9.29, the resolution improves by about 15 %. At high

Table 9.7. Spatial resolution in row direction at the minimum operation threshold for CLICTD sensors with different thicknesses. A bias voltage of -6 V/-6 V is applied to all sensors.

Thickness [µm]	**Flavour**	**Threshold** [e]	**Spatial res. (row)** [µm]
300	Continuous n-implant	139^{+4}_{-5}	4.6 ± 0.2
100	Continuous n-implant	136^{+4}_{-5}	4.6 ± 0.2
50	Continuous n-implant	140^{+4}_{-5}	4.6 ± 0.2
40	Continuous n-implant	181^{+4}_{-5}	5.3 ± 0.2
300	Segmented n-implant	136^{+4}_{-5}	4.6 ± 0.2
100	Segmented n-implant	140^{+4}_{-5}	4.5 ± 0.2
50	Segmented n-implant	131^{+4}_{-5}	4.6 ± 0.2
40	Segmented n-implant	130^{+4}_{-5}	4.8 ± 0.2

Table 9.8. Spatial resolution at the minimum operation threshold for CLICTD sensors with different wafer materials. Both sensors have a segmented-implant and are 100 µm thick. A bias voltage of -6 V/-6 V is applied.

Material	**Threshold** [e]	**Spatial res.** [µm]
Epi	131^{+4}_{-5}	4.5 ± 0.2
Cz	151^{+4}_{-5}	3.9 ± 0.2

thresholds, the mean cluster size converges to one resulting in an identical resolution within the uncertainties.

With increasing substrate bias voltage, the depleted region expands evoking a higher signal that leads to a larger cluster size as presented above. Therefore, the spatial resolution improves in the same manner, as illustrated in Fig 9.30 for high-resistivity Czochralski samples with segmented n-implant and extra deep p-well. The samples were operated at comparably high detection thresholds due to the modified front-end operation settings (cf. Section 7.3). A further improvement in spatial resolution is expected, if the front-end is adapted to the high-resistivity material, as it would allow for smaller detection thresholds.

9.5 Time Resolution

A time resolution below approximately 5 ns is required to guarantee efficient background suppression in the CLIC experiment. This section is thus dedicated to the determination of the time resolution of CLICTD and to studying the impact of different sensor designs

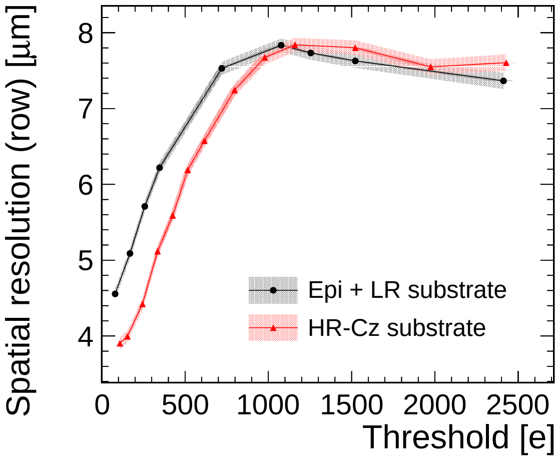

Figure 9.29. Spatial resolution in row direction as a function of detection threshold for a sample with epitaxial layer and a high-resistivity Czochralski substrate. Both samples have a segmented n-implant, a thickness of 100 µm and are biased at -6 V/-6 V.

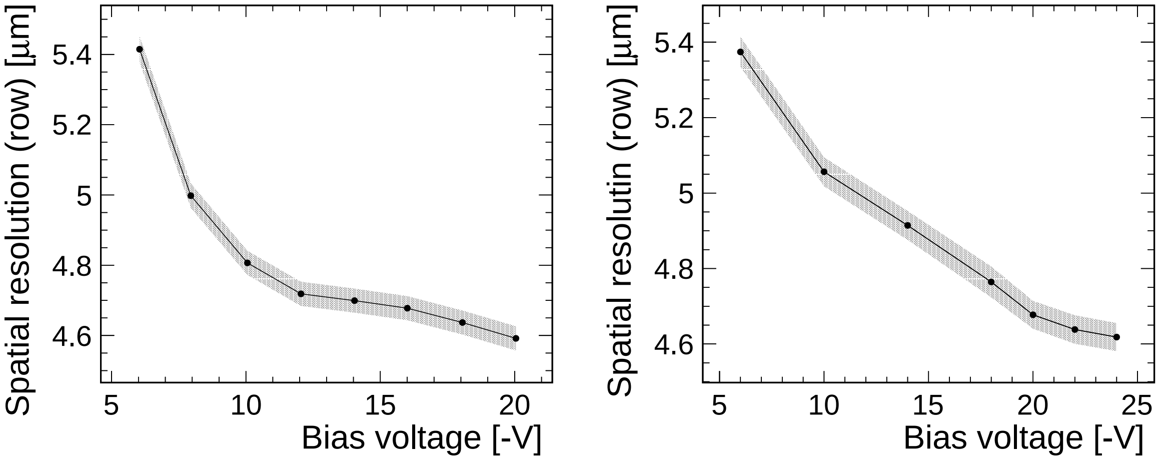

(a) Segmented n-implant at a detection threshold of 348 e.

(b) Extra deep p-well at a detection threshold of 488 e.

Figure 9.30. Spatial resolution in row direction as a function of substrate bias voltage for a high-resistivity Czochralski sample. The samples have a (a) segmented n-implant and (b) extra deep p-well and a thickness of 100 µm The p-well bias voltage is fixed to -6 V.

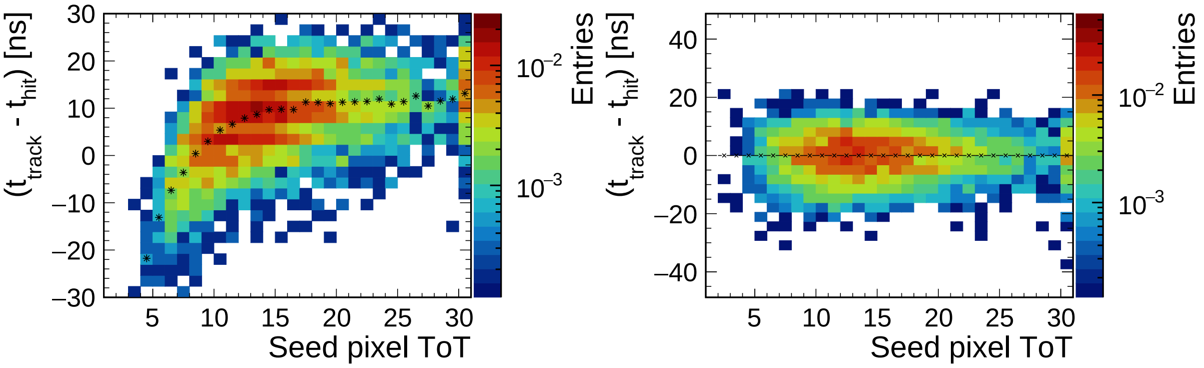

(a) Before time-walk correction (b) After time-walk correction

Figure 9.31. Residuals between track time stamp and reconstructed cluster time stamp as a function of seed pixel charge (a) before and (b) after time-walk correction for the standard configuration. The black crosses denote the mean of each ToT bin.

and operation conditions. The total time resolution of the device is a convolution of the sensor and front-end time resolution. In the laboratory measurements in Section 5.5.7, a front-end time resolution of several nanoseconds was found. This already places a limit on the achievable detector resolution, which is presented in the following section. An estimation of the sensor resolution excluding front-end effects is provided by simulations discussed in Section 11.2.8.

Standard Configuration In Fig. 9.31a, the time residuals are depicted as a function of the seed pixel ToT for the standard configuration. As expected, the signal-dependent time-walk effect leads to a slower response at low signal heights (cf. Section 3.2). A time-walk correction is performed for each ToT bin separately by subtracting the mean time difference between the track time stamp and the measured ToA. The time residuals after correction as a function of the seed pixel ToT are shown in Fig. 9.31b. While the signal-dependence of the mean time residuals is largely removed, the width of the time residuals is still slightly larger for low seed signals due to the stronger impact of amplitude noise causing a time jitter. The time jitter is inversely proportional to the slope of the signal at the threshold-crossing point. As the slope flattens towards the peak of the signal, lower signal heights have a smaller amplitude slope at the threshold-crossing point leading to a stronger impact of time jitter on the time resolution.

A projection of Fig. 9.31 onto the y-axis yields the one-dimensional time residuals distributions, as depicted in Fig. 9.32. The time resolution is calculated using the RMS of the central 99.7% of the distribution, which amounts to 6.6 ns for the residuals after

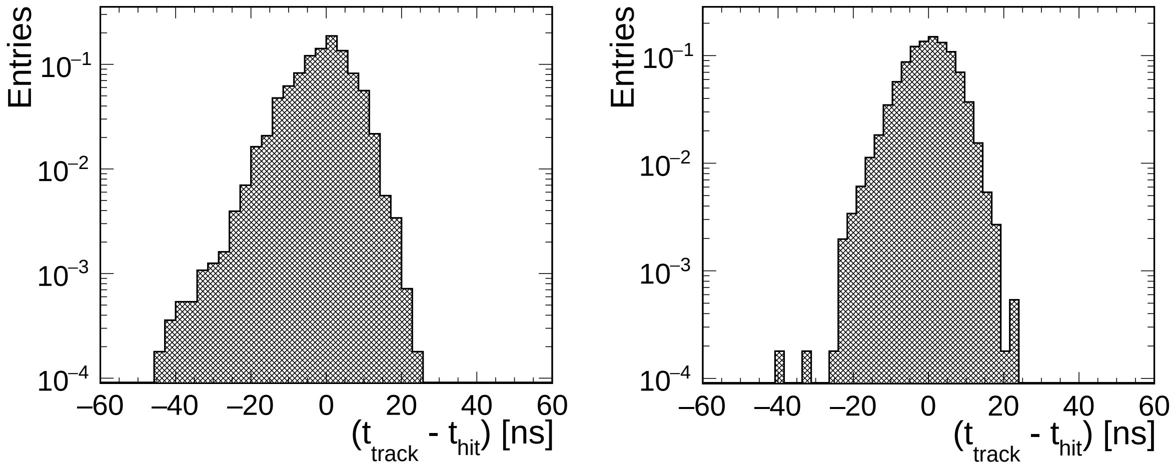

(a) Before time-walk correction

(b) After time-walk correction

Figure 9.32. Time residuals between track time stamp and CLICTD time stamp (a) before and (b) after time-walk correction for the standard configuration.

time-walk correction without subtraction of the track time resolution. The same quantity before time-walk correction evaluates to 8.3 ns, which is more than 20 % higher and underlines the importance of the correction procedure.

The time resolution associated with the track time stamp (1.1 ns) is quadratically subtracted from the RMS of the corrected time residuals, which yields a hit-time resolution of (6.5 ± 0.1) ns. According to the simulations presented in Section 11.2.8, the sensor time resolution is below 3 ns, which confirms that the measured time resolution is dominated by the front-end.

The time resolution depends on the incident position of the particle in the pixel cell, as shown in Fig. 9.33a, where the in-pixel time resolution before time-walk correction is presented. The time walk is particularly strong in the pixel corners, where a lower seed signal is expected. After time-walk correction, the timing is more homogenous across the pixel cell, as illustrated in Fig. 9.33b. The remaining in-pixel pattern suggests that slow signals arise predominantly from incident positions at the pixel corners, which is in agreement with simulations indicating that the time resolution degrades in the pixel edge regions (cf. Section 11.2.8). In addition, the lower signal height coming from hits in the pixel corners lead to a stronger contribution of amplitude jitter and possibly remaining time-walk effects that can further deteriorate the time resolution.

The time resolution deteriorates with increasing threshold as shown in Fig. 9.34. The degradation is linked to time jitter, similar to the effect observed for small signal heights. With increasing threshold, the amplitude slope at the threshold-crossing point decreases leading to an increase in time jitter, which culminates in a deterioration of the time

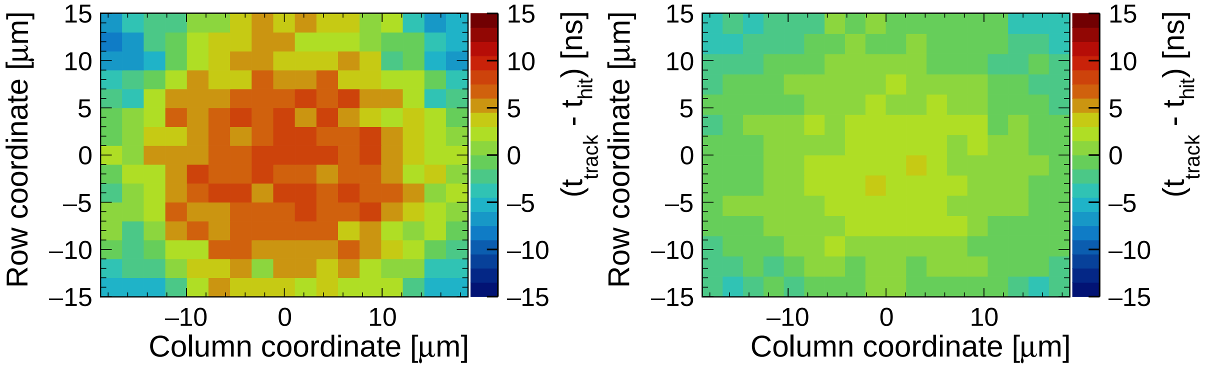

(a) Before time-walk correction **(b)** After time-walk correction

Figure 9.33. In-pixel time residuals for the standard configuration (a) before and (b) after time-walk correction.

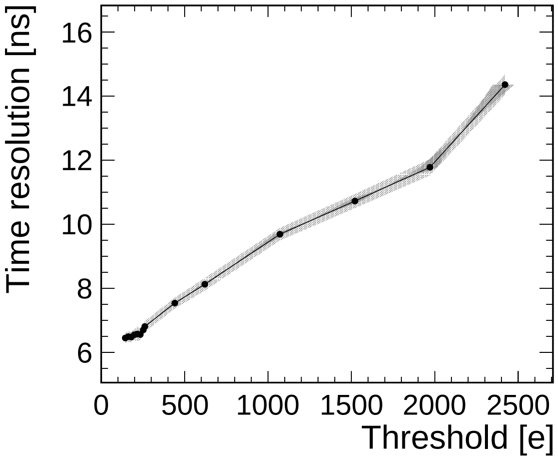

Figure 9.34. Time resolution as a function of the detection threshold in the standard configuration.

Table 9.9. Time resolution for the different pixel flavours. The samples have a thickness of 100 µm and are operated at -6 V/-6 V bias voltage.

Flavour	Thd [e]	Time res. [ns]
Continuous n-implant	139^{+4}_{-5}	6.5 ± 0.1
Segmented n-implant	136^{+4}_{-5}	5.5 ± 0.1
Extra deep p-well	148^{+4}_{-5}	5.5 ± 0.1

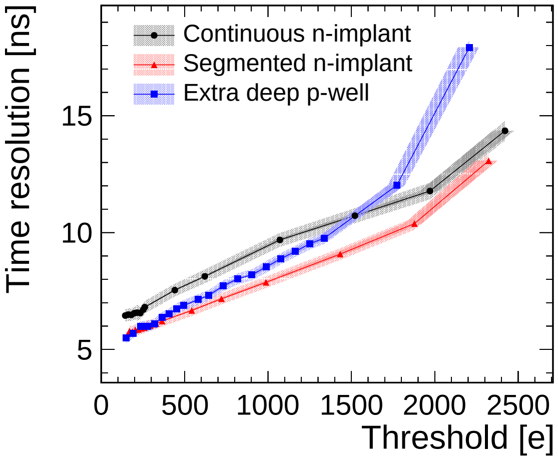

Figure 9.35. Time resolution as a function of detection threshold for different pixel flavours. The sensors have a thickness of 100 µm and are biased at -6 V/-6 V.

resolution [64].

Pixel Flavours The pixel flavours with segmented n-implant and additional deep p-well are optimised to accelerate charge collection, which is expected to improve the time resolution. The results in Fig. 9.35 confirm this trend, although the improvement in time resolution is limited owing to the dominating front-end time resolution. The outliers at high detection thresholds can be attributed to challenges in the time-walk correction. At the minimum threshold presented in Table 9.9, a 15 % improvement in time resolution is observable for the optimised flavours.

Thinned Sensors The time resolution for different sensor thicknesses is presented in Fig. 9.36 for the continuous and segmented n-implant and no significant difference is found. This result is confirmed in Table 9.10, where the resolution at the minimum threshold is listed.

The time resolution of thinned sensors is affected by two competing mechanisms: On the one hand, a smaller seed charge from the thinned sensors is expected to degrade

Table 9.10. Time resolution at the minimum operation threshold for CLICTD sensors with different thicknesses.

Thickness [µm]	**Flavour**	**Threshold** [e]	**Time res.** [ns]
300	Continuous n-implant	139^{+4}_{-5}	6.5 ± 0.1
100	Continuous n-implant	136^{+4}_{-5}	6.5 ± 0.1
40	Continuous n-implant	181^{+4}_{-5}	6.5 ± 0.1
300	Segmented n-implant	136^{+4}_{-5}	5.6 ± 0.1
100	Segmented n-implant	131^{+4}_{-5}	5.5 ± 0.1
40	Segmented n-implant	130^{+4}_{-5}	5.3 ± 0.1

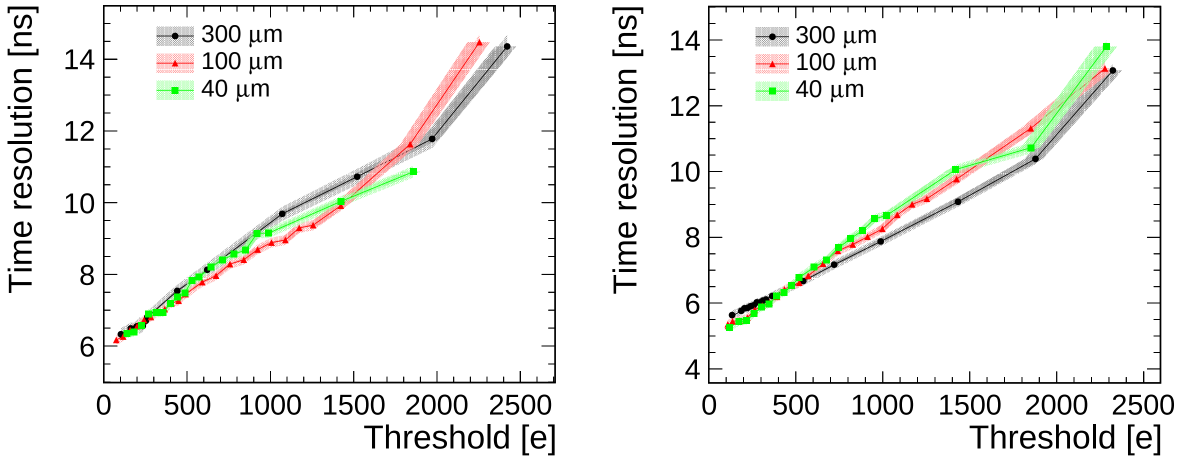

(a) Continuous n-implant

(b) Segmented n-implant

Figure 9.36. Time resolution as a function of detection threshold for different sensor thicknesses. A bias voltage of -6 V/-6 V is applied.

the resolution. On the other hand, time variations in the collection of charge carriers from different sensor depths are reduced. Since the performance for the 40 µm sample is unaffected within the uncertainties, it can be concluded that the net effect resulting from the two mechanisms is overshadowed by the dominant front-end time resolution.

Wafer Material An improvement in time resolution for samples fabricated on high-resistivity Czochralski wafer material is observable in Fig. 9.37. The resolution at the minimum threshold is shown in Table 9.37 and presents a 12 % improvement for the Czochralski sample owing to a higher seed signal, which suppresses time jitter. An increase in substrate bias voltage leads to an additional improvement in time resolution, as shown in Fig. 9.38 for the pixel flavours with segmented n-implant and extra deep

Table 9.11. Time resolution at the minimum operation threshold for CLICTD sensors with different wafer materials. Both sensors have a segmented-implant and are 100 µm thick. A bias voltage of -6 V/-6 V is applied.

Material	Threshold [e]	Time res. [ns]
Epi	131^{+4}_{-5}	5.5 ± 0.1
Cz	151^{+4}_{-5}	4.8 ± 0.1

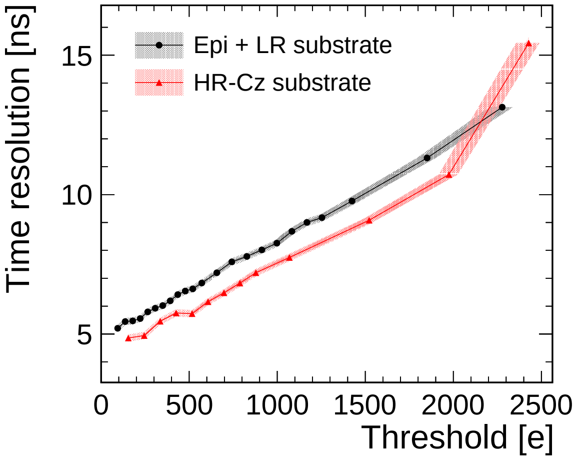

Figure 9.37. Time resolution as a function of detection threshold for different wafer materials. The sensors have a segmented n-implant and a thickness of 100 µm. A bias voltage of -6 V/-6 V is applied.

p-well.

9.6 Performance with Inclined Particle Tracks

The silicon sensors operated at vertex and tracking detectors of HEP collider experiments are typically inclined with respect to the incoming particle tracks. The rotation is related to the bent trajectory of the particles themselves and a mechanical rotation of the modules to compensate for Lorentz drift or improve the spatial resolution [184,185]. This section is thus dedicated to the assessment of the sensor performance using inclined particle tracks. The performance criteria charge sharing, hit detection efficiency as well as spatial and time resolution are investigated.

Charge Sharing The amount of active silicon traversed by particles is varied by rotating the sensor relative to the beam. For high rotating angles, particle tracks cross several adjacent pixel cells, giving rise to a larger cluster size as illustrated in Fig. 9.39 for a

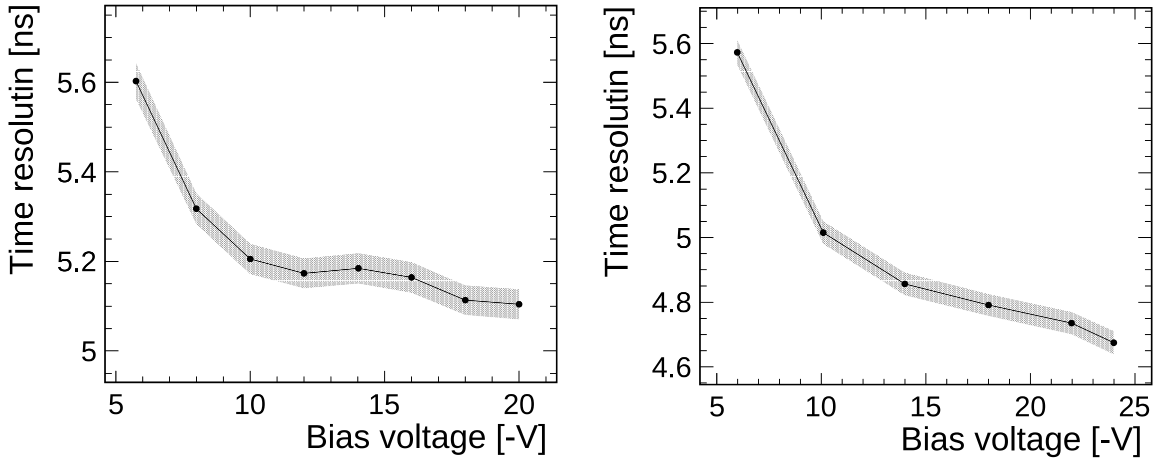

(a) Segmented n-implant at a detection threshold of 348 e.

(b) Extra deep p-well at a detection threshold of 488 e.

Figure 9.38. Time resolution as a function of substrate bias voltage for high-resistivity Czochralski samples with a (a) segmented n-implant and (b) extra deep p-well. The sensors have a thickness of 100 µm and a bias voltage of -6 V is applied to the p-well terminals.

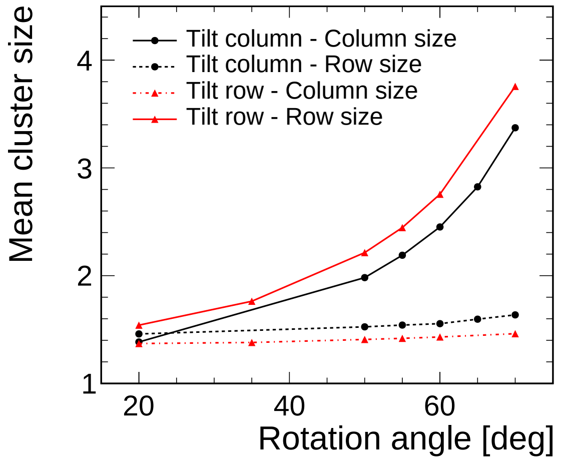

Figure 9.39. Cluster size in column and row direction as a function of the rotation angle for the standard configuration. *Tilt column* denotes a tilt in the column direction and *tilt row* in the row direction.

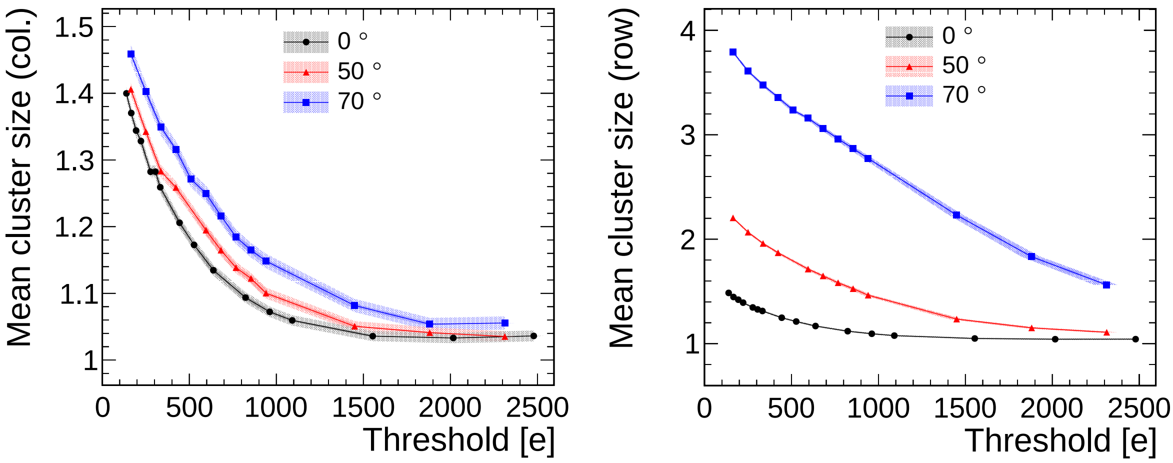

(a) Cluster size in column direction

(b) Cluster size in row direction

Figure 9.40. Cluster size as a function of detection threshold for different rotation angles for the standard configuration. The sensor is tilted in row direction.

sample in the standard configuration. The figure depicts measurements, where the sensor was tilted in column direction (*tilt column*) and row direction (*tilt row*). The cluster size in the tilt direction increases non-linearly, due to the deposition of energy in multiple adjacent pixels. A small increase in the perpendicular direction is observable as well, that is related to an overall increase in the number of liberated electron-hole pairs. Especially the charge carriers created in the lower part of the active sensor material undergo undirected diffusion to neighbouring cells in both directions.

The cluster size as a function of the detection threshold is displayed in Fig. 9.40 for different rotation angles. As the sensor is rotated in row direction, the mean cluster size in column direction increases only slightly due to the higher energy deposition. In row direction, a pronounced increase over a wide threshold range is observable. At 70°, the mean size still exceeds size one at high threshold values above 2000 e.

The cluster size depends on the incident position on the pixel cell, as illustrated in the in-pixel representation of the cluster size in column direction in Fig. 9.41 for two different rotation angles. The sensor depicted in the figure was tilted in column direction. At a small rotation angle of 5°, the cluster size map resembles the maps shown in Fig. 9.4 for perpendicular tracks with an increased cluster size at the pixel edges due to charge sharing by diffusion and a size of one at the pixel centre. Therefore, charge sharing by diffusion still dominates and no significant rotation effects are observable at such a small inclination angle.

For higher rotation angles, the rotation-induced charge sharing dominates, as shown

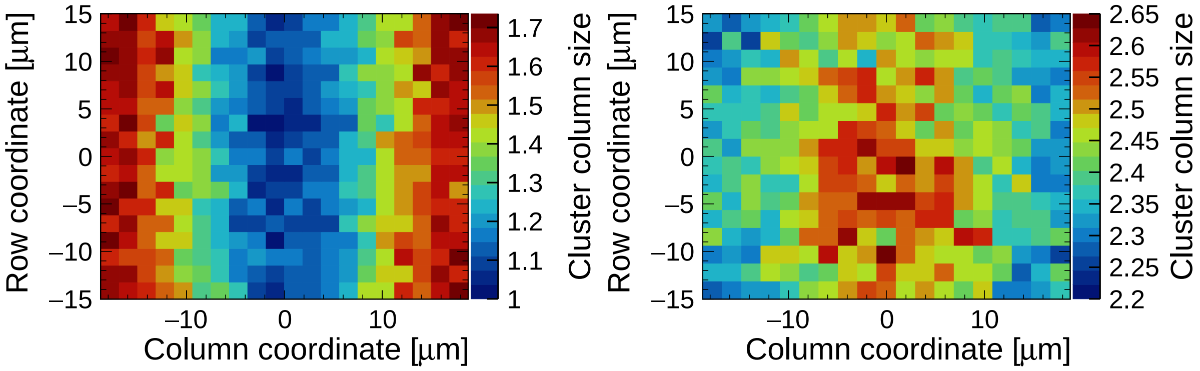

(a) Rotation angle: 5° **(b)** Rotation angle: 60°

Figure 9.41. In-pixel representation of the cluster size in column direction showing two different rotation angles for the standard configuration. The sensor is tilted in column direction.

in Fig. 9.41b for a rotation angle of 60°. A larger cluster size for particles impinging in the pixel centre is visible. The situation is schematically depicted on the right of Fig 9.42. It should be noted that the in-pixel track intercept position for inclined tracks does not correspond to the intersection of the track with the sensor surface. In order to comply with the definition of the reconstructed cluster position, which is based on a charge-weighted centre-of-gravity algorithm, the intersection of the track with the sensor is in the central region of the active silicon traversed by the beam. The exact location of the track intercept with the sensor is determined in the offline alignment procedure, where the detector position is reconstructed such that the spatial residuals between track position and reconstructed cluster position are minimized. In Fig. 9.42, the track position is approximated by a star. Consequently, the left track in the schematic is associated with a hit in the pixel edge and the right track in the pixel centre.

Hit Detection Efficiency With increasing rotation angle, the total energy deposition in the sensor increases due to the longer path in the active sensor region. As a result, a higher signal is detected, which leads to an appreciable increase in efficiency at high thresholds, as depicted in Fig. 9.43. The threshold scans were measured with the standard configuration, while setting three different rotation angles. At a threshold of 2300 e, the increase in efficiency is approximately 75 % between 0° and 70°.

Spatial Resolution The spatial resolution in row direction as a function of the rotation angle is depicted in Fig. 9.44. The sensor is in the standard configuration and was tilted in row direction. For the black curve, only a centre-of-gravity reconstruction is applied,

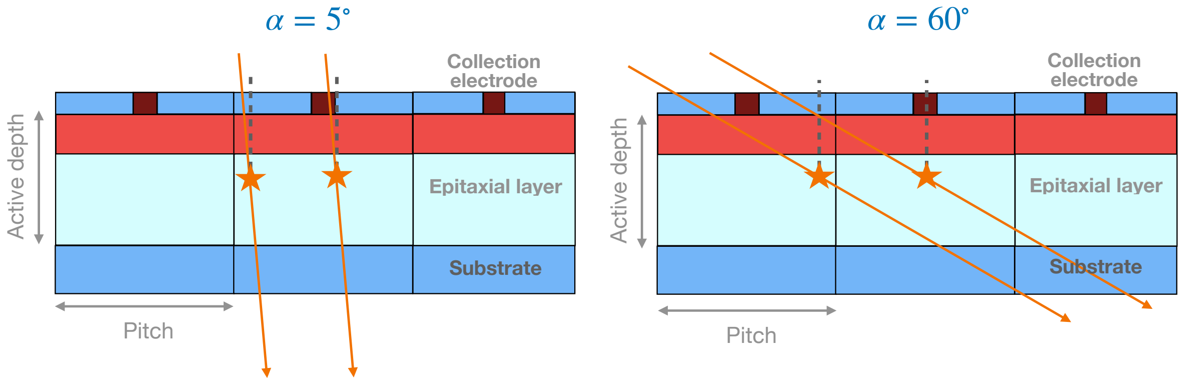
$\alpha = 5°$
Collection electrode
Active depth
Epitaxial layer
Substrate
Pitch
$\alpha = 60°$
Collection electrode
Active depth
Epitaxial layer
Substrate
Pitch

(a) Rotation angle: 5°

(b) Rotation angle: 60°

Figure 9.42. Schematic representation of inclined particle tracks impinging on a pixel cell for two different angles. The stars indicate the reconstructed track intercept with the sensor. Not to scale.

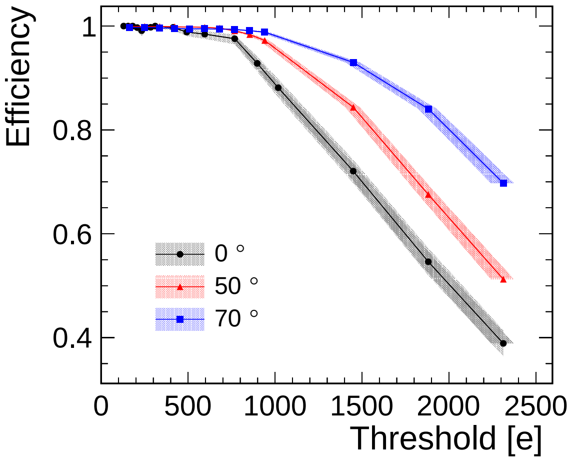

Figure 9.43. Detection efficiency as a function of threshold using different rotation angles for the standard configuration.

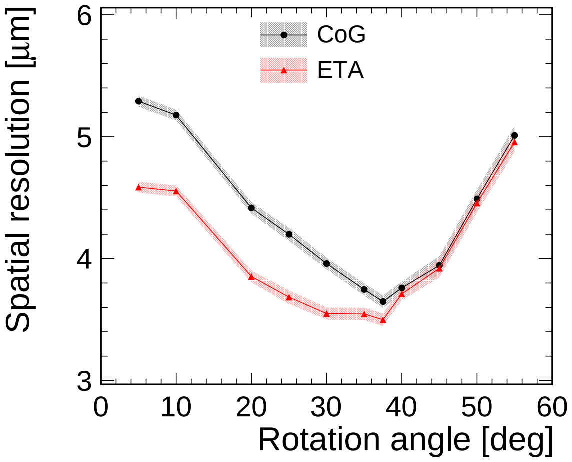

Figure 9.44. Spatial resolution as a function of the rotation angle using a charge-weighted centre-of-gravity algorithm (CoG) and an η-correction (ETA) to reconstruct the cluster position on the DUT.

and for the red curve an additional η-correction is performed. Both curves exhibit an improvement with increasing rotation angle until approximately 40°, where the spatial resolution evaluates to 3.6 ± 0.2µm after η-correction.

The results highlight the necessity of the η-correction for rotation angles below 40°. At higher angles, an increase of cluster size ≥ 3 complicates the application of the η-correction and no improvement with respect to the centre-of-gravity algorithm is achievable. Alternative reconstruction techniques attempting to mitigate this challenge are explored in Section 9.8. However, it should be noted that inclinations angles well above 50° are not relevant for the majority of measurements at HEP vertex or tracking detectors [186, 187]. Therefore, the degradation at high rotation angles is of little practical concern.

Time Resolution The time resolution as a function of the detection threshold for different rotation angles is depicted in Fig. 9.45. A small improvement for high rotation angles is observable that is attributable to a higher cluster seed charge. However, the sensor effects are mostly overshadowed by the time resolution of the front-end. Therefore, no sensible conclusion about the time resolution for inclined particle tracks can be drawn at this stage.

Conclusion Overall, an improvement in sensor performance is measured if particle tracks are inclined with respect to the sensor surface. In particular, the efficiency at high thresholds improves steadily with increasing angle due to the longer particle path in the sensor. For the spatial resolution, an optimal inclination angle of approximately $35 - 40°$

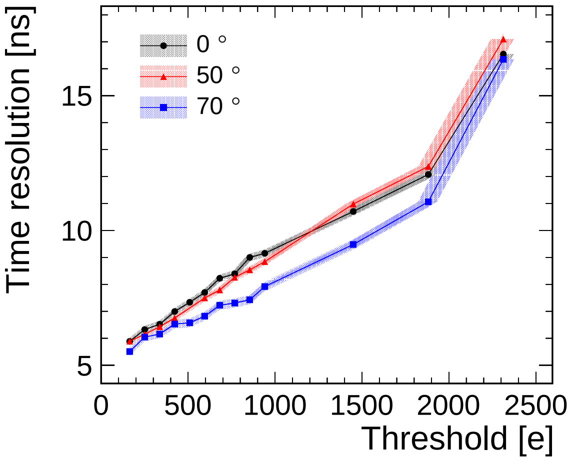

Figure 9.45. Time resolution as a function of the detection threshold for different rotation angles using a sensor in the standard configuration. The sensor is tilted in row direction.

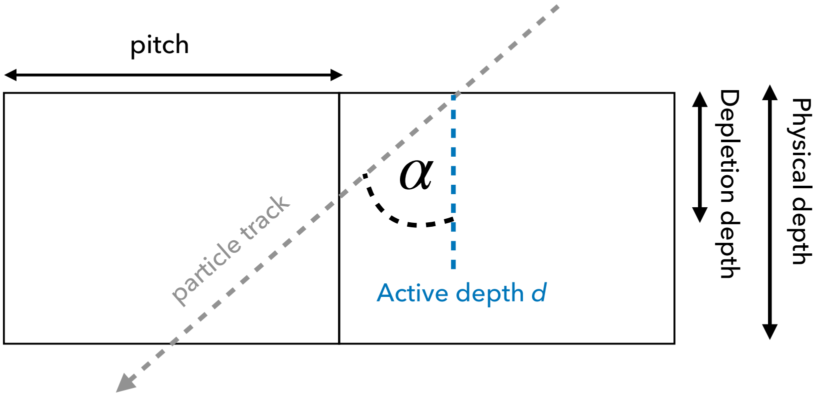

Figure 9.46. Schematic representation of the cluster size dependence on the inclination angle of the particle track.

was found using a charge-weighted centre-of-gravity reconstruction with η-correction.

9.7 Estimation of Active Depth

The size of the active sensor volume determines the number of charge carriers contributing to the signal. Since a higher number is beneficial for an improved signal-to-noise ratio, a large active sensor volume is desirable to maximize the performance of silicon sensors.

The results from the previous sections suggest that only the upper part of the sensors with epitaxial layer are part of the active volume, since thinning the sensors to 50 µm does not affect their performance. To quantify the thickness of the active sensor volume, grazing angle measurements [185] are performed, whereby inclined particle tracks are used to pin down the maximum sensor depth, from which charge carriers contribute to the signal. In the following, the method is described for a sensor in the standard configuration. Subsequently, the active depth of different sensor variants is compared. In all measurements, the sensors were operated at -6 V/-6 V, unless explicitly stated otherwise.

Standard Configuration An estimation of the active sensor depth is given by geometrical considerations, as sketched in Fig. 9.46. The simple geometrical model relates the cluster size in the tilt direction to the incident angle α and the active depth d. Charge carriers created below the active depth do not contribute to the measured signal and thus have no effect on the cluster size.

The following geometrical relation is considered to extract the active depth d:

$$\text{cluster size (tilt direction)} = \frac{d \tan \alpha}{\text{pitch}} + s_0 \tag{9.1}$$

where s_0 is the cluster column size for no rotation ($\alpha = 0$). The active depth is extracted with a linear fit to the mean cluster size as a function of the tangent of the rotation angle, as displayed in Fig. 9.47 for the standard configuration and a tilt in column direction.

The model neglects non-rotation induced charge sharing, i.e. charge sharing via pixel crosstalk or diffusion is not accounted for. Since the cluster size at small rotation angles is dominated by diffusion effects, as demonstrated in Section 9.6, data points below 40° are excluded from the fit. The effect of diffusion-induced charge sharing is considered in the systematic uncertainties by repeating the fit routine four more times with varied fit ranges by including/excluding points at the edges of the fit range. Additional systematic uncertainties related to sub-threshold effects or diffusion-induced charge sharing are discussed in Section 11.2.6, where simulation studies are used to investigate the validity of the model.

The fit in Fig 9.47 yields an active depth of

$$31.4 \pm 0.1 \text{ (stat.)}^{+0.2}_{-2.4} \text{ (syst.)µm.}$$

The value is larger than the simulated depletion depth for this sample, which evaluates to 21 ± 1µm (cf. Section 11.2.2). Therefore, a significant contribution of charge carriers from the undepleted region is possible due to random diffusion into the depleted part of the sensor.

The estimated active depth agrees well with the nominal thickness of the epitaxial layer, which indicates that charge carriers from the undepleted low-resistivity substrate are negligible. The results are in accordance with the high recombination probability in the substrate, which is further discussed in Section 11.2.5.

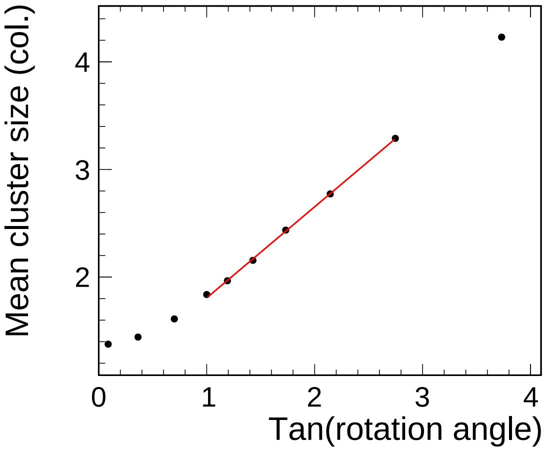

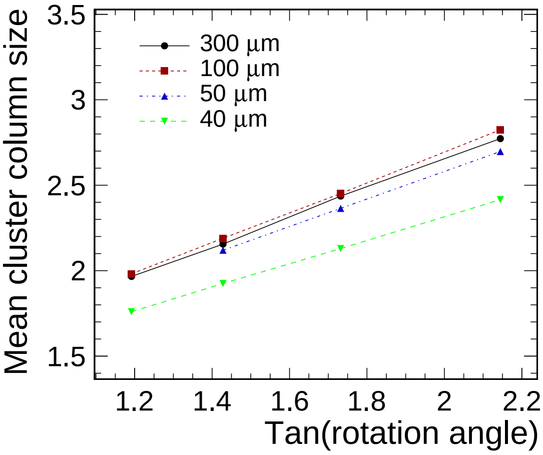

Figure 9.47. Cluster size in column direction as a function of the tangent of the rotation angle for the standard configuration.

Figure 9.48. Cluster size in column direction as a function of the tangent of the rotation angle for different sensor thicknesses.

Table 9.12. Active depth for all investigated sensors with an epitaxial layer and low-resistivity substrate.

Flavour	**Thickness** [µm]	**Active Depth** [µm]
Continuous n-implant	300	31.4 ± 0.1 (stat.)$^{+0.2}_{-2.4}$ (syst.)
Continuous n-implant	100	30.7 ± 0.1 (stat.)$^{+0.3}_{-1.8}$ (syst.)
Continuous n-implant	50	29.4 ± 0.1 (stat.)$^{+0.9}_{-1.0}$ (syst.)
Continuous n-implant	40	26.2 ± 0.1 (stat.)$^{+0.8}_{-1.0}$ (syst.)
Segmented n-implant	300	30.8 ± 0.2 (stat.)$^{+0.4}_{-1.2}$ (syst.)
Segmented n-implant	50	29.8 ± 0.1 (stat.)$^{+0.6}_{-1.0}$ (syst.)

Sensor Thickness The active depth is calculated for sensors with different thicknesses. The fitted curves are displayed in Fig. 9.48 and the fit results are summarised in Table 9.12. All sensors have an epitaxial layer, a continuous n-implant and are biased at -6 V/-6 V.

Although there is a trend towards smaller active depths with decreasing sensor thickness, it is not significant for thicknesses between 50 µm and 300 µm. Only the active depth for the 40 µm sample is clearly smaller compared to the other sensors, which is in agreement with the results from the previous sections, where the reduced signal was attributed to the removal of active material. It should be noted that the total thickness includes the metal stack with a size of approximately 10 µm, leaving a sensor thickness of about 30 µm. Moreover, the backside grinding is expected to introduce defects in the lower layer of the sensor, which justifies the assumption that the lower part of the 30 µm is effectively inactive.

Measurements for the pixel flavour with segmented n-implant are also listed in Table 9.12. The pixel flavour has no noticeable effect on the active depth, as expected from simulations.

It can be concluded that the CLICTD sensors with an epitaxial layer of 30 µm can be thinned down to a total thickness of 50 µm without suffering from a significant loss in sensor performance. For thinner sensors, performance degradations emerge due to the removal or damage of the active sensor volume.

Wafer Material Unlike the samples with epitaxial layer, the depletion for the high-resistivity Czochralski wafers is not limited in depth by the thickness of the epitaxial layer. The increased depletion region gives access to a larger active sensor volume, as illustrated in Fig. 9.49, where the active depth as a function of the substrate voltage is depicted for a high-resistivity Czochralski sample with segmented n-implant.

The active depth at a substrate voltage of -6 V evaluates to

$$34.2 \pm 0.1 \text{ (stat.)}^{+1.5}_{-0.6} \text{ (syst.)}$$

and is therefore slightly larger compared to the samples with epitaxial layer. With higher absolute substrate voltages, the active depth increases and reaches

$$65.4 \pm 0.1 \text{ (stat.)}^{+0.5}_{-0.7} \text{ (syst.)}$$

at a substrate voltage of -16 V. At this voltage, the active depth is twice as large as the depth for the samples with epitaxial layer and a corresponding increase in signal is expected. The higher signal translates into a better performance as shown in the previous section. However, it should be emphasised that the improvement is strongly limited by the front-end, which is not optimised for the large signal generated in the high-resistivity material (cf. Section 4.6.1). It can be expected that an adaptation of the front-end for future sensors would enable a full exhaustion of their potential.

9.8 Alternative Cluster Position Reconstruction

The results for the spatial resolution in Section 9.4 have shown the importance of the η-correction that takes non-linear charge sharing into account. The η-algorithm was originally constructed for clusters with an extent of two pixels in a given spatial dimension [174] and its adaptation to larger clusters is not optimal. Moreover, the original η-correction does not allow for a correlation between column and row direction, since both are treated independently [2].

---

[2] There are advanced versions of the η-correction taking the correlations into account such as [188].

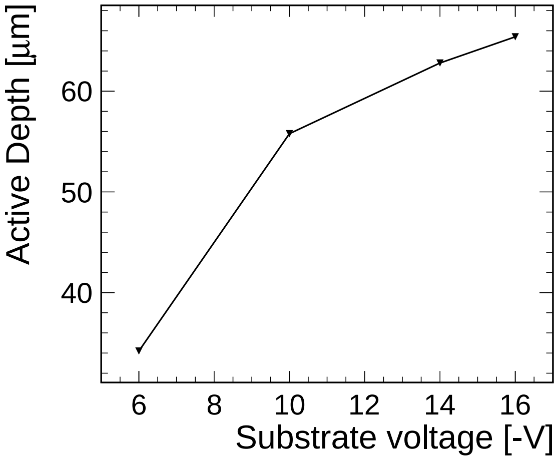

Figure 9.49. Active depth as a function of the substrate voltage for a high-resistivity Czochralski sample with segmented n-implant and a thickness of 100 µm. The p-well bias voltage is fixed to -6 V. The error bars are too small to be visible.

For perpendicular incidence of the particle beam, these limitations are negligible, since the cluster size in both directions is typically smaller than three. In addition, column and row direction exhibit no strong correlation in the relevant threshold range. However, if the particle track is sufficiently inclined with respect to the sensor surface, larger clusters become more frequent and the η-correction in unable to improve the results compared to the charge-weighted centre-of-gravity reconstruction (cf. Section 9.6). These observations justify the investigation of alternative position reconstruction techniques, especially for applications with inclined particle tracks. A technique commonly used for long clusters is the Head-Tail algorithm introduced in Section 8.3. The algorithm only takes the pixel charge of the first and last pixel in the cluster into account and ignores the central ones. Additionally, the cluster position reconstruction using a Multilayer Perceptron is explored, as introduced in the following.

9.8.1 Multilayer Perceptron

The application of neural networks for regression tasks has gained much popularity in the past years, largely due to the possibility to consider high-dimensional input vectors [5]. To investigate the performance of a machine learning approach against the established algorithms presented in Section 8.3, a Multilayer Perceptron (MLP) is employed. Since the MLP plays an important role in the second part of this thesis, more details about its operating principle are given in Section 14.2. Here, the MLP is constructed using the TMVA-toolkit for multivariate data analysis [189].

Table 9.13. Architecture of the Multilayer Perceptron (MLP) used for the cluster position reconstruction.

Hyperparamter	**Value**
Nodes	8 - 32 - 16 - 1
Batch size	30
Activation function	Sigmoid
Loss function	Mean squared error
Optimizer	Adaptive Moment Estimation (Adam)
Initial learning rate	0.02
Training Method	Broyden-Fletcher-Goldfarb-Shannon (BFGS)

The Input Vector Different combinations of input parameters and network architectures were tested. The best results were achieved by considering the ToT values of the four nearest neighbours to the cluster seed charge in row direction. Including pixels in column direction has adverse effects for the regression, due to the channel design of the sensor, where neighbouring sub-pixels in column direction are assigned the same ToT value if they are in the same channel. Since this ambiguity is not easily resolved by a simple MLP, only adjacent sub-pixels in row direction are considered [3]. In addition to the five ToT values, the total cluster size and the cluster size in column and row direction are added to the input vector. All parameters are normalised to the interval [-1, 1] to avoid dominance of a single variable. The reconstruction target is given by the track incident position relative to the centre of the seed pixel.

The data is split into three different samples: 80 k vectors in the training set, 20 k vectors in the testing set and 60 k clusters in the evaluation set. While the training and testing set are used in the training phase, the evaluation set is used in the subsequent evaluation phase to assess the performance of the network.

Network Architecture and Training A simple network architecture of four fully connected layers was chosen, as listed in Table 9.13, where an overview of the hyperparameters for the network is given. The input vectors are presented to the network in batches of 30 in order to speed up the training phase. The mean squared error was selected as loss function, since it is commonly used in regression problems [190]. The Adaptive Moment Estimation (Adam) optimizer is employed, which adapts the initial learning rate

---

[3] A more involved architecture of the MLP and possibly the introduction of additional techniques might cope with the challenges in the column direction. However, these studies are beyond the scope of this thesis.

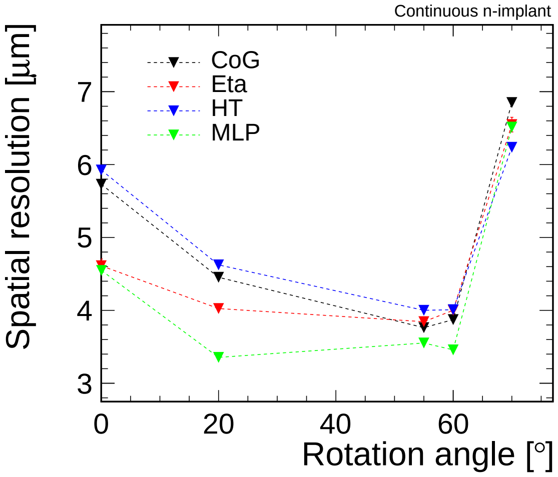

Figure 9.50. Spatial resolution as a function of the rotation angle for different cluster reconstruction techniques using a sensor in the standard configuration. A stand-alone Centre-of-Gravity (CoG) reconstruction, a CoG with an η correction (Eta), the Head-Tail algorithm (HT) and the Multilayer Perceptron (MLP) are considered.

automatically in each training step. The Broyden-Fletcher-Goldfarb-Shannon (BFGS) algorithm [191–194] is chosen as training method. The algorithm is similar to the common back propagation but uses second derivatives to adapt weights, which typically needs less iterations but requires more computing time especially for large networks [189]. As the considered network is comparably small, the longer computing time can be tolerated.

The testing set is fed into the network after every 5 training epochs. If 100 training epochs are completed without a significant improvement in the test error ($< 10^{-6}$), the training is stopped and the evaluation phase is started. A separate network was trained for each rotation angle.

Evaluation In the evaluation phase, the independent evaluation data set is presented to the network. The vectors in the set were not seen before by the network to guarantee an unbiased assessment. The reconstructed cluster position is extracted and the residuals between the track incidence position and the cluster position are calculated. As before, the RMS of the central $3\,\sigma$ of the distribution is extracted and the telescope resolution is quadratically subtracted.

The resulting spatial resolution is plotted as a function of the rotation angle in Fig. 9.50 for a sensor in the standard configuration tilted in row direction. For comparison, the spatial resolution using other reconstruction algorithms is shown as well. The reconstruction using only a Centre-of-Gravity (CoG) algorithm and a CoG with an η-correction (Eta) were already presented before. Additionally, the Head-Tail algorithm (HT) is employed, which is particularly suited for long clusters. The MLP outperforms the other algorithms except for the highest rotation angle, where the Head-Tail algorithm is superior. The η-correction has a similar performance as the MLP for perpendicular incidence but deteriorates with higher rotation angles.

While the MLP allows for a better spatial resolution for nearly all inclination angles, the improvement is limited by the CLICTD channel design that complicates the consideration of information in column direction. In addition, uncalibrated ToT values had to be used in the network. Using a calibration would remove pixel-by-pixel variations in the ToT value and could potentially improve the results (cf. Section 6.6).

Nevertheless, it can be concluded that using neural networks for the cluster position reconstruction can enhance the spatial resolution especially at intermediate rotation angles. The results are especially relevant for applications where offline reconstructions are performed and the larger implementation effort of an MLP can be tolerated. For applications, where only limited statistics are available, the training of an MLP becomes challenging. In this case, robust algorithms such as the CoG or the HT are preferable since they do not rely on the prior computation of a correction function/mechanism.

9.9 Conclusion

In conclusion, various design and operation parameters of the CLICTD technology demonstrator were assessed using charged particle beams. An overview of the main performance parameters in comparison to the requirements of the CLIC tracker is given in Table 9.14. Although the values correspond to measurements with particle beams perpendicular to the sensor surface, which is the worst-case scenario for most performance indicators, the requirements are all met simultaneously.

Most notably, the pixel flavours optimised for fast charge collection exhibit an improved time resolution as well as reduced charge sharing, which leads to a wider efficiency plateau. Moreover, the samples with epitaxial layer can be thinned down to 50 µm without a significant degradation in sensor performance.

The results for samples fabricated on high-resistivity Czochralski wafers are superior to the ones with epitaxial layer due to the larger active sensor region, which gives rise to a higher signal. The advanced wafer material is thus able to reconcile the small collection electrode design with a large active sensor volume, which can inspire future sensor prototypes aiming at high signal-to-noise ratios. For CLICTD, the improvement is still limited by the front-end of the sensor that was not optimised for the high signal, but could be adapted in future versions of the sensor. Likewise, the time resolution is obscured by the front-end resolution and could be improved in the future.

Measurements with inclined particle beams demonstrated an improvement of the ef-

Table 9.14. Principle performance parameters for the CLICTD sensor using particle beams perpendicular to the sensor surface in comparison to the requirements of the CLIC tracker.

Parameter	Required	Epitaxial layer	High-resistivity Czochralski
Spatial resolution	$< 7\,\mu m$	$4.5 \pm 0.2\mu m$	$3.9 \pm 0.2\mu m$
Time resolution	$\sim 5\,ns$	$5.3 \pm 0.1\mu m$	$4.8 \pm 0.1\mu m$
Efficiency	$> 99.7\,\%$	$> 99.7\,\%$	$> 99.7\,\%$

ficiency with increasing inclination angle. The spatial resolution has an optimum at an inclination angle of $35 - 40°$. The inclined particle tracks were also used to estimate the active depth of the different sensor types and operation characteristics. Whereas the samples with epitaxial layer have an active depth of about 30 µm, a two-fold increase in active depth is observed for the high-resistivity Czochralski samples using a substrate bias voltage of -16 V.

Lastly, a novel method for the cluster hit reconstruction was presented and a noteworthy improvement in the spatial resolution was found for intermediate inclination angles.

Chapter 10

Simulation Approach

Sensor simulation studies are essential ingredients in the development of silicon detectors. They are crucial in the design phase by guiding the optimisation of the sensor layout. Simulations also help to comprehend measurement results by providing insight into underlying mechanisms.

The complex non-uniform field configurations in small collection-electrode monolithic silicon sensors require advanced simulation tools. To guarantee an accurate sensor modelling of the underlying fields, finite-element simulations are used. While this simulation approach offers a detailed insight into the electrical properties of the sensor, they require a high computational effort and are therefore unsuited for studies where high-statistics samples are needed. Instead, Monte Carlo simulations enable high simulation event rates by implementing simplified signal formation algorithms. Combining electrostatic finite-element simulations and Monte Carlo simulations leverages the advantages of both approaches, i.e. a precise sensor modelling and high event rates are achieved simultaneously.

In the following, both simulation approaches are introduced and the simulation setup is presented. While this chapter treats the methodical background and implementation, the simulations are validated and applied to specific problems in Chapter 11.

10.1 Finite-Element Simulations

Three-dimensional *Technology Computer Aided Design (TCAD)* simulations with the Synopsys Sentaurus framework [195] are used to model the electromagnetic properties of the sensor as well as its response to charge injection. This approach relies on the finite-element simulation method, whereby the underlying electromagnetic field and transport equations are solved on a discrete simulation grid.

First, an introduction to the simulated geometry is given. Subsequently, the setups

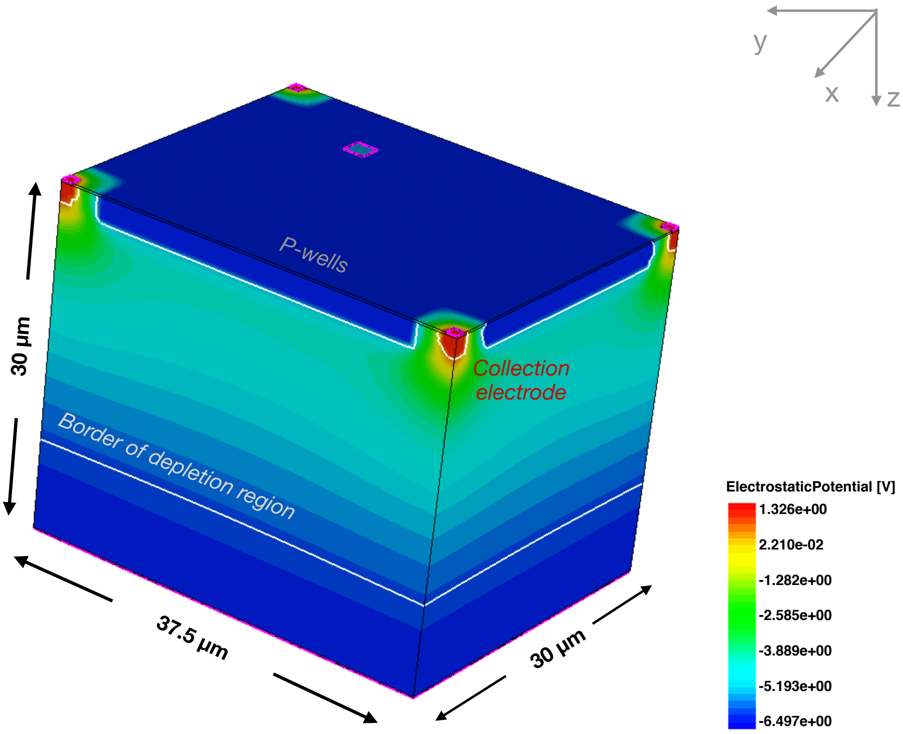

Figure 10.1. Simulated three-dimensional pixel cell of the CLICTD sensor in TCAD. The colour scale denotes the electrostatic potential and the white lines mark the edge of the depleted volume.

of the electrostatic and the transient simulations are presented. The relevant simulation parameters are summarised in the Appendix C.

10.1.1 Geometry

The pixel geometry introduced in Chapter 4, is implemented in TCAD. A three-dimensional model is built (*3D TCAD*), since a two-dimensional projection of the sensor is insufficient to e.g. capture effects at the pixel corners correctly. The simulated structure is displayed in Fig. 10.1 and a schematic of it is shown in Fig. 10.2. While the z-direction follows the sensor depth, the x-direction is parallel to the column direction with the larger pixel pitch (37.5 µm) and the y-direction follows the row direction with the shorter pitch (30 µm). The top view in Fig. 10.2 allows for a visualisation of the simulated volume with respect to the pixel grid. In the schematic, a cut of the xy-plane at the sensor surface is depicted. The simulated volume is centred around a pixel corner and comprises 1/4-th of four neighbouring cells. This choice steers the focus onto the pixel corner that requires particular attention in the sensor optimisation [132]. Only a single pixel structure is simulated to reduce computation times. In a real device, neighbouring pixels modify the field configurations of a given pixel cell. To account for this effect, periodic boundary

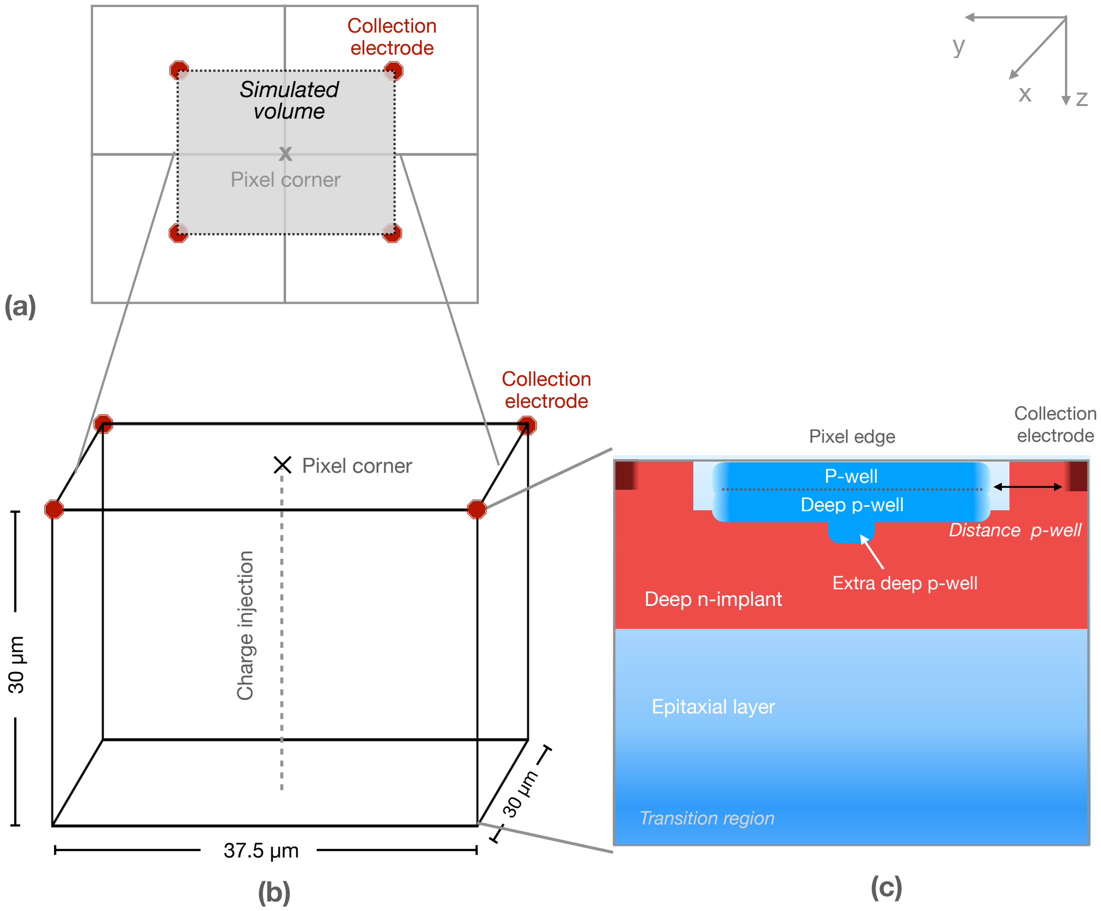
Collection electrode
Simulated volume
x
Pixel corner
(a)
y
x
z
Collection electrode
Pixel corner
Charge injection
30 µm
37.5 µm
30 µm
(b)
Pixel edge
Collection electrode
P-well
Deep p-well
Distance p-well
Extra deep p-well
Deep n-implant
Epitaxial layer
Transition region
(c)

Figure 10.2. Schematic representation of the simulated CLICTD pixel cell. The three-dimensional model is presented in (b) and the top view of the structure in (a) with the shaded square representing the simulation domain, which comprises 1/4-th of four neighbouring pixels. A two-dimensional cross section of the simulated structure showing the doping implants is presented in (c). A Gaussian diffusion at the lateral implant edges and at the lower vertical edge of the epitaxial layer (*transition region*) is included as well. Not to scale.

conditions are applied to the simulation that mimic an infinitely expanding pixel grid.

A schematic of the doping profiles in a two-dimensional cross section is displayed as well in the figure. The TCAD simulations comprise only the epitaxial layer and the implants. The substrate is not included, since contributions from the substrate are negligible for the studies performed with 3D TCAD (cf. Section 11.2.1). The substrate is later included in the Monte Carlo simulations. The circuits in the p-well are also excluded from the simulation, since they are shielded by the p-wells and are therefore not expected to modify the field configurations or the charge collection behaviour. Doping profiles for the p-well implants, the deep n-implants and the collection-electrode implant are obtained from process simulations performed by the foundry [131]. Since the profiles only contain the vertical extent of the implants, they are replicated in the lateral dimension. A diffusion at the implant edges into the bulk is modelled by a Gaussian function. The extent of the diffusion region is essential for the field configurations inside the sensor since it alters the distance between the p-well and the n-implant. Consequently, a significant impact on the charge-collection behaviour is expected, that is discussed in Section 11.1.3.

The doping profile of the epitaxial layer is obtained from measurements using the Spreading Resistance Profiling (SRP) technique [123]. The doping profile of a 18 µm thick epitaxial layer was measured, that is scaled to 30 µm to match the dimensions of the CLICTD sensor. The profile is characterised by a transition region between the high-resistivity epitaxial layer and the low-resistivity substrate, that arises from the diffusion of dopants out of the substrate into the epitaxial layer.

Aluminium metal contacts are placed at the backside, on top of the p-well and on top of the collection electrodes of the simulated structure. They allow for the application of the reset voltage at the collection electrodes and the bias voltages at the backside and the p-well. In the real device, the backside bias voltage is applied via undepleted regions at edge of the pixel matrix (cf. Chapter 4). As the simulation only comprises a single pixel cell and periodic boundary conditions are applied, the bias voltage is connected directly to the backside.

In finite-element simulations, the simulated structure is embedded in a mesh and the solution of the Poisson equation is computed at the mesh edges. The granularity of the mesh is therefore essential for the precision of the simulation. If the mesh is too coarse, no convergence is achievable or the solutions become inaccurate. A cross section of the default mesh is displayed in Fig. 10.3. The mesh is composed of tetrahedrons covering the entire structure. A finer mesh is applied to the regions with a high doping gradient such as the p-wells or at the edges of the implants. A coarser mesh is used for the epitaxial layer, where a low doping gradient is prevalent. The granularity of the mesh is scrutinised by repeating the simulations multiple times with modified mesh granularities

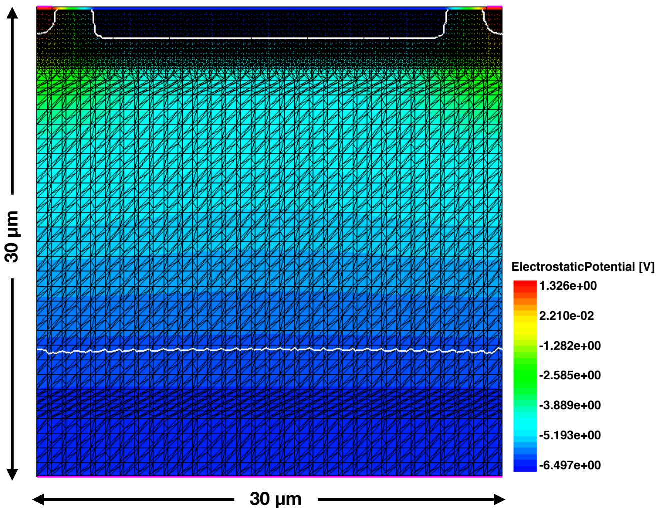

Figure 10.3. Two-dimensional cross section through the three-dimensional simulation model of CLICTD. The mesh is depicted as black lines spanning the entire pixel cell. It is finer in the upper part of the structure, where the collection electrode and the p-wells are located. The white lines indicate the border of the depleted region and the colour denotes the electrostatic potential.

and comparing the results (cf. Section 11.1.1).

10.1.2 Electrostatic Simulation

In the electrostatic simulation, the bias and reset voltages are applied to the metal contacts and the Poisson equation is solved numerically at each mesh point. The solutions give a full electrostatic description of the sensor, including properties such as the electric field configuration, the potential, sensor capacitance or the electron/hole densities.

As an example, the two-dimensional cross section of the electrostatic potential is depicted in Fig. 10.4 for the pixel flavour with continuous n-implant. The complexity and non-uniformity of the potential are a direct consequence of the small collection-electrode design and demands a precise modelling of the sensor for accurate performance predictions. The black arrows denote the electric field streamlines and the star indicates an electric field minimum below the p-wells in the pixel corners. Charge carriers close to these corners first drift into the field minimum before they propagate to the collection electrode, resulting in a slow charge collection and increased charge sharing, as detailed in [132]. As a consequence, the impact of charge carrier diffusion and recombination are crucial in this part of the pixel cell.

The white line at the bottom of the structure shows the border of the depleted volume indicating that the sensor is only partially depleted in depth. Moreover, the depleted volume does not reach into the substrate that is included in the Monte Carlo simulations.

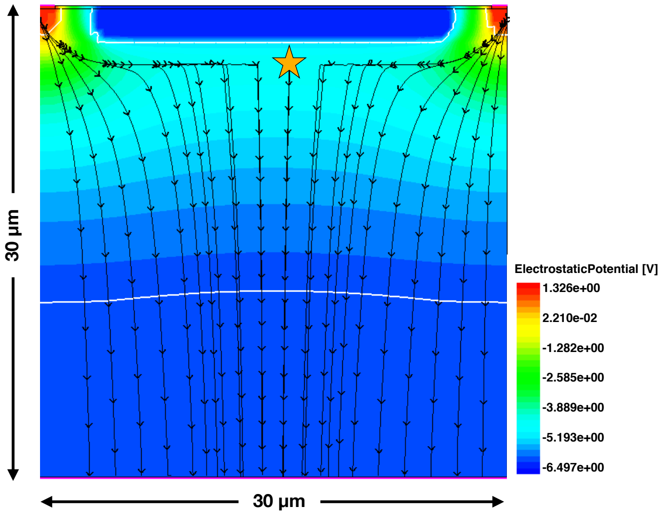

Figure 10.4. Two-dimensional cross section of a 3D TCAD simulation of the CLICTD pixel cell showing the electrostatic potential and electric field streamlines for the pixel flavour with continuous n-implant. The white lines indicate the edge of the depleted volume and the yellow star marks the electric field minimum. The collection electrodes are located at the left and right edge of the structure.

In these regions, the impact of diffusion is particularly high (cf. Section 2.4).

10.1.3 Transient Simulation

Transient simulations allow for an investigation of the sensor response to the injection of charge carriers, which mimics the energy deposition of ionising radiation. In particular the charge collection properties are studied using transient 3D TCAD simulations by iteratively solving the underlying electrodynamic and transport equations in discrete time steps.

In the simulation, charge carriers are injected uniformly along a straight line at the pixel corners as visualised in Fig. 10.2. In total, 63 electron-hole pairs per micrometer [196] are injected and the injection line is smeared laterally by a Gaussian distribution with a standard deviation of 50 nm. The meshing along the injection line is particularly fine, even in the lower part of the epitaxial layer.

After the charge injection, the drift and diffusion equations are numerically solved for each discretised timestep. The alteration of the local electric field by the injected charge carriers is taken into account, which offers a fully self-consistent time-resolved description of the sensor response.

The motion of charge carriers in the vicinity of the collection electrode induces a current on the electrode, that is computed in each simulation step. In this way, the current pulse is determined as a function of time as illustrated in Fig. 10.5. Two exemplary

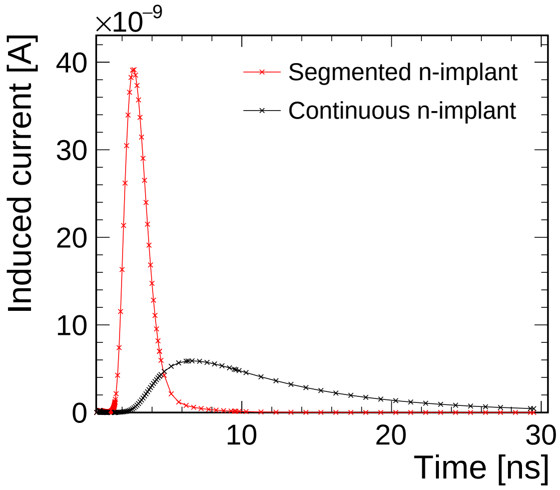

Figure 10.5. Current pulses extracted from transient 3D TCAD simulations after charge injection in the pixel corner for the pixel flavour with continuous n-implant and segmented n-implant . Both flavours are biased at -6 V/-6 V.

curves belonging to sensors with continuous and segmented n-implant are shown. The faster charge collection for the optimised flavour with segmented n-implant is visible by the prompt pulse that peaks at approximately 3 ns after the charge is injected. The slower charge collection for the flavour with continuous n-implant leads to a large tail that extends to tens of nanoseconds (cf. Chapter 4).

10.1.4 Limitations

While finite-element simulations provide a fully self-consistent solution to the field equations, their computing-intensive nature makes them unsuited for applications, where large simulation samples are required. For instance, the charge injection at different points in the pixel cell would require numerous transient simulations. If statistical fluctuations are included as well, the number of simulated charge injection events must be increased even more, which typically results in prohibitively long simulation times.

However, large simulations samples are required to assess certain performance parameters and to simulate a scenario that replicates the measurements with charged particles. Therefore, a different simulation approach is needed that can provide high simulation rates. The *Monte Carlo (MC)* method [197] offers a statistical approach, that delivers solutions with less computational effort.

10.2 Monte Carlo Simulations

MC simulations employ a probabilistic modelling of the underlying processes to create a simplified representation of the simulated scenario. Since the simulations rely on empirical models of the physical processes, they are not fully self-consistent and can only serve as approximations. Compared to finite-element simulations, high precision is traded for simulation speed.

The combination of both simulation approaches - the finite-element simulations and the MC approach - leverages the advantages of both methods, while suppressing their weak points. Electrostatic finite-element simulations are employed to obtain a precise electromagnetic description of the sensor that is imported into the MC simulation. The MC framework then handles the simulation of the particle-sensor interaction, the charge carrier propagation and the digitization based on the static 3D TCAD maps. The modification of the electromagnetic field by the charge carriers is neglected, which is a good approximation due to the low charge carrier density.

In the following, the combined simulation approach is described in more detail. For this purpose, the MC framework Allpix^2 is introduced and the full simulation chain is discussed.

10.2.1 The Allpix Squared Simulation Framework

Allpix^2 is a generic, open-source simulation framework for silicon detectors [198,199], that enables an end-to-end simulation of the interaction of silicon sensor devices with particles. While there are other MC frameworks with similar approaches such as Garfield++ [200], KDetSim [201] or PixelAV [202], Allpix^2 offers a modular structure that is based on a configurable simulation chain. A schematic of the simulation chain that is used to replicate the test-beam measurements is depicted in Fig. 10.6 and Fig. 10.7 and an example configuration file is listed in the Appendix D. The following section gives an overview of each step in the simulation chain.

Building the Geometry First, the `GeometryBuilderGeant4` module is used, which provides an interface to Geant4 [203–205] to create the geometry consisting of a single CLICTD sensor. Instead of simulating an entire telescope setup, only the DUT is simulated and the Monte Carlo information is used to obtain a reference track.

Energy Deposition Different energy deposition modules are used depending on the particular study. For the comparison against 3D TCAD presented in Section 11.1.2, a simplified energy deposition is used to replicate the transient 3D TCAD simulation. To

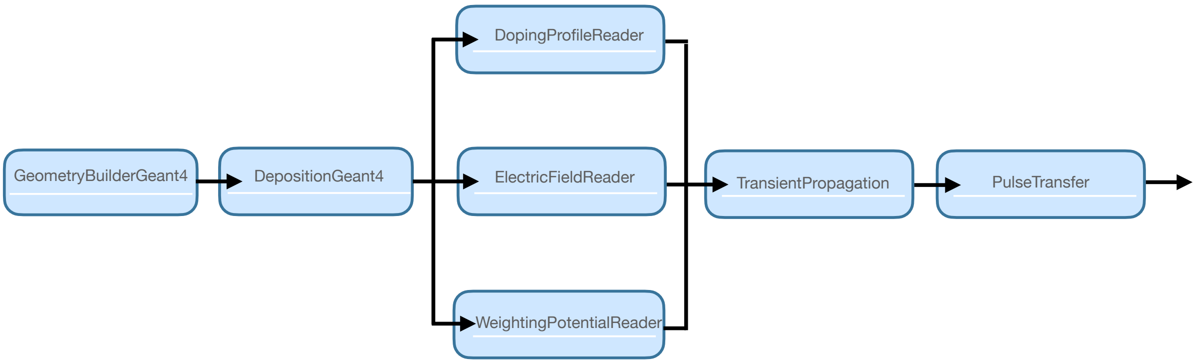
GeometryBuilderGeant4
DepositionGeant4
DopingProfileReader
ElectricFieldReader
WeightingPotentialReader
TransientPropagation
PulseTransfer

Figure 10.6. Schematic of the primary simulation chain for replicating the test-beam measurements.

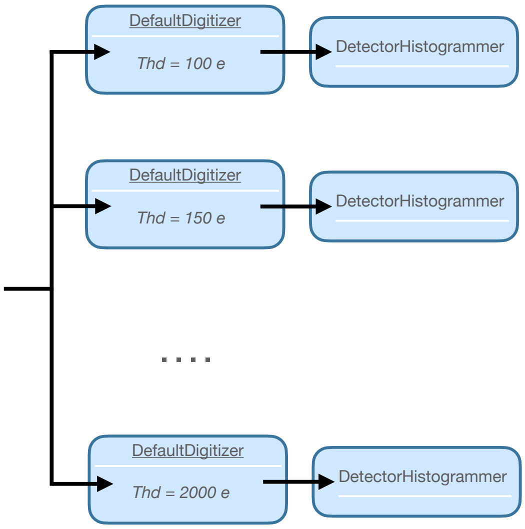
DefaultDigitizer
Thd = 100 e
DetectorHistogrammer
DefaultDigitizer
Thd = 150 e
DetectorHistogrammer
....
DefaultDigitizer
Thd = 2000 e
DetectorHistogrammer

Figure 10.7. Schematic of the digitization step in the simulation chain for replicating the test-beam measurements. The `DefaultDigitizer` module is used multiple times with different threshold (Thd) settings.

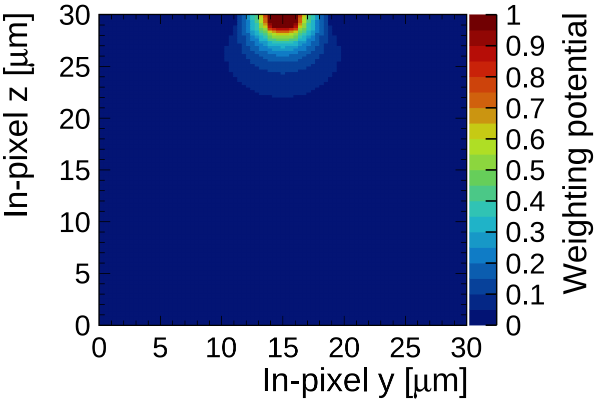

Figure 10.8. Cross section of an exemplary weighting potential for the CLICTD sensor. The collection electrode is located at the centre of the structure.

this end, the `DepositionPointCharge` module is employed to generate a fixed number of electron-hole pairs along a line through the sensor. For all simulations seeking to replicate the test-beam conditions, the `DepositionGeant4` module is selected. The module uses Geant4 to provide a realistic interaction between an incident particle with the silicon sensor including stochastic fluctuations and the creation of secondary particles. A 5.4 GeV electron beam is simulated to match the test-beam measurements and the beam cross-section is chosen much smaller than the sensor surface in order to exclude effects stemming from the matrix edge. The Photoabsorption Ionization (PAI) model is used to improve the description of energy deposition in the sensor, which is essential for sensors with a thin active volume [81]. The Monte Carlo information of the incident particles is stored and is used as a reference in the subsequent analysis.

For the simulations reproducing X-ray measurements, a photon beam is simulated with a fixed mean energy and a Gaussian energy spread around it. The mean energy and the energy spread correspond to the K_α peaks of selected fluorescence spectra (cf. Section 5.5.2).

Importing Field, Doping and Potential Maps To ensure a high accuracy of the sensor simulation, the electric field, the weighting potential and the doping concentration in the epitaxial layer are imported into Allpix^2. The maps are obtained from 3D TCAD and converted to a regularly spaced mesh using the *Mesh Converter* tool [206] in order to speed up the look-up of field values. A mesh granularity of 0.2 µm is selected. It has been verified that the granularity is sufficiently fine, as explained in Section 11.1.1.

Charge Carrier Transport The propagation of charge carriers is simulated using the `TransientPropagation` module, which employs a fourth-order Runge-Kutta-Fehlberg integration method [207].

The combined Masetti-Canali mobility model is used to calculate the charge carrier mobility (cf. Section 2.4). The electric field strength and doping concentration necessary for the calculation are obtained from the converted 3D TCAD maps at any given point in the sensor. Likewise, the doping-dependent charge carrier lifetime is computed in each simulation step using the combined Shockley-Read-Hall and Auger recombination model (cf. Section 2.5).

The induced current on the electrodes is calculated according to the Shockley-Ramo theorem (cf. Section 3.1). For the CLICTD sensor, it is sufficient to consider only the pixel, below which the charge carrier is located and ignore the neighbouring pixels since the weighting potential is concentrated around the collection electrode (*small-pixel effect*) [99]. An exemplary weighting potential map showing the concentration around the collection electrode is depicted in Fig. 10.8.

The charge carrier transport is halted after an integration time of 50 ns, which corresponds to the estimated front-end integration time of CLICTD and is significantly larger than the expected signal formation time for all CLICTD pixel flavours.

Current Pulses and Digitisation For each pixel, the final current pulses are computed using the `PulseTransfer` module. These pulses are analysed in Section 11.1.2. For the comparison against measurements, a simplified front-end simulation is performed with the `DefaultDigitizer` module. The module sets a detection threshold that is adapted to the threshold used in measurements. In addition, electronics noise contributions are simulated by randomly drawing from a Gaussian distribution with configurable width and adding it to the digitized signal. Likewise, the threshold dispersion is emulated by drawing from a Gaussian as well and adding it to the threshold.

For the threshold scans, the primary events are reprocessed with different threshold settings, as schematically depicted in Fig. 10.7.

Reconstruction and Analysis The MC information is used to construct a reference track. First, the MC particles are filtered by selecting only primary particles. Secondary particles pertaining to δ-electrons are not considered. The intercept position of the primary MC particles with the sensor is computed by linear interpolation between the entry and exit points with the sensor surfaces. This position is smeared with a Gaussian distribution to account for the limited track resolution of an external reference system. The width of this Gaussian is adapted to the telescope track resolution of the respective test-beam measurements (cf. Chapter 8). Subsequently, the same reconstruction and analysis steps as for the test-beam data are applied (cf. Section 8.4).

Chapter 11

Validation and Application of Simulation

The simulation of monolithic small collection-electrode sensors is essential for predicting and comprehending their properties and performance. However, the complex field configurations require sophisticated simulation tools that need to be validated in order to avoid wrong predictions and interpretations. The first part of this chapter is therefore dedicated to the validation of the transient Monte Carlo simulations by comparing them to established transient 3D TCAD simulations and test-beam data. In the second part, selected application scenarios will exemplify the usefulness and versatility of the simulations. The illustrative examples tie in with the measurements shown in the previous sections and enable an in-depth understanding of the experimental results. For all studies, the simulation setup introduced in Chapter 10 is used.

11.1 Validation of the Simulation

While finite-element simulations can be considered a well-established technique to model silicon devices [208], combining them with a MC framework is a comparatively novel approach that necessitates validation for sensors with a complex sensor design such as CLICTD. As the MC simulations rely on empirical models, that are typically valid for a limited parameter space, it is especially important to select the appropriate models and confirm their applicability for different sensor types. In the following section, the combined TCAD and MC simulations are therefore scrutinized before they are applied to predict and interpret measurements.

First, systematic uncertainties of the simulation approach are discussed. Next, the transient MC simulations are validated against transient 3D TCAD simulations by comparing current pulses. Before the simulations are compared to data, the influence of doping diffusion at the implant edges is discussed, since they are the main source of uncertainties in the comparison.

11.1.1 Systematic Uncertainties

The spatial and temporal granularity of both the 3D TCAD and the Monte Carlo simulation need to be fine enough to resolve the relevant physical features and processes. The temporal granularity of the simulated charge carrier transport in Allpix^2 is set to 7 ps. The value has been varied from 1 ps to 20 ps and the impact on the final observables was found to be negligible. The 3D TCAD simulation applies an adaptive spatial and temporal granularity, using a fine-grained mesh down to 10 nm for small feature sizes and time steps down to 10 ps. It has been verified that a further decrease in mesh size and temporal granularity does not alter the results. The spatial granularity of the 3D TCAD maps imported in Allpix^2 is fixed to $0.2\,\mu\text{m} \times 0.2\,\mu\text{m} \times 0.2\,\mu\text{m}$. A finer meshing has no significant effect on the final observables.

The charge carrier transport in Allpix^2 is sped up by transporting charge carriers in groups. Here, the number of charge carriers per group is set to 10. The value was varied between 1 and 15 and no significant impact was observed. The time interval in which the charge carriers are transported is fixed to 50 ns. It has been verified that continuing the simulation beyond the 50 ns does not significantly alter the results for the CLICTD pixel flavours confirming that the majority of liberated charge carriers have either recombined or reached the collection electrode within this time window. Smaller values lead to a decrease in the integrated induced signal, as expected. It should be noted that this does not apply to the pixel flavour without the n-implant, which was not used in CLICTD and is therefore not relevant for this discussion.

The principle source of systematic uncertainties is related to the knowledge of the doping profiles. Section 11.1.3 is dedicated to these uncertainties, since it only affects the comparison to data and not the comparison against transient 3D TCAD, which relies on the same doping profiles,

11.1.2 Comparison to Transient 3D TCAD

For the small collection-electrode design, the optimisation of the sensor properties is especially relevant at the pixel corners, since the distance to the collection electrodes is maximal and the charge collection therefore slower compared to the rest of the pixel cell. It also represents a challenging simulation scenario, since charge carriers created at the pixel corners traverse a large part of the active sensor volume, thereby probing the field distribution inside the pixel cell.

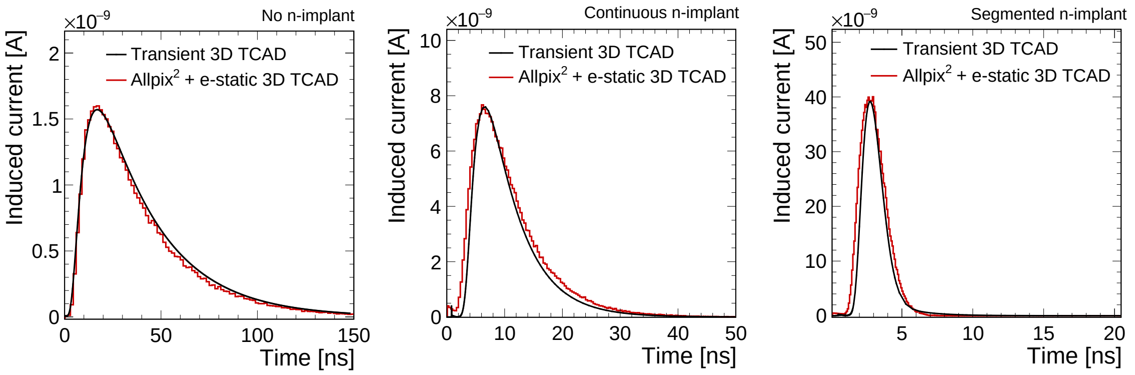

(a) No n-implant **(b)** Continuous n-implant **(c)** Segmented n-implant

Figure 11.1. Transient current pulses for transient 3D TCAD and Allpix^2 combined with electrostatic 3D TCAD after charge injection at the pixel corner. Three different sensor designs were tested: a design with (a) no n-implant, (b) continuous n-implant, (c) segmented n-implant for the CLICTD geometry using a pixel pitch of 37.5 µm × 30 µm and an epitaxial layer thickness of 30 µm.

In transient 3D TCAD, the pixel corner is investigated by injecting electron-hole pairs along a straight line at the intersection of four neighbouring pixels, as explained in Section 10.1.3. The same simulation conditions are replicated with Allpix^2 using the static field maps obtained from the electrostatic 3D TCAD simulation. The average pulse of 50 Allpix^2 simulation events is computed to smooth out statistical fluctuations, except for the design without the deep n-implant, where 200 simulation events are averaged. The simulation time per event is about 0.1 - 0.2 s compared to typically 8 h using 3D TCAD on the same machine and the same number of CPUs.

The resulting current pulses induced on one pixel cell are shown in Fig. 11.1 for transient 3D TCAD and Allpix^2 combined with electrostatic 3D TCAD. The pulses for all three sensor designs are displayed.

The different pixel flavours have significant differences in charge collection times and field configurations, but it can be seen that the two different simulation approaches give compatible results in all cases. The combination of Allpix^2 and electrostatic 3D TCAD is therefore suitable for a range of different devices without the need for prior adaptation of the simulation setup to the sensor design.

11.1.3 Uncertainty on Doping Profiles

The sensor properties were found to be highly sensitive to the doping profiles used to model the sensor. This section therefore seeks to quantify the uncertainties related to the

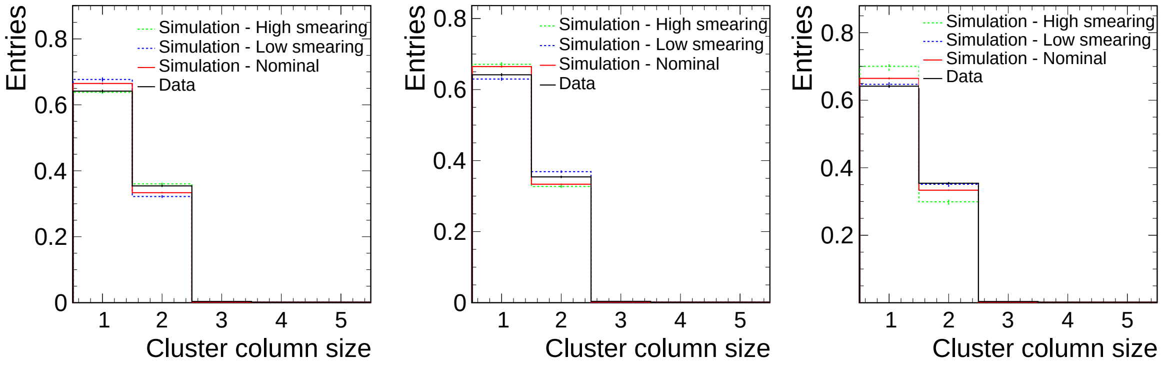

(a) Varied diffusion at p-wells

(b) Varied diffusion at collection electrode

(c) Varied diffusion of the substrate dopants into the epitaxial layer

Figure 11.2. Cluster size in column direction for different degrees of diffusion at the (a) p-well, (b) collection electrode and (c) substrate into the epitaxial layer. The distributions are recorded at the minimum threshold using a sample with epitaxial layer and continuous n-implant biased at -6 V/-6 V.

Table 11.1. Simulation of cluster size for different diffusions of the collection electrode, p-well implants and the substrate. The upper uncertainty represents the reduced and the lower value the increased diffusion.

Parameter	Nominal	C-electrode	P-well	Substrate
Cluster size [pixels]	1.99	$^{-0.04}_{+0.01}$	$^{+0.05}_{-0.05}$	$^{+0.02}_{-0.09}$
Cluster row size [pixels]	1.49	$^{-0.07}_{+0.01}$	$^{+0.01}_{-0.03}$	$^{+0.02}_{-0.05}$
Cluster column size [pixels]	1.37	$^{-0.03}_{+0.01}$	$^{+0.02}_{-0.03}$	$^{+0.01}_{-0.03}$

doping profiles in order to provide a proper treatment in the comparison against data.

The Spreading Resistance Profiling (SRP) technique [209] was used to measure the resistivity of a 18 µm thick epitaxial layer, that was scaled to 30 µm to match the investigated sensor design [123] (cf. Section 10.1.1). The profile is characterised by a transition region between the high-resistivity epitaxial layer and the low-resistivity substrate, that arises from the diffusion of dopants out of the substrate into the epitaxial layer. The slope of the transition region was varied by a factor of three in both directions to account for uncertainties in the SRP measurement and the scaling of the profile to 30 µm. For the collection electrode and the p-well implant, the vertical extent of the doping profiles are taken from process simulations performed by the foundry. The lateral diffusion of these profiles is not known and is therefore accounted for by varying the nominal diffusion value by a factor of three in both directions.

The uncertainty is determined by varying the lateral diffusion at the p-well and at the collection electrode as well as the vertical diffusion of the substrate individually and repeating the simulation. As an example, the cluster column size distributions for the nominal diffusion and the varied values is depicted in Fig. 11.2. The diffusion of the collection electrode implant in Fig 11.2a has an impact on the electric field configuration and thus on the charge sharing. The effective size of the collection electrode is larger for the higher diffusion, which gives rise to an increased electric field and consequently a smaller cluster size. Similar effects can be observed for different diffusions of the p-well implant, as displayed in the centre of the same figure. For higher diffusion values, the effective distance between collection electrode and p-well implant is decreased leading to a smaller lateral electric field, which promotes charge sharing and consequently a larger cluster size. Lastly, a higher diffusion of the substrate doping reduces the sensitive volume of the sensor, resulting in a smaller signal and therefore a smaller cluster size, as illustrated in Fig 11.2c.

The mean cluster size as well as the mean size in column and row direction are presented in Table 11.1 for the varied diffusion values. The different sources of uncertainty are assumed to be uncorrelated and for each observable, the residuals between the simulations with nominal values and the ones with varied doping profiles are determined and then summed quadratically to determine the systematic uncertainty.

11.1.4 Comparison to Test-Beam Data

In the following, different observables from the test-beam measurements and the simulation are compared for sensors in the standard configuration at the minimum operation threshold of approximately 150 e, as well as in a threshold scan applying charge thresholds between approximately 100 e and 2000 e. The comparison for other pixel flavours is qualitatively the same and is therefore not shown in this thesis, but can be found in other publications by the author [210, 211]. While the experimental results were already discussed in Chapter 9, this section focuses on the comparison between data and simulation.

Charge Sharing

The cluster size is strongly influenced by charge sharing between neighbouring pixel cells. It is therefore well-suited to study the electric field especially around the pixel edges and in the corners.

Fig. 11.3 compares the total cluster size distribution observed in data and simula-

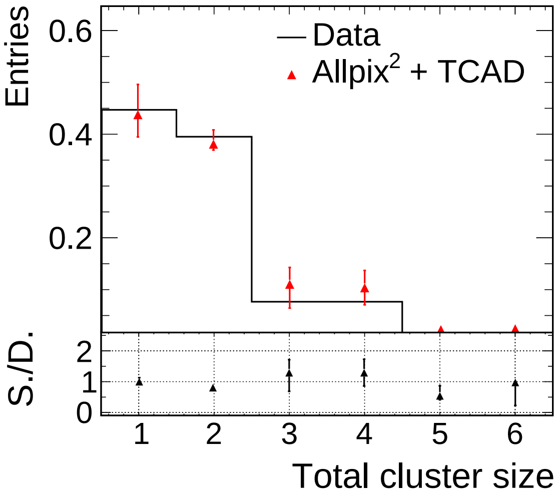

Figure 11.3. Cluster size distributions of the total cluster size for data and simulation in the standard configuration.

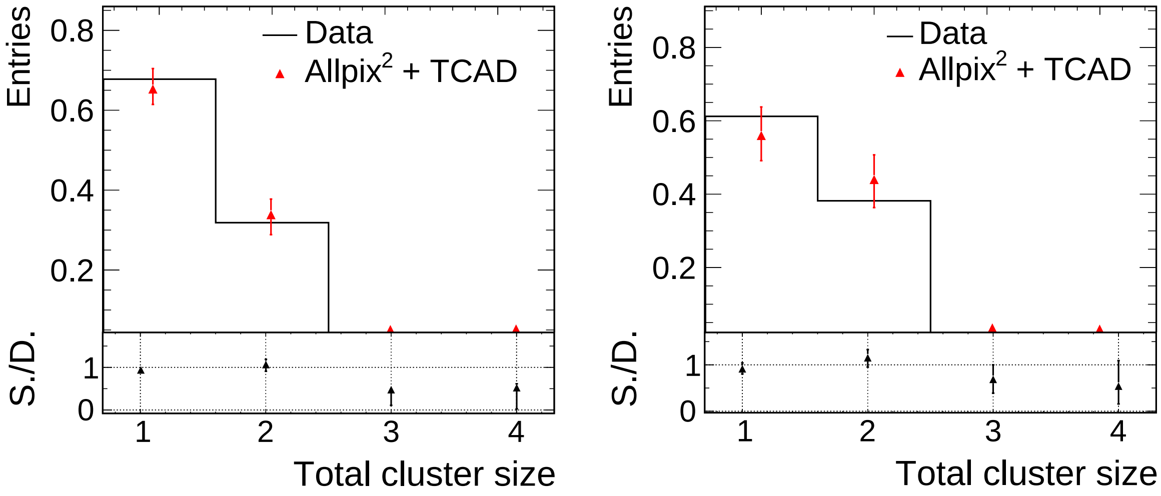

(a) Cluster size in column direction

(b) Cluster size in row direction

Figure 11.4. Cluster size distributions of the size in (a) column and (b) row direction for data and simulation in the standard configuration.

Table 11.2. Mean cluster size and spatial resolution in row direction for data and simulation for the standard configuration.

Parameter	**Data**	**Simulation**
Total cluster size	1.94 ± 0.01	$2.00^{+0.05}_{-0.12}$
Cluster column size	1.36 ± 0.01	$1.37^{+0.03}_{-0.04}$
Cluster row size	1.44 ± 0.01	$1.49^{+0.06}_{-0.07}$
Spatial resolution (row)	$4.4 \pm 0.2\,\mu\text{m}$	$4.3^{+0.43}_{-0.04}\,\mu\text{m}$

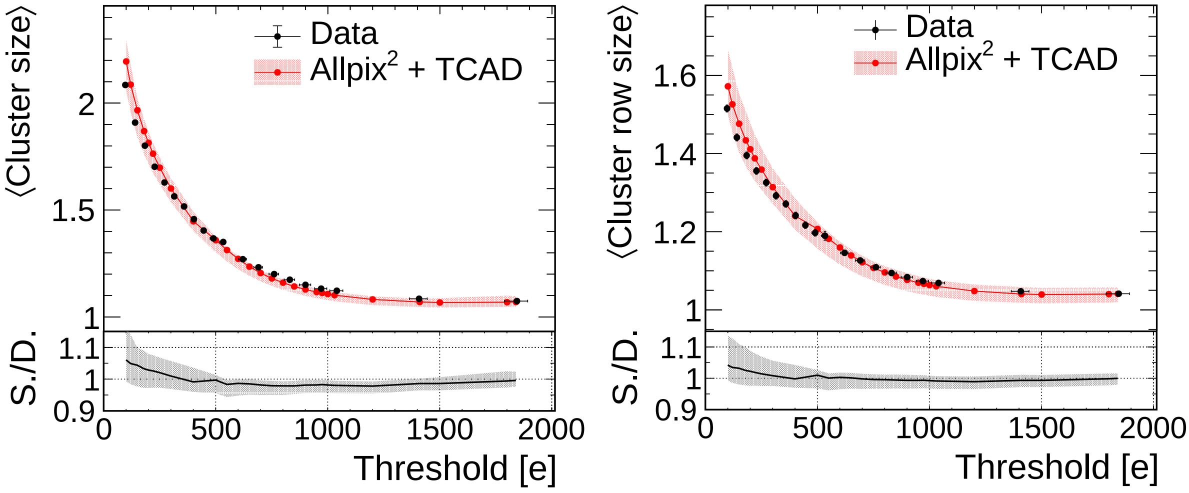

(a) Total cluster size

(b) Cluster size in row direction

Figure 11.5. (a) Total cluster size and cluster size in (b) row direction as a function of the detection threshold for data and simulation in the standard configuration.

tion operated at the minimum operation threshold in the standard configuration. The projections on the column and row dimensions are shown in Fig. 11.4a and Fig. 11.4b, respectively. The indicated uncertainties correspond to the contributions from the diffusion of the doping profiles.

The overall shape of the size distribution is well captured both for the total cluster size as well as the projections, and the differences between data and simulation are within the systematic uncertainties that dominate over the statistical ones. It can be observed that the uncertainties on cluster size in the row direction obtained from simulation are larger than in the column direction. This is a direct effect of the shorter pixel pitch in that direction and the resulting stronger effect of the lateral electric field components in the edge region on the charge sharing behaviour. The results are summarised in Table 11.2. The statistical uncertainty is of the order of 10^{-4} for both data and simulation.

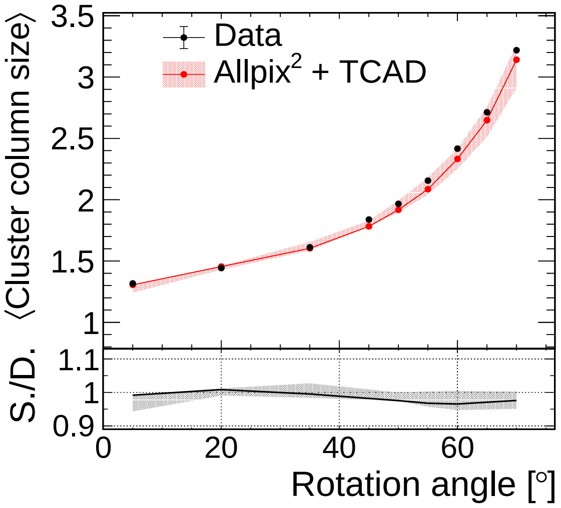

Figure 11.6. Mean cluster column size as a function of the rotation angle for data and simulation in the standard configuration.

Threshold scan With increasing threshold the cluster size decreases, as more and more pixels fall below the detection threshold. Fig. 11.5a demonstrates this effect both for data and simulation, and it can be observed that the agreement between the two curves is well within the uncertainty over the full threshold range. The same holds true for the projected cluster sizes as a function of the detection threshold, shown e.g. for the row direction in Fig. 11.5b. The maximum deviation is of the order of 5 % for very low detection thresholds and is covered by the systematic uncertainties. This agreement over a wide range indicates that both the electric field and the charge propagation model replicate the physical situation in the sensor sufficiently well.

Rotation scan The agreement in charge sharing can be further probed by performing incident angle studies, in which the sensor is rotated relative to the particle beam and therefore the total path length traversed in silicon by a charged particle is changed. With increasing rotation angles, the cluster size increases and charge carriers are created in different depths of the sensor in the pixels along the cluster. Owing to the different electric field strength in the sensor regions as well as the different dominant effects of charge collection via diffusion or drift, the size of the resulting clusters is very sensitive to a correct modelling of the signal formation.

For these measurements, the sensor was rotated around its vertical axis along a pixel column, and correspondingly an increase of the cluster column size is expected. This is demonstrated in Fig. 11.6, where the mean cluster column size is shown as a function of rotation angle.

While the agreement is excellent for low rotation angles, a slightly higher deviation can

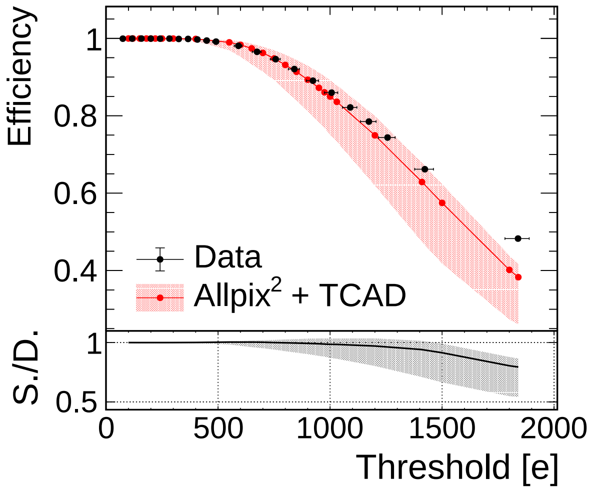

Figure 11.7. Detection efficiency as a function of the applied threshold for data and simulation in the standard configuration.

be observed towards larger rotation angles that is however still covered by the systematic uncertainty. Here, additional signal contributions from the upper part of the substrate and the transition region between substrate and epitaxial layer have a significant impact on the cluster size, and the increasing difference can be attributed to the simplified modelling of this transition region. The systematic deviation towards larger cluster sizes in data indicates that a lower substrate diffusion in the simulation better describes the sensor under these operating conditions.

Hit-Detection Efficiency

A comparison of the hit-detection efficiency as a function of the detection threshold in data and simulation is shown in Fig. 11.7. While data indicates a larger detection efficiency than predicted by simulation for very high thresholds, the efficiency is adequately reproduced for low detection thresholds. The distribution of the efficiency throughout the pixel cell at a threshold of approximately 1850 e is presented in Fig. 11.8a and Fig. 11.8b for data and simulation, respectively. The simulated efficiency drops more rapidly from the centre of the pixel cell towards the edges than observed in the data - an indication that diffusion effects at the pixel implants are not modelled correctly. This is in agreement with the findings from the previous section.

Spatial Resolution

The spatial resolution is calculated from the width of the residual distribution between reconstructed cluster position and the track position or the Monte Carlo particle position, for data and simulation, respectively. The width is defined as the reduced RMS of the

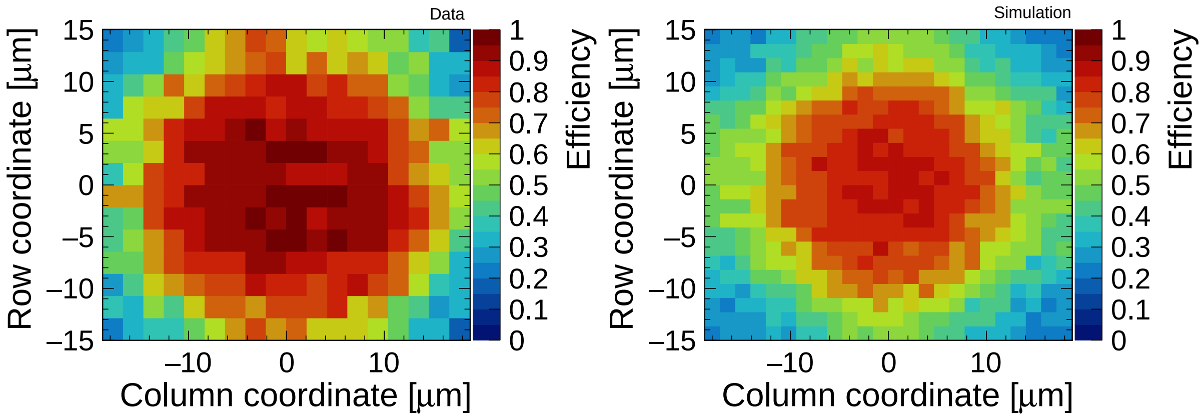

(a) In-pixel efficiency – Data

(b) In-pixel efficiency – Simulation

Figure 11.8. In-pixel distribution of the detection efficiency as a function of the particle incidence position for data (a) and simulation (b) at a detection threshold of approximately 1850 e for a sensor in the standard configuration.

central 3σ (99.7 %) of the distribution. The track resolution is subtracted quadratically from the width, to obtain the intrinsic sensor resolution

The residuals between the reconstructed cluster position and the particle incident position on the sensor are shown in Fig. 11.9 for the row direction. The width evaluates to 5.3 µm for data and 5.2 µm for simulation. The telescope track resolution of 2.8 ± 0.1 µm is quadratically subtracted from the RMS, yielding a spatial resolution of 4.4 ± 0.2 µm in data and $4.3^{+0.43}_{-0.04}$ µm in simulation, which is in excellent agreement.

Threshold scan The spatial resolution in the row direction is presented in Fig. 11.10 as a function of the detection threshold for data and simulation. The degradation of the spatial resolution with increasing threshold as well as the artificial improvement at very high thresholds (cf. Section 9.4) are faithfully reproduced in the simulation. The maximum deviation is approximately 5 % and still within the uncertainty band.

Conclusion

The combined electrostatic finite-element and transient Monte Carlo simulations exhibit excellent agreement with transient 3D TCAD as well as test-beam data over a wide parameter range. The limiting factors in the simulation precision are found to pertain to the available information on the doping profiles. The good agreement confirms that the simulations can be applied to interpret and complement the experimental results, as presented in the next section.

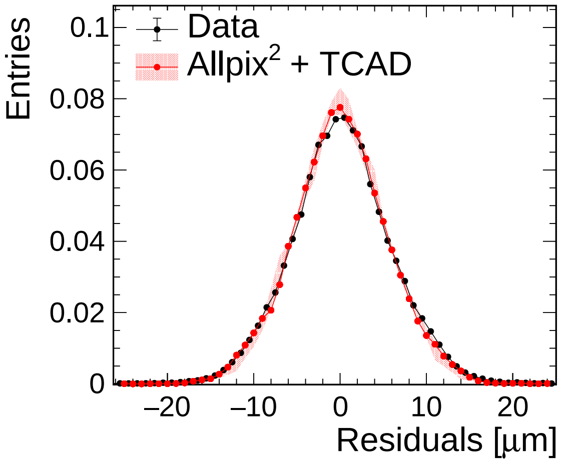

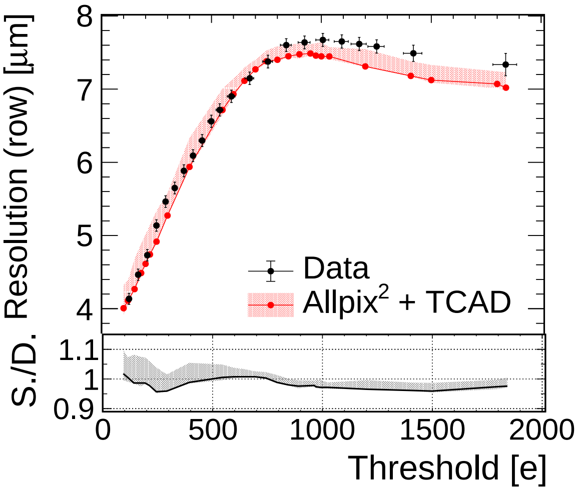

Figure 11.9. Distribution of the spatial residuals between cluster and track position for data and simulation in the standard configuration. The telescope resolution is not subtracted.

Figure 11.10. Spatial resolution as a function of the detection threshold for data and simulation in the standard configuration. The telescope resolution is subtracted

11.2 Application of the Simulation

With the simulations validated against data, they can be applied to optimise sensor designs, interpret measurement results or enrich data by providing additional insight into the sensor response. In this section, various applications of the simulations are presented to showcase their predictive and explanatory power. First, stand-alone 3D TCAD simulations are used to investigate the sensor capacitance and the depletion depth in order to gain a more profound understanding of the measurement results from Chapter 6 and Chapter 9. Next, the advantages of the combined 3D TCAD and Monte Carlo simulations are presented by investigating transient pulses using high-statistics simulation samples. These simulations are then employed to validate the geometrical model used to extract the active depth in Section 9.7. In addition, systematic uncertainties in the X-ray calibration measurement are studied and the sensor time resolution is investigated.

11.2.1 Sensor Capacitance

A low sensor capacitance is beneficial to obtain a high signal-to-noise ratio (cf. Section 2.6.2). Sensor variants or operation characteristics that lead to an increased capacitance are penalised with a reduced signal gain and consequently a high minimum operation threshold (cf. Section 6.2), which is detrimental for all figures of merit. The minimisation of the sensor capacitance is therefore of utmost importance to maximise the sensor performance. In the small collection-electrode design, the capacitance is closely

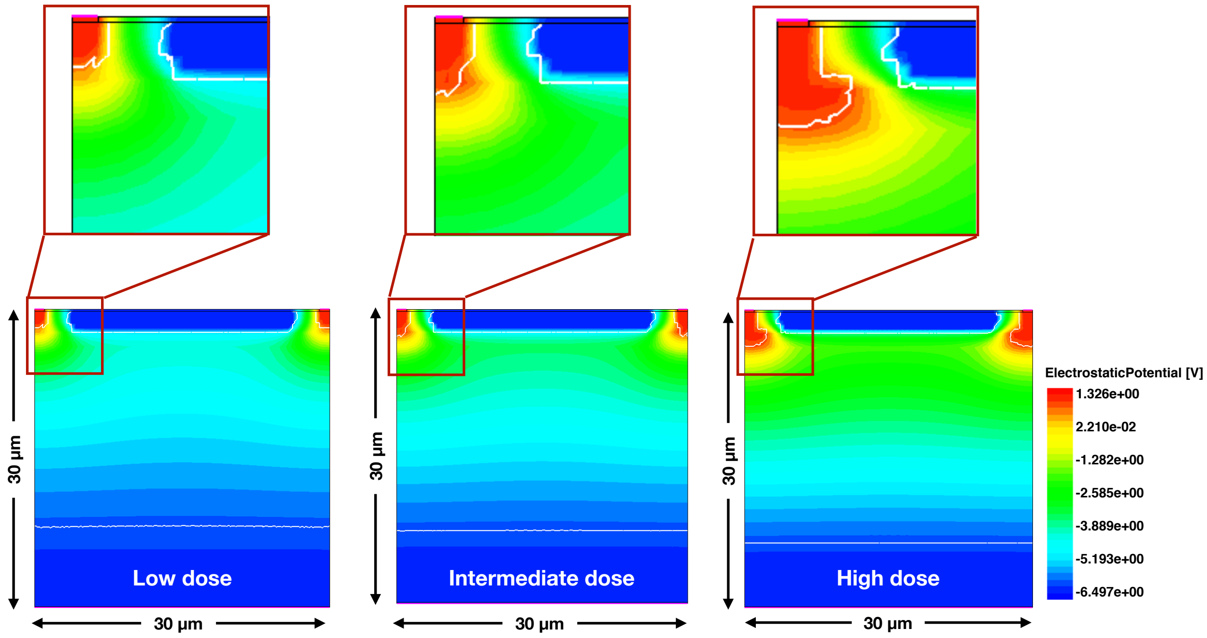

Figure 11.11. Two-dimensional cross section of the electrostatic potential for three different doping levels of the deep n-type implant. The edge of the depleted volume is shown as a white line. The collection electrodes are at the edges of the structure and the p-wells are in the centre.

related to the size of the collection electrode. While the physical size of the electrode is the same for all investigated CLICTD samples, the depletion region around it can be different, which affects the *effective* size of the electrode and thus the sensor capacitance. The phenomenon is visualised in the cross-sections of the simulated electrostatic field map in Fig 11.11. Three different doping levels of the deep n-implant were used that correspond to the three expected concentrations in the real devices. The white lines mark the borders of the depleted volume.

Whereas the region around the collection electrode is fully depleted for the structure with the low n-implant dose, the depleted volume for the high n-implant dose does not evolve all the way to the collection electrode, leading to an increase in sensor capacitance. In case of the intermediate dose, the undepleted area around the electrode is only slightly enlarged. The different evolution of the depletion region is caused by the effective doping levels in the n-implant, as predicted by Eq. 2.16 [1].

A similar effect is visible for lower absolute p-well bias voltage, as illustrated in Fig. 11.12. The area around the collection electrode is not fully depleted leading to a higher sensor capacitance.

The increase in capacitance is quantified in Fig. 11.13, where the capacitance is de-

---

[1] The formula for the depleted volume was derived for a simple plate capacitor and is therefore not able to capture the complex fields of the small collection-electrode design. However, it still gives an qualitative description of the underlying processes.

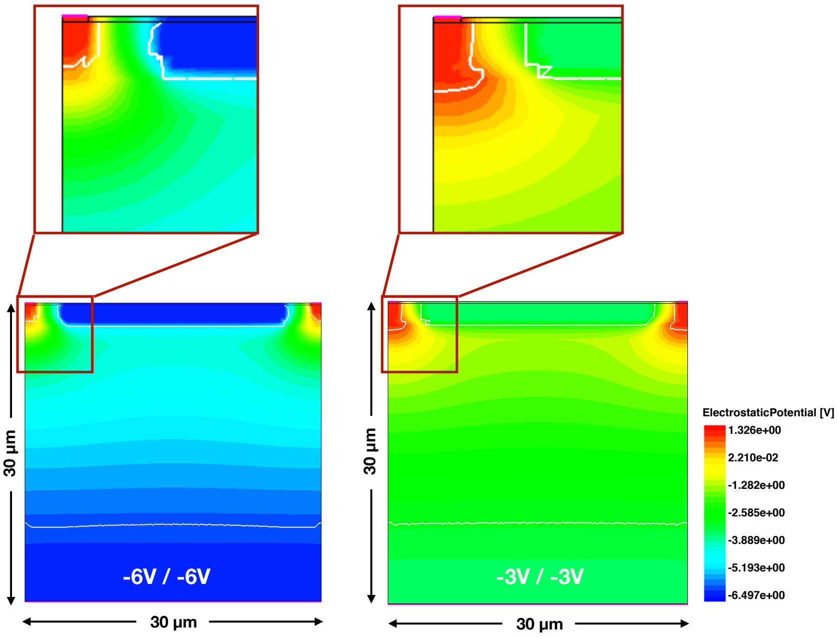

Figure 11.12. Two-dimensional cross section of the electrostatic potential for different bias voltages at the p-wells/substrate for sensors with epitaxial layer. The white line marks the edge of the depleted volume.

picted as a function of the p-well voltage for the three different doping concentrations. At a bias voltage of -6 V, the capacitance is approximately 30 % higher for the intermediate dose compared to the low dose and approximately twice as large for the high dose. Similarly, the increase in capacitance at lower absolute bias voltages evaluates to approximately 60 % between -6 V and -3 V for the low doping concentration of the n-type implant, which agrees well with the change in signal gain presented in Section 6.2.1. This result underlines the importance of a high absolute bias voltage at the p-well in this sensor design.

11.2.2 Depletion Depth for Sensors with Epitaxial Layer

The depletion depth for sensors with epitaxial layer is estimated using the simulations shown in Fig. 11.11. For the sensor in standard configuration, the depletion depth evaluates to 21 ± 1µm. The uncertainty accounts for different measurement lines, since the depletion depth is slightly lower if the measurement is performed from the p-well to the edge of the depleted volume instead of the sensor surface between p-well and collection electrode. The depth is limited by the thickness of the epitaxial layer or more specifically the extent of the transition region to the low-resistivity substrate. Therefore, the depletion depth is independent of the different n-type implants and even the bias voltage at the p-wells and substrate, as illustrated in Fig. 11.12. The depletion depth of the sensors

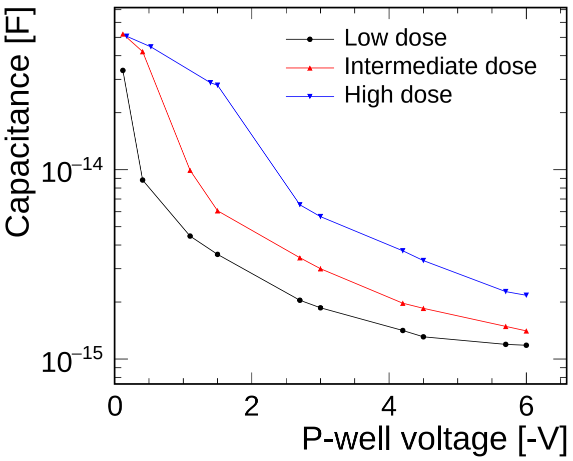

Figure 11.13. Simulated sensor capacitance as a function of the p-well bias voltage for the three different doping levels of the deep n-implant.

fabricated on high-resistivity Czochralski wafers, on the other hand, depends strongly on the bias voltage, as presented in the next section.

11.2.3 Depletion Depth for Sensors on Czochralski Wafers

Estimation of Doping Levels No information about the substrate doping concentration of the high-resistivity Czochralski wafers were available at the time they were measured in the laboratory and test beam. This lack of knowledge poses a problem for simulation studies since the outcome is highly sensitive to the doping levels in the sensor. Since excellent agreement between data and simulation was already demonstrated when a decent modelling of doping profiles is available, the simulation is used to extract the unknown observable from data. Once a good agreement is established between data and simulation for a specific doping concentration, it is assumed that the given concentration is a good estimate for subsequent studies.

To this end, the cluster size in the simulated test-beam scenario is determined, as presented in Fig. 11.14 for a sensor on a high-resistivity Czochralski wafer, segmented n-implant and bias voltage of -6 V/-6 V. The measured curve is plotted as well to compare it against three example simulations with different doping levels. With higher doping levels, the depletion depth increases in accordance with Eq. 2.16. As a consequence, more charge carriers contribute to the signal leading to a larger cluster size.

The simulation with a doping level of 4.4 kΩ cm exhibits the best agreement with data and is thus used in the following to estimate the depletion depth for different substrate bias voltages. It should be noted that this study aims to investigate the depletion depth on a qualitative level. For a quantitative study, a more precise determination of the

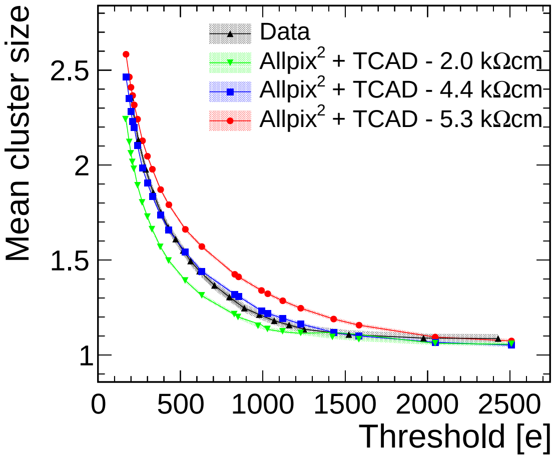

Figure 11.14. Cluster size as a function of detection threshold for data and simulations assuming different doping levels of the Czochralski wafer material.

doping levels would be required.

Depletion Depth The high-resistivity Czochralski samples yield the best measurement results for all performance parameters investigated in this thesis. The superiority of these samples was attributed to the larger signal that results from an increased active depth (cf. Section 9.7), resulting from a larger depletion region that extends deeper into the sensor volume, compared to the sensors with epitaxial layer. To quantify the increase in depleted volume, electrostatic 3D TCAD simulations showing the potential and depleted volume for high-resistivity Czochralski samples are displayed in Fig. 11.15. A bias voltage of -6 V is applied to the p-wells of both sensors. For the left sensor, the substrate bias voltage is fixed at -6 V, resulting in a depletion depth of 34.5 ± 1µm, which is more than 10 µm larger compared to sensors with epitaxial layer and the same bias configuration. If the substrate bias voltage is increased to -16 V, the depletion depth evolves further into the silicon bulk and reaches 71.5 ± 1µm.

The depletion depth as a function of the substrate bias voltage is presented in Fig. 11.16. The p-well voltage is fixed to -6 V and the band around the curve represents different measurement lines. The depletion depth increases non-linearly with increasing substrate voltage and resembles the trend observed for the active depth in Fig. 9.49. This trend qualitatively agrees with Eq. 2.16, which predicts an increase in the depletion region with the square root of the applied bias voltage.

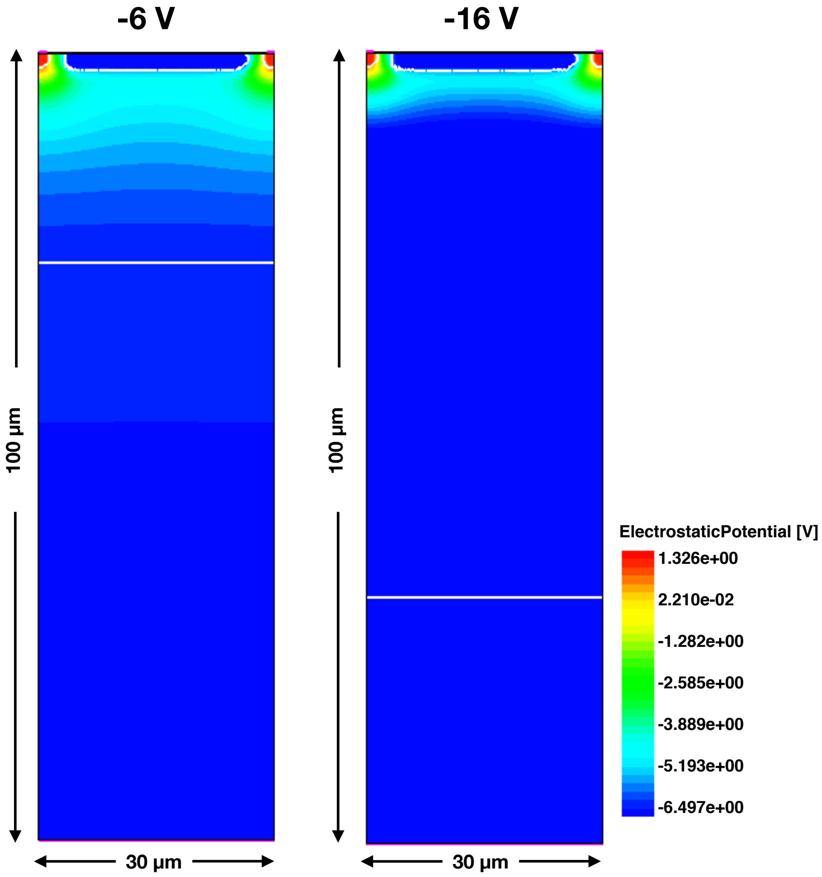
-6 V
-16 V
100 µm
100 µm
30 µm
30 µm
ElectrostaticPotential [V]
1.326e+00
2.210e-02
-1.282e+00
-2.585e+00
-3.889e+00
-5.193e+00
-6.497e+00

Figure 11.15. Electrostatic potential for high-resistivity Czochralski samples. The white line marks the edge of the depleted volume. The substrate bias voltage is at (a) -6 V and (b) -16 V and the p-well voltage is -6 V in both cases.

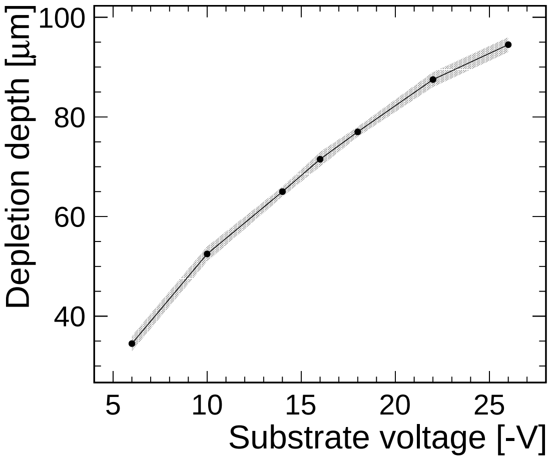

Figure 11.16. Simulated depletion depth as a function of substrate voltage. The p-well bias voltage is fixed to -6 V. The band represents different measurement lines.

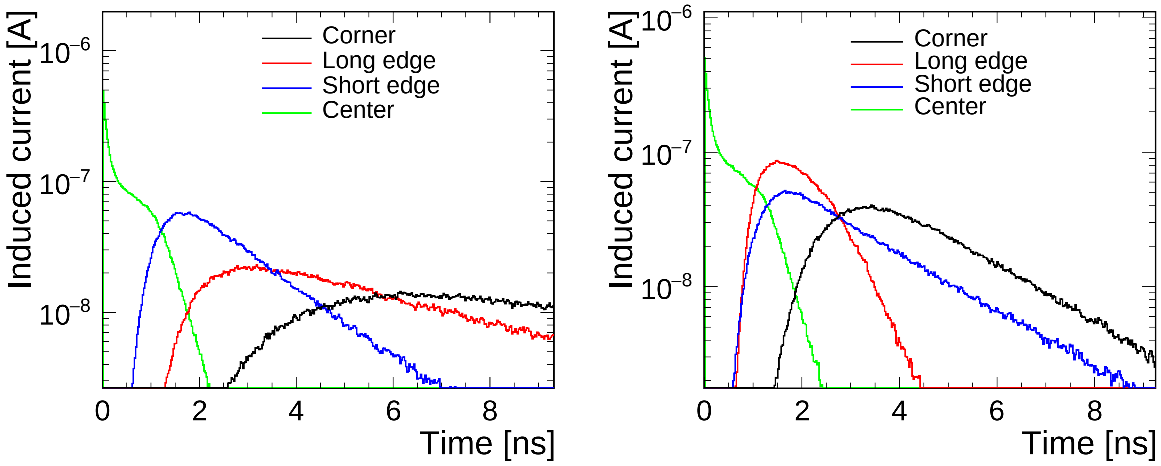

(a) Continuous n-implant **(b)** Segmented n-implant

Figure 11.17. Transient current pulses for different charge injection positions for (a) the flavour with continuous n-implant and (b) the flavour with segmented n-implant. In the CLICTD pixel geometry, the segmentation is only applied at the long pixel edge.

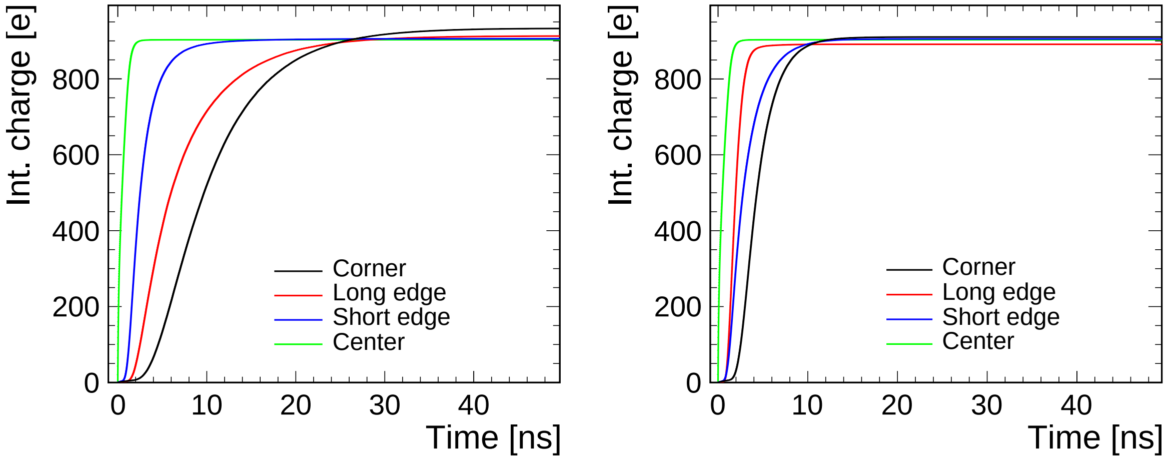

(a) Continuous n-implant **(b)** Segmented n-implant

Figure 11.18. Integrated induced charge for different charge injection positions for (a) the flavour with continuous n-implant and (b) the flavour with segmented n-implant. In the CLICTD pixel geometry, the segmentation is only applied at the long pixel edge.

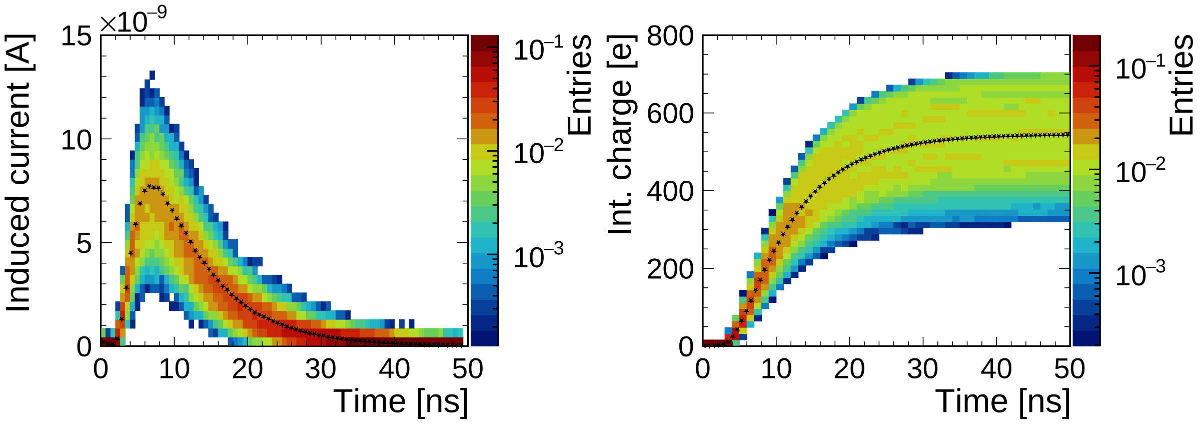

(a) Transient sensor response **(b)** Integrated charge

Figure 11.19. (a) Transient pulse distribution and (b) integrated charge for the pixel design with continuous n-implant, obtained from a full Monte Carlo simulation including secondary particles and energy deposition fluctuations. The black stars represent the average pulse height and integrated charge per bin, respectively.

11.2.4 Transient Current Pulses

In the previous sections, the capabilities of stand-alone 3D TCAD simulations were presented to study the electromagnetic properties of the sensors. Combining these simulations with Allpix^2 allows for the generation of high-statistics simulation samples, from which the sensor response can be studied for different charge injections positions over the pixel cell. In Fig. 11.17 the transient pulses for four different positions are depicted using two different pixel flavours and the CLICTD pixel geometry. As expected, charge injection in the pixel centre leads to the fastest response due to the close vicinity of charge carriers to the collection electrode. The pulses for injection at the long pixel edge are distinctly different for the two pixel flavours due to the altered field configuration. The segmentation gives rise to a higher lateral electric field and consequently an accelerated charge collection leading to a current pulse that peaks around 2 ns, in contrast to the flavour with continuous n-implant, that exhibits a heavy tail extending to tens of nanoseconds. In addition, the transient pulse for injection in the pixel corner, which represents the worst case scenario in terms of sensor time performance, is improved for the flavour with segmented n-implant.

Similar effects are visible in the integrated induced charge for the different injection positions in Fig. 11.18. While charge carriers injected in the pixel centre are collected after about 1 ns, the charge collection at the pixel corner requires approximately 30 ns for the flavour with continuous n-implant and 15 ns for the one with segmented n-implant.

In addition, the time resolution is affected by variations of charge carrier collection times and consequently by the spread between the curves in Fig. 11.18. The larger variation for the flavour with continuous n-implant indicates a worse sensor time resolution compared to the more homogenous response of the flavour with segmented n-implant.

Statistical fluctuations of the charge deposition as well as the generation of secondary particles such as δ-rays can also be taken into account with reasonable statistics in the MC simulation. In Allpix^2 this can be achieved by switching the charge deposition stage of the simulation to the `DepositionGeant4` module (cf. Section 10.2.1)

The transient pulse distribution for particles incident on the pixel corners is displayed in Fig. 11.19a and their integrated induced current in Fig. 11.19b. Here, the black stars indicate the average pulse height value and integrated charge in the respective time bin. The pulse-by-pulse variations underline the importance of including statistical effects in the simulation setup.

11.2.5 Charge Carrier Recombination

For sensors with epitaxial layer, the active depth measurements in Section 9.7 yielded a value of approximately 30 µm, which corresponds to the nominal thickness of the epitaxial layer. Consequently, charge carriers created below the depleted volume still contribute to the measured signal, since the the depletion depth evaluates to only 21 ± 1µm. However, these results also imply that charge carriers created in the low-resistivity bulk have no sizeable contribution to the signal, which is expected to result from the high charge carrier recombination rate in the substrate. Simulation studies using the recombination models from Section 2.5 are used to investigate this assumption in more detail.

A two-dimensional map of the recombination rate for a sensor in the standard configuration is depicted in Fig. 11.20. The figure shows a cross-section in the yz-plane, where z goes along the sensor depth. The collection electrode is located at the central position in the y-direction and the p-wells are at the edges. No recombinations are registered inside the p-wells, since electrons in the upper part of the structure drift towards the collection electrode, making propagation into the p-wells unlikely. The high recombination rate at the collection electrode has no physical significance, since charge carriers are considered to be *collected* when they arrive at the electrode.

As expected, the recombination rate in the epitaxial layer is very low, since the lifetime of charge carriers is of the order of milliseconds [212]. In the transition region between epitaxial layer and low-resistivity substrate (approx. 20 - 25 µm on the z-axis), the recombination rate increases drastically. In this region, Auger recombination starts to dominate over SRH recombination due to the high doping concentration (cf. Section 2.5)

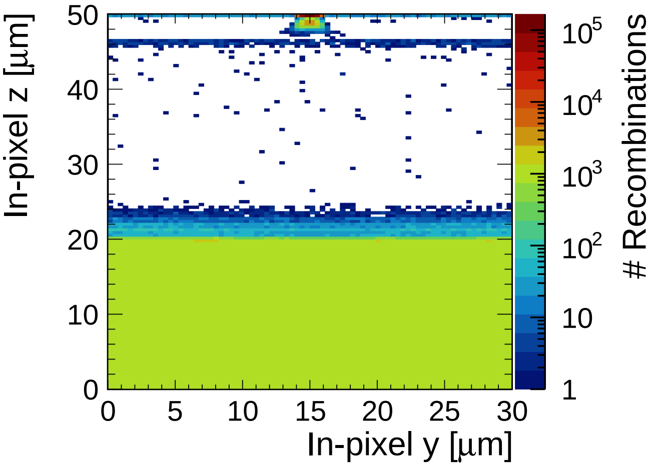

Figure 11.20. Two-dimensional map of the recombination rate for a cross section of the yz plane through the sensor volume. The nominal thickness of the epitaxial layer is 30 µm and thus extends from $z = 50$ µm to $z = 20$ µm.

Table 11.3. Estimation of active depth for different detection thresholds. The results are obtained for simulations using a sensor in the standard configuration and the nominal diffusion values.

Threshold [e]	**Active depth** [µm]
140	26.7 ± 0.1 (stat.)$^{+0.4}_{-0.2}$ (syst.)
180	26.7 ± 0.1 (stat.)$^{+0.2}_{-0.2}$ (syst.)
300	26.5 ± 0.1 (stat.)$^{+0.2}_{-0.1}$ (syst.)

and the lifetime of charge carriers is of the order of tens of nanoseconds. The high recombination rate prevents them from contributing to the signal, which renders the low-resistivity substrate inactive.

11.2.6 Active Depth Model

In Section 9.7, the active depth was estimated using a simple geometrical model based on the incident particle angle and the cluster size. Two fundamental effects are not considered in the model: First, the detection threshold is not accounted for, which could give rise to potential sub-threshold effects in the cluster size. Second, charge sharing by diffusion is not inherent in the model, which could bias the results. To exclude the introduction of systematic effects, it is imperative to study the impact of both effects on the estimated active depth using simulations.

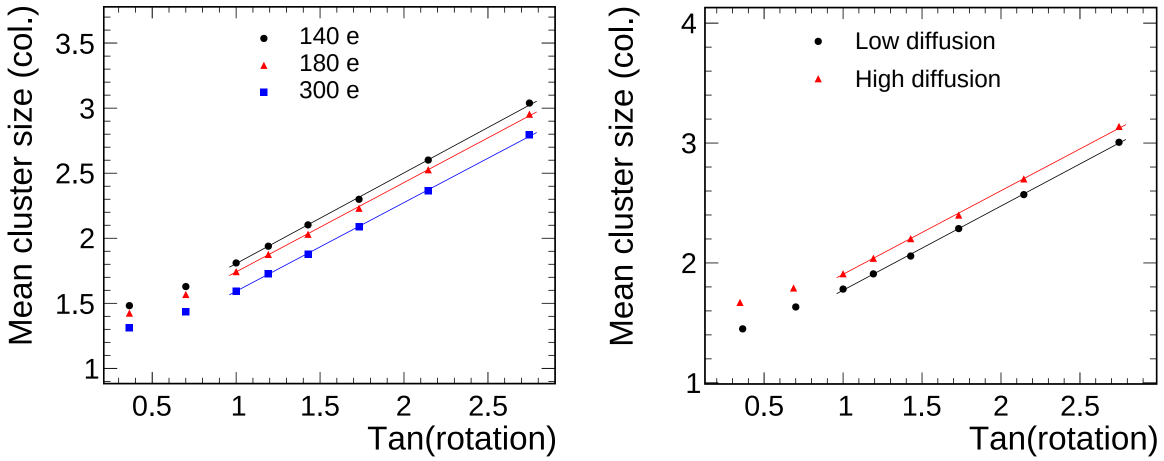

(a) Different thresholds

(b) Different lateral diffusion at the p-well implants.

Figure 11.21. Mean cluster column size as a function of the tangent of the rotation angle for (a) different thresholds and (b) different lateral diffusions at the p-well implant. The solid lines are linear fits to the simulated points.

Detection Threshold The active depth studies are replicated in simulation and the impact of the detection threshold on the active depth estimation is investigated by applying different thresholds to the simulation and repeating the analysis. The mean cluster size as a function of the rotation angle for three different thresholds is displayed in Fig. 11.21a. While lower thresholds lead to an offset of the curve owing to an overall larger cluster size, the slope of the curve remains unaltered. The fit results in Table 11.3 confirm the invariance of the slope within the uncertainties. The influence of the detection threshold on the estimated active depth is therefore considered to be negligible. It should be noted that the systematic uncertainties only cover the ones related to the active depth model and not the doping-dependent uncertainties, since no direct comparison to data is needed.

Charge Sharing by Diffusion of Charge Carriers To investigate the sensitivity of the active depth model to charge sharing by diffusion of charge carriers, the simulations are repeated for different lateral diffusions at the p-well implants. Differences in the doping diffusion lead to alterations in the charge sharing behaviour and are therefore an appropriate check for the robustness of the model. The corresponding distributions with linear fits are displayed in Fig. 11.21b and the fit results are listed in Table 11.4. The active depth values are compatible within their uncertainties, which implies that moderate differences in the charge sharing leave the results unchanged.

Table 11.4. Estimation of active depth for different lateral diffusions at the p-well implants. The results are obtained for simulations using a sensor in the standard configuration and the nominal diffusion values for the other implants. The threshold is fixed to 140 e.

Diffusion at p-well implants	**Active depth** [µm]
Low	26.7 ± 0.1 (stat.)$^{+0.4}_{-0.2}$ (syst.)
High	27.1 ± 0.1 (stat.)$^{+0.3}_{-0.3}$ (syst.)

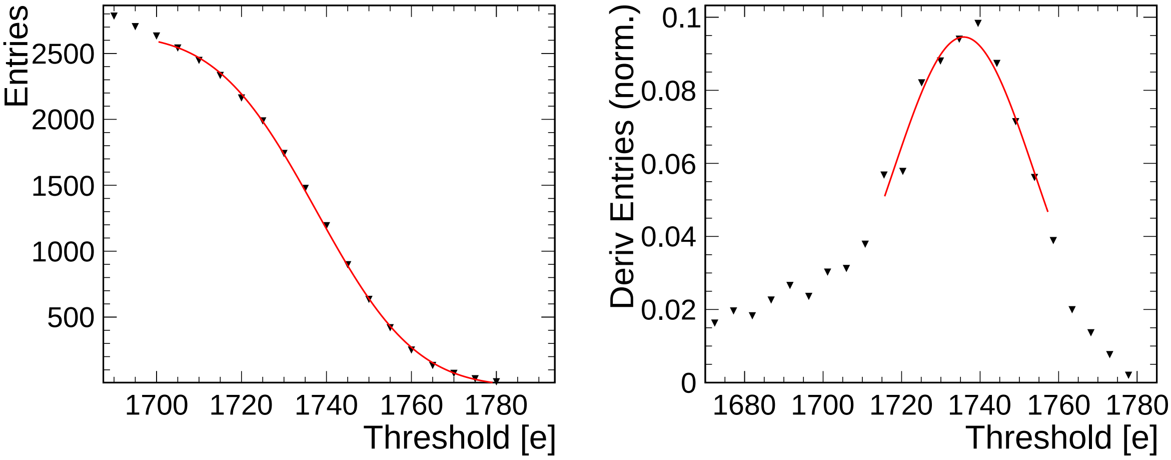

(a) Pixel hits as a function of the detection threshold

(b) Derivative of the number of pixel hits as a function of the detection threshold

Figure 11.22. Simulation of the threshold-calibration procedure.

11.2.7 Systematic Uncertainties in X-ray Measurement

The X-ray calibration measurements presented in Section 6.2 are replicated in simulation to investigate systematic uncertainties in the analysis. The Allpix^2 module `DepositionGeant4` is used to simulate a monochromatic X-ray beam with a mean energy of 6.4 keV in accordance with the values for iron fluorescence in Table 5.2.

The threshold is varied in the simulation and the number of pixel hits recorded, as illustrated in Fig. 11.22a for the standard configuration. The red line marks the S-curve fit with Eq. 5.1 and the fit result are listed in Table 11.5. The derivative of the distribution

Table 11.5. X-ray energies using an S-curve and a Gaussian fit. The theoretical value was calculated in Section 5.5.2.

Theoretical value [e]	**S-curve fit** [e]	**Gaussian fit** [e]
1749	1731 ± 3	1732 ± 2

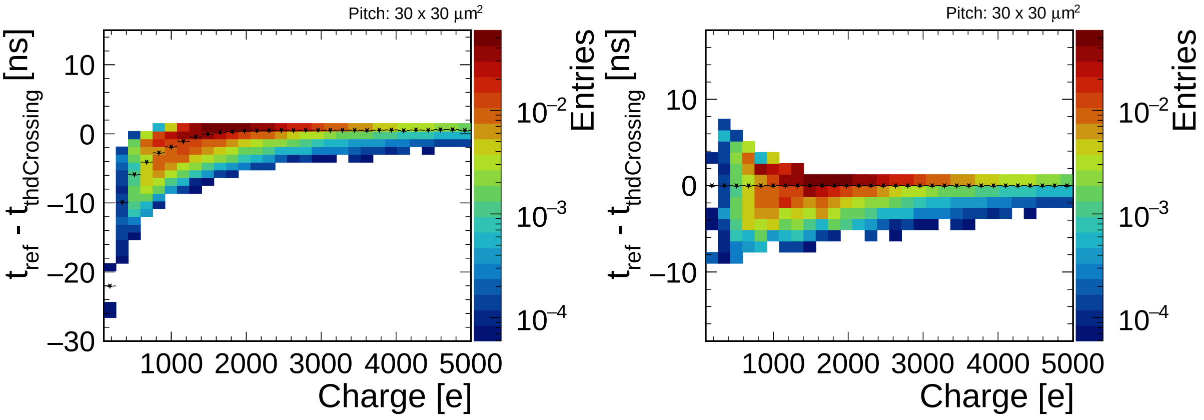

(a) Time residuals before correction

(b) Time residuals after correction

Figure 11.23. Time residuals as a function of the highest single pixel charge in a cluster before (a) and after (b) correction of the charge-dependent threshold crossing time. The black stars denote the mean of each charge bin.

in Fig. 11.22b exhibits the characteristic K_α peak, that is fitted with a Gaussian to cross check the results. While the estimated mean from the Gaussian and the S-curve fit agree within their respective uncertainties, a deviation of approximately 20 e to the theoretical value is observable that is related to charge loss owing to charge carrier recombination.

To account for this difference in the energy calibration, the deviation is propagated to the measured calibration parameters and the detection threshold in electrons (cf. Section 5.5.2). At the minimum threshold, the difference amounts to $1 - 2\,\mathrm{e}$ and is therefore much smaller than the threshold DAC step, which is of the order of 10 e. The deviation is used as systematic uncertainty instead of modifying the nominal value in order to comply with the threshold calibration procedure used in other sensors (e.g. [122, 133, 213]) and to maintain comparability.

11.2.8 Sensor Time-Resolution Studies

Laboratory and test-beam measurements indicate that the time resolution of CLICTD is dominated by front-end effects instead of the sensor time performance. This assumption is put to the test by using simulations to investigate the sensor time resolution independent from direct contributions of the readout electronics. In this study, the inclusion of all relevant statistical elements of the signal formation is particularly important to provide a realistic prediction about the sensor time resolution. Here, the approach is exemplified by evaluating the time resolution for different pixel pitches and the sensor with continuous n-implant, i.e. the CLICTD pixel geometry is slightly modified to investigate the impact

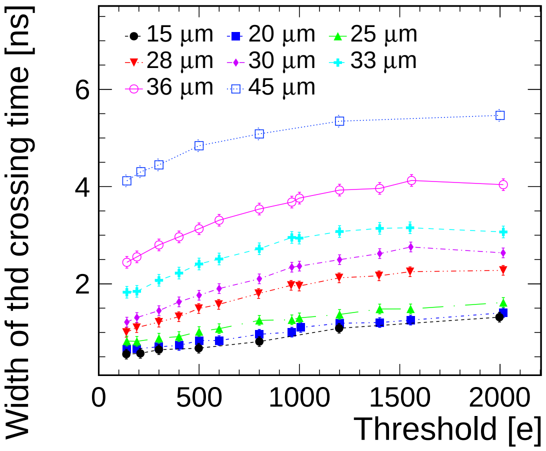

Figure 11.24. Width of the threshold-crossing time as a function of the detection threshold for different pixel pitches.

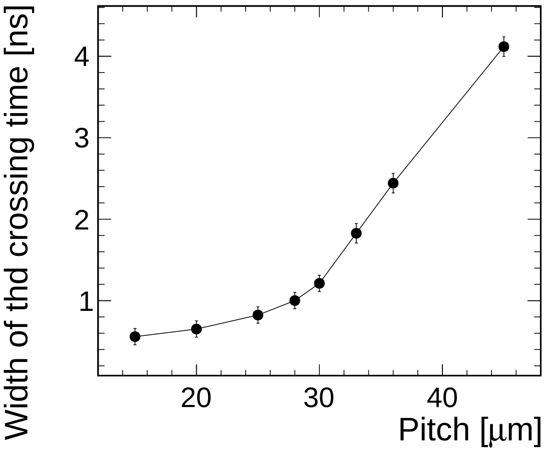

Figure 11.25. Width of the threshold-crossing time as a function of the pixel pitch at a detection threshold of 150 e.

of the pixel pitch. Similar to the functioning of many detector front-ends, the time at which the current pulse crosses the chosen detection threshold (*threshold-crossing time*) is used to compute the time residuals of the sensor.

Fig. 11.23a shows the time residual distribution as a function of the signal charge for a sensor with a pixel pitch of 30 µm × 30 µm. Small transient pulses cross the threshold later, which leads to a tail observable for low signal values. This charge-dependence in threshold crossing time is corrected by subtracting the mean time offset for each charge bin separately, yielding the corrected distribution displayed in Fig. 11.23b. The observed behaviour matches very well the time-walk effect known from measurements (cf. Section 9.5). The simulated time however only comprises the effects related to the signal formation in the sensor such as longer charge collection times in the pixel corners but not the additional contributions from the front-end electronics.

Using this corrected time residual distribution, the time resolution of the sensor can be extracted and the width of the distribution can be compared between different prototype designs. Here, the width of the time residual distribution is quoted as the RMS of the central 3σ. Fig. 11.24 shows the width of the distribution as a function of the applied detection threshold for different pixel pitches. As expected, the time resolution improves for smaller pixel pitches due to a more homogeneous time response across the pixel cell. The improvement starts to converge to about 100 ps, as visualised in Fig. 11.25 for the threshold-crossing time at a detection threshold of 150 e. With increasing detection threshold, a deterioration of the time resolution can be observed, owing to the flattening shape of the signal resulting in a stronger contribution of time jitter.

11.3 Conclusion

The combination of electrostatic finite-element and Monte Carlo simulations profits from a detailed sensor modelling and the simultaneous access to high-statistics simulation samples. Simulations for the small collection-electrode monolithic sensor design were compared to transient finite-element simulations as well as test-beam data and excellent agreement over a wide parameter range was found with deviations mostly below 5 % and still covered by the systematic uncertainties.

Several example applications of the simulations were shown that complement the laboratory and test-beam mismeasurements. For instance, the capacitance was shown to depend critically on the depletion region around the collection electrode and the depletion depth was found to be limited to approximately 20 µm. Moreover, the sensor time resolution was investigated and determined to be a few nanoseconds, which confirms that the time resolution of the CLICTD sensor is limited by the front-end resolution.

The simulations will be used for further development of monolithic CMOS silicon sensor with similar sensor designs, in particular in the stages of sensor optimisation and experimental assessment.

Part II

Anomaly Detection in Belle II Pixel-Detector Data

Chapter 12

The Belle II Experiment

The Belle II experiment is a next-generation flavour factory operating at the intensity frontier of particle physics. The experiment is located at the high-luminosity electron-positron collider SuperKEKB, that is designed for collision energies in the energy region of the Υ resonances.

Belle II is the successor of the Belle experiment [214] that was operational from 1999 to 2010. Results from the Belle experiment such as measurements of CP asymmetries in B decays, discoveries in charm and tau lepton physics or hadron spectroscopy had a crucial impact on our understanding of hadron and particle physics. The success of the Belle experiment motivated the upgrade to Belle II, which also involved an update of the accelerator KEKB to SuperKEKB to further increase luminosity.

The following chapter introduces the Belle II experiment by starting with a brief overview of its physics motivation. Next, the SuperKEKB accelerator is described and lastly the detectors, trigger and data acquisition system of Belle II are outlined.

12.1 Physics Motivation

Belle II has a rich and diverse physics programme, that optimally complements analyses at the LHC, BES III and other collider and non-collider experiments. The general experimental orientation of the Belle II physics programme builds upon the findings from its predecessor Belle.

The well-defined initial state and the clean collision environment allow for measurements with unprecedented precision. Through indirect observations, the mass reach for searches beyond the Standard Model can be as high as $\mathcal{O}(100\,\mathrm{TeV})$ [26].

A few selected highlights of the physics programme are given in the following:

- The measurement of charge-parity (CP) violations are a principal objective at

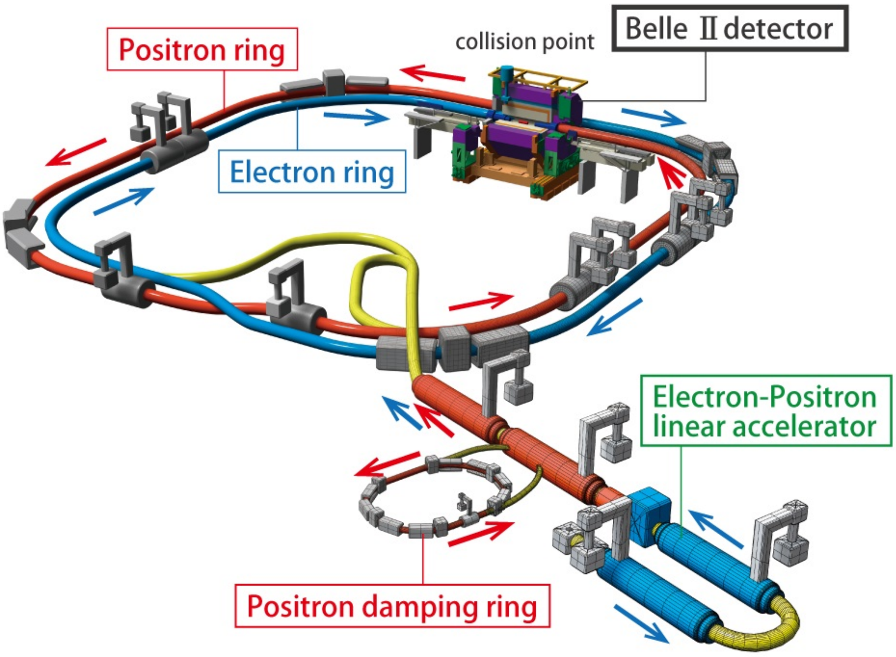

Figure 12.1. Schematic of the SuperKEKB collider. The accelerator complex consists of the linear electron-positron acceleration units, a positron damping ring and the main electron-positron storage rings. The Belle II detector is located the interaction point. From [221]

Belle II. Studies for both direct and indirect CP-violation are targeted, with a particular focus on potential new CP-violating phases in the quark sector [215].

- Lepton Flavour Violation beyond the SM is investigated by analysing decays of τ leptons [216].
- Charmonium spectroscopy in B-decays enables access to a large set of different quantum numbers, complementary to dedicated charm factories such as BES III or BaBar. Most notably, the discovery and investigation of exotic states are a major goal in order to refine our understanding of their nature [217].
- Various direct and indirect searches for dark-matter candidates are performed, involving for instance Axion-like particles (ALPs) [218, 219] or a new massive vector boson Z' [220].

Details about on-going and planned analyses at Belle II are summarised in [26].

12.2 The SuperKEKB Collider

The SuperKEKB is an asymmetric electron-positron collider at the High Energy Accelerator Research Organisation (KEK) [222, 223].

A schematic of the SuperKEKB accelerator complex is displayed in Fig. 12.1. The main storage units are arranged in a double-ring structure, with the High Energy Ring (HER) for electron storage and the Low Energy Ring (LER) for the storage of positrons. Before injection into the main rings, the electrons are accelerated to 7 GeV and the positrons to 4 GeV using linear electron-positron acceleration units. To guarantee a low emittance of the positron beam, the particles are guided through a Positron Damping Ring, where radiation damping is employed to reduce emittance.

The particles are brought to collision at the interaction point, where the Belle II detector is positioned. The default centre-of-mass energy is 10.58 GeV, which corresponds to the rest mass of the $\Upsilon(4S)$ resonance. The asymmetric collision energies are responsible for a boost ($\beta\gamma = 0.28$) in the direction of the electron beam, allowing for an improved identification of displaced vertices of B-mesons.

The commissioning of the accelerator and therefore also of Belle II is divided into three phases. Phase 1 in early 2016 was dedicated to accelerator operations without any particle collisions. Phase 2 in 2018 saw first collisions and even enabled the Belle II detector to take relevant data and Phase 3 is on-going since March 2019.

12.2.1 Luminosity

The ambitious design luminosity of $8 \times 10^{35}\,\mathrm{cm^{-2}\,s^{-1}}$ foreseen for the SuperKEKB accelerator requires advanced acceleration and collision schemes [1]. The luminosity $\mathcal{L}$ can be expressed as [222]

$$\mathcal{L} = \frac{\gamma_\pm}{2er_e}\left(1 + \frac{\sigma_y^*}{\sigma_x^*}\right)\frac{I_\pm \zeta_{y,\pm}}{\beta_{y,\pm}^*}\frac{R_L}{R_{\zeta_y}}. \tag{12.1}$$

The subscripts +/− stand for the electron/positron beam. γ denotes the Lorentz factor, σ_y^*/σ_x^* the beam size aspect ratio, r_e and e the classical electron radius and charge, respectively, I the beam current, ζ_y the beam-beam parameter and β_y^* the vertical β-function. R_L and $R_{\zeta,y}$ are the luminosity and vertical beam-beam reduction factors with a ratio close to one.

Besides an increase in beam currents, the generation of *nano-beams* is the main ingredient to achieve the luminosity objective, whereby the vertical beam size is strongly reduced close to the interaction point, which minimises the β-function.

12.3 The Belle II Detector

The Belle II detector is positioned at the interaction point (IP) of the SuperKEKB collider. Its design is optimised for the physics objectives, experimental conditions and in

---

[1] The instantaneous luminosity is about 30 times larger compared to the predecessor KEKB.

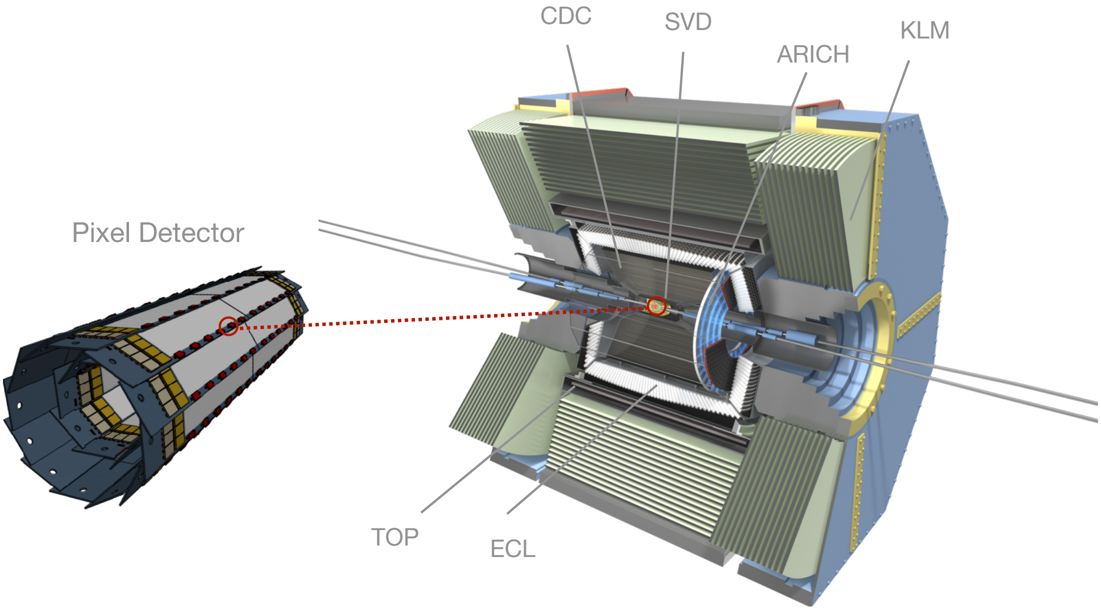

Figure 12.2. Schematic of the Belle II detector. The Pixel Detector (PXD) and the Silicon Vertex Detector (SVD) are the innermost sub-detectors, followed by the Central Drift Chamber (CDC), the Time of Propagation (TOP) detector, the Electromagnetic Calorimeter (ECL) and the K_L-muon (KLM) detector. An Aerogel Ring Imaging Cherenkov (ARICH) detector is positioned in the forward direction. Modified from [224, 225]

particular the high luminosity provided by the SuperKEKB collider.

A schematic of the detector is displayed in Fig. 12.2. The z-axis of the right-handed coordinate system is aligned with the direction of the electron beam. The y-axis is oriented vertically upwards and the x-axis points outside of the ring. Accordingly, ϕ is the azimuthal angle and θ the zenith angle [226]. The acceptance region of the detector covers the full azimuthal angle and a zenith angle of $17° < \theta < 150°$.

Belle II consists of various sub-detectors that are briefly introduced in the following section.

12.3.1 The Vertex Detector (VXD)

The Vertex Detector (VXD) is responsible for precise measurements of decay vertices. It consists of two components: the inner Pixel Detector (PXD) and the outer Silicon Vertex Detector (SVD). The PXD constitutes the main focus of this study and is therefore described in detail in Section 12.4.

The SVD is composed of four layers of Double-sided Silicon Strip Detectors (DSSDs) [227]. The DSSDs consist of an n-doped silicon bulk positioned between p- and n-doped strip implants. The passage of ionising radiation through the silicon bulk creates electron-hole pairs that induce a signal on the strips. Different sensor shapes are employed in the forward region (trapezoidal shape) and in the barrel (rectangular shape).

12.3.2 The Central Drift Chamber (CDC)

The Central Drift Chamber (CDC) is the principle tracking detector of Belle II [228]. By measuring the trajectories of charged particles in the magnetic solenoid field, their momentum is reconstructed. Additionally, the energy loss of charged particles is determined, which delivers essential information for particle identification. The CDC also contributes trigger information, as explained in 12.5.

The CDC surrounds the VXD in the barrel region of the detector. It consists of 14366 sense wires and 42240 field wires to generate an electric field. The sense wires are arranged in 9 super-layers, each of which are divided into 6 layers, except for the innermost super-layer, which has two more layers to deal with the increased occupancy. The sense wires are either oriented parallel to the beam (*axial layers*) or tilted by -74 mrad to 70 mrad (*stereo layers*).

The CDC volume is filled with a gas mixture of 50 % helium and 50 % ethane, which is ionised by the passage of a charged particle. The drift of the liberated electrons induces a signal on the sense wires. The position of the wire and the signal time allow for the reconstruction of the particle trajectory.

12.3.3 Particle Identification

The particle identification system of Belle II is based on the detection of Cherenkov photons [229]. It consists of the Time of Propagation Counter (TOP) in the barrel region and the Aerogel Ring-Imaging Cherenkov Detector (ARICH) in the forward endcap [230]. Charged particles faster than the speed of light in a given medium emit Cherenkov radiation, that follows a distinct angular distribution determined by:

$$\cos\Theta = \frac{1}{\beta n(\lambda)}, \tag{12.2}$$

where Θ is the opening of the Cherenkov cone, $n(\lambda)$ the refractive index of the radiator material for a given wavelength λ and β the particle velocity over the speed of light.

The TOP is composed of 16 modules hosting rectangular quartz radiators. The passage of charged particles exceeding the speed of light in quartz generates Cherenkov photons that are internally reflected at the radiator walls until they impinge on photoelectric sensors at the end of the quartz block. The sensors are arranged as 32 micro-channel plate photomultiplier tubes (MCP-PMTs) and a prism is positioned before the sensors to expand the detectable area.

The MCP-PMTs have a time resolution of approximately 50 ps [231], which allows for a time-tagged measurement of the Cherenkov light between the bunch crossings. The propagation time of the Cherenkov photons depends on the angle Θ that is different for the particle species at a given momentum. Using the tracking information of the CDC, a likelihood estimation is calculated in order to obtain probabilities for different particle hypothesis.

The ARICH operates in a similar manner. It consists of an Aerogel radiator, where Cherenkov photons are produced when a charged particle with a sufficiently high velocity passes through the volume. The Cherenkov cone is directed towards a photon-detector plane composed of Hybrid Avalanche Photodetectors (HAPDs). Particle identification is then based on the measured Cherenkov angle Θ.

12.3.4 Electromagnetic Calorimeter (ECL)

The Electromagnetic Calorimeter (ECL) has a high energy resolution and efficiency and is thus able to differentiate between photons in an energy range from tens of MeV to several GeV [232]. In addition, the ECL provides an identification criterium for electrons and photons and contributes crucial information for the trigger system.

The ECL consists of 8736 thallium-doped caesium iodine CSI(TI) crystals equipped with a pair of Hamamatsu S2744-08 photodiodes. Particles traversing the crystals deposit energy by ionisation or generation of particle showers. The scintillating crystals generate photons that are detected by photodiodes and digitised by Flash ADCs.

12.3.5 Superconducting Solenoid

A superconducting solenoid magnet envelops the inner sub-detectors and immerses them in a magnetic field of 1.5 T. The field lines are aligned with the main detector axis in z-direction. Charged particles are subjected to the Lorentz force when they traverse the magnetic field. The curvature of the particle trajectories allows for a reconstruction of their momenta using the tracking detectors.

12.3.6 K_L and Muon Detector (KLM)

The K_L and Muon Detector (KLM) is designed for the detection of long-lived K_L mesons and muons. It exploits the magnet return yoke for particle detection by interleaving it with detection layers. In the outer layers, Resistive Plate Chambers (RPCs) are used and in the inner layers and endcaps Silicon Photo Multipliers (SiPMs) are employed to handle high particle rates.

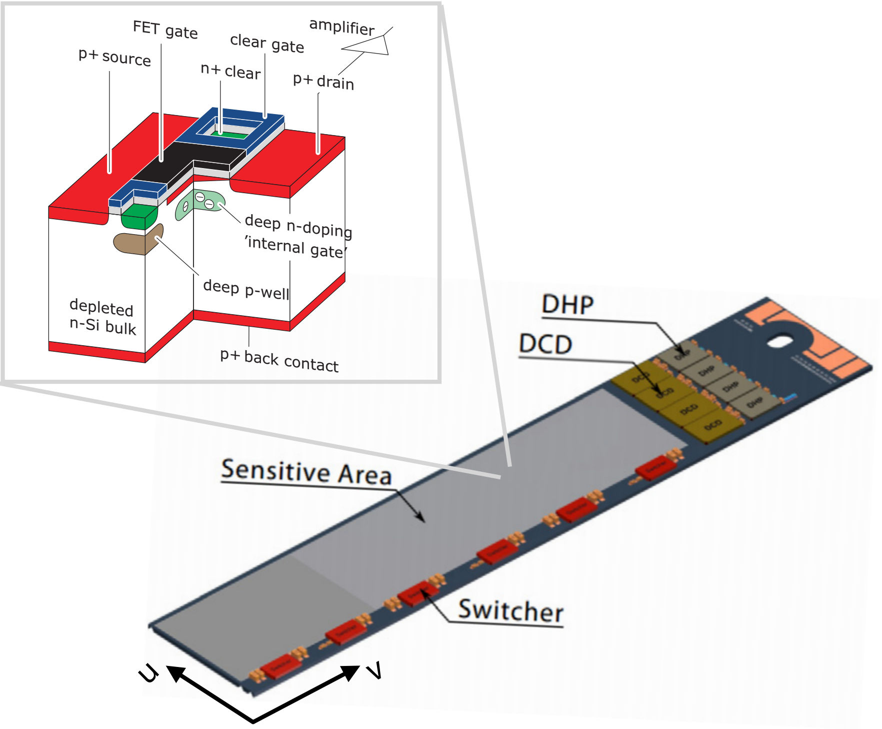
FET gate
amplifier
clear gate
p+ source
n+ clear
p+ drain
deep n-doping
'internal gate'
deep p-well
depleted
n-Si bulk
p+ back contact
DHP
DCD
Sensitive Area
Switcher
u
v

Figure 12.3. PXD module consisting of the active pixel matrix and the readout ASICs (Switcher, Drain Current Digitizer (DCD) and Digital Handling Processor (DHP)). A schematic of the DEPFET pixel design is depicted at the top. Modifed from [233, 234]

While K_L mesons are recognized by particle showers that they generate during their passage through the KLM, muons traversing the detector are identified using a likelihood fit involving CDC track information.

12.4 The Pixel Detector (PXD)

The PXD is the innermost sub-detector, with the principle objective of precise measurements of secondary vertices. Its close proximity to the IP demands high resilience against background events and sophisticated data handling to cope with large data rates.

The PXD consists of 40 modules arranged in two layers of a windmill-like structure, as depicted on the left of Fig. 12.2. The layers are positioned at radii of 14 mm and 22 mm from the IP, respectively. Presently, the inner layer is fully assembled and in the outer layer four modules are installed. Each module is populated with *DEPleted Field Effect Transistor (DEPFET)* pixel detectors [65, 235] and dedicated readout ASICs, which are introduced in the following.

12.4.1 The DEPFET Pixel Sensors

The monolithic DEPFET pixel sensors are characterised by an extremely low material content of $0.2\,\%X_0$ which is achieved with sensors thinned down to 75 µm. The reduced material budget enables a high vertex resolution owing to the suppression of multiple scattering.

A schematic of the sensor design is depicted on the top of Fig 12.3. A p-channel MOSFET is combined with a high-resistivity silicon bulk [235], which can be fully depleted by sufficiently high bias voltages applied to the backside. The detection principle is based on a potential minimum created below the transistor channel, which is formed by a phosphorous implant referred to as *internal gate*. The passage of charged particles generates electron-hole pairs in the sensor. The electrons drift to the internal gate, where they modulate the channel current [236]. The amplification change in drain current is a measure for the number of generated electrons and consequently for the amount of deposited energy. After readout, the electrons are *cleared* from the internal gate by applying a positive voltage to an n^+ contact, which provokes a punch-through to the internal gate.

The pixel pitch can vary between 55 µm to 80 µm depending on the layer and the distance to the IP.

12.4.2 The PXD Module

The DEPFET sensors are placed on PXD modules, that provide a light-weight support structure as well as dedicated readout ASICs. A schematic of the module design is displayed in Fig 12.3.

A local coordinate system is defined on the modules, with the v-axis parallel to the global z-axis and the u-axis perpendicular to it. The sensitive pixel matrix can be divided into two segments with respect to their distance to the IP: the inner segment consisting of 256×250 pixels in $u \times v$ direction and the outer one housing 512×250 pixels with slightly larger pixel pitches due to the lower occupancy.

The readout chain on the modules is handled by dedicated ASICs. The sensors are read out in a *rolling-shutter mode*, where four rows are processed in parallel. Six *Switchers* at the rim of the modules initiate the readout by driving gate and clear voltages of selected pixels [237]. The source-drain current is monitored by Drain Current Digitizer (DCD) chips and subsequently digitized in an 8-bit ADC [238]. The Digital Handling Processor (DHP) stores the data in a ring buffer until it receives a trigger signal (cf. Section 12.5) [239]. After pedestal subtraction and zero suppression, the DHP sends the data package to the data acquisition system.

12.5 The Trigger System

The Belle II trigger system is divided into two parts: the Level 1 (L1) trigger operating on hardware level and the Level 2 (L2) trigger, which is software-based.

For the L1 trigger, the sub-trigger input from different sub-detectors is combined in the *Global Reconstruction Logic (GRL)* and then sent to the *Global Decision Logic (GDL)* that is responsible for a final trigger decision. In particular, the CDC and the ECL provide essential information for the trigger decision. If a trigger is issued, it is distributed to all sub-detectors to initiate further data acquisition.

While the L1 trigger is able to sustain a maximum rate of 30 kHz, the rate is further reduced to maximum 10 kHz by the L2 or *High Level Trigger (HLT)* [242]. The software trigger bases its decision on an offline reconstruction involving all sub-detectors except for the PXD. If the event topology meets the trigger conditions, data is written to permanent storage.

During Phase 2, the HLT was operated in pass-through mode. With increasing luminosity in Phase 3, the HLT is switched on to ensure a tolerable data rate.

12.6 The Data Acquisition System

The Data Acquisition System (DAQ) is responsible for the collection and transfer of data after a L1 trigger is issued. A unified readout link called *Belle2Link* [240] delivers the data to the Common Pipeline Platform for Electronics Readout (COPPER) [241], where sub-event building is performed. The HLT performs a full event reconstruction using data from all sub-detectors except for the PXD. Based on predefined trigger patterns, the HLT decides to discard events or write them to permanent storage. If the event is kept, PXD data is added in a subsequent event building step.

12.6.1 The PXD Data Acquisition

The DAQ of the PXD has to handle high data rates due to the large number of readout channels and the high occupancy caused by the close proximity to the IP. Even though a maximum trigger rate of 30 kHz and a maximum occupancy of 3 % is tolerated, the expected data rate is still exceeding 20 GB/s [243]. Therefore, an innovative readout scheme is necessary to apply an online data reduction, while keeping pixel hits related to potentially relevant physics events.

The on-module ASICs are read out by the Data Handling Hub (DHH) [244], which features a two-layer architecture. The first layer is based on Data Handling Engines (DHEs), which receive pixel data from the DHP. The DHE reformats and enriches the data with meta information before sending it to the second layer - the Data Handling Concentrator (DHC). The DHC adds more metadata and performs 5-to-4 multiplexing. In addition, it provides an interface to trigger and clock components via slow control.

Th FPGA-based Online Selection Node (ONSEN) is responsible for online data reduction in a two-step procedure [243]. First, the HLT decision is taken into account by discarding all data from events unassociated to a HLT trigger. While this filter reduces data by a factor of three, the second stage is based on Regions of Interest (ROIs). Particle tracks reconstructed by the HLT event building are extrapolated to the PXD layers, where ROIs are defined in a specified area around the intersection point between PXD layer and extrapolated track. The size of the ROI is determined by the track resolution. Pixel hits located outside of ROIs are discarded leading to a reduction by a factor of 10.

It is foreseen that ROI generation is also allowed by a second system using only SVD data. The FPGA-based Data Acquisition Tracking and Concentrator Online Node (DATCON) [224] performs track building using hits from the four SVD layers and IP. The intersection of these tracks with the PXD layers define additional ROIs. However, the DATCON is unable to override the trigger decision i.e. if pixel hits are not associated to a HLT trigger, they are discarded regardless of the DATCON decision.

12.7 Background at the Belle II PXD

The operation characteristics and the high luminosity of the SuperKEKB collider give rise to significant contributions of background events. Especially the PXD is subject to high background levels due to its close proximity to the interaction region. The main background contributions can be differentiated by their source of origin into *beam-induced* and *luminosity-dependent* background [245]. Whereas the former is related to the beams circulating in the storage ring, the luminosity-dependent background arises from the collisions themselves. In the following, the main background production mechanisms are outlined.

12.7.1 Beam-Induced Background

Particle beams circulating in the HER and LER storage rings are constantly subject to interactions with residual gas, the beam pipe or with other particles in a bunch. As a result, individual beam particles are eventually lost leading to a limited lifetime of the beam. If beam particles leave their nominal trajectory in the vicinity of the Belle II detector, primary or secondary particles can scatter into the sensitive volume of the detector, which manifests itself as beam-induced background.

Touschek effect The *Touschek effect* [246] is a prominent background source at Belle II, owing to the operation conditions at the SuperKEKB collider. The nano-beam scheme demands a small bunch size, which results in a a high particle density in each bunch. As a consequence, intra-bunch scattering is increased, whereby individual particles in the bunch interact with each other, which can lead to their diversion from the bunch. If the Touschek process occurs close to the detector, the diverted beam particles collide with the beam pipe and can thus create a particle shower that enters the detector, which gives rise to background hits.

Touschek scattering scales with the number of particles per bunch squared and is inversely proportional to the square of the beam size. The scattering rate decreases with E^{-3} due to relativistic effects, where E denotes the beam energy [247]. Compared to KEKB, the scattering rate is 20 - 30 times higher in SuperKEKB due to the higher particle density in the bunches. Movable beam masks are available to collimate the beam and reduce the impact of the Touschek background.

Beam-gas scattering Beam-gas scattering occurs when particles interact with residual gas in the beam pipe [248]. For SuperKEKB, the main contributions are expected to originate from hydrogen and carbon monoxide gas molecules. As a result of the scattering events, beam particles can leave their nominal orbit and give rise to particle showers, which can enter the detector.

Beam-gas scattering is proportional to the beam current and to the partial pressure of the residual gas. The rate is expected to be approximately 50 % smaller than the rate associated with the Touschek effect [245].

Synchrotron radiation A third prominent background source for lepton colliders is related to synchrotron radiation generated by the passage of electrons and positrons through the bending and focusing magnets along the storage rings [249, 250]. In particular, the final-focusing magnets before the interaction point are a principle source of synchrotron radiation that increases background levels in the detectors.

Synchrotron radiation is proportional to the beam current and to the fourth power of the beam energy [251]. Dedicated shielding components and a gold layer covering the beam pipe at the interaction region are employed to reduce to impact of synchrotron radiation.

12.7.2 Luminosity-Dependent Background

Luminosity-dependent background is generated by the electron-positron collisions and thus emerges directly from the interaction region. Unlike the beam-induced background, luminosity-dependent background scales with the luminosity of SuperKEKB and cannot be mitigated by e.g. shielding.

Radiative Bhabha scattering Radiative Bhabha scattering describes the interaction of an electron with a positron in the following scattering process [252]

$$e^+e^- \rightarrow e^+e^-\gamma.$$

The process is classified depending on the opening angle between the two leptons. For a wide opening angle, the leptons can enter the detector directly resulting in background hits. However, the cross section of the process favours small scattering angle, where both leptons continue along the storage ring. Depending on the angle, they can collide with the beam pipe or magnets and create particle showers, that can backscatter into the detector.

Two-photon effect The dominant background source for the PXD is based on the *two-photon process*, given by the QED interaction [253, 254]

$$e^+e^- \rightarrow e^+e^-\gamma\gamma \rightarrow e^+e^-e^+e^-.$$

As the leptons are generated with a low transverse momentum p_t, they typically follow a curled trajectory in the magnetic field and therefore affect mainly the inner layers of the tracking detectors. At Belle II, the impact of the two-photon effect is higher compared to Belle, due to the small radius of the PXD layers making it sensitive to low-p_t tracks.

12.7.3 Conclusion

At the target luminosity, the two-photon background is expected to dominate over all other background components. It is approximately five times larger than radiative Bhabha scattering and synchrotron radiation and at least three orders of magnitude higher than the Beam-Gas and Touschek background.

Detailed information about the origin, distributions and occupancies of the above mentioned background components in the PXD can be found elsewhere [245].

12.8 The Belle II Analysis Software Framework

The Belle II Analysis Software Framework (`basf2`) is a versatile software framework for numerous tasks such as data reconstruction and analysis as well as full-detector simulations [255]. It is also employed for online tasks related to data acquisition and data-quality monitoring and is an essential part of the HLT.

The software is composed of Belle II-specific code written in C++, external dependencies such as ROOT and tools for e.g. software installation. Python scripts steer the execution of the code. The architecture of the framework adheres to a modular design. The user builds a processing chain from an assembly of `modules`, which have dedicated functionalities such as reading/writing of data or track reconstruction.

12.8.1 Full-Detector Simulation

A full-detector simulation involves the generation of particles as well as their propagation through and interaction with the simulated Belle II detector. `basf2` employs a Monte-Carlo-based simulation approach, whereby a simulation chain is set up using the aforementioned `modules`. First, event generators are used to simulate the primary physics process based on theoretical models such as `EvtGen` for the decay of B and D mesons or `PYTHIA` for the continuum production of light quark pairs.

The detector simulation is based on the Geant4 framework. The software transports each particle through the detector in discretized simulation steps and takes statistical fluctuation and production of secondary particles into account. Detailed information about the physics lists used in Geant4 are given elsewhere [26]. The hit information with sensitive detector material are handled in dedicated `basf2` modules. For instance, the creation of electron-hole pairs, their drift and diffusion and signal induction is simulated for the PXD [256]. In subsequent steps, the simulation is reconstructed and analysed just like real data.

12.8.2 Background Simulation

The simulation of background is handled by different third-party software frameworks. The following list provides an overview of the simulation tools that are relevant for this thesis:

- For the **Touschek background** and the **beam-gas scattering**, the *Strategic Accelerator Design (SAD)* software [257] is employed to model the beam loss along the storage ring.

- The simulation of **synchrotron radiation** is handled by Geant4.

- **Radiative Bhabha scattering** is divided into two classes depending on the polar scattering angle $\theta_{e^\pm}$. Scattering angles larger than 0.5° for both leptons are considered to be *wide* and the generator BHWIDE [258] is used to simulate the events. For small scattering angles, the Monte Carlo software BBBREM [259] is employed.

- The luminosity-dependent **two-photon background** is handled by another Monte Carlo tool referred to as AAFH [260].

Chapter 13

Highly-Ionising Particles

Unlike MIPs, Highly-Ionising Particles (HIPs) are characterised by a strikingly high energy loss in matter. Exotic candidates for HIPs include magnetic monopoles [261], particles carrying electric and magnetic charge (*dyons*) [262] or particles with a high electric charge such as Q-balls [263].

If the lifetime of HIPs is sufficiently high to interact with detector components, a prominent event signature involving high energy depositions would be detectable. However, despite the unique signature, the reconstruction of these particles remains challenging for numerous reasons. First of all, detectors are typically not designed for particles with massive energy depositions. Saturation of the readout electronics or a limited dynamic energy range can inhibit direct detection. If the particles are trapped in the innermost detection layers, additional challenges arise owing to an incomplete event signature. In this thesis, the identification of HIPs in Belle II is studied using an example HIP candidate: hypothetical magnetic monopoles. While the results are obtained for this particle species, the general concepts are expected to apply to other HIP candidates as well.

To be consistent with contemporary literature about HIPs, the speed of light c is set equal to 1.

13.1 Magnetic Monopoles

The existence of magnetically charged particles is a burning question that has triggered remarkable theoretical and experimental efforts. Presently, no experimental evidence confirming or completely disproving their existence is available. From a theoretical perspective, there are numerous approaches that would permit or even actively predict the existence of particles carrying magnetic charge. In the following, a brief introduction in selected theoretical concepts of magnetic monopoles is presented. More detailed reviews are for instance given in [264, 265].

Most prominently, Dirac was preoccupied with the existence of magnetic monopoles as early as 1931 [266], when he related the quantization of the electric charge to the existence of magnetic monopoles and predicted the fundamental magnetic charge to be $g_M = 68.5\,\mathrm{e}$. Although Dirac provided no prediction about the monopole mass range, rough estimations based on the equivalence of the classical electron radius and the classical monopole radius yield a mass of approximately 2.4 GeV for a singly-charged monopole [267].

Subsequently, Polyakov [268] and 't Hooft [269] showed that magnetic monopoles arise from the unification of fundamental interactions. Depending on the unification scale, the monopole mass is of the order of $10^{17} - 10^{18}$ GeV [270], which is out of the energetic reach of modern collider experiments. However, other theoretical approaches predict lower masses such as the electroweak Cho-Maison monopole, which can be considered a hybrid between Dirac and the 't Hooft-Polyakov monopole [271].

The aim of this dissertation is to develop a model-agnostic search for highly-ionising particles, which is independent of a specific monopole model. However, for the evaluation of the search strategy, the simulation of magnetic monopoles is required. Minimal assumption arising from the Dirac theory are therefore adopted such as the quantization of magnetic charge. In addition, some cross-model concepts about monopole production mechanisms, energy loss in matter or trajectories in a magnetic field are used for the simulation setup, which are presented in the following.

13.1.1 Production Mechanism

A simple model of monopole pair production assumes a Drell-Yan production process involving one virtual photon γ^* [272, 273]

$$e^+e^- \to \gamma^* \to M^+M^-,$$

where M^+M^- represents the monopole pair. This model is based on a monopole-photon coupling, which scales with the monopole velocity according to $g_M\beta$, where $\beta = v/c$ and $g_M = 68.5\,\mathrm{e}$ [270, 274]. The large charge results in a strong monopole-photon coupling, that also has important implications for the monopole energy loss, as discussed below. Detailed derivations of the Drell-Yan production mechanism for monopoles are beyond the scope of this thesis and can be found elsewhere [275, 276]. Since a pair-production process is considered, both monopoles and anti-monopoles are studied in this thesis. For the sake of brevity, the generic term monopole implies both the particle and anti-particle. In studies, where they are considered separately, the change in phrasing is explicitly mentioned.

13.1.2 Energy Loss in Matter

Unlike electrically charged particles, the interaction of magnetic monopoles with matter involves the magnetic dipole moment of the medium [277]. Different interaction mechanisms can be differentiated depending on the monopole energy.

For fast magnetic monopoles with $\beta \gtrsim 10^{-1}$, a modification of the original Bethe formula can be derived [278]:

$$-\frac{\mathrm{d}E}{\mathrm{d}x} = C\frac{Z}{A}g^2\left[\ln(\frac{2m_e c^2\beta^2\gamma^2}{I}) - \frac{1}{2} + \frac{k}{2} - \frac{\delta}{2} - B_m\right]\mathrm{MeVg^{-1}cm^2} \tag{13.1}$$

with

$$C = \frac{e^4}{4\pi\epsilon_0^2 m_u m_e}. \tag{13.2}$$

The unified atomic mass units is denoted by m_u, the mean ionization potential by I and the other parameters as presented in Section 2.3.1. The last terms are correction factors, where δ accounts for density effects [279], k applies QED corrections and B_m is the Bloch correction [280].

At $\beta\gamma \sim 3$, where the energy loss for electrically charged particles is minimal (cf. Section 2.3.1), the energy loss of magnetic monopoles is approximately three orders of magnitude higher. However, in contrast to electrically charged particles, the energy loss decreases with decreasing velocity.

For slow monopoles with velocities $10^{-4} \lesssim \beta$, the energy transfer becomes comparable to the binding energy of electrons to nuclei and different energy loss models are required [281]. For instance, a semi-classical approach, where the material is treated as a degenerate Fermi gas of non-interacting electrons was put forward by Ahlen and Kinoshita [282].

13.1.3 Trajectory in a Magnetic Field

The duality of electric and magnetic charge implies a Lorentz-like force law, where particles carrying magnetic charge are accelerated along the magnetic field lines [283]:

$$\vec{F}_m = g_M(\vec{B} - \vec{\beta} \times \vec{E}). \tag{13.3}$$

In contrast to particles with an electric charge, the motion of a magnetically-charged particle remains unperturbed in the direction perpendicular to the magnetic field, which corresponds to the $r\phi$-plane in the Belle II detector. In the rz-plane on the other hand, a magnetically-charged particle is accelerated along the field lines and the trajectory therefore resembles a parabola as presented in Fig. 13.1. The trajectories are simulated using

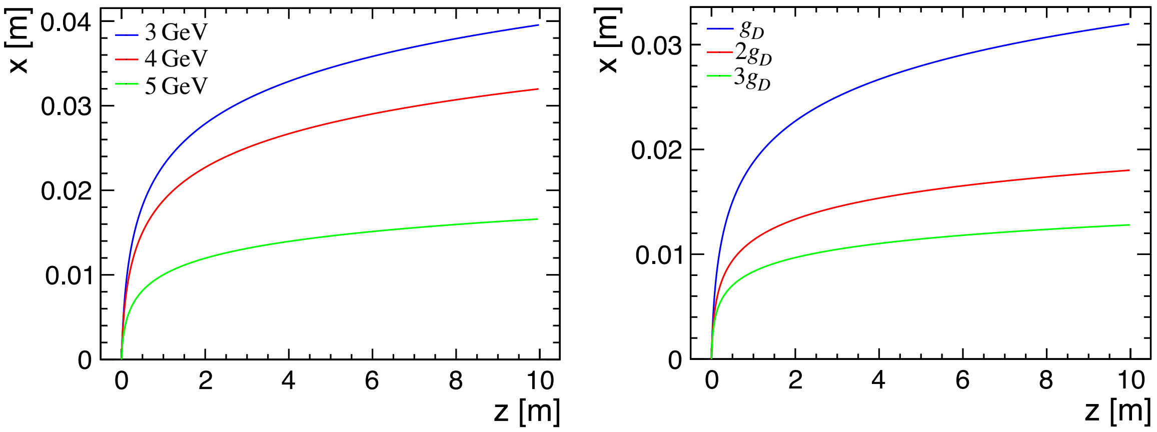

(a) Different monopole masses for a fixed magnetic charge of 68.5 e

(b) Different magnetic charges for a fixed mass of 4 GeV

Figure 13.1. Trajectories of magnetically-charged particles with initial momenta perpendicular to the magnetic field lines for (a) different monopole masses and (b) different magnetic charge values. The 1.5 T magnetic field is parallel to the z-axis. Based on [284].

an analytical solution of Eq. 13.3 for particles with an initial momentum perpendicular to a 1.5 T magnetic field, whose field lines are parallel to the z-axis.

On the left-hand side, the monopole mass is varied from 3 GeV to 5 GeV, while the magnetic charge is fixed to the Dirac charge $g_D = 68.5\,\mathrm{e}$. The magnitude of the initial momentum is determined by energy conservation given the centre-of-mass energy in the collision 10.58 GeV and the monopole mass. A large monopole mass therefore results in a low initial momentum and consequently in a strong curvature of its trajectory.

On the right-hand side of Fig. 13.1, the monopole mass is fixed to 4 GeV and the magnetic charge is varied from unit Dirac charge g_D up to $3g_D$. Due to the force law Eq. 13.3, the curvature of the trajectory increases with increasing magnetic charge.

For this thesis, the definition is adopted that anti-monopoles are accelerated antiparallel and monopoles parallel to the field lines. This property has important consequences for the motion in the Belle II detector, where a 1.5 T magnetic solenoid field is present in the inner parts of the detector (cf. Section 16.3.6).

13.1.4 Detection Sensitivity in the Belle II Detector

A diverse search campaign for magnetic monopoles has yielded no positive results so far [7]. Search strategies included monopoles trapped in matter [285], in cosmic radiation [286, 287] and various direct and indirect analyses in collider experiments [288, 289], with several of them performed in electron-positron collisions [282].

The Belle II experiment operating at the high-intensity frontier has a unique sensitivity to magnetic monopoles, due to its high-precision, low-mass detector setup. Nevertheless, the trigger and data reduction scheme hinder direct detection for two reasons (cf. Section 12.6): First, the L1 and HLT trigger conditions are unsuitable for monopole signatures in the detector. In particular, magnetic monopoles with a mass above 1 GeV have a prohibitively low detection efficiency for the current trigger menus. However, these challenges could be partially mitigated by adaptation of the trigger conditions to achieve a better match. A detailed review about the trigger efficiency of magnetic monopoles is given elsewhere [290].

Second, magnetic monopoles are discarded by the ROI selection owing to the lack of a reconstructable track. Current tracking algorithms are unable to recognize monopole trajectories, which are distinctly different from electrically charged particles (cf. Section 13.1.3). However, first steps towards tracking algorithms appropriate for particles with magnetic charge were successfully tested [291]. The high energy loss in the detector material weighs even more heavily, since it restricts the monopole range to the innermost tracking detectors [284]. Without hits in the CDC, no track is reconstructed and the monopole hits in the PXD and SVD are discarded. This challenge is not unique to magnetic monopoles but also affects other particles with low transverse momenta that can escape tracking.

To anyway guarantee a high signal efficiency, a machine-learning-based veto system is proposed. A proof-of-principal for an online veto system dedicated to the identification of slow pions has already been presented in the past [292] and offline studies for slow-pion identification using solely PXD observables are conducted with various machine-learning techniques [294, 295]. Complementary to these studies, this thesis focuses on a veto system for exotic or *anomalous* particle signatures. The selected algorithms and techniques for this system are presented in the subsequent chapter and its evaluation is shown in Chapter 16 using hypothetical magnetic monopoles as example signal.

Chapter 14

Machine Learning Techniques

Machine learning has proven to be a valuable tool in reconstruction and analysis tasks for High-Energy Physics (HEP) [5]. In particular, the classification of signal and background using machine learning algorithms has sparked significant interest in recent times. In particular, the search for dark matter candidates has benefited from a machine-learning approach, since it enables the processing of large datasets and is therefore suitable to operate directly on minimally-processed data coming from the detector instead of reconstructed objects.

The following chapter lays the methodological basis for the evaluation of different machine-learning techniques in Chapter 16. The algorithms are introduced with a focus on binary classification problems of signal against background in order to relate advantages and disadvantages of the methods directly to the task at hand. While the same principles hold true for other applications as well such as multi-class classification or regression, they are not explicitly mentioned.

14.1 Supervised and Unsupervised Training

Before a machine learning classifier is put to use, it is trained to accomplish a specific task. There are two main training principles: *supervised* training, where the training relies on a prior definition of signal provided by a theoretical framework and simulations and *unsupervised* training aiming at the identification of signal features while minimizing assumptions about signal or background [1].

Supervised training benefits from a precise signal definition, which improves control over the training process and makes training results less ambiguous. However, detector signatures corresponding to elusive beyond the Standard Model Physics (BSM) processes

---

[1] There are also training principles operating in-between these two extremes, which are commonly referred to as *semi-supervised* training [293].

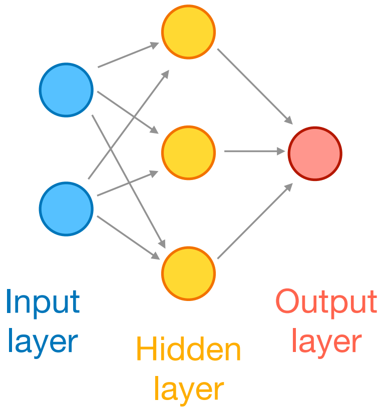

Figure 14.1. Schematic of a Multilayer Perceptron (MLP) with one hidden layer between the input and output layers.

might be missed owing to a narrow signal definition or a mis-modelling of either signal or background.

Unsupervised and semi-supervised methods aim at the identification of signal features with little to no need for assumptions about signal or background. A data-driven approach is adopted allowing for a model-agnostic analysis that has the advantage of being independent from theoretical assumptions and therefore not confined to specific signal hypotheses and background modelling.

14.2 Artificial Neural Networks

An Artificial Neural Network is a collection of interconnected simple processing units, which are commonly referred to as *neurons*. In Feedforward Neural Networks (FNN) the neurons are arranged in layers, where each layer is connected to the next without a formation of loops [296]. A schematic representation of a shallow FNN with three layers is displayed in Fig 14.1. While the first layer (*input layer*) is activated by external data, the inner layers (*hidden layers*) respond to stimuli provided by the preceding layer. Due to the existence of several processing layers, this architecture is referred to as Multilayer Perceptron (MLP) [297].

The response of a neuron is described by an *activation function* [298]. Given an input from a preceding neuron or an external stimuli, the activation function determines the output of the neuron, which is sent to the next unit or to the output layer. Typically, non-linear, real-valued functions such as *tanh* or a sigmoid function are selected as activation function. Another popular choice is a *Rectified Linear Unit (ReLu)* which filters the

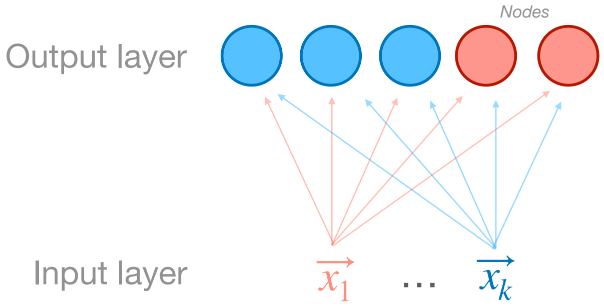

Figure 14.2. Schematic representation of a Self-Organising Map (SOM).

positive part of an argument x_i [299]:

$$r(x_i) = \max(0, x_i).$$

In a supervised MLP, the weights between neurons are adapted during the training phase in order to optimise the output of the network. To this end, the disagreement between the current output and the desired result is calculated using a *loss function* [300] such as the Euclidean distance between the two (*mean squared error*). Different techniques have emerged to adjust the weights in an effort to minimise the loss function. The *Stochastic Gradient Descent (SGD)* method estimates the gradient of the loss function $\nabla_w E$ by uniform sampling of the input vectors using a small sample size to speed up computation times. The weights are then adjusted according to [301]

$$w^{(i+1)} = w^i - \nu \nabla_w E, \tag{14.1}$$

where w^i are the set of weights in the i-th iteration and ν is the learning rate. An extension to the SGD method called *Adaptive Moment Estimation (Adam)* computes an adaptive learning rate by estimating first and second moments of gradients [302].

14.3 Self-Organising Maps

Self-Organising Maps (SOMs) apply competitive learning [303] in order to provide a low-dimensional discretised representation of high-dimensional input vectors [304]. Despite the reduction in dimensionality, SOMs preserve the topology of the input to the best degree possible [305].

During training a topologically correct map of the high-dimensional input signal is formed by the lower-dimensional processing units, which are often referred to as *nodes*. A schematic of a SOM with k input vectors is presented in Fig. 14.2. A local feedback is responsible for the self-organised mapping process. A SOM is categorized as an unsupervised learning algorithm, since no comparison with a desired output is required.

SOMs consist of two mathematical spaces: a node space of dimension n and a feature space of dimension m. The feature space consists of the high-dimensional input vectors and the node space is represented by low-dimensional (here: one-dimensional) vectors. For the following motivation of the learning algorithm, it is assumed that N nodes are present in node space, which are located at fixed positions $r^{(n)} \in \mathbb{R}^n$. Each node is associated with a feature vector with position $r^{(m)} \in \mathbb{R}^m$ that can be modified during learning.

14.3.1 The Learning Algorithm

A SOM is trained by adapting the feature vectors based on their distance to the input vector. The smallest distance of the i-th input vector $v_i^{(m)}$ to the feature vectors is determined using a chosen metric. The closest feature vector is referred to as *winner vector* and the associated node as *winner node* $r_w^{(n)}$. A local feedback around the winner node induces the adaptation of the feature vectors associated with nodes in the vicinity of the winner node:

$$r_j^{(m)}(t+1) = r_j^{(m)}(t) + h_{w,j}(t) \cdot (v_i^{(m)} - r_j^{(m)}(t)), \tag{14.2}$$

where the subscript j denotes the j-th feature vector. The parameter t labels each step with an integer number. The *neighbourhood function* $h_{w,j}(t)$ determines the local relaxation process of the nodes. It is calculated from the distance between the winner node $r_w^{(n)}$ to all other nodes $r_j^{(n)}$, where j runs from 1 to N. For this thesis, a Gaussian kernel is used, which reads

$$h_{w,j}(t) = \alpha(t) \exp\left(-\frac{\|r_w^{(n)}(t) - r_j^{(n)}(t)\|^2}{2\sigma^2(t)} \right) \tag{14.3}$$

for the node $r_j^{(n)}$. The timestep-dependent parameter $\alpha(t)$ is considered to be the current *learning rate* and te width of the Gaussian kernel $\sigma(t)$ determines the range of the relaxation process. For this thesis, they were chosen as follows:

$$\alpha(t) = \alpha_0(1 - \frac{t}{t_{\max}}) \tag{14.4}$$

$$\sigma(t) = \sigma_0(1 - \frac{t}{t_{\max}}) \tag{14.5}$$

14.4 Autoencoder

An Autoencoder (AE) used for anomaly detection is a feed-forward multi-layer neural network that aims at reproducing the input vector without using an identity mapping.

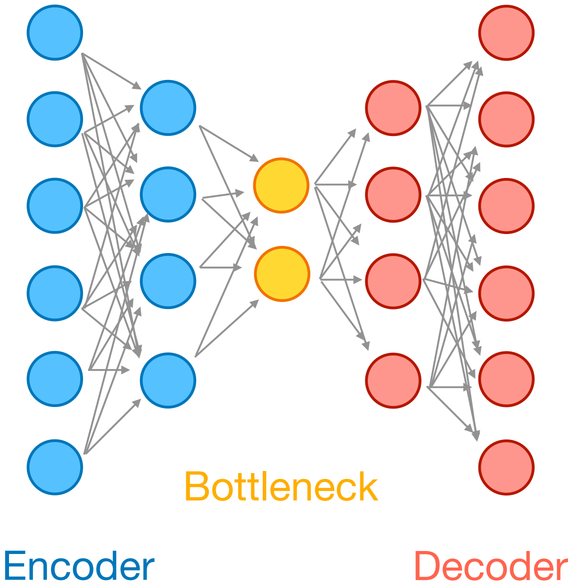

Figure 14.3. Schematic of an Autoencoder consisting of an encoder, a bottleneck layer and a decoder.

It consists of two parts: an encoder E and decoder D, as depicted schematically in Fig. 14.3. While the encoder compresses the input to a lower-dimensional vector, the decoder reconstructs the original input from the reduced representation. The latent space in the centre of the AE is an information bottleneck that enforces the selection of relevant patterns from the input data.

The AE solves the following optimization problem [306]:

$$E_R = \min_{D,E} |X - D(E(X))|, \tag{14.6}$$

where E_R denotes the reconstruction error and X the input data. For this thesis, the Euclidean distance is used to evaluate the expression.

Autencoder-based anomaly detection uses the reconstruction error as an anomaly score to identify anomalous data that was not used in the training process i.e. large reconstruction errors are associated with anomalous events. This method exploits the optimised reconstruction of normal data to filter out anomalies in an unsupervised manner. The anomaly detection is performed such that it can be considered a sophisticated filter mechanism that defines a potential signal region for further statistical analysis.

14.5 Performance Metrics

The following section introduces selected performance metrics to assess the classification performance. First, the general concept of the Receiver Operating Characteristics is outlined and subsequently the specific application to anomaly detection is described.

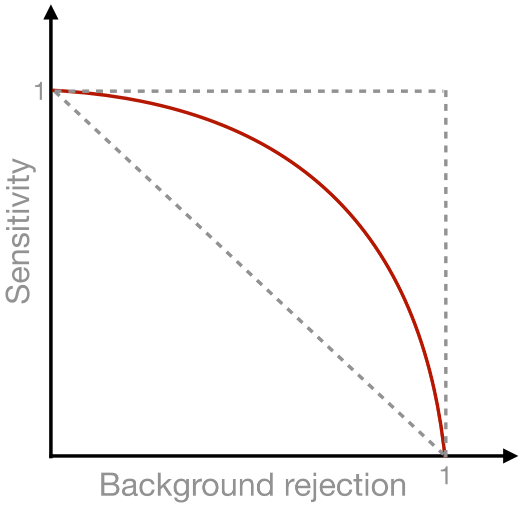

Figure 14.4. Schematic of a Receiver Operating Characteristic (ROC) curve. While the box-function represents a perfect classifier, the diagonal is the worst-case scenario in case of random guessing.

14.5.1 Receiver Operating Characteristic

The Receiver Operating Characteristic (ROC) diagram allows for an assessment of the diagnostic abilities of a classifier [307]. While there are various manifestations of ROC curves, in this thesis the *sensitivity* is evaluated against the *background rejection*, as schematically depicted in Fig. 14.4. The sensitivity corresponds to the signal efficiency and is given by the number of correctly identified signal events divided by the total number of signal events. The background rejection is given by (1 - background efficiency).

An ideal classifier would exhibit a *box function*, since perfect background rejection is achieved simultaneously with optimal signal sensitivity [308]. Random guessing on the other hand, would result in the diagonal line in Fig. 14.4. In all other cases, the ROC curves are between the two extremes. The *Area Under Curve (AUC)* is a measure for the classification performance, with perfect classifiers achieving a maximum area of one [309].

14.5.2 Performance Evaluation

The machine learning algorithms presented in this thesis operate on an event-by-event basis and label each event as anomalous or normal based on an *anomaly score*. While the scope of the anomaly score depends on the selected algorithm, the definition is adopted that low anomaly values represent normal and high values anomalous events.

The different methods are evaluated by means of ROC curves. To this end, the signal efficiency ϵ_S is scanned and the background rejection ϵ_B is recorded, which allows for an assessment of the prevalence of target anomalies at a given background level. The

Area-Under-Curve (AUC) is computed and compared between the algorithms.

For anomaly detection, a high background rejection is particularly desirable. Therefore, the signal efficiency at three different operation points featuring a high background rejection level are studied as well, i.e. the signal efficiencies $\epsilon_S(\epsilon_B = 10^{-2})$, $\epsilon_S(\epsilon_B = 10^{-3})$ and $\epsilon_S(\epsilon_B = 10^{-4})$ are extracted, where ϵ_B denotes the background efficiency.

Uncertainties The uncertainty is extracted by repeating the training and evaluation five times with random shuffling of input vectors i.e. a vector in the training set in the first iteration can be assigned to the evaluation set in the second one. In each iteration, the performance metrics are determined. Their mean represents the nominal value and the quadratic sum of deviations from it is used as uncertainty.

Chapter 15

Reconstruction Strategy and Pre-Processing

Before the application of machine learning algorithms, a pre-processing is advisable to guarantee a high data quality. Although this study aims at developing a classification strategy that is closely tied to the underlying hardware and the raw data objects, which implies a minimal pre-processing procedure, an appropriate event selection and a proper preparation of the input vectors is required. Therefore, this chapter presents the reconstruction steps to select suitable events for training, testing and evaluating the algorithms. In addition, the construction of input vectors is described such that they are suitable for all machine learning algorithms. In all steps, the long-term goal of developing an online application is taken into account and all pre-processing steps are kept minimal.

15.1 Event Simulation and Selection

A monopole pair production is simulated (cf. Section 13.1.1). The monopole masses were varied in a range from 500 MeV to 5 GeV in steps of 500 MeV. The simulated monopoles are propagated through the Belle II detector using a Geant 4-based simulation approach and the energy loss formulae described in Section 13.1.2.

The event selection requires monopole hits in at least one of the PXD layers. The interaction of secondary particles with the PXD is not sufficient, since a direct detection of the monopoles is foreseen. The Monte Carlo truth information is exploited to filter the magnetic monopoles from secondary particles. In addition, the information is used to create simulation sets containing only monopoles and only anti-monopoles to evaluate their detection probability separately.

As a consequence of the event selection, the training, testing and evaluation sets do not contain monopoles with masses higher than 4 GeV, as they decay before reaching the PXD layers. The number of simulated events is chosen such that 1000 k monopole events are collected, except for the 4 GeV monopoles, where only 200 k events are used. The smaller event set is caused by the poor efficiency of reaching the PXD, which leads to prohibitively long simulation times. Examples of PXD hits associated with magnetic monopoles are shown in Fig. 15.1a. The clusters are marked by high charge values in the individual pixel hits.

PXD background data was recorded in dedicated beam-background runs taken in 2020 [310]. For these runs, only a single particle beam circulated in the SuperKEKB storage ring and the generation mechanisms described in Section 12.7 are responsible for background particles impinging on the PXD. All PXD hits are assumed to originate from beam background and are therefore selected for the training, testing and evaluation set. The possibility of having signal in the background set is addressed in Section 16.3.1. In Fig 15.1b, example clusters generated by background particles are displayed. The PXD hits are characterised by a small charge signal in each pixel and typically a long-stretched shape owing to the shallow entry angle into the PXD.

Typically, the raw pixel hits are pre-processed by applying an energy calibration and by filtering out noise hot spots. In particular the calibration is needed for a uniform pixel response and to iron out pixel-by-pixel variations in the energy measurement (cf. Section 6.3). However, in order to stick to a detector-near treatment in view of possible online applications, these steps are omitted and no pre-processing is performed. Nevertheless, to avoid the introduction of unaccountable systematic effects, a simulation of beam background is performed as well and the results from data are compared to simulation, where challenges such as noise hot spots can be controlled. It should be noted, that this study does not include a comparison between real and simulated background, as this can be found elsewhere [251, 310].

The simulated background also enables the selection of specific background processes. Therefore, simulation sets for different background mechanisms are investigated in Section 16.3.4. After the events are selected, the input vectors are created in a processing step denoted as object reconstruction.

15.2 Object Reconstruction

For each simulated event and for the background events, the charge values of a pixel matrix are considered around the PXD hit with the highest charge value (*seed pixel*). The size of the matrix should capture the majority of pixels responding to a given particle, while being as small as reasonably possible to reduce computation times. The cluster

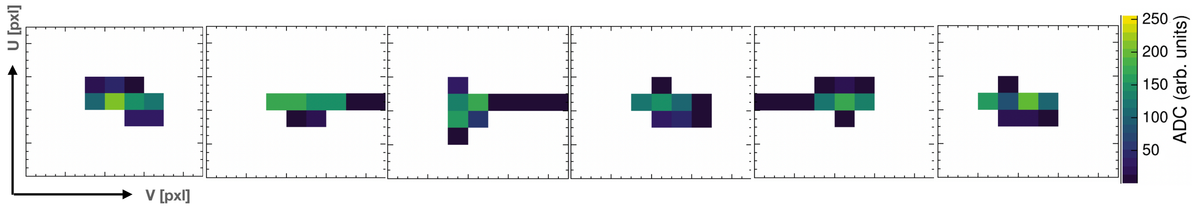

(a) Matrices associated with simulated magnetic monopoles with a mass of 3 GeV

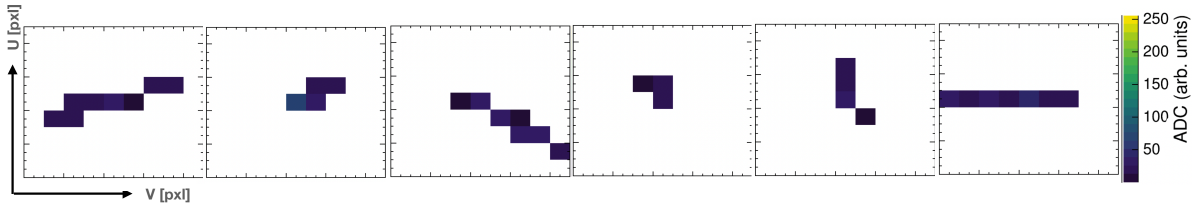

(b) Matrices associated with background particles

Figure 15.1. 9×9 pixel matrices for (a) real background data and (b) simulated magnetic monopoles. The pixel charge is given in ADC values.

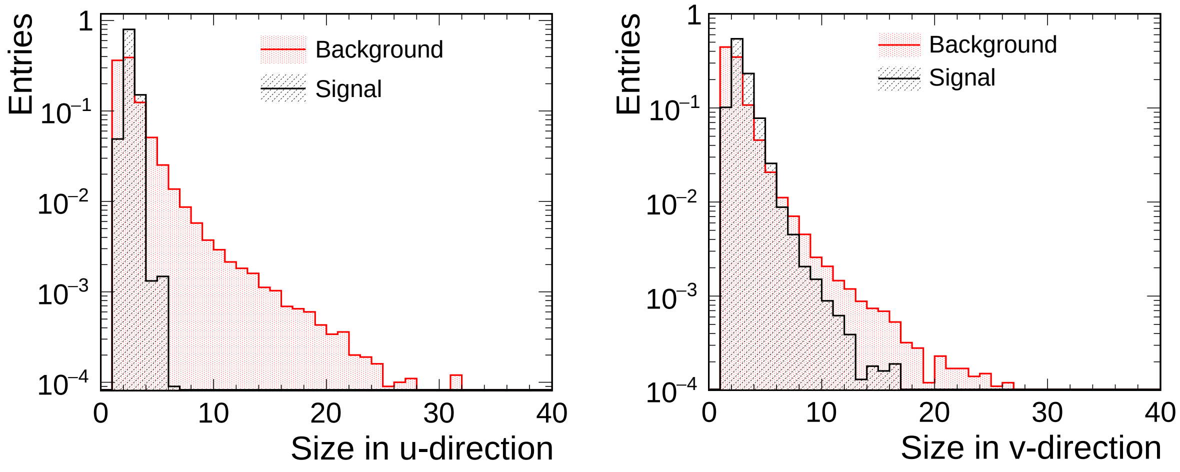

(a) Cluster size in u-direction **(b)** Cluster size in v-direction

Figure 15.2. PXD cluster size in (a) u- and (b) v-direction for beam background and simulated magnetic monopoles with a mass of 3 GeV.

size distributions in u-and v-direction for beam background and magnetic monopoles with a mass of 3 GeV are considered to estimate the optimal size of the pixel matrix. The distributions are displayed in Fig. 15.2. Cluster sizes larger than 10 are suppressed by more than three orders of magnitude in both directions and for both particle categories. Therefore, the default size of the pixel matrix is set to 9×9. Larger matrices of 15×15 and 25×25 are explored in Section 16.3.2 to ensure that the smaller 9×9 matrix captures all relevant information.

In addition to the pixel matrix, the global three-dimensional position of the seed pixel within the PXD is extracted. In total, 84 features are considered when the default matrix is used. The values are normalized to the range [0, 1] to avoid dominance of a single parameter. Dimensionality reduction using e.g. a Principle Component Analysis has exhibited adverse effects on the performance of the considered algorithms and is therefore not employed [311].

Chapter 16

Comparison of Supervised and Unsupervised Anomaly Detection

The performance of unsupervised anomaly detection is compared to an established supervised machine learning technique to assess its performance for the aforementioned classification problem.

First, a default training, testing and evaluation set is used, which consists of real data for the background events and simulated magnetic monopoles with a mass of 3 GeV for the signal events. No division between monopole and anti-monopole is made in the default sets. Other input sets for example for simulated background events or monopoles with different masses are studied in dedicated sections after the three algorithms are compared to each other.

16.1 Supervised Multi-Layer Perceptron

First, a supervised machine learning technique is considered, to which the unsupervised learning approaches are compared. A convolutional Multilayer Perceptron (MLP) is selected, since it is considered an established technique for binary classification problems. The network is trained on real background data and simulated hypothetical monopoles with a mass of 3 GeV. Therefore, assumptions about the signal enter the training process, as described in Section 14.1.

The network was implemented in the `PyTorch` framework [312,313]. Details about the network architecture can be found in the Appendix F and the hyperparamters are listed in Table 16.1. The network is optimised for a high background rejection. In the following, the training procedure of the MLP is outlined and an evaluation of its performance is shown.

Table 16.1. Hyperparameters for the Multilayer Perceptron.

Parameter	**Value**
Activation function	Rectified Linear Unit (ReLu)
Loss function	Cross Entropy
Optimizer	Stochastic Gradient Descent (SGD)
Learning Rate	1e-4
Momentum	0.9

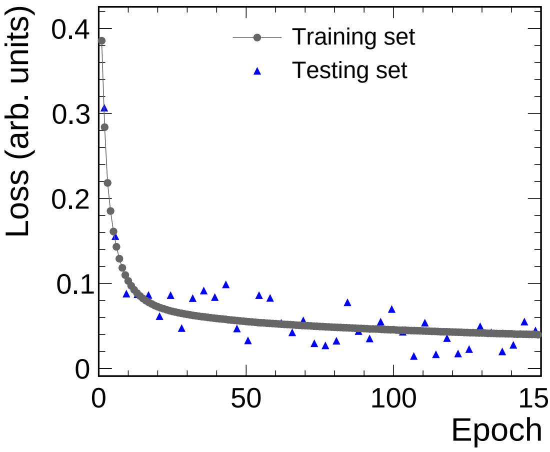

Figure 16.1. MLP loss as a function of training epoch for training and testing set.

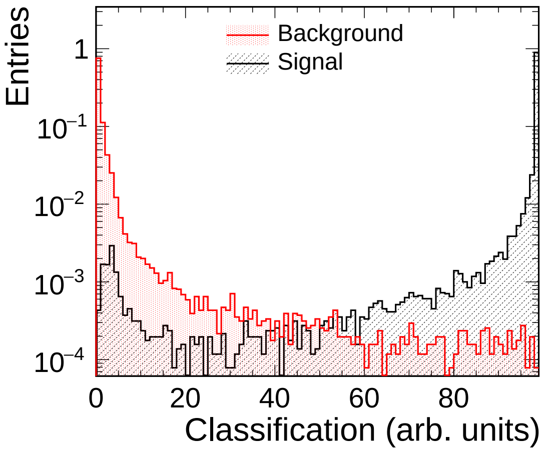

Figure 16.2. MLP classification distribution for signal and background.

Training The training is performed using 350 k background and signal events each. After very tenth training epoch, a dedicated testing set is presented to the MLP containing additional 150 k events for both classes. The training is stopped automatically once the reduction of the predicted error (*loss*) from the testing set is only marginal. The loss as a function of the training epoch is shown in Fig. 16.1. While conversion is achieved within the first 20 epochs of training, a shallow improvement of the MLP is still observable for high epoch numbers. The loss values for training and testing set agree reasonably well, which indicates that no overtraining has taken place.

Evaluation After training, an evaluation set comprising 500 k events for each class is considered to assess the performance of the algorithm. The one-dimensional classification distribution for both classes is presented in Fig. 16.2. For low/high classification values the signal/background is suppressed by approximately three orders of magnitude.

The corresponding ROC is shown in Fig. 16.3a. In Fig. 16.3b, a close-up is displayed of the parameter region, where simultaneously high background rejection and high sen-

Table 16.2. Performance metrics of the investigated machine learning techniques for the default evaluation set.

Algorithm	AUC [%]	$\epsilon_S(10^{-1})$ [%]	$\epsilon_S(10^{-2})$ [%]	$\epsilon_S(10^{-3})$ [%]	$\epsilon_S(10^{-4})$ [%]
MLP	$99.86^{+0.01}_{-0.02}$	100*	$97.3^{+0.2}_{-0.2}$	$82.4^{+1.2}_{-1.6}$	$30.0^{+4.3}_{-3.8}$
SOM	$98.15^{+0.04}_{-0.04}$	$97.3^{+0.2}_{-0.2}$	$94.0^{+0.8}_{-1.6}$	$88.7^{+3.8}_{-5.4}$	$56.8^{+7.1}_{-8.8}$
AE	$98.86^{+0.05}_{-0.02}$	$98.2^{+0.1}_{-0.3}$	$95.9^{+1.2}_{-0.4}$	$87.4^{+1.4}_{-1.2}$	$60.1^{+3.3}_{-2.7}$

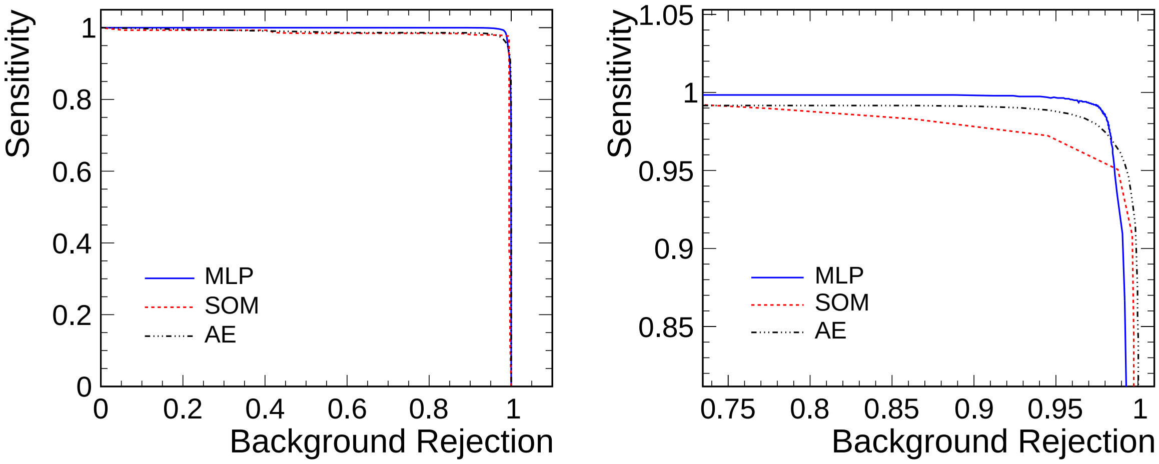

(a) Full axes range

(b) Close-up of the upper part of the ROC.

Figure 16.3. ROC for the Multilayer Perceptron (MLP), Self-Organizing Map (SOM) and Autoencoder (AE).

sitivity is achieved. The performance indicators are listed in Table 16.2. The AUC evaluates to $99.86^{+0.01}_{-0.02}$ % , which indicates an overall good classification performance. At high background rejection levels of $\epsilon_S(\epsilon_B = 10^{-4})$, the signal efficiency deteriorates to $30.0^{+4.3}_{-3.8}$ %.

16.2 Self-Organising Maps

A Self-Organizing Map (SOM) is an unsupervised machine learning technique, enabling the transformation of a high-dimensional dataset to a low-dimensional discrete grid, while keeping the topological structure. After training, inputs that are close in the high-dimensional input space are represented by adjacent grid points in the low-dimensional space (cf. Section 14.3). It is therefore well-suited to tag anomalous input structures, since they visually separate from normal data.

Typically, the low-dimensional space is represented by a two-dimensional map, where

Table 16.3. Hyperparameters used for the Self-Organizing Map

Parameter	**Value**
Nodes	70
Neighbourhood function	Gaussian
Gaussian width	7
Learning rate	0.01
Number of epochs	70 k - 100 k

accumulations of grid points mark similarities between input vectors. However in this study, the dimension of the low-dimensional grid space is set to one to allow for a comparable performance evaluation as for the other two machine learning techniques. The calculations of a ROC for a two-dimensional SOM would either require assumptions about the signal/background distribution or complex geometrical cuts in the map, that could introduce systematic uncertainties. It should be noted, that this is not a disadvantage of the SOM itself but only affects its comparability to other algorithms when a ROC is considered. The low-dimensional representation will therefore span only a single line, with the aim to have grid points responding to background cluster on the one end and signal on the other end.

The SOM was implemented in the python-based MiniSom software [314]. The hyperparameters of the SOM are listed in Tab 16.3. The 70 nodes were found to be sufficiently large to separate the two classes, while keeping reasonable training durations of about two hours.

Training The same training and testing set as for the MLP is used, except that the SOM is not presented with the target values. The lack of a loss function renders it challenging to monitor the training process. Therefore, a fixed number of training epochs is chosen and the result for the training and testing set is evaluated afterwards. It has been verified that an increase in the number of training epochs does not alter the results, which implies that stable convergence is achieved and no overtraining takes place.

Evaluation The trained one-dimensional grid serves as classification axis and is displayed in Fig. 16.4 for the evaluation set. The ROC displays a similar performance as the MLP, as shown in Fig. 16.3. While the AUC is $98.15^{+0.04}_{-0.04}\,\%$ and therefore lower than for the MLP, the signal efficiency at $\epsilon_S(\epsilon_B = 10^{-4})$ background rejection evaluates to $56.8^{+7.1}_{-8.8}\,\%$, which is superior to the MLP.

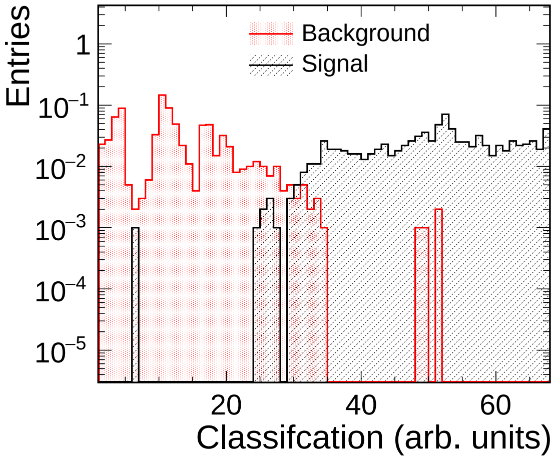

Figure 16.4. SOM classification distribution for signal and background.

Table 16.4. Hyperparameters used for the Autoencoder.

Parameter	**Value**
Activation function	Rectified Linear Unit (ReLu)
Loss function	Mean squared error
Optimizer	Adaptive Moment Estimation (Adam)
Learning rate	1e-4

16.3 Autoencoder

During training, only background events are presented to the AE and their reconstruction error is minimised, making the AE specialized in the reproduction of background events. In the evaluation phase, the AE is able to recognize background events by a low reconstruction error. Signal events appear anomalous to the AE and are characterised by a high error, that can therefore serve as an anomaly score [315].

Like the Multilayer Perceptron, the `PyTorch` framework was used to implement the AE. The architecture of the AE is shown in the Appendix F and the hyperparameters are listed in Tab 16.4.

Training The same amount of background events for training and testing as for the MLP are used. No signal events are presented to the AE during training. The reconstruction loss as a function of training epoch is depicted in Fig. 16.6 for the training and testing set. Convergence is achieved already after 10 – 20 epochs. The testing set exhibits similar reconstruction loss values as the training set, which indicates that no overtraining has taken place and the AE can generalize to unseen input sets.

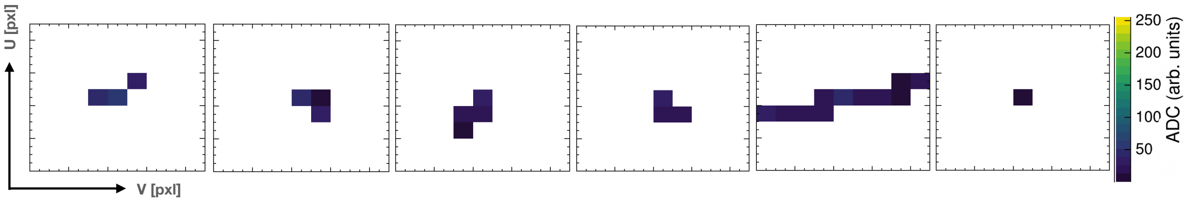

(a) Input matrices

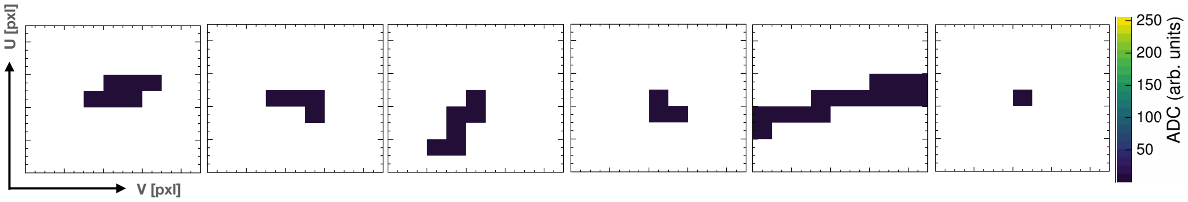

(b) Reconstructed matrices

Figure 16.5. (a) Input and (b) reconstructed pixel matrices associated with background particles.

Example clusters before and after reconstruction are depicted in Fig. 16.5. The upper row shows the input matrices of background events. In the lower row, the output of the AE is displayed with matrices in the same column belonging to the same event. While the overall shape is faithfully reproduced, the AE has a tendency to add more pixel hits to the matrix, which is related to the sparsity of the input matrix. Extensions of the traditional AE are proposed in the literature to mitigate this challenge [316,317]. It should be noted, that the AE does not aim for a perfect reconstruction but only for capturing the shape of the distribution. For this study, the reproduction is considered to be sufficient and therefore no extensions to account for sparse input matrices is needed.

Evaluation The classification distribution for the default evaluation set is displayed in Fig. 16.7. While there is a considerable overlap region for low reconstruction errors, a high signal purity is observable at high values. Example matrices of signal before and after reconstruction are depicted in Fig. 16.8. The unfamiliar shape and in particular the high ADC values pose a problem for the AE. While some shape characteristics are still preserved, the AE distorts the matrices in a way that they appear to be more background-like, i.e. instead of the concentrated pixel hit distribution, the distributions become long-stretched and the high ADC values are transformed to low ones. It is instructive to observe this behaviour, as it gives to some extent insight into the features learnt by the AE.

The resulting ROC of the AE is presented in Fig. 16.3 and the results are summarised in Table 16.2. The AUC evaluates to $98.86^{+0.05}_{-0.02}\,\%$ and is therefore worse compared to

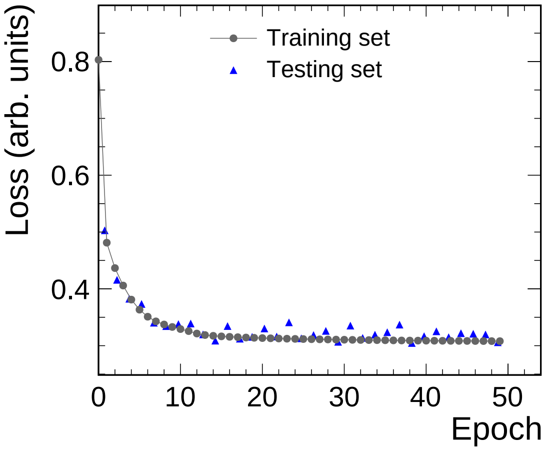

Figure 16.6. AE loss as a function of training epochs for training and testing set.

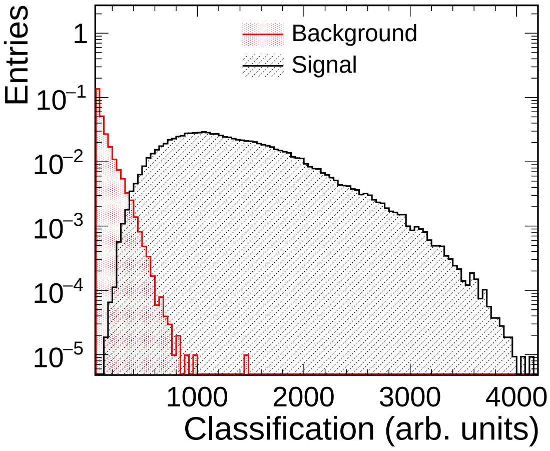

Figure 16.7. AE classification distribution for signal and background.

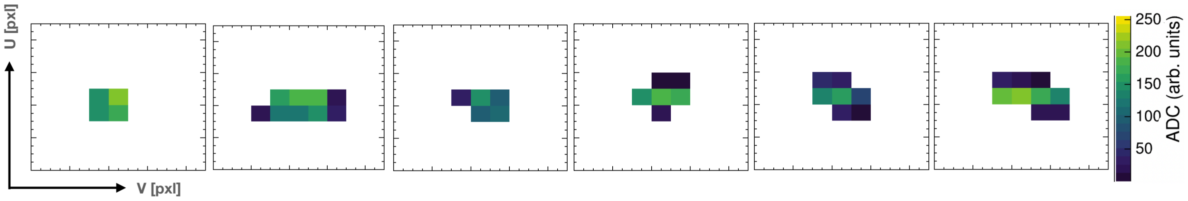

(a) Input matrices

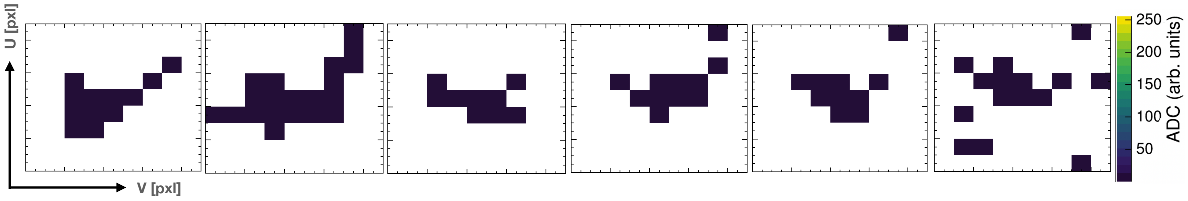

(b) Reconstructed matrices

Figure 16.8. (a) Input and (b) reconstructed pixel matrices associated with simulated magnetic monopoles.

the MLP but superior to the SOM. The signal efficiency at high background rejection levels still reaches $60.1^{+3.3}_{-2.7}\,\%$ showing that the AE outperforms the other two algorithms. Therefore, the performance of the AE is considered in more detail by addressing potential challenges such as an impure training set, technical details such as the size of the pixel matrix and the effect of specific signal and background properties. All studies are based on the comparison of ROCs or the performance matrices, since they allow for a direct assessment of the impact on the final results (cf. Section 14.5.2).

16.3.1 Signal in Training Data

No harsh selection filters on the pixel matrices in the background training set are applied. Therefore, the question arises if a hypothetical contamination of the background set with signal events affects the results. As a consequence of an impure training set, the AE is already exposed to signal during training and will consequently adapt to it, potentially resulting in a lower reconstruction error for signal and therefore a weaker classification performance. To evaluate the impact of a contaminated data set, 0.01 % / 0.1 % / 1 % of the training events are replaced by signal and the analysis is repeated. It should be noted that this study only aims at assessing the robustness of the AE, since the production of hypothetical magnetic monopoles in a single circulating beam without electron-positron collisions would not match with prevalent theories about monopole production.

The resulting ROCs are presented in Fig. 16.9. The performance of the AE deteriorates slightly at 1 % signal in the data but is not affected for the lower contamination values. It can be concluded that a signal component in the training set has to be sufficiently rare to guarantee the optimal performance of the AE. In the case of magnetic monopoles, a signal contamination of more than 1 % is considered highly improbable, assuming the production mechanisms and the theoretical approaches outlined in Section 13.1.

16.3.2 Size of Pixel Matrix

Based on the cluster size distribution shown in Section 15.2, the default size of the pixel matrix was fixed to 9×9. However, there are events, for which the pixel matrix does not capture the full extent of the cluster. With pixel hits being cut off, the classification performance is potentially compromised, since information of outer pixel hits is missing.

To investigate the impact of larger pixel matrices, the simulation and data events pertaining to the default matrix sets are considered and larger pixel matrices are extracted. The training, testing and evaluation steps are repeated and three ROCs belonging to matrix sizes of 9×9, 15×15 and 25×25 are computed, as illustrated in Fig. 16.10. An improvement for larger matrix sizes at low background rejection levels is observable. As

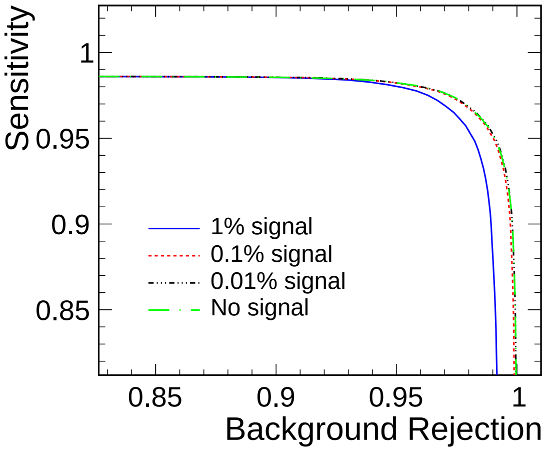

Figure 16.9. ROC for different signal levels in the training sample.

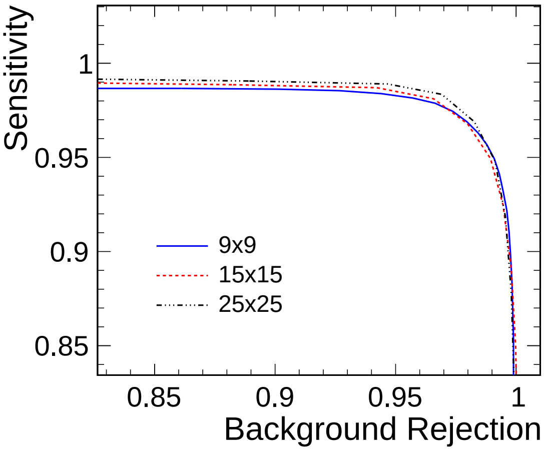

Figure 16.10. ROC for different sizes of the pixel matrix.

the improvement is comparably small, the concrete application of the AE decides about trading computation time for a slightly better performance. For this study, the improvement is considered too small to justify an increase in the matrix size and therefore the 9×9 is kept.

16.3.3 Simulated Background

Data from the PXD is subject to various effects that were not explicitly accounted for in this study such as particularly noisy pixels or pixel-by-pixel variations resulting in a slightly different AUC value for the same energy deposition. In online applications, correcting for these effects is not easily feasible. It is therefore beneficial to examine their impact on the classification performance. To this end, dedicated beam-background simulations are performed, involving all beam background mechanisms described in Section 12.7. The extraction of pixel matrices is conducted in the same manner as for data and an AE is trained and evaluated on the simulation.

The resulting ROC is compared to the one from data in Fig. 16.11. Good agreement between the two curves is achieved, which implies an excellent background modelling in simulation. In addition, remaining differences between data and simulation related to noisy pixels or pixel-by-pixel variations do not affect the results. Although noisy pixels have the potential to disturb the training, the results from the previous section imply that a disturbance of about 1 % of the considered matrices is necessary to affect the AE. While the pixel-by-pixel variations introduce uncertainties in the ADC values, the large difference in energy deposition between background and signal are not sensitive to these comparably small variations.

Table 16.5. Performance metrics for the AE trained on different simulated background sources.

Background	AUC [%]	$\epsilon_S(10^{-1})$ [%]	$\epsilon_S(10^{-2})$ [%]	$\epsilon_S(10^{-3})$ [%]	$\epsilon_S(10^{-4})$ [%]
Two photon	$99.52^{+0.06}_{-0.07}$	$98.6^{+0.3}_{-0.5}$	$94.4^{+0.6}_{-0.2}$	$87.9^{+0.8}_{-0.8}$	$60.4^{+0.8}_{-0.9}$
Bhabha (wide)	$98.97^{+0.05}_{-0.04}$	$97.0^{+0.2}_{-0.5}$	$93.1^{+0.2}_{-0.6}$	$87.3^{+0.9}_{-0.8}$	$59.8^{+1.3}_{-0.8}$
Bhabha (small)	$99.2^{+0.02}_{-0.04}$	$97.9^{+0.3}_{-0.2}$	$95.0^{+0.9}_{-0.7}$	$87.2^{+1.0}_{-0.9}$	$60.2^{+1.8}_{-2.6}$
Beam Gas	$98.2^{+0.1}_{-0.07}$	$96.0^{+0.2}_{-0.3}$	$93.9^{+1.0}_{-0.8}$	$86.2^{+1.1}_{-1.0}$	$58.1^{+1.3}_{-1.4}$
Touschek	$98.0^{+0.03}_{-0.07}$	$95.8^{+0.5}_{-0.4}$	$93.2^{+0.4}_{-0.6}$	$85.6^{+0.9}_{-1.1}$	$57.2^{+1.8}_{-2.4}$

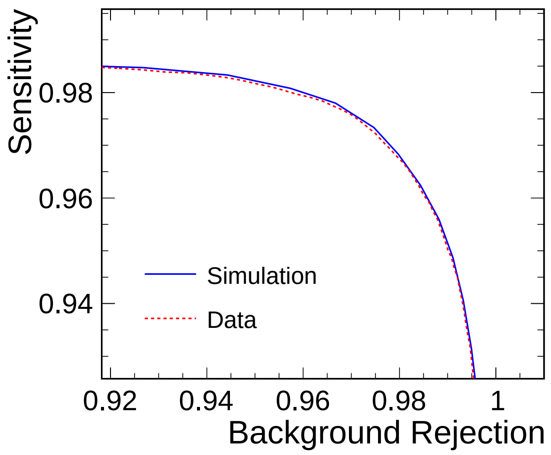

Figure 16.11. ROC for two Autoencoders trained on clusters from real background data and from simulated background.

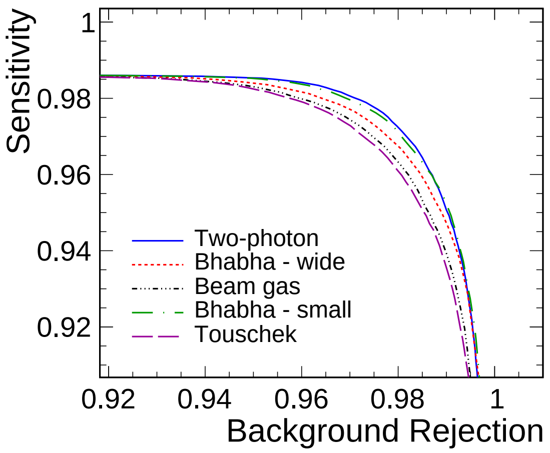

Figure 16.12. ROC for Autoencoders trained on simulated clusters from different background processes.

16.3.4 Different Background Sources

After the technical integrity of the AE was addressed, the effect of specific background and signal properties is studied in the following. For this purpose, the simulated background is considered, as it can be divided into the different background components introduced in Section 12.7.

A separate AE is trained for the principle background sources arising from the Touschek effect, beam-gas scattering, the two-photon process and radiative Bhabha scattering. The last process is split into events with a wide opening angles between the final-state leptons and a small angle. Even though the two-photon and the radiative Bhabha scattering are luminosity-dependent background sources, they are nevertheless tested in view of future applications, where a wider range of background sources is used to train the AE. Most importantly, the two-photon process is expected to become the dominant background source once the SuperKEKB accelerator runs at full luminosity [245].

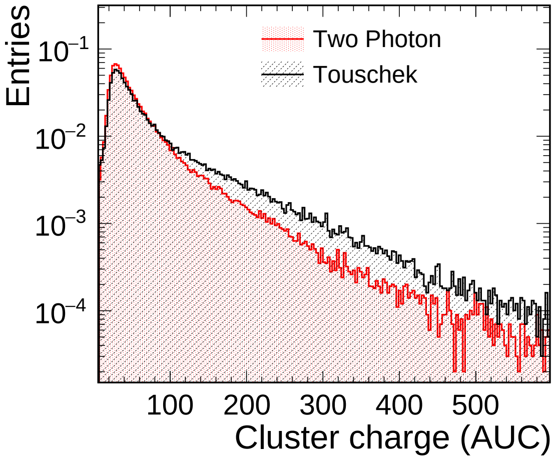

Figure 16.13. Cluster charge distribution from two-photon and Touschek background particles.

It is therefore essential to study the implications for future anomaly detection campaigns.

The ROC for the different background mechanisms are displayed in Fig. 16.12 and the performance metrics are listed in Table 16.5. While there is no significant difference between the background types, there is a tendency towards better identification results for luminosity-dependent background. Beam-background typically enters the PXD at a shallow angle, since the background particles are produced along the beam pipe and not directly at the interaction point. The shallow angle with respect to the PXD modules leads to larger clusters with a higher cluster charge (cf. Section 9.6), as can be seen for example in the cluster charge distributions for the luminosity-dependent two-photon process and the Touschek beam background depicted in Fig. 16.13. In particular the higher cluster charge is a property that is attributed to monopole clusters and therefore degrades the separation power.

16.3.5 Monopole Mass

The mass of the magnetic monopole determines the maximum initial momentum they can carry, since the centre-of-mass energy is fixed to 10.58 GeV. Therefore, high-mass monopoles have a smaller initial momentum, which can affect the cluster shape and consequently the AE performance. To investigate this effect, the AE is evaluated using five different monopole masses in the range from 0.5 GeV to 4 GeV. The ROCs are shown in Fig. 16.14 and the performance metrics are summarised in Table 16.6. Although the results are similar, there is a trend towards improved signal sensitivity at low/intermediate background rejection levels for low-mass monopoles. The difference is related to long-stretched clusters in v-direction, which are characteristic signature for beam-background

Table 16.6. Performance metrics for the AE evaluated with pixel matrices from magnetic monopoles with different masses.

Mass [GeV]	AUC [%]	$\epsilon_S(10^{-1})$ [%]	$\epsilon_S(10^{-2})$ [%]	$\epsilon_S(10^{-3})$ [%]	$\epsilon_S(10^{-4})$ [%]
0.5	$99.29^{+0.09}_{-0.07}$	$98.0^{+0.1}_{-0.1}$	$95.0^{+0.3}_{-0.4}$	$88.4^{+1.0}_{-0.9}$	$62.0^{+1.3}_{-0.8}$
1	$99.24^{+0.04}_{-0.06}$	$97.9^{+0.3}_{-0.4}$	$94.6^{+0.9}_{-0.9}$	$88.8^{+1.3}_{-0.7}$	$60.8^{+2.1}_{-0.8}$
2	$98.94^{+0.02}_{-0.04}$	$98.1^{+0.2}_{-0.3}$	$96.2^{+0.9}_{-0.7}$	$85.4^{+1.2}_{-1.1}$	$61.1^{+2.8}_{-3.1}$
3	$98.86^{+0.05}_{-0.02}$	$98.2^{+0.1}_{-0.3}$	$95.9^{+1.2}_{-0.4}$	$87.4^{+1.4}_{-1.2}$	$60.1^{+3.3}_{-2.7}$
4	$96.5^{+0.1}_{-0.0.6}$	$94.2^{+0.8}_{-0.3}$	$91.2^{+0.8}_{-0.4}$	$88.2^{+1.0}_{-1.1}$	$61.1^{+2.2}_{-3.7}$

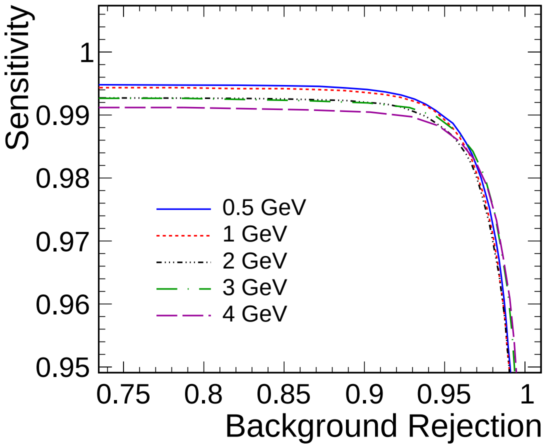

Figure 16.14. ROC for Autoencoders trained on clusters from magnetic monopoles with different masses.

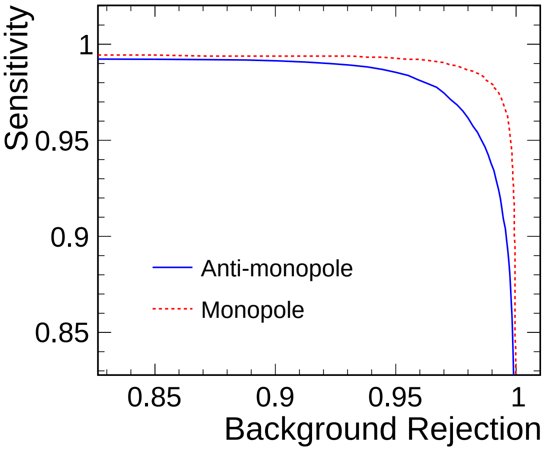

Figure 16.15. ROC for Autoencoders trained on simulated clusters from monopoles and anti-monopoles.

particles. The low initial momentum of high-mass monopoles leads to trajectories with a shallow angle between beam pipe and track due to the dominant acceleration along the magnetic field lines. As a result, the particles can enter the PXD in a shallow angle similar to beam-background particles created along the beam pipe. The similarity leads to a small deterioration in identification power for increasing mass.

16.3.6 Monopoles and Anti-Monopoles

So far, all simulated samples contained both monopoles and anti-monopoles. However, the difference in magnetic charge has important implications for their trajectories in the detector, since monopoles are accelerated in the direction of the electron beam and anti-monopoles in the opposite direction. As the collision is boosted in the electron beam direction, the maximum momentum of magnetic monopoles is higher compared to anti-

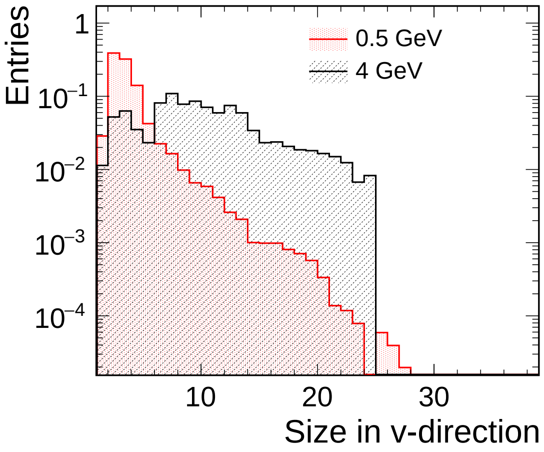

Figure 16.16. Cluster size in v-direction for different monopole masses.

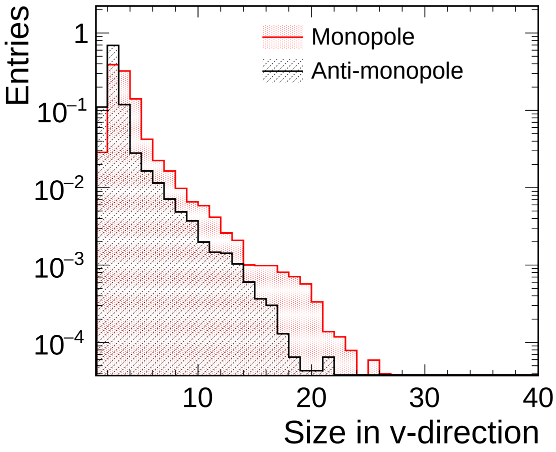

Figure 16.17. Cluster size in v-direction for monopoles and anti-monopoles.

Table 16.7. Performance metrics for the Autoencoder evaluated separately with monopoles and anti-monopoles.

Particle	AUC [%]	$\epsilon_S(10^{-1})$ [%]	$\epsilon_S(10^{-2})$ [%]	$\epsilon_S(10^{-3})$ [%]	$\epsilon_S(10^{-4})$ [%]
Monopoles	$97.82^{+0.06}_{-0.09}$	$97.8^{+0.3}_{-0.2}$	$94.1^{+0.2}_{-0.3}$	$82.4^{+0.8}_{-0.9}$	$51.3^{+1.3}_{-0.9}$
Anti-Monopoles	$99.34^{+0.04}_{-0.05}$	$98.0^{+0.1}_{-0.1}$	$95.6^{+0.9}_{-0.7}$	$89.0^{+9.8}_{-0.9}$	$62.1^{+1.8}_{-1.2}$

monopoles, for which acceleration and boost direction are anti-parallel. The different kinematics affect the AE results, as illustrated in the respective ROCs in Fig. 16.15 and the performance metrics in Table 16.7. The identification of anti-monopoles is more efficient, even at higher background rejection levels. The worse results for monopoles is related to their shallow entry angle into the PXD resulting in longer clusters as displayed in Fig. 16.17, similar to the results from the previous section. The long-stretched cluster shape is reminiscent of background clusters and therefore worsens the identification power.

16.3.7 Extensions to the Autoencoder

Further attempts to improve the AE or to find alternative but similar anomaly detection techniques have been made with no notable improvements. The most important ones are outlined in the following:

- The architecture of the AE was altered by e.g. including convolutional layers or adding more neurons to the latent space. No significant improvement in the performance was found, even though the reproduction of background matrices generally improves with a larger number of neurons in the latent space.

- Alternative hyper-parameters such as different loss functions were tested. The results either deteriorated or remained invariant. Likewise, a prolongation of the training duration also leaves the results unaltered, which confirms that stable convergence is achieved.

- Extensions to the AE and alternative algorithms were tested. For instance, a *Variational Autoencoder (VAE)* was implemented, which differs from a normal AE in the structure of the latent space. For a VAE, each neuron in the latent space is represented by the mean and standard deviation of a normal distribution. The decoder reconstructs the input vector by drawing from the set of distributions. The loss function is extended by a term enforcing a normal distribution of the latent space.

  The concepts behind anomaly detection with a VAE are identical to the normal AE. However, another layer of abstraction is added by sampling from normal distributions instead of the one-dimensional output of neurons in the latent space. In this way, the network is expected to achieve a better generalisation and capture the relevant features of the input vectors in well-defined distributions. Since the VAE has shown inferior results than the normal AE, it is not considered further. Adaptations to the VAE architecture might improve their results but are beyond the scope of this thesis.

  Alternatively, Generative Adversarial Networks [318] were tested as well. Although they have exhibited promising results in other studies [319, 320], where the reconstruction of input vectors was demanded, their comparably complex training procedure has proven to be unsuited for this work.

16.3.8 Conclusion

The AE has shown to keep up with the supervised MLP in terms of overall classification power and even outperform it for high background-rejection levels. Moreover, the AE has exhibited robustness against technical uncertainties related to the purity of the training set. Although this study only used data from beam background for training, the encouraging results for simulated luminosity-dependent background imply that future background campaigns involving other background sources will also yield satisfactory results. The positive validation of the approach enables a first test on collision data, that is presented in the following.

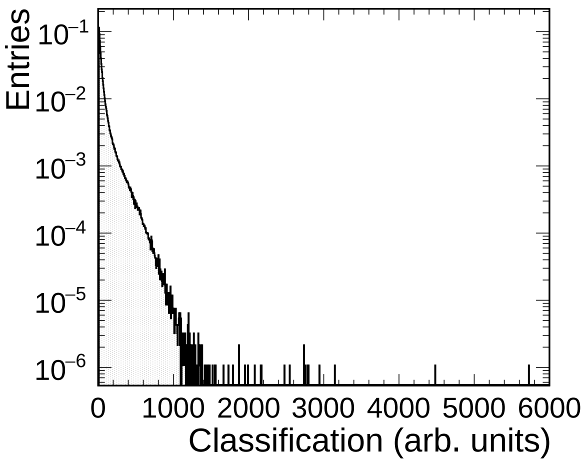

Figure 16.18. Classification distribution for data pertaining to randomly triggered events.

16.4 Search for Anomalies in Data

After the Autoencoder is trained and evaluated using simulations, it is applied to a data set recorded during Phase 3. The HLT was configured in pass-through mode to guarantee that no potentially relevant events are deleted. As the ROI selection was switched off, all PXD hits were recorded and written to permanent storage. In total, $0.67\,\mathrm{fb}^{-1}$ are considered.

Only randomly triggered events are selected, since the L1 trigger is largely insensitive to monopoles with masses exceeding 1 GeV (cf. Section 13.1.4). Two random trigger bits are available in the investigated data: the *Bhabha trigger*, that is issued 50 µs after the detection of a Bhabha event, and the *pseudo-random trigger* based on an independent local clock [245].

The same object reconstruction as for the simulations is applied, yielding the 9×9 pixel matrices plus the three-dimensional position in the PXD. The matrices are then presented to the trained Autoencoder and the resulting classification curve is displayed in Fig. 16.18. As expected, the distribution peaks at low classification values that indicate a low reconstruction loss and therefore background-like clusters. A few anomaly candidates are observable at higher classification values. To investigate them in more detail, a cut at classification value 1800 is applied. In total, 18 clusters pass the cut. They are shown in Fig. 16.19 and their cluster seed charge distribution is displayed in Fig. 16.20. Although the distribution is very sparse due to the low number of anomalous events, a trend towards exceptionally high seed charge values is observable. It can be concluded that the Autoencoder is indeed filtering events associated with very high energy depositions, without explicitly training it for this task.

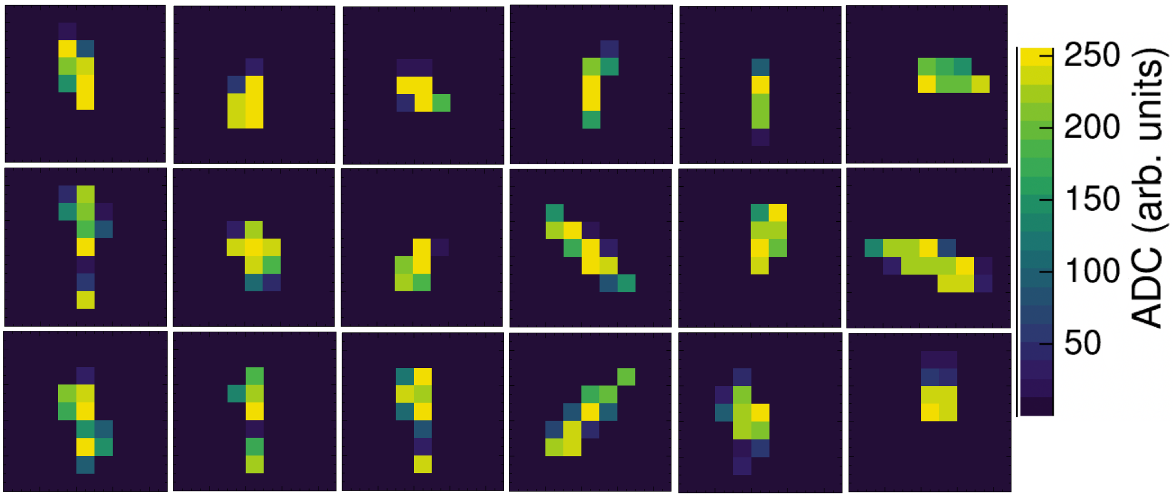

Figure 16.19. Pixel matrices with classification loss exceeding 1800.

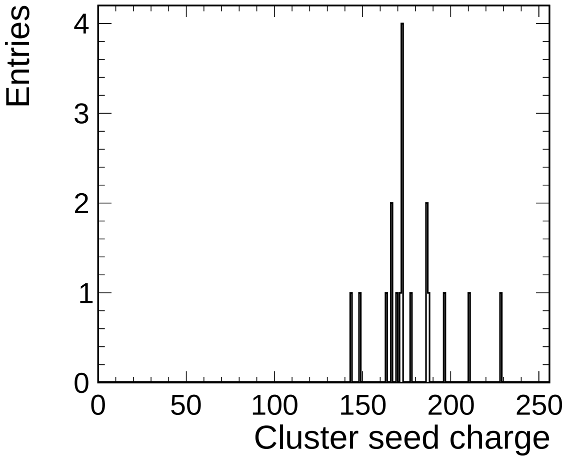

Figure 16.20. Cluster seed charge distribution for the clusters with classification loss exceeding 1800.

Chapter 17

Summary and Prospects

Present and future HEP experiments push the boundaries of current knowledge to extend our understanding of the fundamental properties of nature. For this purpose, particle colliders and multi-purpose detectors operate at the energy and intensity frontier using advanced technologies and data analysis methods. This dissertation has demonstrated the development of novel instruments and methods for present and future experiments by characterising and assessing a monolithic silicon sensor technology demonstrator and investigating advanced anomaly detection techniques for minimally-processed pixel-detector data.

A list of publications summarising the findings of this thesis is given in the Appendix G and an overview of the contributions to larger projects is presented in Appendix H.

Characterisation of a Small Collection-Electrode Monolithic CMOS Sensor Future experiments at particle colliders focusing on precision measurements of Higgs boson properties require an excellent secondary vertex and momentum resolution. This demand combined with the challenging operation environment at next-generation colliders, pose stringent requirements on the inner vertex and tracker detectors. Monolithic CMOS pixel sensors with a small collection electrode are attractive candidates for these detectors, since they offer a low material content and a high signal-to-noise ratio. The CLICTD technology demonstrator is designed in a 180 nm CMOS process and allows for the assessment of the monolithic small collection-electrode design. It targets the requirements of the CLIC tracker and was fabricated with different design characteristics regarding the pixel flavour, wafer material and sensor thickness. Investigating the advantages and disadvantages of the individual designs is an essential endeavour, which has important implications for future sensor designs.

In this thesis, CLICTD was first characterised in laboratory studies. For a successful operation of the sensor, the front-end settings were tuned and different CLICTD sensor designs and operation settings were investigated. It was shown that designs and settings that achieve a low input capacitance perform best with low noise levels of < 15 e and equally low noise-free detection thresholds of < 150 e. The innovative front-end design of CLICTD involves segmented detection channels consisting of sub-pixels with their own analogue front-end that share a common digital logic. In this way, the digital footprint is minimised and a small sub-pixel pitch is achieved. The laboratory studies allowed for a detailed investigation of the front-end design and confirmed its functionality.

The sensors were exposed to charged particle beams to asses their performance in a realistic operation environment. To this end, six test-beam measurement campaigns at the DESY II Test-Beam Facility were performed and the analysis of about 80×10^6 events of the available data was shown in this thesis. The charge-sharing properties, the hit-detection efficiency as well as the spatial and time resolution were investigated for a wide range of operation parameters by varying the detection threshold and bias voltages. It was found that the pixel flavours optimised for accelerated charge collection reduce the charge sharing and consequently improve the hit-detection efficiency and the time resolution. The best performance was achieved with sensors fabricated on high-resistivity Czochralski wafers, since they profit from a large active sensor volume, which leads to a higher signal.

All requirements for the CLIC tracker were found to be fulfilled for the optimised pixel flavours. A position resolution down to (3.9 ± 0.2) µm combined with a time resolution of (4.8 ± 0.1) ns was measured for perpendicular incidence of the particle beam despite limitations in the front-end. The hit-detection efficiency is higher than 99.7 % for a threshold range of several hundred electrons.

The sensors were also characterised using inclined particle tracks and a significant improvement in hit-detection efficiency at high thresholds was found owing to the longer particle path through the active sensor material. The spatial resolution is optimal around an inclination angle of 40°, where it evaluates to (3.6 ± 0.2) µm. In addition, the active sensor depth was determined using grazing angle measurements. For sensors with a high-resistivity epitaxial layer, the active depth was found to correspond to the nominal thickness of 30 µm of the epitaxial layer. For high-resistivity Czochralski sensors, the active depth scales with the substrate bias voltage and is about 60 µm at a voltage of -16 V.

As the pixel layout of high-performance silicon sensors becomes increasingly complex, advanced simulation frameworks are required to optimise design choices and predict the sensor performance. In this thesis, combined electrostatic finite-element and Monte Carlo simulations were presented that enable a high-precision sensor modelling as well as high simulation rates. The simulations were validated against transient finite-element simulations and test-beam measurements and excellent agreement was found over a wide parameter range. For instance, the maximum deviation of the cluster size is of the order of 5% and covered by the systematic uncertainties. The limiting factors in the simulation precision were found to pertain to the available information on the doping profiles and not to the simulation approach itself.

Once validated, example applications were shown, that complemented the laboratory and test-beam measurements and illustrated the versatility of the simulation approach. For instance, the sensor time resolution was investigated and determined to be of the order of a few ns, which confirmed that the front-end time resolution of CLICTD dominates the resolution of the device.

Prospects: Before a large-scale production of CLICTD could be initiated, a new submission of the sensor with a larger pixel matrix and an improved front-end design is necessary. In subsequent steps, the development and testing of a demonstrator detector module would be required, including e.g. chip-to-chip powering and communication.

The characterisation results of CLICTD sensors contribute to the development and validation of design choices in the small collection-electrode pixel layout, which is the basis for future developments using 65 nm CMOS technology. The smaller transistor size allows for a higher transistor density, which is beneficial for a reduced pixel size. As these devices have a thin active layer, which limits the measured signal, the optimised pixel flavours are crucial to achieve a high hit-detection efficiency [183].

The results from sensors with high-resistivity Czochralski substrate are important as well, especially for sensors where a significant amount of charge sharing is needed to optimise the spatial resolution for e.g. sensors in test-beam telescopes [321].

The simulation approach of combining three-dimensional finite-element simulations with the Monte Carlo method is a powerful instrument to optimise and evaluate silicon detectors regardless of their sensor design and applications. The results in this thesis illustrate the success of this method and the established simulation chain lays the foundation for a wide variety of applications. The pixel design of the novel 65 nm CMOS sensors is optimised using this simulation approach as well.

Comparison of Supervised and Unsupervised Anomaly Detection in Belle II Pixel Detector Data In the second part of this thesis, the identification of anomalous pixel-detector data at Belle II was investigated. Belle II profits from the high luminosity provided by the SuperKEKB collider as well as well-defined initial conditions of the colliding electron-positron beams. The Belle II detector is designed to deliver high-precision measurements to enable a rich physics programme that also involves the search for new physics scenarios. Despite the sophisticated design of the detector, the sensitivity to anomalous Highly-Ionising Particles (HIPs) is reduced due to the readout scheme of the detector. Particles with a sufficiently high energy loss or low momentum do not reach the outer sub-detectors and only generate hits in the inner tracking layers. However, pixel hits in the innermost sub-detector - the pixel detector (PXD) - are only considered if they are associated with a reconstructed particle track. The lack of data in the outer detectors prohibits the reconstruction of such a track and the relevant PXD data is thus filtered out making these particles undetectable. In this thesis, the feasibility of adding a veto system to the current readout design, relying solely on PXD data, is investigated to rescue potentially relevant PXD data. In particular, anomalous event signatures are targeted, as they could pertain to unaccounted physics scenarios. To validate the approach, hypothetical magnetic monopoles were simulated and identified against beam background data.

A machine-learning-based veto system was selected and the importance of unsupervised learning stressed, to avoid possible errors due to mis-modelling of background or signal. As an example, Self-Organising Maps and Autoencoders were considered and evaluated against a supervised convolutional Multilayer Perceptron. All three algorithms exhibited superb performance with AUCs well above 97 %.

To evaluate the suitability for anomaly detection purposes, the signal sensitivity at high background-rejection levels was extracted. While the Multilayer Perceptron is limited to signal efficiencies of approximately 30 %, the Self-Organizing Maps and the Autoencoder outperform the Multilayer Perceptron with 56 % and 60 %, respectively,

Using the Autoencoder, technical matters related to the size of the investigated pixel matrix or potentially impure datasets were addressed. Additionally, the impact of various background and signal properties on the performance of the classifier were studied. While results typically varied by less than 5 % to the nominal value, important features about the pixel-hit signatures of background and signal were discovered.

In conclusion, the feasibility of an unsupervised anomaly detection was successfully shown, which strengthens the case for data analyses using unsupervised machine learning.

Prospects: This thesis motivated the importance of alternative search strategies for undiscovered physics and showed the possibility of employing unsupervised anomaly detection. The offline analysis of the recorded data is an important milestone in this endeavour and paves the way towards potential online applications. In particular, the integration of a veto system into the PXD readout chain (e.g. on the ONSEN) would mark an important step to increase sensitivity to highly-ionising particles or particles with low momentum.

Appendix A

Mobility Parametrisation

For the MC simulations presented in this thesis, the Masetti-Canali charge carrier mobility was used:

$$\mu_{\text{MasettiCanali}} = \frac{\mu_m(N)}{\left(1 + (\mu_m(N) \cdot E/v_m)^{\beta}\right)^{1/\beta}}. \tag{A.1}$$

The phenomenological parameters v_m and β are taken from [322] as:

$$v_{m,e} = 1.53 \times 10^9 \cdot T^{-0.87} \text{cm}\,\text{s}^{-1} \qquad v_{m,h} = 1.62 \times 10^8 \cdot T^{-0.52} \text{cm}\,\text{s}^{-1}$$

$$\beta_e = 2.57 \times 10^{-2} \cdot T^{0.66} \qquad \beta_h = 0.46 \times 10^{-2} \cdot T^{0.17},$$

with e denoting electrons and h holes. The temperature dependence requires T to be given in Kelvin without including the unit in the calculation . The doping-dependent Masetti mobility $\mu_{m,e/h}(N)$ is given by [323]:

$$\mu_{m,e}(N) = \mu_{0,e} + \frac{\mu_{\max,e} - \mu_{0,e}}{1 + (N/C_{r,e})^{\alpha_e}} - \frac{\mu_{1,e}}{1 + (C_{s,e}/N)^{\beta_e}} \tag{A.2}$$

for electrons and

$$\mu_{m,h}(N) = \mu_{0,h} + \frac{\mu_{\max,h} - \mu_{0,h}}{1 + (N/C_{r,h})^{\alpha_h}} - \frac{\mu_{1,h}}{1 + (C_{s,h}/N)^{\beta_h}} + e^{P_c/N} \tag{A.3}$$

for holes. The phenomenological constants are obtained by numerical fitting to data. For this thesis, they are adopted from [323] as :

$$\begin{aligned} \mu_{0,e} &= 52.2\,\text{cm}^2\,\text{V}^{-1}\,\text{s}^{-1} \\ \mu_{\max,e} &= 1417\,\text{cm}^2\,\text{V}^{-1}\,\text{s}^{-1} \cdot (T/300\,\text{K})^{-2.5} \\ C_{r,e} &= 9.68 \times 10^{16}\,\text{cm}^3 \\ \alpha_e &= 0.68 \\ \mu_{1,e} &= 43.4\,\text{cm}^2\,\text{V}^{-1}\,\text{s}^{-1} \\ C_{s,e} &= 3.43 \times 10^{20}\,\text{cm}^3 \\ \beta_e &= 2.0 \end{aligned}$$

$$\begin{aligned} \mu_{0,h} &= 44.9\,\text{cm}^2\,\text{V}^{-1}\,\text{s}^{-1} \\ \mu_{\max,h} &= 470.5\,\text{cm}^2\,\text{V}^{-1}\,\text{s}^{-1} \cdot (T/300\,\text{K})^{-2.2} \\ C_{r,h} &= 2.23 \times 10^{17}\,\text{cm}^3 \\ \alpha_h &= 0.719 \\ \mu_{1,h} &= 29.0\,\text{cm}^2\,\text{V}^{-1}\,\text{s}^{-1} \\ C_{s,h} &= 6.1 \times 10^{20}\,\text{cm}^3 \\ \beta_h &= 2.0 \\ P_c &= 9.23 \times 10^{16}\,\text{cm}^3. \end{aligned}$$

Appendix B

Default CLICTD Configuration

Table B.1. Default configuration of the slow control registers of the CLICTD sensor. Deviations from the default values are mentioned explicitly in the text.

DAC	Value
VBIASResetTransistor	3
VRESET	104
VBIASLevelShift	9
VANALOG1	*scanned*
VANALOG2	*scanned*
VBIASPREAMPN	5
VNCASC	91
VPCASC	130
VFBK	71
VBIASIKRUM	4
VBIASDISCN	8

DAC	Value
VBIASDISCP	9
VBIASDAC	7
VNCASCCOMP	118
VBIASLevelShiftstby	1
VBIASPREAMPNstby	1
VBIASDISCNstby	1
VBIASDISCPstby	1
VBIASDACstby	1
VBIASSlowBuffer	15
AdjustDACRange	3
VLVDSD	15

Appendix C

Simulation Parameters of TCAD

The following Sentaurus TCAD tools from version 2019.12 are used:

- `SDE` as a structure editor to create the geometry
- `SDevice` for the device simulation to simulate the electrical characteristics of the sensor
- `SVisual` to visualise and analyse the simulation results.

In the the SDevice tool, the following physics models and parameters are selected:

```
Physics{
 Temperature = 300K

 Mobility (
 DopingDependence
 eHighFieldSaturation
 hHighFieldSaturation
 Enormal
 CarrierCarrierScattering
 )

 Recombination (
 SRH (DopingDependence)
 Band2Band (Hurkx)
 Auger (withGeneration)
 )
 EffectiveIntrinsicDensity (OldSlotboom)
}
```

Listing 1: Physics models and parameters used in the 3D TCAD simulations using the SDevice tool.

To obtain the electrostatic properties of the sensor, `Quasistationary` simulations are used, whereby voltages applied to all contacts are ramped up gradually until the target voltages are reached. In each step, the uncertainty on the electrostatic solution is required to be below a certain threshold, which ensures convergence of the final results. The capacitance is extracted from `ACCoupled` simulations, which allows for a small-signal AC analysis. The transient response to charge injection is calculated using a `Transient` simulation and the `HeavyIon` model is used to simulate charge injection.

Appendix D

Allpix Squared Configuration Files

```
[AllPix]
log_level = "INFO"
number_of_events = 500000
detectors_file = "detector.conf"
model_paths = "./"
root_file = "file_name.root"

[GeometryBuilderGeant4]
world_material = "air"

[DepositionGeant4]
physics_list = FTFP_BERT_EMZ
enable_pai = true
particle_type = "e-"
number_of_particles = 1
source_energy = 5.4GeV
source_position = 0um 0um -50mm
source_type = "beam"
beam_size = 0.3mm
beam_direction = 0 0 1
max_step_length = 1.0um

[DopingProfileReader]
model = "mesh"
file_name = "file_name.init"
field_offset = 0.5 0.5

[WeightingPotentialReader]
model = "mesh"
file_name = "file_name.init"
```

```
[ElectricFieldReader]
model = "mesh"
file_name = "file_name.init"
field_offset = 0.5 0.5

[TransientPropagation]
temperature = 293K
charge_per_step = 10
timestep = 0.0005ns
recombination_model = "srh"
mobility_model = "masetti_canali"
integration_time = 50ns
induction_matrix = 1,1

[PulseTransfer]

[DefaultDigitizer]
threshold = 150e
threshold_smearing = 30e
adc_resolution = 0
electronics_noise = 12e

[DetectorHistogrammer]
name = "dut"

[ROOTObjectWriter]
file_name = "file_name.root"
exclude = DepositedCharge, PropagatedCharge
```

Listing 2: Exemplary configuration file for the Allpix Squared simulations to replicate the test-beam measurements using version 2.0.

Appendix E

Corryvreckan Configuration Files

```
[Corryvreckan]
detectors_file = /path/to/detector_file
detectors_file_updated = /path/to/detector_file_updated

[EventLoaderEUDAQ2]
type = "CLICTD"
file_name = /path/to/CLICTD/data
get_time_residuals = true
pixel_value_toa = 0
countingmode = 0
longcnt = 0
inclusive = false

[EventLoaderEUDAQ2]
type="Timepix3"
file_name = /path/to/Timepix3/data
inclusive = false

[EventLoaderEUDAQ2]
type="TLU"
file_name = /path/to/TLU/data
inclusive = false

[EventLoaderEUDAQ2]
type="MIMOSA26"
file_name = /path/to/Mimosa26/data
inclusive = false
shift_triggers = 1

[Clustering4D]
time_cut_abs = 1ms
```

```
[Correlations]
do_time_cut = true
time_cut_abs = 10us

[Tracking4D]
min_hits_on_track = 7
spatial_cut_rel = 60 # M26: 4um,4um / TPX3: 10um,10um
exclude_dut = true
require_detectors = "Timepix3_0"
timestamp_from = "Timepix3_0"
momentum = 5.4GeV
track_model = "gbl"

[DUTAssociation]
spatial_cut_abs = 45um,56um
time_cut_abs = 2s
use_cluster_center = false

[EtaCorrection]
# Example values
eta_constants_x_CLICTD_0 = -0.00010162 1.35417 12.8879 -11341.2 -54473.3
↪  3.09228e+07
eta_constants_y_CLICTD_0 = -0.00122155 0.560778 1.14387 -1202.72 2766.75
↪  7.27664e+06

[AnalysisDUT]
chi2ndof_cut = 3

[AnalysisEfficiency]
chi2ndof_cut = 3
inpixel_bin_size = 1um
```

Listing 3: Example configuration file for the test-beam analysis with the Corryvreckan framework using version 2.0.

```
[TLU_0]
orientation = 0,0,0
orientation_mode = "xyz"
position = 0,0,0
role = "auxiliary"
type = "tlu"
```

```
[MIMOSA26_0]
mask_file = "path/to/mask/file/MIMOSA0"
material_budget = 0.00075
number_of_pixels = 1152, 576
orientation = -0.712759deg,-6.07713deg,-0.379642deg
orientation_mode = "xyz"
pixel_pitch = 18.4um,18.4um
position = -424.885um,1.81242mm,0
spatial_resolution = 4um,4um
time_resolution = 230us
type = "mimosa26"

[MIMOSA26_1]
mask_file = "path/to/mask/file/MIMOSA1"
material_budget = 0.00075
number_of_pixels = 1152, 576
orientation = 2.43805deg,2.9175deg,-0.152292deg
orientation_mode = "xyz"
pixel_pitch = 18.4um,18.4um
position = -1.21342mm,2.06874mm,277mm
spatial_resolution = 4um,4um
time_resolution = 230us
type = "mimosa26"

[MIMOSA26_2]
mask_file = "path/to/mask/file/MIMOSA2"
material_budget = 0.00075
number_of_pixels = 1152, 576
orientation = 2.69995deg,2.45913deg,0.0328878deg
orientation_mode = "xyz"
pixel_pitch = 18.4um,18.4um
position = -1.22653mm,1.85388mm,305mm
spatial_resolution = 4um,4um
time_resolution = 230us
type = "mimosa26"

[CLICTD_0]
mask_file = "path/to/mask/file/CLICTD"
material_budget = 0.00043
number_of_pixels = 128, 128
orientation = 176.953deg,2.70029deg,89.6465deg
orientation_mode = "xyz"
pixel_pitch = 37.5um,30um
position = 403.006um,2.86996mm,329mm
role = "dut"
```

```
spatial_resolution = 10.8um,8.7um
time_resolution = 6ns
type = "clictd"

[MIMOSA26_3]
mask_file = "path/to/mask/file/MIMOSA3"
material_budget = 0.00075
number_of_pixels = 1152, 576
orientation = 2.97543deg,2.08035deg,0.0261842deg
orientation_mode = "xyz"
pixel_pitch = 18.4um,18.4um
position = -551.174um,2.1176mm,348mm
spatial_resolution = 4um,4um
time_resolution = 230us
role = "reference"
type = "mimosa26"

[MIMOSA26_4]
mask_file = "path/to/mask/file/MIMOSA4"
material_budget = 0.00075
number_of_pixels = 1152, 576
orientation = -3.02058deg,-2.1573deg,-0.348244deg
orientation_mode = "xyz"
pixel_pitch = 18.4um,18.4um
position = -607.802um,2.01054mm,375mm
spatial_resolution = 4um,4um
time_resolution = 230us
type = "mimosa26"

[MIMOSA26_5]
mask_file = "path/to/mask/file/MIMOSA5"
material_budget = 0.00075
number_of_pixels = 1152, 576
orientation = -3.71855deg,-1.48155deg,0.147078deg
orientation_mode = "xyz"
pixel_pitch = 18.4um,18.4um
position = -656.691um,2.01103mm,623mm
spatial_resolution = 4um,4um
time_resolution = 230us
type = "mimosa26"

[Timepix3_0]
material_budget = 0.01068
number_of_pixels = 256, 256
orientation = 176.059deg,-0.634379deg,0.115394deg
```

```
orientation_mode = "xyz"
pixel_pitch = 55um,55um
position = -1.04743mm,955.904um,668mm
spatial_resolution = 10um,10um
time_resolution = 1ns
type = "timepix3"
```

Listing 4: Example geometry configuration file for the test-beam analysis with the Corryvreckan framework.

Appendix F

Architecture of Machine Learning Algorithms for Anomaly Detection

Table F.1. Network architecture of the MLP.

Layer	Kernel	Padding	Nodes	Activation
Convolutional 2D	3×3	1×1	84	Leaky ReLU
Convolutional 2D	3×3	1×1	128	Leaky ReLU
Convolutional 2D	3×3	1×1	256	Leaky ReLU
Linear	-	-	128	Leaky ReLU
Linear	-	-	32	Leaky ReLU
Linear	-	-	1	-

Table F.2. Network architecture of the AE.

Layer	Nodes	Activation
Linear	84	ReLU
Linear	64	ReLU
Linear	16	ReLU
Linear	8	ReLU
Linear	16	ReLU
Linear	64	ReLU
Linear	84	ReLU

Appendix G

List of Publications

Results presented in this thesis are published in the following journal articles and conference proceedings:

03/2022 **Comparison of Different Sensor Thicknesses and Substrate Materials for the Monolithic Small Collection-Electrode Technology Demonstrator CLICTD**
In CLICdp collaboration review, to be submitted to Nucl. Instr. Meth. A
Corresponding author

02/2022 **Comparison of Supervised and Unsupervised Anomaly Detection in Belle II Pixel Detector Data**
Submitted to Eur. Phys. J. C, arXiv:2202.07935
Corresponding author

12/2021 **Transient Monte Carlo Simulations for the Optimisation and Characterisation of Monolithic Silicon Sensors**
Nucl. Instrum. Meth. A 1031 (2022) 166491
Corresponding author

12/2021 **Performance of the FASTPIX sub-nanosecond CMOS Pixel Sensor Demonstrator**
Instruments 6 (2022) 13
Co-author

08/2021 **Test-beam characterisation of the CLICTD technology demonstrator- a small collection electrode High-Resistivity CMOS pixel sensor with simultaneous time and energy measurement**
Nucl. Instr. Meth. A 1006 (2021) 165396
Corresponding author

06/2021 **Test-beam and simulation studies for the CLICTD technology demonstrator - a monolithic CMOS pixel sensor with a small collection diode**
Submitted to JPS Conf. Proc., arXiv:2106.12925
Corresponding author

03/2021 **Corryvreckan: a modular 4D track reconstruction and analysis software for test beam data**
JINST 16 (03) (2021) P03008
Co-author

11/2020 **The CLICTD monolithic CMOS sensor**
Proceedings of the 29th International Workshop on Vertex Detectors (VERTEX2020)
Corresponding author

10/2020 **Silicon Vertex and Tracking Detector R&D for CLIC**
Proceedings of 40th International Conference on High Energy physics - PoS(ICHEP2020)
Corresponding author

10/2020 **Design and Characterization of the CLICTD Pixelated Monolithic Sensor Chip**
IEEE Trans. Nucl. Sci. 67 (10) (2020) 2263–2272
Co-author

06/2020 **Combining TCAD and Monte Carlo methods to simulate CMOS pixel sensors with a small collection electrode using the Allpix^2 framework**
Nucl. Instr. Meth. Phys. A 964 (2020) 163784
Co-author

04/2020 **Strategic R&D Programme on Technologies for Future Experiments - Annual Report 2020**
Annual Report CERN-EP-RDET-2021-001
Co-author

Appendix H

Contributions From the Author

The author contributed to the following overarching projects and software frameworks while working on this thesis. The project concerning anomaly detection in Belle II pixel-detector data was entirely planned and conducted by the author.

Test-Beam Campaigns and Laboratory Measurements of Various Silicon Detectors

The author contributed to all of the five one-week and one two-week test-beam campaigns for the CLICTD sensor, which were conducted at the DESY II Test-Beam Facility. The author compiled the measurement programme in consultation with the various experts in the group and prepared all of the sensors for the test-beam measurements, which included preparatory activities such as the organisation of the wire bonding of the sensor to the chipboard and laboratory measurements (IV characteristics, pixel-matrix equalisations, X-ray measurements, determination of the minimum threshold etc.). During the test beam, the author was involved in all activities such as assembling the measurement setup, monitoring and data-quality checks in collaboration with other team members. The reconstruction and analysis of the data was performed by the author.

The author was also involved in test-beam measurements of other silicon detectors and prototypes, namely the CLICpix2 ASIC bump bonded to planar silicon sensors, the Timepix3 ASIC interconnected with anisotropic conductive films to planar silicon sensors, the ATLASPix HV-CMOS sensor and the FASTPIX sensor. Besides the test-beam campaigns at DESY, the measurements were performed in four additional campaigns at the SPS at CERN. The author was mainly involved in monitoring activities and data-quality checks as well as in laboratory preparations for the CLICpix2 ASIC.

The Corryvreckan Reconstruction and Analysis Framework

The contribution of the author included code extensions and improvements to the framework, which involved the implementation of new features as well as testing and debugging of code from other developers. The author also presented a tutorial of the framework in an international detector school to master and PhD students.

The Allpix Squared Simulation Framework

The author contributed to new features within the framework, most importantly to the integration of different charge carrier mobility and recombination models. Contributions to the implementation of the Shockley-Ramo theorem for calculating the transient current were made as well, especially in the testing and debugging phase. Furthermore, the author supervised a student that initiated the integration of hexagonal pixel cells into the framework.

The author tested and optimised the combination of 3D TCAD simulations with the Allpix^2 framework and presented the results in several conferences and workshops. In particular, the author co-organised an Allpix^2 User Workshop to bring together the community, share results and discuss new developments.

All simulations shown in this thesis were performed by the author.

Simulation Studies for 65 nm CMOS Monolithic Silicon Sensors

The author contributed to the optimisation of the sensor layout for novel monolithic 65 nm CMOS sensors fabricated in the small collection-electrode design. The sensors are developed and characterised in an collaborative effort of various groups and institutes inside and outside of CERN. The contributions of the author focused mainly on transient Monte Carlo simulations.

Bibliography

[1] L. Evans and P. Bryant, "LHC machine," *JINST*, vol. 3, no. 08, p. S08001, 2008.

[2] G. Aad *et al.*, "Observation of a new particle in the search for the Standard Model Higgs boson with the ATLAS detector at the LHC," *Phys. Lett. B*, vol. 716, no. 1, pp. 1–29, 2012.

[3] S. Chatrchyan *et al.*, "Observation of a new boson at a mass of 125 GeV with the CMS experiment at the LHC," *Phys. Lett. B*, vol. 716, no. 1, pp. 30–61, 2012.

[4] G. Apollinari, O. Brüning, and L. Rossi, "High Luminosity LHC Project Description," Tech. Rep. CERN-ACC-2014-0321, CERN, 2014. `https://cds.cern.ch/record/1974419`.

[5] K. Albertsson *et al.*, "Machine learning in high energy physics community white paper," vol. 1085, no. 2, p. 022008, 2018.

[6] M. Thomson, *Modern particle physics.* Cambridge University Press, 2013.

[7] P. D. Group *et al.*, "Review of particle physics," *Prog. Theor. Exp. Phys.*, vol. 2020, no. 8, p. 083C01, 2020.

[8] M. D. Schwartz, *Quantum field theory and the Standard Model.* Cambridge University Press, 2014.

[9] E. Fermi, "Tentativo di una teoria dei raggi β," *Il Nuovo Cimento (1924-1942)*, vol. 11, no. 1, pp. 1–19, 1934.

[10] L. Di Lella and C. Rubbia, "The Discovery of the W and Z Particles," in *60 Years of CERN Experiments and Discoveries*, pp. 137–163, World Scientific, 2015.

[11] R. P. Feynman, "Mathematical formulation of the quantum theory of electromagnetic interaction," *Phys. Rev.*, vol. 80, no. 3, p. 440, 1950.

[12] J. Schwinger, "Quantum electrodynamics. I. A covariant formulation," *Phys. Rev.*, vol. 74, no. 10, p. 1439, 1948.

[13] S. L. Glashow, "Partial-symmetries of weak interactions," *Nucl. Phys. A*, vol. 22, no. 4, pp. 579–588, 1961.

[14] A. Salam, "8th Nobel Symposium Lerum," *Proc. C*, vol. 680519, p. 367, 1968.

[15] S. Weinberg, "Physical processes in a convergent theory of the weak and electromagnetic interactions," *Phys. Rev. Lett.*, vol. 27, no. 24, p. 1688, 1971.

[16] F. Englert and R. Brout, "Broken symmetry and the mass of gauge vector mesons," *Phys. Rev. Lett.*, vol. 13, no. 9, p. 321, 1964.

[17] P. W. Higgs, "Broken symmetries and the masses of gauge bosons," *Phys. Rev. Lett.*, vol. 13, no. 16, p. 508, 1964.

[18] J. Goldstone, A. Salam, and S. Weinberg, "Broken symmetries," *Phys. Rev.*, vol. 127, no. 3, p. 965, 1962.

[19] G. S. Guralnik, C. R. Hagen, and T. W. Kibble, "Global conservation laws and massless particles," *Phys. Rev. Lett.*, vol. 13, no. 20, p. 585, 1964.

[20] G. Aad *et al.*, "Combined Measurement of the Higgs Boson Mass in pp Collisions at $\sqrt{s} = 7$ and 8 TeV with the ATLAS and CMS Experiments," *Phys. Rev. Lett.*, vol. 114, no. 19, p. 191803, 2015.

[21] M. Robinson, *Symmetry and the standard model.* Springer, 2011.

[22] P. A. M. Dirac, "The quantum theory of the electron," *Proc. R. Soc.*, vol. 117, no. 778, pp. 610–624, 1928.

[23] C. D. Anderson, "The positive electron," *Phys. Rev.*, vol. 43, no. 6, p. 491, 1933.

[24] M. Blagojevic and F. W. Hehl, "Gauge theories of gravitation," *arXiv:1210.3775*, 2012.

[25] A. D. Sakharov, "Violation of CP-invariance, C-asymmetry, and baryon asymmetry of the Universe," in *In The Intermissions... Collected Works on Research into the Essentials of Theoretical Physics in Russian Federal Nuclear Center, Arzamas-16*, pp. 84–87, World Scientific, 1998.

[26] E. Kou *et al.*, "The Belle II physics book," *Prog. Theor. Exp. Phys.*, vol. 2019, no. 12, p. 123C01, 2019.

[27] A. A. Alves Jr *et al.*, "The LHCb detector at the LHC," *JINST*, vol. 3, no. 08, p. S08005, 2008.

[28] M. Persic, P. Salucci, and F. Stel, “The universal rotation curve of spiral galaxies—I. The dark matter connection,” *Mon. Notices Royal Astron. Soc.*, vol. 281, no. 1, pp. 27–47, 1996.

[29] N. Kaiser and G. Squires, “Mapping the dark matter with weak gravitational lensing,” *Astrophys. J.*, vol. 404, pp. 441–450, 1993.

[30] J. Einasto, “Dark matter,” *Braz. J. Phys.*, vol. 43, no. 5, pp. 369–374, 2013.

[31] R. H. Sanders and S. S. McGaugh, “Modified Newtonian dynamics as an alternative to dark matter,” *Annu. Rev. Astron. Astrophys.*, vol. 40, no. 1, pp. 263–317, 2002.

[32] P. D. Mannheim, “Alternatives to dark matter and dark energy,” *Prog. Part. Nucl.*, vol. 56, no. 2, pp. 340–445, 2006.

[33] S. Perlmutter *et al.*, “Supernovae, dark energy, and the accelerating universe,” *Phys. Today*, vol. 56, no. 4, pp. 53–62, 2003.

[34] R. Murgia, S. Gariazzo, and N. Fornengo, “Constraints on the coupling between dark energy and dark matter from CMB data,” *J. Cosmol. Astropart. Phys.*, vol. 2016, no. 04, p. 014, 2016.

[35] R. N. Cahn, “The eighteen arbitrary parameters of the Standard Model in your everyday life,” *Rev. Mod. Phys.*, vol. 68, no. 3, p. 951, 1996.

[36] M. Ibe, A. Kusenko, and T. T. Yanagida, “Why three generations?,” *Phys. Lett. B*, vol. 758, pp. 365–369, 2016.

[37] P. Fayet and S. Ferrara, “Supersymmetry,” *Phys. Rep.*, vol. 32, no. 5, pp. 249–334, 1977.

[38] P. Langacker, “Grand unified theories and proton decay,” *Phys. Rep.*, vol. 72, no. 4, pp. 185–385, 1981.

[39] L. Randall and R. Sundrum, “Large mass hierarchy from a small extra dimension,” *Phys. Rev. Lett.*, vol. 83, no. 17, p. 3370, 1999.

[40] J. Ellis, “Outstanding questions: physics beyond the Standard Model,” *Philos. Trans. R. Soc. A*, vol. 370, no. 1961, pp. 818–830, 2012.

[41] H. M. Lee, “Lectures on physics beyond the Standard Model,” *Korean Phys. Soc.*, pp. 1–33, 2021.

[42] H. Abramowicz and R. Forty, "Physics Briefing Book [Input for the European Strategy for Particle Physics Update 2020]," 2019. `https://www.osti.gov/biblio/1573232`.

[43] A. Abada *et al.*, "FCC-ee: the lepton collider," *Eur. Phys. J.: Spec. Top.*, vol. 228, no. 2, pp. 261–623, 2019.

[44] T. Charles *et al.*, "The Compact Linear e+e- Collider (CLIC)-2018 Summary Report," *CERN Yellow Report Monographs*, 2018.

[45] H. Abramowicz *et al.*, "Higgs physics at the CLIC electron–positron linear collider," *Eur. Phys. J. C*, vol. 77, no. 7, pp. 1–41, 2017.

[46] J. de Blas *et al.*, "The CLIC potential for new physics," *CERN Yellow Reports: Monographs*, 2018.

[47] H. Abramowicz *et al.*, "Top-quark physics at the CLIC electron-positron linear collider," *J. High Energy Phys.*, vol. 2019, no. 11, pp. 1–88, 2019.

[48] E. Accomando *et al.*, "Physics at the CLIC multi-TeV linear collider," *hep-ph/0412251*, 2004.

[49] A. Robson and P. Roloff, "Updated CLIC luminosity staging baseline and Higgs coupling prospects," *arXiv:1812.01644*, 2018.

[50] M. Aicheler *et al.*, "The Compact Linear Collider (CLIC)-project implementation plan," *arXiv:1903.08655*, 2019.

[51] S. Riemann, "Status and prospects of e^+e^- linear collider projects," tech. rep., Deutsches Elektronen-Synchrotron (DESY), 2015.

[52] D. Schulte, *Study of Electromagnetic and Hadronic Background in the Interaction Region of the TESLA Collider*. PhD thesis, 1997.

[53] D. Arominski, A. Sailer, and A. Latina, "Beam-induced backgrounds in CLICdet," Tech. Rep. CLICdp-Note-2019-007, CERN, 2019. `https://cds.cern.ch/record/2704642`.

[54] "The CLICdp webpage." Online : `https://clicdp.web.cern.ch`, accessed 12/2021.

[55] "Detector technologies for CLIC," *CERN Yellow Report Monographs*, May 2019.

[56] A. Tehrani *et al.*, “CLICdet: The post-CDR CLIC detector model,” Mar 2017. `https://cds.cern.ch/record/2254048`.

[57] M. Thomson, “Particle flow calorimetry and the PandoraPFA algorithm,” *Nucl. Instr. Meth. A*, vol. 611, no. 1, pp. 25–40, 2009.

[58] M. J. Williams, *Evaluation of fine-pitch hybrid silicon pixel detector prototypes for the CLIC vertex detector in laboratory and test-beam measurements.* PhD thesis, University of Glasgow, 2021. `https://cds.cern.ch/record/2766510`.

[59] A. M. Nurnberg and D. Dannheim, “Requirements for the CLIC tracker readout,” tech. rep., CERN, Apr 2017. `https://cds.cern.ch/record/2261066`.

[60] G. Blanchot, D. Dannheim, and C. Fuentes, “Power-pulsing schemes for vertex detectors at CLIC,” *JINST*, vol. 9, no. 01, p. C01005, 2014.

[61] F. Duarte Ramos, W. Klempt, and F.-X. Nuiry, “Experimental tests on the air cooling of the CLIC vertex detector,” Tech. Rep. CLICdp-Note-2016-002, 2016. `https://cds.cern.ch/record/2138963`.

[62] N. Wermes, “From hybrid to CMOS pixels... a possibility for LHC’s pixel future?,” *J. Instrum.*, vol. 10, no. 12, p. C12023, 2015.

[63] H. Spieler, *Semiconductor detector systems.* Oxford university press, 2005.

[64] H. Kolanoski and N. Wermes, *Teilchendetektoren.* Springer, 2016.

[65] G. Lutz *et al.*, *Semiconductor radiation detectors.* Springer, 2007.

[66] K. Seeger, *Semiconductor Statistics.* Springer, 2004.

[67] A. Kahn, “Fermi level, work function and vacuum level,” *Materials Horizons*, vol. 3, no. 1, pp. 7–10, 2016.

[68] A. M AL-Sheikh and K. S Hameed, “Theoretical study of energy gap for silicon and germanium under high pressure,” *Rafidain Journal of Science*, vol. 22, no. 3, pp. 58–68, 2011.

[69] A. Sproul and M. Green, “Improved value for the silicon intrinsic carrier concentration from 275 to 375 K,” *J. Appl. Phys.*, vol. 70, no. 2, pp. 846–854, 1991.

[70] S. S. Li and W. R. Thurber, “The dopant density and temperature dependence of electron mobility and resistivity in n-type silicon,” *Solid State Electron. Lett.*, vol. 20, no. 7, pp. 609–616, 1977.

[71] H. A. Bethe, “Passage of radiations through matter,” *Experimental Nuclear Physics*, 1953.

[72] V. Khodyrev, “On the origin of the Bloch correction in stopping,” *J. Phys. B*, vol. 33, no. 22, p. 5045, 2000.

[73] E. Fermi, “The ionization loss of energy in gases and in condensed materials,” *Phys. Rev.*, vol. 57, no. 6, p. 485, 1940.

[74] P. Sigmund and A. Schinner, “Notes on Barkas-Andersen effect,” *Eur. Phys. J. D*, vol. 68, no. 10, pp. 1–8, 2014.

[75] H. Bichsel, “Straggling in thin silicon detectors,” *Rev. Mod. Phys.*, vol. 60, no. 3, p. 663, 1988.

[76] L. D. Landau, “On the energy loss of fast particles by ionization,” *J. Phys.*, vol. 8, pp. 201–205, 1944.

[77] P. Vavilov, “Ionization losses of high-energy heavy particles,” *Soviet Phys. JETP*, vol. 5, 1957.

[78] S. Meroli, D. Passeri, and L. Servoli, “Energy loss measurement for charged particles in very thin silicon layers,” *JINST*, vol. 6, no. 06, p. P06013, 2011.

[79] W. Allison and J. Cobb, “Relativistic charged particle identification by energy loss,” *Annu. Rev. Nucl. Part. Sci.*, vol. 30, no. 1, pp. 253–298, 1980.

[80] F. Wang, S. Dong, B. Nachman, M. Garcia-Sciveres, and Q. Zeng, “The impact of incorporating shell-corrections to energy loss in silicon,” *Nucl. Instr. Meth. A*, vol. 899, pp. 1–5, 2018.

[81] J. Apostolakis, S. Giani, L. Urban, M. Maire, A. Bagulya, and V. Grichine, “An implementation of ionisation energy loss in very thin absorbers for the GEANT4 simulation package,” *Nucl. Instr. Meth. A*, vol. 453, no. 3, pp. 597–605, 2000.

[82] K. A. Olive *et al.*, “Review of particle physics,” *Chinese Phys. C*, vol. 38, no. 9, p. 090001, 2014.

[83] V. L. Highland, “Some practical remarks on multiple scattering,” *Nucl. Instr. Meth.*, vol. 129, no. 2, pp. 497–499, 1975.

[84] G. R. Lynch and O. I. Dahl, “Approximations to multiple Coulomb scattering,” *Nucl. Instr. Meth. B*, vol. 58, no. 1, pp. 6–10, 1991.

[85] O. Klein and Y. Nishina, “Über die Streuung von Strahlung durch freie Elektronen nach der neuen relativistischen Quantendynamik von Dirac,” *Zeitschrift für Physik*, vol. 52, no. 11, pp. 853–868, 1929.

[86] “Atlas user’s manual,” tech. rep., Silvaco Int. Santa Clara, CA, 2011. `https://www.eng.buffalo.edu/~wie/silvaco/atlas_user_manual.pdf`.

[87] G. Masetti, M. Severi, and S. Solmi, “Modeling of carrier mobility against carrier concentration in arsenic-, phosphorus-, and boron-doped silicon,” *IEEE Trans. Elec. Dev.*, vol. 30, no. 7, pp. 764–769, 1983.

[88] C. Canali, G. Majni, R. Minder, and G. Ottaviani, “Electron and hole drift velocity measurements in silicon and their empirical relation to electric field and temperature,” *IEEE Trans. Elec. Dev.*, vol. 22, no. 11, pp. 1045–1047, 1975.

[89] A. Einstein, “Über die von der molekularkinetischen Theorie der Wärme geforderte Bewegung von in ruhenden Flüssigkeiten suspendierten Teilchen,” *Annalen der Physik*, vol. 4, 1905.

[90] M. Von Smoluchowski, “Zur kinetischen Theorie der Brownschen Molekularbewegung und der Suspensionen,” *Annalen der Physik*, vol. 326, no. 14, pp. 756–780, 1906.

[91] R. N. Hall, “Electron-hole recombination in germanium,” *Phys. Rev.*, vol. 87, no. 2, p. 387, 1952.

[92] W. Shockley, Wand Read Jr, “Statistics of the recombinations of holes and electrons,” *Phys. Rev.*, vol. 87, no. 5, p. 835, 1952.

[93] J. Fossum and D. Lee, “A physical model for the dependence of carrier lifetime on doping density in nondegenerate silicon,” *Solid-State Electron. Lett.*, vol. 25, no. 8, pp. 741 – 747, 1982.

[94] J. G. Fossum, “Computer-aided numerical analysis of silicon solar cells,” *Solid-State Electron. Lett.*, vol. 19, no. 4, pp. 269 – 277, 1976.

[95] J. Fossum, R. Mertens, D. Lee, and J. Nijs, “Carrier recombination and lifetime in highly doped silicon,” *Solid-State Electron. Lett.*, vol. 26, no. 6, pp. 569–576, 1983.

[96] M. Kerr and A. Cuevas, “General parametrization of Auger Recombination in crystalline silicon,” *J. Appl. Phys.*, vol. 91, 2002.

[97] J. Dziewior and W. Schmid, "Auger coefficients for highly doped and highly excited silicon," *Appl. Phys. Lett.*, vol. 31, no. 5, p. 346, 1977.

[98] M. Garcia-Sciveres and N. Wermes, "A review of advances in pixel detectors for experiments with high rate and radiation," *Rep. Prog. Phys.*, vol. 81, no. 6, p. 066101, 2018.

[99] L. Rossi, P. Fischer, T. Rohe, and N. Wermes, *Pixel Detectors: From Fundamentals to Applications.* Springer, 2006.

[100] Z. Li, "Radiation damage effects in Si materials and detectors and rad-hard Si detectors for SLHC," *JINST*, vol. 4, no. 03, p. P03011, 2009.

[101] W. Snoeys *et al.*, "FASTPIX: sub-nanosecond radiation tolerant CMOS pixel sensors." `https://phase1.attract-eu.com/wp-content/uploads/2019/05/FASTPIX.pdf`.

[102] T. Kugathasan *et al.*, "Monolithic CMOS sensors for sub-nanosecond timing," *Nucl. Instr. Meth. A*, vol. 979, p. 164461, 2020.

[103] W. Shockley, "Currents to conductors induced by a moving point charge," *J. Appl. Phys.*, vol. 9, no. 10, pp. 635–636, 1938.

[104] S. Ramo, "Currents induced by electron motion," *Proceedings of the IRE*, vol. 27, no. 9, pp. 584–585, 1939.

[105] W. Riegler and G. A. Rinella, "Point charge potential and weighting field of a pixel or pad in a plane condenser," *Nucl. Instr. Meth. A*, vol. 767, pp. 267 – 270, 2014.

[106] F. Krummenacher, "Pixel detectors with local intelligence: an IC designer point of view," *Nucl. Instr. Meth. A*, vol. 305, no. 3, pp. 527–532, 1991.

[107] L. Palotas *et al.*, *Elektronik für Ingenieure: Analoge und digitale integrierte Schaltungen.* Vieweg+Teubner Verlag, 2013.

[108] M. J. Buckingham, "Noise in electronic devices and systems," *John Wiley & Sons, Inc.*, 1983.

[109] H. Theuerer, J. Whelan, H. Bridgers, and E. Buehler, "Heat Treatment of Silicon Using Zone Heating Techniques," *J. Electrochem. Soc.*, vol. 104, no. 12, p. 721, 1957.

[110] J. Czochralski, “Ein neues Verfahren zur Messung der Kristallisationsgeschwindigkeit der Metalle,” *Zeitschrift für physikalische Chemie*, vol. 92, no. 1, pp. 219–221, 1918.

[111] H. G. Heiner Ryssel, *Ion Implantation Techniques.* Springer, 1982.

[112] I. Kremastiotis *et al.*, “Design and standalone characterisation of a capacitively coupled HV-CMOS sensor chip for the CLIC vertex detector,” *JINST*, vol. 12, no. 09, p. P09012, 2017.

[113] M. Aleksa *et al.*, “Strategic R&D Programme on Technologies for Future Experiments,” Tech. Rep. CERN-OPEN-2018-006, CERN, Geneva, Dec 2018. `https://cds.cern.ch/record/2649646`.

[114] M. Bazilchuk, S. R. Pettersen, H. Kristiansen, Z. Zhang, and J. He, “Electromechanical characterization of individual micron-sized metal coated polymer particles,” *J. Appl. Phys.*, vol. 119, no. 24, p. 245102, 2016.

[115] F. Anghinolfi *et al.*, “RD19: status report and addendum, development of hybrid and monolithic silicon micropattern detectors,” tech. rep., CERN, 1993. `"https://cds.cern.ch/record/291180"`.

[116] K. Becks *et al.*, “Commissioning of the DELPHI pixel detector,” *Nucl. Instr. Meth. A*, vol. 418, no. 1, pp. 15–21, 1998.

[117] R. Turchetta *et al.*, “CMOS Monolithic Active Pixel Sensors (MAPS): New ‘eyes’ for science,” *Nucl. Instr. Meth. A*, vol. 560, no. 1, pp. 139–142, 2006.

[118] M. Winter *et al.*, “Achievements and perspectives of CMOS pixel sensors for charged particle tracking,” *Nucl. Instr. Meth. A*, vol. 623, no. 1, pp. 192–194, 2010.

[119] L. Greiner *et al.*, “A MAPS based vertex detector for the STAR experiment at RHIC,” *Nucl. Instr. Meth. A*, vol. 650, no. 1, pp. 68–72, 2011.

[120] I. Perić, “A novel monolithic pixelated particle detector implemented in high-voltage CMOS technology,” *Nucl. Instr. Meth. A*, vol. 582, no. 3, pp. 876–885, 2007.

[121] H. Augustin *et al.*, “The MuPix high voltage monolithic active pixel sensor for the Mu3e experiment,” *JINST*, vol. 10, no. 03, p. C03044, 2015.

[122] J. Kröger, *Characterisation of a High-Voltage Monolithic Active Pixel Sensor Prototype for Future Collider Detectors.* PhD thesis, University of Heidelberg, 2021. `https://cds.cern.ch/record/2784385`.

[123] J. W. van Hoorn, *Study and Development of a novel Silicon Pixel Detector for the Upgrade of the ALICE Inner Tracking System*. PhD thesis, TU Vienna, 2015. `https://cds.cern.ch/record/2119197`.

[124] B. Abelev *et al.*, “Technical design report for the upgrade of the ALICE inner tracking system,” *J. Phys. G: Nucl. Part. Phys.*, vol. 41, no. 8, p. 087002, 2014.

[125] M. Koziel *et al.*, “The prototype of the Micro Vertex Detector of the CBM Experiment,” *Nucl. Instr. Meth. A*, vol. 732, pp. 515–518, 2013.

[126] I. Kremastiotis, *Implementation and characterisation of monolithic CMOS pixel sensors for the CLIC vertex and tracking detectors*. PhD thesis, KIT, Karlsruhe, 2020.

[127] I. Kremastiotis *et al.*, “Design and characterisation of the CLICTD pixelated monolithic sensor chip,” *IEEE Trans. Nucl. Sci.*, vol. PP, pp. 1–1, 08 2020.

[128] W. Snoeys, “Monolithic pixel detectors for high energy physics,” *Nucl. Instr. Meth. A*, vol. 731, pp. 125–130, 2013.

[129] G. A. Rinella *et al.*, “The ALPIDE pixel sensor chip for the upgrade of the ALICE Inner Tracking System,” *Nucl. Instr. Meth. A*, vol. 845, pp. 583–587, 2017.

[130] D. Dannheim *et al.*, “Comparison of small collection electrode CMOS pixel sensors with partial and full lateral depletion of the high-resistivity epitaxial layer,” *Nucl. Instr. Meth. A*, vol. 927, pp. 187–193, 2019.

[131] W. Snoeys *et al.*, “A process modification for CMOS monolithic active pixel sensors for enhanced depletion, timing performance and radiation tolerance,” *Nucl. Instr. Meth. A*, vol. 871, pp. 90 – 96, 2017.

[132] M. Munker *et al.*, “Simulations of CMOS pixel sensors with a small collection electrode, improved for a faster charge collection and increased radiation tolerance,” *JINST*, vol. 14, pp. C05013–C05013, May 2019.

[133] M. Munker, *Test beam and simulation studies on High Resistivity CMOS pixel sensors*. PhD thesis, University of Bonn, 2018. `https://cds.cern.ch/record/2644054?ln=de`.

[134] N. Semiconductors, “I2C-bus specification and user manual UM10204.” Online: `http://www.nxp.com/documents/user_manual/UM10204.pdf`, accessed 01/2022.

[135] R. Cardella *et al.*, “MALTA: an asynchronous readout CMOS monolithic pixel detector for the ATLAS High-Luminosity upgrade,” *JINST*, vol. 14, no. 06, p. C06019, 2019.

[136] J. Prabket *et al.*, “Resistivity profile of epitaxial layer for the new ALICE ITS sensor,” *JINST*, vol. 14, no. 05, p. T05006, 2019.

[137] H. Pernegger *et al.*, “Radiation hard monolithic CMOS sensors with small electrodes for High Luminosity LHC,” *Nucl. Instr. Meth. A*, vol. 986, p. 164381, 2021.

[138] H. Liu *et al.*, “Development of a modular test system for the silicon sensor R&D of the ATLAS Upgrade,” *JINST*, vol. 12, no. 01, p. P01008, 2017.

[139] T. Vanat, “Caribou – A versatile data acquisition system,” *PoS*, vol. TWEPP2019, p. 100, 2020.

[140] “The Caribou framework.” Online: `https://gitlab.cern.ch/Caribou/Caribou`, accessed 01/2022.

[141] “ZC706 Evaluation Board for the Zynq-7000 XC7Z045 SoC.” Online : `https://www.xilinx.com/support/documentation/boards_and_kits/zc706/ug954-zc706-eval-board-xc7z045-ap-soc.pdf`, accessed 12/2021.

[142] “SEARAY High-Density Open-Pin-Field Arrays.” Online : `https://www.samtec.com/connectors/high-speed-board-to-board/high-density-arrays/searay`, accessed 12/2021.

[143] “Staystik 571 - Silver Filled Electrically Conductive Film.” Online: `https://www.macdermidalpha.com/sites/default/files/2021-08/STAYSTIK-571-EN-19Sep19-TDS.pdf`, accessed 01/2022.

[144] “Keithley 2400 Graphical Series SMU instruments.” Online : `https://www.tek.com/en/products/keithley/source-measure-units/2400-graphical-series-sourcemeter`, accessed 12/2021.

[145] “The Peary software.” Online: `https://gitlab.cern.ch/Caribou/peary`, accessed 01/2022.

[146] P. D. Group, “Atomic and nuclear properties of materials,” *Eur. Phys. J. C*, vol. 15, pp. 80–81, 2000.

[147] C. Adler, “Radiation length of the ALICE TRD,” 2006. `https://www-physics.lbl.gov/~gilg/PixelUpgradeMechanicsCooling/Material/Radiationlength.pdf`.

[148] "X'Pert PRO System - User's Guide 040501." Online : `https://labs.jhu.edu/wp-content/uploads/2016/04/Introduction-to-XPert-Pro.pdf`, accessed 01/2022.

[149] M. Plakhotnyuk, *Nanostructured Heterojunction Crystalline Silicon Solar Cells with Transition Metal Oxide Carrier Selective Contacts.* PhD thesis, DTU Nanotech, 2018.

[150] M. O. Krause and J. Oliver, "Natural widths of atomic K and L levels, K_α X-ray lines and several KLL Auger lines," *J. Phys. Chem. Ref. Data*, vol. 8, no. 2, pp. 329–338, 1979.

[151] F. Scholze, H. Rabus, and G. Ulm, "Mean energy required to produce an electron-hole pair in silicon for photons of energies between 50 and 1500 eV," *J. Appl. Phys.*, vol. 84, no. 5, pp. 2926–2939, 1998.

[152] M. Mazziotta, "Electron–hole pair creation energy and Fano factor temperature dependence in silicon," *Nucl. Instr. Meth. A*, vol. 584, no. 2-3, pp. 436–439, 2008.

[153] J. A. Bearden, "X-ray wavelengths," *Rev. Mod. Phys.*, vol. 39, no. 1, p. 78, 1967.

[154] J. Chen and I. De Wolf, "Study of damage and stress induced by backgrinding in Si wafers," *Semicond. Sci. Technol.*, vol. 18, no. 4, p. 261, 2003.

[155] N. Bacchetta *et al.*, "Improvement in breakdown characteristics with multiguard structures in microstrip silicon detectors for CMS," *Nucl. Instr. Meth. A*, vol. 461, no. 1-3, pp. 204–206, 2001.

[156] N. Alipour Tehrani, *Test-beam measurements and simulation studies of thin pixel sensors for the CLIC vertex detector.* PhD thesis, ETH Zurich, 2017. `https://cds.cern.ch/record/2270788?ln=de`.

[157] R. Diener *et al.*, "The DESY II Test Beam Facility," *Nucl. Instr. Meth. A*, vol. 922, pp. 265–286, 2019.

[158] H. Jansen *et al.*, "Performance of the EUDET-type beam telescopes," *EPJ Tech. Instrum.*, vol. 3, pp. 1–20, 2016.

[159] Y. Liu *et al.*, "EUDAQ2—A flexible data acquisition software framework for common test beams," *JINST*, vol. 14, no. 10, p. P10033, 2019.

[160] P. Baesso, D. Cussans, and J. Goldstein, "The AIDA-2020 TLU: a flexible trigger logic unit for test beam facilities," *JINST*, vol. 14, no. 09, p. P09019, 2019.

[161] J. Baudot *et al.*, "First test results of MIMOSA-26, a fast CMOS sensor with integrated zero suppression and digitized output," *2009 IEEE Nuclear Science Symposium Conference Record (NSS/MIC)*, pp. 1169–1173, 2009.

[162] C. Hu-Guo *et al.*, "First reticule size MAPS with digital output and integrated zero suppression for the EUDET-JRA1 beam telescope," *Nucl. Instr. Meth. A*, vol. 623, no. 1, pp. 480–482, 2010.

[163] T. Poikela *et al.*, "Timepix3: a 65k channel hybrid pixel readout chip with simultaneous ToA/ToT and sparse readout," *JINST*, vol. 9, no. 05, pp. C05013–C05013, 2014.

[164] J. Visser, M. Van Beuzekom, H. Boterenbrood, B. Van Der Heijden, J. Muñoz, S. Kulis, B. Munneke, and F. Schreuder, "SPIDR: a read-out system for Medipix3 & Timepix3," *JINST*, vol. 10, no. 12, p. C12028, 2015.

[165] F. Pitters *et al.*, "Time resolution studies of Timepix3 assemblies with thin silicon pixel sensors," *JINST*, vol. 14, no. 05, p. P05022, 2019.

[166] "Data sheet M-060, M-061, M-062 Präzisionsdrehtisch." Online: `https://www.physikinstrumente.de/de/produkte/rotationstische/m-060-m-061-m-062-praezisionsdrehtisch-703100/`, accessed 12/2021.

[167] D. Dannheim *et al.*, "Corryvreckan: A Modular 4D Track Reconstruction and Analysis Software for Test Beam Data," *JINST*, vol. 16, no. 03, p. P03008, 2021.

[168] J. Kröger, S. Spannagel, and M. Williams, "Corryvreckan User Manual." `https://project-corryvreckan.web.cern.ch/project-corryvreckan/`, accessed 12/2021.

[169] "The Corryvreckan project." Online : `https://gitlab.cern.ch/corryvreckan/corryvreckan/`, accessed 12/2021.

[170] J. Kröger and L. Huth, "Efficient Analysis of Test-beam Data with the Corryvreckan Framework," in *Proceedings of the 29th International Workshop on Vertex Detectors (VERTEX2020)*, p. 010024, 2021.

[171] C. Kleinwort, "General Broken Lines as advanced track fitting method," *Nucl. Instr. Meth. A*, vol. 673, pp. 107–110, 2012.

[172] V. Blobel, C. Kleinwort, and F. Meier, "Fast alignment of a complex tracking detector using advanced track models," *Comput. Phys. Commun.*, vol. 182, no. 9, pp. 1760–1763, 2011.

[173] F. James and M. Roos, “Minuit-a system for function minimization and analysis of the parameter errors and correlations,” *Comput. Phys. Commun.*, vol. 10, no. 6, pp. 343–367, 1975.

[174] E. Belau *et al.*, “Charge collection in silicon strip detectors,” *Nucl. Instr. Meth. Phys. Res.*, vol. 214, no. 2, pp. 253 – 260, 1983.

[175] K. Akiba *et al.*, “Charged Particle Tracking with the Timepix ASIC,” *Nucl. Instr. Meth. A*, vol. 661, pp. 31–49, 2012.

[176] R. Turchetta, “Spatial resolution of silicon microstrip detectors,” *Nucl. Instr. Meth. A*, vol. 335, no. 1, pp. 44–58, 1993.

[177] T. Kawasaki *et al.*, “Measurement of the spatial resolution of wide-pitch silicon strip detectors with large incident angle,” *IEEE Trans. Nucl. Sci.*, vol. 44, no. 3, pp. 708–712, 1997.

[178] S. Spannagel and H. Jansen, “GBL Track Resolution Calculator v2.0, 2016.” `https://github.com/simonspa/resolution-simulator`, accessed 01/202.

[179] F. M. Pitters, *Silicon detector technologies for future particle collider experiments.* PhD thesis, TU Wien, 2019. `https://cds.cern.ch/record/2714709?ln=de`.

[180] C. J. Clopper and E. S. Pearson, “The use of confidence of fiducial limits illustrated in the case of the binomial,” *Biometrika*, vol. 26, pp. 404–413, 12 1934.

[181] Y. Mizushima, Y. Kim, T. Nakamura, R. Sugie, H. Hashimoto, A. Uedono, and T. Ohba, “Impact of back-grinding-induced damage on Si wafer thinning for three-dimensional integration,” *Jpn. J. Appl. Phys.*, vol. 53, no. 5S2, p. 05GE04, 2014.

[182] M. Šuljić, “The Novel ALICE Inner Tracking System (ITS3) Based on Truly Cylindrical, Wafer-Scale Monolithic Active Pixel Sensors,” *Proceedings of the 29th International Workshop on Vertex Detectors (VERTEX2020)*, p. 010011, 2021.

[183] J. Hasenbichler, *Development of Novel Pixel CMOS Sensors Optimized for Time Resolution.* PhD thesis, TU Wien, 2021.

[184] V. Bartsch *et al.*, “An algorithm for calculating the Lorentz angle in silicon detectors,” *Nucl. Instr. Meth. A*, vol. 497, no. 2-3, pp. 389–396, 2003.

[185] B. Henrich and R. Kaufmann, “Lorentz-angle in irradiated silicon,” *Nucl. Instr. Meth. A*, vol. 477, no. 1-3, pp. 304–307, 2002.

[186] W. Adam *et al.*, "The CMS Phase-1 pixel detector upgrade," *JINST*, vol. 16, no. 02, p. P02027, 2021.

[187] B. Smart, "ATLAS pixel detector design for the HL-LHC," *JINST*, vol. 12, no. 02, p. C02011, 2017.

[188] S. Cartier, *Development of a 25 micron pixel detector for phase-contrast imaging.* PhD thesis, ETH Zurich, 2017.

[189] J. Therhaag *et al.*, "TMVA-Toolkit for multivariate data analysis," in *AIP Conference Proceedings*, vol. 1504, pp. 1013–1016, 2012.

[190] F. Nwanganga and M. Chapple, *Practical Machine Learning in R.* John Wiley & Sons, 2020.

[191] C. G. Broyden, "The convergence of a class of double-rank minimization algorithms: 2. The new algorithm," *IMA J. Appl. Math.*, vol. 6, no. 3, pp. 222–231, 1970.

[192] R. Fletcher, "A new approach to variable metric algorithms," *Comput. J.*, vol. 13, no. 3, pp. 317–322, 1970.

[193] D. Goldfarb, "A family of variable-metric methods derived by variational means," *Math. Comput.*, vol. 24, no. 109, pp. 23–26, 1970.

[194] D. F. Shanno, "Conditioning of quasi-Newton methods for function minimization," *Math. Comput.*, vol. 24, no. 111, pp. 647–656, 1970.

[195] "Synopsys sentaurus device." Online : `https://www.synopsys.com`, accessed 12/2021.

[196] S. Meroli, D. Passeri, and L. Servoli, "Energy loss measurement for charged particles in very thin silicon layers," *JINST*, vol. 6, p. P06013, 2011.

[197] N. Metropolis and S. Ulam, "The Monte Carlo method," *J. Am. Stat. Assoc.*, vol. 44, no. 247, pp. 335–341, 1949.

[198] S. Spannagel *et al.*, "Allpix^2: A modular simulation framework for silicon detectors," *Nucl. Instr. Meth. A*, vol. 901, pp. 164 – 172, 2018.

[199] "The Allpix Squared project." Online : `https://cern.ch/allpix-squared/`, accessed 12/2021.

[200] "Garfield++ Simulation Toolkit." Online: `https://garfieldpp.web.cern.ch/garfieldpp/`, accessed 02/2022.

[201] G. Kramberger, "KDetSim - a simple way to simulate detectors." Online: `http://kdetsim.org`, accessed 02/2022.

[202] M. Swartz, "A detailed simulation of the CMS pixel sensor," tech. rep., CERN, 2002. CERN-CMS-NOTE-2002-027.

[203] S. Agostinelli *et al.*, "Geant4 – a simulation toolkit," *Nucl. Instr. Meth. A*, vol. 506, no. 3, pp. 250 – 303, 2003.

[204] J. Allison *et al.*, "Geant4 developments and applications," *IEEE T. Nucl. Sci.*, vol. 53, pp. 270–278, 2 2006.

[205] J. Allison *et al.*, "Recent developments in Geant4," *Nucl. Instr. Meth. A*, vol. 835, no. Supplement C, pp. 186 – 225, 2016.

[206] M. Vicente Barreto Pinto, *New pixel-detector technologies for the ATLAS ITk upgrade and the CLIC vertex detector.* PhD thesis, Geneva University, 2019. `https://cds.cern.ch/record/2707117`.

[207] E. Fehlberg, "Low-order classical Runge-Kutta formulas with stepsize control and their application to some heat transfer problems," NASA Technical Report NASA-TR-R-315, NASA, 1969. `https://ntrs.nasa.gov/search.jsp?R=19690021375`.

[208] C. K. Maiti, *Introducing Technology Computer-Aided Design (TCAD): Fundamentals, Simulations, and Applications.* Jenny Stanford Publishing, 2017.

[209] R. Mazur and D. Dickey, "A spreading resistance technique for resistivity measurements on silicon," *J. Electrochem. Soc.*, vol. 113, no. 3, p. 255, 1966.

[210] D. Dannheim *et al.*, "Combining TCAD and Monte Carlo Methods to Simulate CMOS Pixel Sensors with a Small Collection Electrode using the Allpix^2 Framework," *Nucl. Instr. Meth. A*, vol. 964, p. 163784, 2020.

[211] K. Dort, "Test-beam and simulation studies for the CLICTD technology demonstrator - a monolithic CMOS pixel sensorwith a small collection diode," Tech. Rep. CLICdp-Conf-2021-003, CERN, Geneva, Jun 2021. `hhttps://cds.cern.ch/record/2773808`.

[212] G. Deptuch, *New generation of monolithic active pixel sensors for charged particle detection.* PhD thesis, Université Louis Pasteur-Strasbourg I, 2002.

[213] F. Iguaz *et al.*, "Characterization of a depleted monolithic pixel sensors in 150 nm CMOS technology for the ATLAS Inner Tracker upgrade," *Nucl. Instr. Meth. A*, vol. 936, pp. 652–653, 2019.

[214] J. Brodzicka *et al.*, "Physics achievements from the Belle experiment," *Prog. Theor. Exp. Phys.*, vol. 2012, no. 1, 2012.

[215] L. L. Gioi *et al.*, "Belle achievements and Belle II prospects for CP violation," *J. Phys. Conf. Ser.*, vol. 873, no. 1, p. 012022, 2017.

[216] T. Konno, "Tau LFV and LNV at Belle II," in *The 21st international workshop on neutrinos from accelerators*, p. 89, 2019.

[217] S. Godfrey and S. L. Olsen, "The exotic XYZ charmonium-like mesons," *Annu. Rev. Nucl. Part. Sci.*, vol. 58, pp. 51–73, 2008.

[218] F. Abudinén *et al.*, "Search for Axionlike Particles Produced in e+ e- Collisions at Belle II," *Phys. Rev. Lett.*, vol. 125, no. 16, p. 161806, 2020.

[219] M. J. Dolan, T. Ferber, C. Hearty, F. Kahlhoefer, and K. Schmidt-Hoberg, "Revised constraints and Belle II sensitivity for visible and invisible axion-like particles," *J. High Energ. Phys*, vol. 2017, no. 12, pp. 1–29, 2017.

[220] I. Adachi *et al.*, "Search for an invisibly decaying Z boson at Belle II in e+ e- $\rightarrow$ μ+ μ-(e$\pm\mu$) plus missing energy final states," *Phys. Rev. Lett.*, vol. 124, no. 14, p. 141801, 2020.

[221] "KEK News Website." Online : `https://www.kek.jp/en/newsroom/2019/03/11/1600/`, accessed 12/2021.

[222] K. Akai *et al.*, "SuperKEKB collider," *Nucl. Instr. Meth. A*, vol. 907, pp. 188–199, 2018.

[223] Y. Ohnishi *et al.*, "Accelerator design at SuperKEKB," *Prog. Theor. Exp. Phys.*, vol. 2013, no. 3, 2013.

[224] F. Bernlochner, B. Deschamps, J. Dingfelder, C. Marinas, and C. Wessel, "Online Data Reduction for the Belle II Experiment using DATCON," *EPJ Web of Conf.*, vol. 150, p. 00014, 2017.

[225] H.-G. Moser *et al.*, "The Belle II DEPFET pixel detector," *Nucl. Instr. Meth. A*, vol. 831, pp. 85–87, 2016.

[226] T. Hara, T. Kuhr, and Y. Ushiroda, "Belle II coordinate system and guideline of Belle II numbering scheme," *Belle II Note.* `https://indico.mpp.mpg.de/event/2308/contributions/4092/attachments/3414/3799/Belle2NumberingScheme.pdf`.

[227] M. Friedl *et al.*, “The Belle II silicon vertex detector,” *Nucl. Instr. Meth. A*, vol. 732, pp. 83–86, 2013.

[228] N. Taniguchi, “Central drift chamber for Belle-II,” *JINST*, vol. 12, no. 06, p. C06014, 2017.

[229] A. A. Watson, “The discovery of Cherenkov radiation and its use in the detection of extensive air showers,” *Nucl. Phys. B*, vol. 212, pp. 13–19, 2011.

[230] E. Torassa *et al.*, “Particle identification with the TOP and ARICH detectors at Belle II,” *Nucl. Instr. Meth. A*, vol. 824, pp. 152–155, 2016.

[231] K. Inami *et al.*, “MCP-PMT production for Belle II TOP detector and further R&D,” *Nucl. Instr. Meth. A*, vol. 936, pp. 556–557, 2019.

[232] V. Aulchenko *et al.*, “Electromagnetic calorimeter for Belle II,” in *J. Phys. Conf. Ser.*, vol. 587, p. 012045, 2015.

[233] C. Lacasta, “The DEPFET pixel detector for the Belle II experiment at Super KEKB,” in *Proceedings of the 22nd International Workshop on Vertex Detectors (Vertex2013). 15-20 September*, p. 5, 2013.

[234] H. Ye *et al.*, “Commissioning and performance of the Belle II pixel detector,” *Nucl. Instr. Meth. A*, vol. 987, p. 164875, 2021.

[235] R. H. Richter *et al.*, “Design and technology of DEPFET pixel sensors for linear collider applications,” *Nucl. Instr. Meth. A*, vol. 511, no. 1-2, pp. 250–256, 2003.

[236] K. Gärtner and R. Richter, “DEPFET sensor design using an experimental 3D device simulator,” *Nucl. Instr. Meth. A*, vol. 568, no. 1, pp. 12–17, 2006.

[237] I. Perić, P. Fischer, J. Knopf, and T. H. H. Nguyen, “DCDB and SWITCHERB, the readout ASICS for Belle II DEPFET pixel detector,” in *2018 IEEE Nucl. Sci. Symp. Med. Imaging Conf. NSS/MIC 2018 - Proc.*, pp. 1536–1539, 2011.

[238] J. Knopf, P. Fischer, C. Kreidl, and I. Peric, “A 256 channel 8-Bit current digitizer ASIC for the Belle-II PXD,” *JINST*, vol. 6, no. 01, p. C01085, 2011.

[239] H. Krüger *et al.*, “Front-end electronics for DEPFET pixel detectors at SuperBelle (BELLE II),” *Nucl. Instr. Meth. A*, vol. 617, no. 1-3, pp. 337–341, 2010.

[240] D. Sun *et al.*, “Belle2Link: A global data readout and transmission for Belle II experiment at KEK,” *Phys. Procedia*, vol. 37, pp. 1933–1939, 2012.

[241] T. Higuchi *et al.*, "Development of a PCI based data acquisition platform for high intensity accelerator experiments," *hep-ex/0305088*, 2003.

[242] R. Itoh, T. Higuchi, M. Nakao, S. Suzuki, and S. Lee, "Data flow and high level trigger of Belle II DAQ system," *IEEE Trans. Nucl. Sci.*, vol. 60, no. 5, pp. 3720–3724, 2013.

[243] T. Geßler, W. Kühn, J. S. Lange, Z. Liu, D. Münchow, B. Spruck, and J. Zhao, "The ONSEN data reduction system for the Belle II pixel detector," *IEEE Trans. Nucl. Sci.*, vol. 62, no. 3, pp. 1149–1154, 2015.

[244] D. Levit, I. Konorov, D. Greenwald, and S. Paul, "FPGA based data read-out system of the Belle II pixel detector," *IEEE Trans. Nucl. Sci.*, vol. 62, no. 3, pp. 1033–1039, 2015.

[245] A. Moll, *Comprehensive study of the background for the Pixel Vertex Detector at Belle II.* PhD thesis, LMU Munich, 2015.

[246] A. Piwinski, "The Touschek effect in strong focusing storage rings," *physics/9903034*, 1999.

[247] H. Nakano and H. Yamamoto, "A simulation study of beam backgrounds at the KEKB and Super KEKB colliders," 2011. Tohoku University, Master thesis.

[248] S. Hashimoto, M. Hazumi, J. Haba, J. Flanagan, and Y. Ohnishi, "Letter of intent for KEK Super B Factory," tech. rep., High Energy Accelerator Research Organization, 2004.

[249] J. Schwinger, "On the classical radiation of accelerated electrons," *Phys. Rev.*, vol. 75, no. 12, p. 1912, 1949.

[250] F. Elder, A. Gurewitsch, R. Langmuir, and H. Pollock, "Radiation from electrons in a synchrotron," *Phys. Rev.*, vol. 71, no. 11, p. 829, 1947.

[251] A. Paladino, "Beam background evaluation at SuperKEKB and Belle II," *JINST*, vol. 15, no. 07, p. C07023, 2020.

[252] H. Bhabha, "The scattering of positrons by electrons with exchange on Dirac's theory of the positron," *Proc. R. Soc. A*, vol. 154, no. 881, pp. 195–206, 1936.

[253] V. Balakin, A. Bukin, E. Pakhtusova, V. Sidorov, and A. Khabakhpashev, "Evidence for electron-positron pair electroproduction," *Phys. Lett. B*, vol. 34, no. 7, pp. 663–664, 1971.

[254] V. Baier and V. Fadin, “Description of Electroproduction Processes by Using the Approximation of Quasi-real Photons,” *Sov. Phys. JETP*, vol. 36, no. 3, 1973.

[255] T. Kuhr, C. Pulvermacher, M. Ritter, T. Hauth, and N. Braun, “The Belle II core software,” *Comput. Softw. Big Sci.*, vol. 3, no. 1, pp. 1–12, 2019.

[256] Z. Drasal, K. Prothmann, and B. Schwenker, “Silicon simulation code for Belle II and ILC,” in *The 20th Anniversary International Workshop on Vertex Detectors*, vol. 137, p. 027, SISSA Medialab, 2012.

[257] “Strategic Accelerator Design.” Online : `https://acc-physics.kek.jp/SAD/`, accessed 01/2022.

[258] S. Jadach, W. Płaczek, and B. Ward, “BHWIDE 1.00: O (α) YFS exponentiated Monte Carlo for Bhabha scattering at wide angles for LEP1/SLC and LEP2,” *Phys. Lett. B*, vol. 390, no. 1-4, pp. 298–308, 1997.

[259] R. Kleiss and H. Burkhardt, “BBBREM—Monte Carlo simulation of radiative Bhabha scattering in the very forward direction,” *Comput. Phys. Commun.*, vol. 81, no. 3, pp. 372–380, 1994.

[260] F. A. Berends, P. Daverveldt, and R. Kleiss, “Complete lowest-order calculations for four-lepton final states in electron-positron collisions,” *Nucl. Phys. B*, vol. 253, pp. 441–463, 1985.

[261] J. Preskill, “Magnetic monopoles,” *Annu. Rev. Nucl. Part. Sci.*, vol. 34, no. 1, pp. 461–530, 1984.

[262] J. Schwinger, “Magnetic charge and quantum field theory,” *Phys. Rev.*, vol. 144, no. 4, p. 1087, 1966.

[263] A. Kusenko, L. C. Loveridge, and M. Shaposhnikov, “Supersymmetric dark-matter Q-balls and their interactions in matter,” *Phys. Rev. D*, vol. 72, no. 2, p. 025015, 2005.

[264] N. E. Mavromatos and V. A. Mitsou, “Magnetic monopoles revisited: Models and searches at colliders and in the Cosmos,” *Int. J. Mod. Phys. B*, vol. 35, no. 23, p. 2030012, 2020.

[265] V. A. Mitsou, “Searches for magnetic monopoles: A review,” in *Multidisciplinary Digital Publishing Institute Proceedings*, vol. 13, p. 10, 2019.

[266] P. A. M. Dirac, “Quantised singularities in the electromagnetic field,” *Proc. R. Soc. Lond. A*, vol. 133, no. 821, pp. 60–72, 1931.

[267] J. Pinfold *et al.*, “Technical design report of the MoEDAL experiment,” Tech. Rep. MoEDAL-TDR-001, 2009. `https://cds.cern.ch/record/1181486`.

[268] A. Polyakov, “Spectrum of particles in quantum field theory,” *JETP Lett.*, vol. 20, pp. 430–433, 1974.

[269] G. ’t Hooft, “Magnetic monopoles in unified theories,” *Nucl. Phys. B*, vol. 79, pp. 276–284, 1974.

[270] P. Langacker and S.-Y. Pi, “Magnetic monopoles in grand unified theories,” *Phys. Rev. Lett.*, vol. 45, no. 1, p. 1, 1980.

[271] Y. Cho and D. Maison, “Monopole configuration in Weinberg-Salam model,” *Phys. Lett. B*, vol. 391, no. 3-4, pp. 360–365, 1997.

[272] G. Kalbfleisch, K. Milton, M. Strauss, L. Gamberg, E. Smith, and W. Luo, “Improved experimental limits on the production of magnetic monopoles,” *Phys. Rev. Lett.*, vol. 85, no. 25, p. 5292, 2000.

[273] G. Kalbfleisch, W. Luo, K. Milton, E. Smith, and M. Strauss, “Limits on production of magnetic monopoles utilizing samples from the D0 and CDF detectors at the Fermilab Tevatron,” *Phys. Rev. D*, vol. 69, no. 5, p. 052002, 2004.

[274] T. Dougall and S. D. Wick, “Dirac magnetic monopole production from photon fusion in proton collisions,” *Eur. Phys. J. A*, vol. 39, no. 2, pp. 213–217, 2009.

[275] M. Drees, R. M. Godbole, M. Nowakowski, and S. D. Rindani, “$\gamma\gamma$ processes at high energy pp colliders,” *Phys. Rev. D*, vol. 50, no. 3, p. 2335, 1994.

[276] S. Baines, N. Mavromatos, V. Mitsou, J. Pinfold, and A. Santra, “Monopole production via photon fusion and Drell–Yan processes: MadGraph implementation and perturbativity via velocity-dependent coupling and magnetic moment as novel features,” *Eur. Phys. J. C*, vol. 78, no. 11, pp. 1–36, 2018.

[277] L. Bracci, G. Fiorentini, and R. Tripiccione, “On the energy loss of very-slowly-moving magnetic monopoles,” *Nucl. Phys. B*, vol. 238, no. 1, pp. 167–180, 1984.

[278] S. Ahlen and K. Kinoshita, “Calculation of the stopping power of very-low-velocity magnetic monopoles,” *Phys. Rev. D*, vol. 26, no. 9, p. 2347, 1982.

[279] P. Musset, M. Price, and E. Lohrmann, “Search for magnetic monopoles in electron-positron collisions at 34 GeV CM energy,” *Phys. Lett. B*, vol. 128, no. 5, pp. 333–335, 1983.

[280] J. Derkaoui, G. Giacomelli, T. Lari, A. Margiotta, M. Ouchrif, L. Patrizii, V. Popa, and V. Togo, “Energy losses of magnetic monopoles and of dyons in the earth,” *Astropart. Phys.*, vol. 9, no. 2, pp. 173–183, 1998.

[281] J. Lindhard, “On the properties of a gas of charged particles,” *Dan. Vid. Selsk Mat.-Fys. Medd.*, vol. 28, p. 8, 1954.

[282] L. Patrizii and M. Spurio, “Status of Searches for Magnetic Monopoles,” *Annu. Rev. Nucl. Part. Sci.*, vol. 65, pp. 279–302, 2015.

[283] M. J. Mulhearn, “A direct search for Dirac magnetic monopoles,” tech. rep., Fermi National Accelerator Lab.(FNAL), Batavia, IL (United States), 2004.

[284] K. Dort, “Search for Highly Ionizing Particles with the Pixel Detector in the Belle II Experiment,” 2019. Master thesis.

[285] D. E. Groom, “In search of the supermassive magnetic monopole,” *Phys. Rep.*, vol. 140, no. 6, pp. 323–373, 1986.

[286] D. P. Hogan, D. Z. Besson, J. P. Ralston, I. Kravchenko, and D. Seckel, “Relativistic magnetic monopole flux constraints from RICE,” *Phys. Rev. D*, vol. 78, no. 7, p. 075031, 2008.

[287] M. Detrixhe *et al.*, “Ultrarelativistic magnetic monopole search with the ANITA-II balloon-borne radio interferometer,” *Phys. Rev. D*, vol. 83, no. 2, p. 023513, 2011.

[288] M. Fairbairn, A. Kraan, D. Milstead, T. Sjöstrand, P. Skands, and T. Sloan, “Stable massive particles at colliders,” *Phys. Rep.*, vol. 438, no. 1, pp. 1–63, 2007.

[289] K. A. Milton, “Theoretical and experimental status of magnetic monopoles,” *Rep. Prog. Phys.*, vol. 69, no. 6, p. 1637, 2006.

[290] I. Prudiev. Master thesis - in preparation.

[291] D. Neverov, “Dark sector physics with Belle II,” *PoS (ICHEP 2018)*, vol. 73, 2018.

[292] S. Bähr, O. Sander, M. Heck, C. Pulvermacher, M. Feindt, and J. Becker, “Online-analysis of hits in the Belle-II pixeldetector for separation of slow pions from background,” vol. 664, no. 9, p. 092001, 2015.

[293] X. J. Zhu, “Semi-supervised learning literature survey,” tech. rep., University of Wisconsin-Madison Department of Computer Sciences, 2005.

[294] J. Bilk and J. S. Lange, “Employing Deep Learning to Find Slow Pions in the Pixel Detector in the Belle II Experiment,” 2021. Justus-Liebig-University Giessen, Master thesis.

[295] T. Schellhaas and J. S. Lange, “Identification of slow pions by Support Vector Machines: Identifizierung von langsamen Pionen durch Support Vector Machines,” 2022. Justus-Liebig-University Giessen, Bachelor thesis.

[296] J. Schmidhuber, “Deep learning in neural networks: An overview,” *Neural Netw.*, vol. 61, pp. 85–117, 2015.

[297] H. Ramchoun, M. A. J. Idrissi, Y. Ghanou, and M. Ettaouil, “Multilayer Perceptron: Architecture Optimization and Training,” *Int. J. Interact. Multim. Artif. Intell.*, vol. 4, no. 1, pp. 26–30, 2016.

[298] S. Sharma, S. Sharma, and A. Athaiya, “Activation functions in neural networks,” *Int. J. Appl. Sci. Eng*, vol. 6, no. 12, pp. 310–316, 2017.

[299] J. Brownlee, “A gentle introduction to the rectified linear unit (ReLU),” *Machine learning mastery*, vol. 6, 2019.

[300] K. Janocha and W. M. Czarnecki, “On loss functions for deep neural networks in classification,” *arXiv:1702.05659*, 2017.

[301] S.-i. Amari, “Backpropagation and stochastic gradient descent method,” *Neurocomputing*, vol. 5, no. 4-5, pp. 185–196, 1993.

[302] D. P. Kingma and J. Ba, “Adam: A method for stochastic optimization,” *arXiv:1412.6980*, 2014.

[303] D. E. Rumelhart and D. Zipser, “Feature discovery by competitive learning,” *Cogn. Sci.*, vol. 9, no. 1, pp. 75–112, 1985.

[304] T. Kohonen, “Self-organized formation of topologically correct feature maps,” *Biological cybernetics*, vol. 43, no. 1, pp. 59–69, 1982.

[305] K. Kiviluoto, “Topology preservation in Self-Organizing Maps,” in *Proceedings of International Conference on Neural Networks (ICNN’96)*, vol. 1, pp. 294–299, IEEE, 1996.

[306] C. Zhou and R. C. Paffenroth, “Anomaly detection with robust deep autoencoders,” in *Proceedings of the 23rd ACM SIGKDD international conference on knowledge discovery and data mining*, pp. 665–674, 2017.

[307] T. Fawcett, “An introduction to ROC analysis,” *Pattern Recognit. Lett.*, vol. 27, no. 8, pp. 861–874, 2006.

[308] C. E. Metz, “Basic principles of ROC analysis,” in *Semin. Nucl. Med.*, vol. 8, pp. 283–298, Elsevier, 1978.

[309] J. A. Hanley and B. J. McNeil, “The meaning and use of the area under a receiver operating characteristic (ROC) curve,” *Radiology*, vol. 143, no. 1, pp. 29–36, 1982.

[310] H. Tanigawa *et al.*, “Beam background study for the Belle II Silicon Vertex Detector,” *Nucl. Instr. Meth. A*, vol. 982, p. 164580, 2020.

[311] S. Käs, “Multiparameter Analysis of the Belle II Pixeldetector’s Data Using Principal Components Analysis and Neural Networks,” 2019. Bachelor thesis, Justus-Liebig-Universität Giessen.

[312] “PyTorch GitHub Repository.” Online : `https://github.com/pytorch/pytorch`, accessed 01/2022.

[313] “PyTorch Website.” Online : `https://pytorch.org`, accessed 01/2022.

[314] G. Vettigli, “MiniSom: minimalistic and NumPy-based implementation of the Self Organizing Map,” 2018. Online : `https://github.com/JustGlowing/minisom/`, accessed 01/2022.

[315] J. An and S. Cho, “Variational autoencoder based anomaly detection using reconstruction probability,” *Special Lecture on IE*, vol. 2, no. 1, pp. 1–18, 2015.

[316] H. Steck, “Embarrassingly shallow autoencoders for sparse data,” in *The World Wide Web Conference*, pp. 3251–3257, 2019.

[317] A. Ng *et al.*, “Sparse autoencoder,” *CS294A Lecture notes*, vol. 72, no. 2011, pp. 1–19, 2011.

[318] A. Creswell, T. White, V. Dumoulin, K. Arulkumaran, B. Sengupta, and A. A. Bharath, “Generative adversarial networks: An overview,” *IEEE Signal Process. Mag.*, vol. 35, no. 1, pp. 53–65, 2018.

[319] M. Erdmann, J. Glombitza, and T. Quast, “Precise simulation of electromagnetic calorimeter showers using a Wasserstein Generative Adversarial Network,” *Comput. Softw. Big Sci.*, vol. 3, no. 1, pp. 1–13, 2019.

[320] R. Di Sipio, M. F. Giannelli, S. K. Haghighat, and S. Palazzo, “DijetGAN: a Generative-Adversarial Network approach for the simulation of QCD dijet events at the LHC,” *J. High Energy Phys.*, vol. 2019, no. 8, pp. 1–17, 2019.

[321] “The Tangerine project: Development of high-resolution 65 nm silicon MAPS.” Online : `https://indico.cern.ch/event/1044975/contributions/4663650/`, accessed 01/2022.

[322] C. Canali, G. Majni, R. Minder, and G. Ottaviani, “Electron and hole drift velocity measurements in silicon and their empirical relation to electric field and temperature,” *IEEE Trans. Elec. Dev.*, vol. 22, no. 11, pp. 1045–1047, 1975.

[323] G. Masetti, M. Severi, and S. Solmi, “Modeling of carrier mobility against carrier concentration in arsenic-, phosphorus-, and boron-doped silicon,” *IEEE Trans. Elec. Dev.*, vol. 30, no. 7, pp. 764–769, 1983.

Acknowledgements

Science is a collaborative effort
- John Bardeen

In these last pages, I would like to express my deepest gratitude to the people who supported this work and helped it come to fruition. I feel enormously privileged to work in a collaborative and supportive environment alongside brilliant mentors, inspiring role models and encouraging friends.

First, a sincere thanks and my deepest respect to apl. Prof. Dr. Sören Lange, who selflessly encouraged and supported me in all aspects of this work. Besides his excellent supervision, tireless counsels and insightful ideas, I feel profoundly inspired by his wide-ranging experience and wisdom of sub-atomic physics, that were a main driving force for me to pursue first a master and then a PhD in this field..

Furthermore, I am profoundly grateful for Prof. Dr. Michael Düren for accepting to be the second referee for this thesis.

My special thanks goes to my supervisor Dr. Dominik Dannheim, who never hesitates to clear the way to make impossible tasks possible, be it in a perpetual struggle for higher beam intensities, access to clean rooms, laboratories and workshops, travel to test-beam facilities or conferences, to name only a small subset. I have profited profoundly from his expertise, motivating attitude and ingenuity that never ceases to amaze me.

Moreover, I would like to express my sincere gratitude to Dr. Magdalena Munker, from whom I learnt innumerable aspects of silicon sensor development and characterisation. My heartfelt thanks and appreciation for all the valuable explanations, guidance and for tirelessly answering my questions.

$> 1.7\,\mathrm{k}$Thanks thanks to Dr. Simon Spannagel for sharing his vast knowledge with me and in particular for his patient coding lessons. His immeasurable enthusiasm is a great source of inspiration and I consider myself extremely lucky to have learnt from him.

To write about all the amazing people at CERN that have been kind and welcoming to me, would fill an entire book, but I would like to point out a few people in particular. Thanks to the amazing ex-EP-LCD and the new EP-DT-TP groups, that effortlessly embraced me into their team. In particular, I would like to thank Dr. Lucie Linssen. In my eyes, she is the very definition of an inspiring, supportive and selfless group leader that always puts the people first and does her utmost to keep hurdles down and morale up. Especially during the hard lockdowns, having her support was invaluable for me.

A big thanks also to the vertex and tracker detector sub-group. I may be biased but I truly believe I joined the best R&D team ever. Thank you for the amazing unforgettable test-beam periods. Each one was a small adventure and even though it was hard work I loved every minute of them. In this context, a big thanks to the DESY test-beam support team that provided continuous technical and motivational assistance that were invaluable for the success of our test-beam campaigns.

Furthermore, there are several friends in the EP-ESE, EP-DT, EP-AID, EP-SFT and EP-ADE groups that I would like to thank for the fruitful discussions and selfless help, that I can hardly do justice in this single sentence. I consider myself highly fortunate to work with such amazing people that have sharp minds and big hearts at the same time. In particular, I would like to express my heartfelt thanks to Dr. Iraklis Kremastiotis and Dr. Rafael Ballabriga for their patient lessons in electrical engineering that empowered me to understand the subtitles of the CLICTD front-end and digital logic. Likewise, a big thank you to Dr. Tomas Vanat for his immediate expert help when it came to readout and slow-control, especially during stressful test-beam periods. Moreover, I appreciate the continuous support and valuable explanations from Dr. Walter Snoeys.

Thanks a lot to the Giessen *Neuro* team for the frequent meetings that made it possible to keep constantly in touch with my home university. I have profited a lot from the useful feedback from so many smart minds. In this context, I would also like to express my heartfelt thanks to Igor Prudiev for his hard work on the monopole studies despite unimaginably difficult times and for his insightful results that were extraordinarily helpful.

A big thanks also to the QCD- and XYZ-*Exoten* team in Giessen. The dynamic and topically diverse environment of our group is delighting and gave me the opportunity to see the bigger picture of our field of research. Additionally, a big thanks to Prof. Dr. Claudia Höhne for kindling my enthusiasm for sub-atomic physics and for being an admirable and altogether amazing group leader.

I am utterly grateful to the CLICdp, Medipix and Belle II collaborations that supported and encouraged this work and offered me the opportunity to learn about various aspects

of High-Energy Physics and beyond.

Thanks a lot to the following people, that dedicated their time to reading parts of this thesis and giving me their valuable feedback and suggestions: Johannes Bilk, Dr. Eric Buschmann, Dr. Dominik Dannheim, Dr. Lennart Huth, Felix Keil, Matthäus Krein, Dr. Iraklis Kremastiotis, Dr. Lucie Linssen, Dmytro Meleshko, Dr. Magdalena Munker, Milou Van Rijnbach, Dr. Simon Spannagel, Dr. Adrian Weber, Philipp Zehetner.

Last but definitely not least, I am forever indebted to my amazing family and friends for their relentless support. To my parents, you are one of my greatest role models and I admire your hard work and treasure your endless support in all matters of life. To my sister, I cannot express how I cherish your well-reflected and thought-provoking views on topics far beyond my horizon and your hilarious humour. Thanks for always having an open ear and the right words.

I acknowledge the support of the Wolfgang Gentner Programme of the German Federal Ministry of Education and Research (grant no. 13E18CHA) and the ideational support of the German Academic Scholarship Foundation.

The measurements leading to these results have been performed at the Test Beam Facility at DESY Hamburg (Germany), a member of the Helmholtz Association (HGF). This project has received funding from the European Union's Horizon 2020 Research and Innovation programme under Grant Agreement no. 654168

Selbstständigkeitserklärung

Hiermit versichere ich, die vorgelegte Thesis selbstständig und ohne unerlaubte fremde Hilfe und nur mit den Hilfen angefertigt zu haben, die ich in der Thesis angegeben habe. Alle Textstellen, die wörtlich oder sinngemäß aus veröffentlichten Schriften entnommen sind, und alle Angaben die auf mündlichen Auskünften beruhen, sind als solche kenntlich gemacht. Bei den von mir durchgeführten und in der Thesis erwähnten Untersuchungen habe ich die Grundsätze gute wissenschaftlicher Praxis, wie sie in der ‚Satzung der Justus-Liebig-Universität zur Sicherung guter wissenschaftlicher Praxis' niedergelegt sind, eingehalten. Gemäß § 25 Abs. 6 der Allgemeinen Bestimmungen für modularisierte Studiengänge dulde ich eine Überprüfung der Thesis mittels Anti-Plagiatssoftware.

______________________________ ______________________________

Datum Unterschrift